Forming Behaviour of Multilayer Metal/Polymer/Metal Systems

Dissertation

zur Erlangung des Doktorgrades
der Ingenieurwissenschaften

vorgelegt von

Mohamed Abd El Hamid Mohamed Harhash

aus Gharbeya / Ägypten

genehmigt von der
Fakultät für Natur- und Materialwissenschaftlichen
der Technischen Universität Clausthal

Tag der mündlichen Prüfung

21.04.2017

Vorsitzender der Promotionskommission:	Prof. Dr.-Ing. Karl-Heinz Spitzer
Hauptberichterstatter:	Prof. Dr.-Ing. Heinz Palkowski
Mitberichterstatter:	Prof. Dr. habil. Adele Carradó
	Prof. Dr.-Ing. Gerhard Ziegmann

Acknowledgments

This doctoral study was carried out in the Department of Metal Forming and Processing, Institute of Metallurgy – Clausthal University of Technology.

All praises to Allah the Almighty for giving me the blessing, chance, strength and endurance to complete this study.

Firstly, I owe my supervisor Prof. Dr.-Ing. Heinz Palkowski a debt of gratitude for the kind invitation to perform the study tasks and additionally for the continuous guidance, support and the chance to attend several German and international scientific events that enrich my knowledge.

I am grateful to the German Academic Exchange Service (DAAD) and the Egyptian Ministry of Higher Education (MoHE) for the financial support in the framework of the German Egyptian Research Long-term Scholarship program (GERLS). Further thanks to the German Research Foundation (DFG) and the PROCOPE scheme for financing the required materials and travel expenses.

The revision and consulting efforts of Prof. Dr. habil. Adele Carradó and Prof. Dr.-Ing. Gerhard Ziegmann are commendable. I thank Prof. Dr.-Ing. Karl-Heinz Spitzer, the faculty dean and Chairperson of the examination committee, for the smooth examination process. Furthermore, I thank Mr. Prof. Dr.-Ing. Stefan Hartmann for the fruitful discussions.

Further thanks are directed to “thyssenkrupp-Rasselstein GmbH” and “Salzgitter Flachstahl GmbH” for providing the different steel materials.

Kind acknowledgments I owe to my current colleagues: Dr. M. Soliman, Mr. F. Foadian, Mr. H. Ibrahim and Mr. J. Nietsch and the previous ones: Dr. O. Sokolova, Ms. V. Harms, Mr. J. Orend, Mr. M. Kühn and Mr. M. Akdesir for their friendly and scientific assist. Moreover, I would like to thank the technical staff of the institute, especially Mrs. N. Bruns, Mrs. S. Lenk, Mr. E. Reinert and Mr. S. Fischer for their technical support. Furthermore, I owe thanks to my students and trainees who supported me performing the experimental tasks.

I cannot thank my family – especially my wife Eman Elfeky and my daughters Shaimaa, Alzahraa, Esraa and Ghaidaa – enough for their motivation, patience and support all over the studying time. Sincere dedication to the memory of my father, who would have been very happy for me. Additionally, great thanks to my mother and brothers for their continuous prayers and support.

This page intentionally left blank

Contents

Nomenclature

Greek symbols

Symbol	Term	Unit
$ß_{0,max}$ or LDR	Maximum or limiting drawing ratio	[-]
$ß_0$	Drawing ratio	[-]
ε_1	Major strain	[-]
ε_2	Minor strain	[-]
ε_t or ε_3	True thickness strain ($\varepsilon_3 = -(\varepsilon_1 + \varepsilon_2)$)	[-]
α	Major/minor strain ratio: $\alpha = \varepsilon_2/\varepsilon_1$	[-]
γ	Shear strain	[-]
ε_w	True strain in width at tensile testing	[-]
θ	Angle to the rolling direction	[°]
τ	Shear stress	[MPa]
Ø	Diameter	[mm]
σ	True stress	[MPa]
ρ	Material density	[g.cm^{-3}]
σ_f	Flow stress	[MPa]
η	Deep drawing efficiency	[-]
k	Tabulated correction factor	[-]
μ	Friction coefficient	[-]

Latin symbols

Symbol	Term	Unit
Δr	Planar anisotropy	[-]
ΔL	Elongation or change in length $\Delta L = L-L_0$	[mm]
mm^{Ø}	Diameter size	[mm]
A	Area	[mm^2]
A_{BH}	Area of the blank under the blank holder	[mm^2]
b	Specimen width	[mm]
d	Instantaneous flange diameter	[mm]
D_0	Blank diameter in deep drawing	[mm]
d_0	Punch diameter in deep drawing	[mm]
D_d	Inner drawing die diameter	[mm]

$d_{F,max}$	Flange diameter at the maximum drawing force ~ 0.77 D_0	[mm]
d_m	Mean deep drawn cup diameter ($d_m = d_0 + t_0$)	[mm]
E	Elastic modulus	[GPa]
e	Engineering strain	[%]
e_f	Strain at failure	[%]
e_u	Uniform strain	[%]
F_{BH}	Blank holder force	[kN]
f_c	Volume fraction of the polymeric core	[-]
F_d	Drawing force	[N]
$F_{d,max}$	Maximum drawing force	[kN]
F_{id}	Ideal forming force	[kN]
F_{shear}	Shear force	[kN]
h	Cup height in deep drawing or dome height in stretch forming	[mm]
I	Second moment of area	[mm^4]
K	Strength coefficient	[MPa]
L	Specimen length	[mm]
L_{OV}	Overlapping length in the single lap shear test	[mm]
L_{OV-Op}	Optimum overlapping length in the single lap shear test	[mm]
n	Strain hardening exponent	[-]
r	Plastic strain ratio or the normal anisotropy	[-]
R	Average normal anisotropy	[-]
R_a	Average surface roughness	[µm]
r_P	Punch corner radius	[mm]
R_z	Maximum height of the roughness profile	[µm]
S	Engineering stress	[MPa]
t or t_0	Thickness or initial sheet thickness	[mm]
T_g	Glass transition temperature	[°C]
T_m	Melting temperature	[°C]
UTS or R_m	Ultimate tensile strength	[MPa]
YS or R_p	Yield strength	[MPa]

Abbreviations

Acronym	Term
BIW	Body-in-white
AR	As-received
Ann	Annealed condition
c	Core layer
DD	Deep drawing/Deep-drawable steel grade
DD1	Deep-drawable steel grade TS245 (0.49 and 0.24 mm thick)
DD2	Deep-drawable steel grade TH470 (0.49 mm thick)
DIC	Digital image correlation
DP	Dual-phase steel; here the HCT500XD grade (0.52 mm thick)
FLC	Forming limit curve or flow limit curve
FML	Fiber metal laminate
FRP	Fiber-reinforced polymers
G-/C-FRP	Glass-/carbon- fiber reinforced polymer
KTL	Cataphoretic painting (in German: kathodische Tauchlackierung, KTL)
LDR	Limiting drawing ratio
LOM	Light optical microscope
MPM	Metal/polymer/metal laminate
PA	Polyamide
PE	Polyethylene
PET	Polyethylene terephthalate
PMT	Peak metal temperature
PP	Polypropylene
PP-PE	Polypropylene-Polyethylene thermoplastic foil
RD	Rolling direction
RE	Reinforcement
ROM	Rule of mixtures
RT	Room temperature
RTM	Resin transfer molding
SLC	“SuperLightCar” project
SPS	Steel/polymer/steel laminate
SRPP	Self-reinforced PP matrix with PP fibers
SS	Stainless steel sheet; here grade 316L (0.5 mm thick)
Ti	Titanium sheet; here the Ti-grade 1 (0.5 mm thick)

1. Motivation and objectives

Due to the increasing demands for energy saving and better environmental impact of vehicles, the need to develop new lightweight materials becomes more essential. Metal/polymer/metal (MPM) sandwich materials provide an innovative substitute for the used commercial sheets because of their lightweight potential with enhanced specific stiffness and thermal and acoustic isolation advantages. An example for that is the reduced structure-borne acoustic levels of Bondal® in the automotive industry compared to conventional solid steel sheet, as shown in **Figure 1.1**. This is due to the viscoelastic core layer that absorbs the vibration energy. Additionally, Bondal® can be applied, for instance, in oil sumps, valve covers and dash panels.

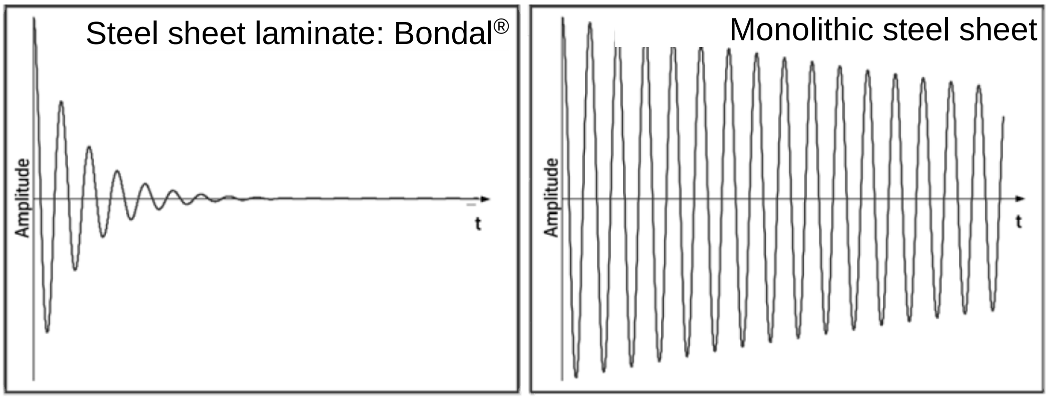

Figure 1.1: Damping properties of Bondal® compared to a conventional steel sheet [Thy09b].

Developing new materials for the body-in-white (BIW) in the automotive application is the focus of some European projects, for instance, the “SuperLightCar - SLC” project [Ber09, Goe05, Goe09]. This project aimed at reducing the BIW by 30% to compensate the overweight of the comfort and security installations while maintaining or even improving the performance compared to a reference car, for instance, developing a new BIW concept for the VW Golf V and Audi TT [Jür09]. This development was achieved using high strength steels, new aluminium alloys and additionally hybrid materials. The weight and material distribution of the SLC concept are shown in **Figure 1.2**. Such concept can result in ~37% weight reduction but with ~12% rise in costs.

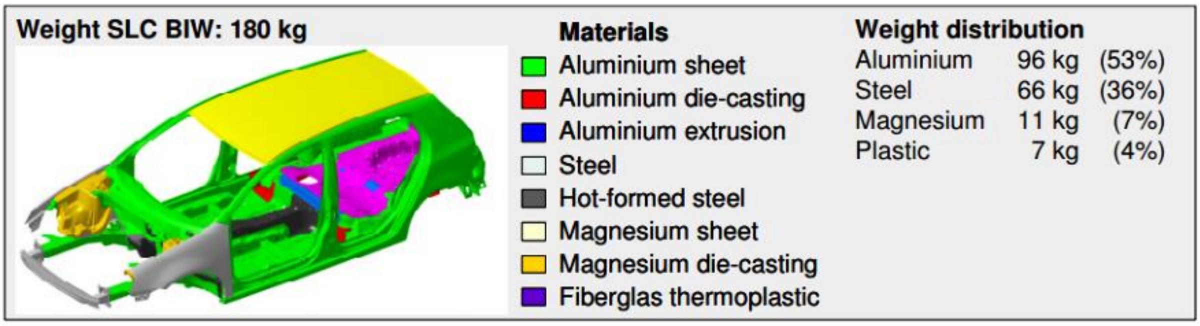

Figure 1.2: Weight and material distribution in the SLC concept of the chosen reference model, i.e. the VW Golf V [Ber09].

After that, 3A Composites GmbH developed several grades of Al/polymer/Al sandwich systems, such as:

1. Alucobond® (0.5 mm Al skin with PE core) [3A15b]. Alucobond® is applied mainly in the transport section, such as rail and transport vehicles, shipbuilding, machine casing and interior construction,
2. Dibond® (0.3 mm Al skin with PE core protected with PS foils) for graphic applications [3A15a] and
3. Hylite® (0.2 mm Al skin with PP core) [3A15c]. Hylite® can ensure service conditions up to 150°C. Hylite® is already applied the automotive market, such as the bonnet of VW Lupo and the deep drawn floor sheets of Audi A2 where about 30% and 65% weight saving can be reached in respect to aluminum and steel sheets, respectively [Bur05].

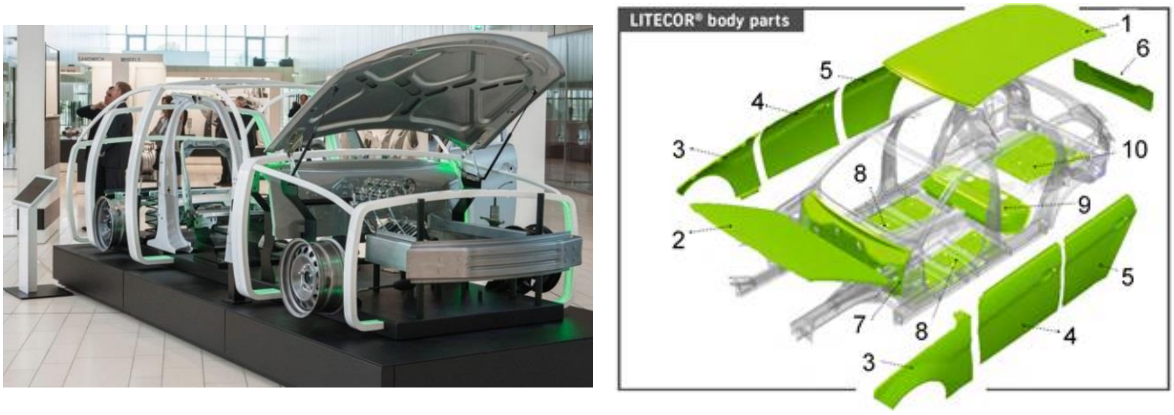

Part No (thickness in [mm])

1. Roof outer panel (0.85)
2. Hood outer panel (0.85)
3. Fender front right/left (0.85)
4. Front door outer panel right/left (0.85)
5. Rear door outer panel right/left (0.85)
6. Tailgate outer panel (0.85)
7. Firewall (0.9)
8. Main floor middle right/left (0.8)
9. Floor panel rear seat (0.9)
10. Floor Rear (0.8)

Figure 1.3: Litecor® applications in car body components and their thicknesses in VW Polo R WRC [Thy14e, Thy14a].

Later, the thyssenkrupp “InCar®plus” project was concerned with a major contribution to the weight reduction of the vehicle body as well as the other fields, such as cost-efficiency and sustainability. InCar®plus solutions aimed at saving up to 60% on weight and up to 10 % on cost. In the frame of this project, several parts of steel/polymer/steel (SPS) laminates called “Litecor®” (steel/PA-PE/steel) are involved in “VW Polo R WRC”, as shown in **Figure 1.3** [Thy14a]. The main advantage of Litecor®, besides the weight saving potential, is that it can withstand higher processing and service temperatures like the KTL (Cataphoretic painting) coating conditions due to the higher melting temperature of its thermoplastic core, namely the PA/PE blend, compared to the PP core of Hylite®.

1.1. Objectives of the study

Despite the powerful weight reduction contribution of the MPM-laminates, several challenges face their production and processing due to their inhomogeneous laminar structure. Therefore, several theses, such as [Bol14, Buh14, Jas12, Lan06, Nut08, Sok12] were concerned with characterizing different laminated systems, mostly commercial ones.

The current thesis gives a contribution to the earlier studies by means of characterizing tailored formable MPM-laminates that can realize the demand for complex structures in various engineering applications, such as the automotive industry.

Figure 1.4 shows an overview of the study approaches and experimental methodologies in order to reach that general goal. The main aims of this study are to deliver design guidelines for production and shaping of formable, symmetric and asymmetric multilayered sandwich sheets considering different surface conditions and thicknesses.

For achieving these general goals, the following solution approaches were proposed:

1. Selecting the proper material combinations to achieve the application constraints. The applicability of such MPM can be extended to consider the biomedical fields in addition to the engineering ones based on the used material combinations. Therefore, the materials for the skin, core and the adhesive layers were properly selected to achieve these goals.
2. Processing the MPM through a fast, reproducible production scheme. The production of the sheet-like MPM was accomplished using a compatible metal/polymer adhesive agent in the lab scale by roll bonding technology simulating the so-called “coil coating process”. This process enables a continuous production operation with fast production time. The advantage here is the flexibility in tailoring arbitrary structures of the MPM with the desired properties which enable defining the processing limits.

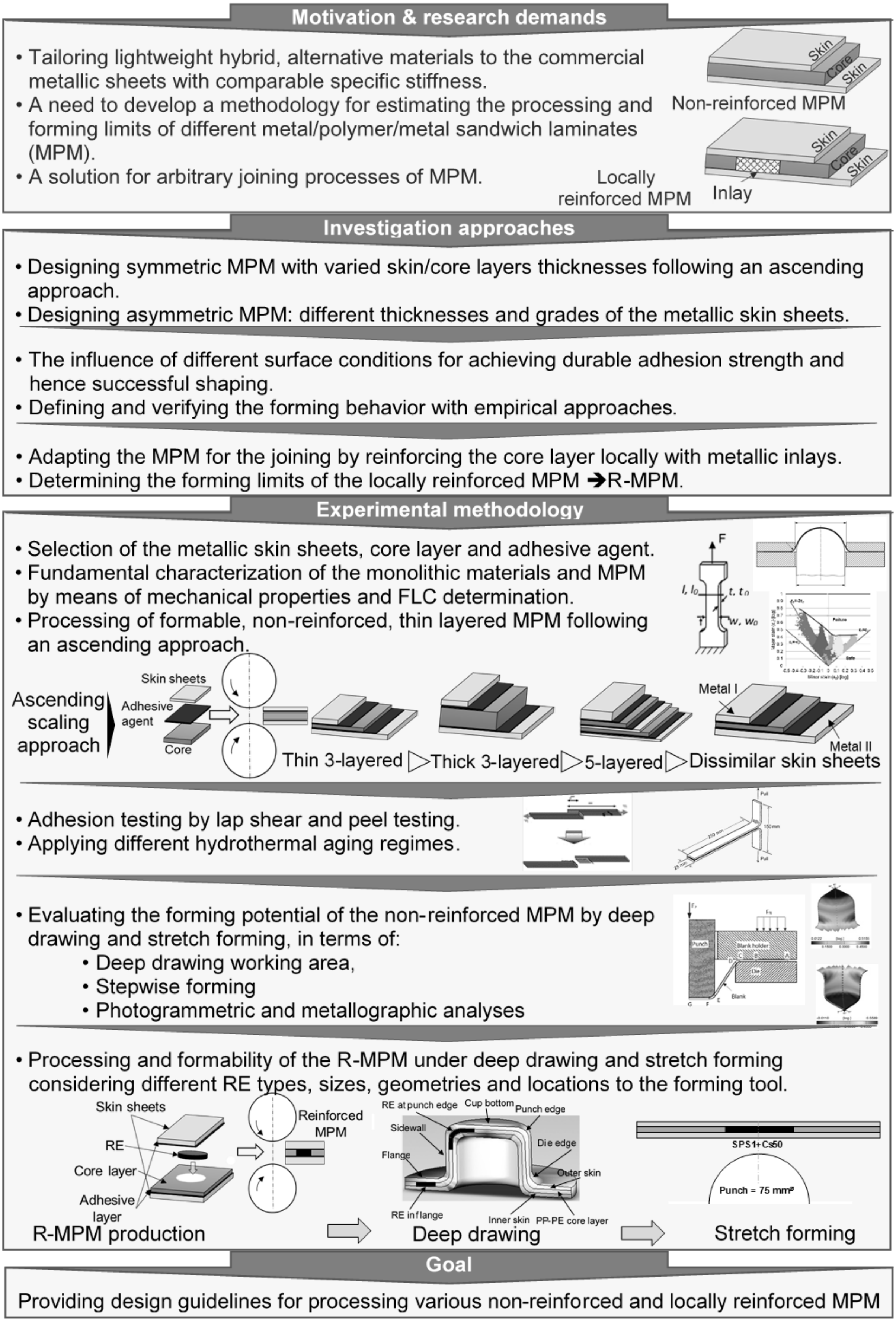

Motivation & research demands

- Tailoring lightweight hybrid, alternative materials to the commercial metallic sheets with comparable specific stiffness.
- A need to develop a methodology for estimating the processing and forming limits of different metal/polymer/metal sandwich laminates (MPM).
- A solution for arbitrary joining processes of MPM.

Investigation approaches

- Designing symmetric MPM with varied skin/core layers thicknesses following an ascending approach.
- Designing asymmetric MPM: different thicknesses and grades of the metallic skin sheets.

- The influence of different surface conditions for achieving durable adhesion strength and hence successful shaping.
- Defining and verifying the forming behavior with empirical approaches.

- Adapting the MPM for the joining by reinforcing the core layer locally with metallic inlays.
- Determining the forming limits of the locally reinforced MPM ➔R-MPM.

Experimental methodology

- Selection of the metallic skin sheets, core layer and adhesive agent.
- Fundamental characterization of the monolithic materials and MPM by means of mechanical properties and FLC determination.
- Processing of formable, non-reinforced, thin layered MPM following an ascending approach.

- Adhesion testing by lap shear and peel testing.
- Applying different hydrothermal aging regimes.

- Evaluating the forming potential of the non-reinforced MPM by deep drawing and stretch forming, in terms of:
  - Deep drawing working area,
  - Stepwise forming
  - Photogrammetric and metallographic analyses

- Processing and formability of the R-MPM under deep drawing and stretch forming considering different RE types, sizes, geometries and locations to the forming tool.

Goal

Providing design guidelines for processing various non-reinforced and locally reinforced MPM

Figure 1.4: Flowchart of the study approaches and experimental methodologies.

3. Achieving adequate metal/polymer adhesive strength that enable the MPM to withstand the shearing and peeling stresses initiating during processing.
4. Evaluation of the metal/polymer interface quality under different loading conditions for various MPM structures considering different surface properties, mainly of the skin sheets.
5. Characterizing the service life durability of the metal/polymer interface according to different accelerated aggressive hydrothermal aging regimes.
6. Determining the forming limits of various non-reinforced MPM considering the following parameters:
   a. An ascending scaling approach starting from the monolithic materials, then sheet metal laminates (metal/metal), MPM laminates with different structures.
   b. The number of the MPM layers. In this regard, five-layered laminates in addition to the traditional three-layered ones were studied. The reason for tailoring five-layered MPM is to decrease the expected dimensional distortion of the core layer during mechanical joining and, additionally improving the fatigue resistance.
   c. The adhesion quality. The influence of varied metal/polymer adhesion conditions on the forming potential was studied.
   d. The sandwich symmetry. In this context, the symmetry is defined as utilizing either dissimilar metallic skin sheet grades or different skin sheet thicknesses of the same grade in the same MPM.

   The aim of the MPM containing dissimilar metallic sheets is to understand their influence on the mechanical properties and the forming potential. Moreover, to determine whether the results can follow some simple approaches like the rule of mixtures (ROM). Another aim of processing these MPM containing dissimilar metal skins is, beyond gaining the weight saving potential, to enable their application in various service conditions at each side of the sandwich sheet. This can be achieved by combining the advantages of each skin sheet in a single sandwich, such as improved corrosion, better specific strength and stiffness or improved formability under the same or even improved stiffness conditions.

For these investigation approaches, the mechanical properties and the forming limit curves of the MPM's and their skin sheets were determined in order to predict and interpret the later forming processes namely deep drawing and stretch forming. The strain distribution was determined by optical methods based on photogrammetry. The thickness reduction of the MPM in the single layers was determined additionally with metallographic methods using light optical microscope.

In order to overcome the local defects that can arise during shaping and joining the MPM-laminates, especially the ones containing thinner metallic skin sheets, local reinforcing of the core layer is proposed. The motivation or rather the expected forming problems for developing the locally reinforced MPM-laminates are described in **Figure 1.5**:

1. Local thinning under forming: an example for this is the local thinning of the outer skin of the car door [Thy14c].
2. Local melting and dimensional distortion during thermal and mechanical joining processes due to the existing soft, electrically and thermally insulating core layer.

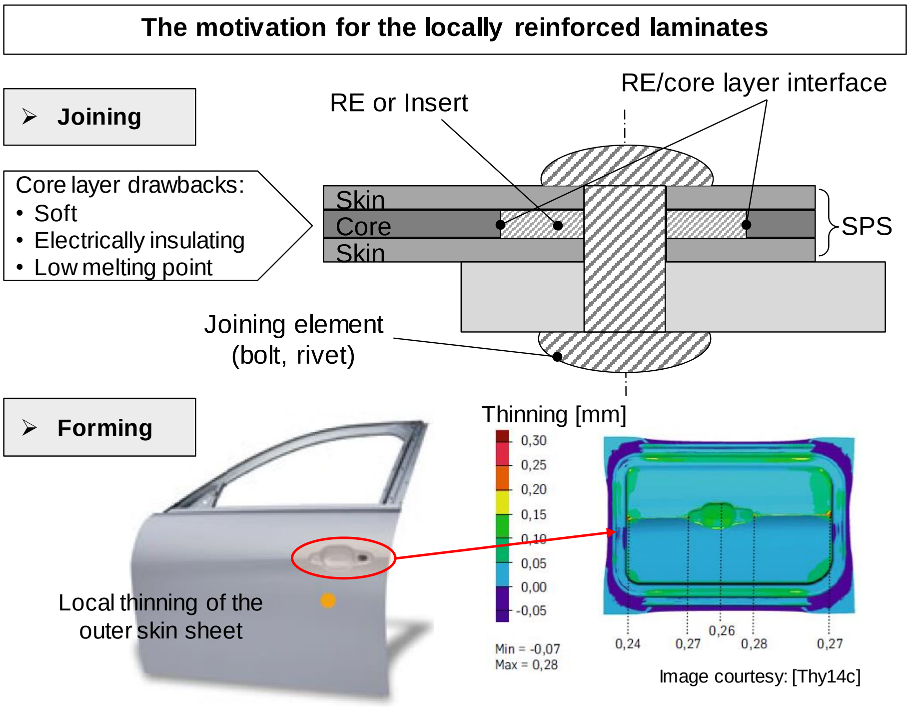

Figure 1.5: The Motivation behind developing the locally reinforced MPM-laminates.

In previous studies, the joining behaviour of the locally reinforced sandwich laminates was covered in, for instance [Fin13, Pal11]. Therefore, studying the forming potential of such locally reinforced MPM is an essential need that will be covered in the current study. In this regard, the thermoplastic core of the MPM is locally reinforced with metallic reinforcements (RE). The formability of reinforced MPM (R-MPM) is expected to be different or particularly lower. That is due to the arisen interface between the RE and neighbour polymeric core that leads to inhomogeneities and stress concentration regions. The formability was characterized by deep drawing and stretch forming. Various parameters were studied, such as:

1. Varied skin/core layer’s thicknesses and mechanical properties.
2. Diverse RE features (geometries, types, sizes and location in respect to the forming tool).

1.2. Thesis outline

This thesis consists of eight chapters including this one, annexes (**Chapter 8**) and bibliography.

Chapter 2 presents the actual state of the art and the subject-related theoretical background focusing on MPM hybrid materials, e.g. their structures, categories, applications and their behaviour under various loading conditions.

Chapter 3 is concerned with the fundamental characterization of the used materials, i.e. the skin, core layer and the MPM. The monomaterials and the adhesive agent are specified. Moreover, the MPM production method is described in addition to evaluating the adhesion strength and the service life durability. In the framework of the principal characterization, the mechanical properties and the forming limit curves are included in this chapter. The outcome of this is utilized in **Chapter 4**, where the deep drawing and stretch forming behaviour are given. **Chapter 5** addresses the effect of reinforcing the polymeric core locally with metallic inlays on the forming behaviour of the MPM. The main results of this thesis are summarized in **Chapter 6** and additionally in German in **Chapter 7**. Therein, an outlook of some complementary future activities is given, too.

This page intentionally left blank

2. Literature survey

Recently, there is a significant interest worldwide to minimize CO_2 emissions. According to the International Energy Agency, IEA, data of 2013, about 23% of the total CO_2 worldwide is produced in the transport section [IEA15]. In this regard, the EU made a considerable contribution in reducing the emission starting from 1990. Among the EU members, Germany in 2006 has recorded about 2% reduction in road traffic emissions [VDA09] in respect to the level of the 1990, as observed in **Figure 2.1**. Several methods achieved this change; one of them was developing alternative materials. Metal/polymer/metal laminates (MPM) and others offer an appropriate solution for reducing the vehicle weight. Therefore, this chapter will cover the actual literature survey about available MPM including their types, structures, advantages and limitations, production technologies, joining and forming potential.

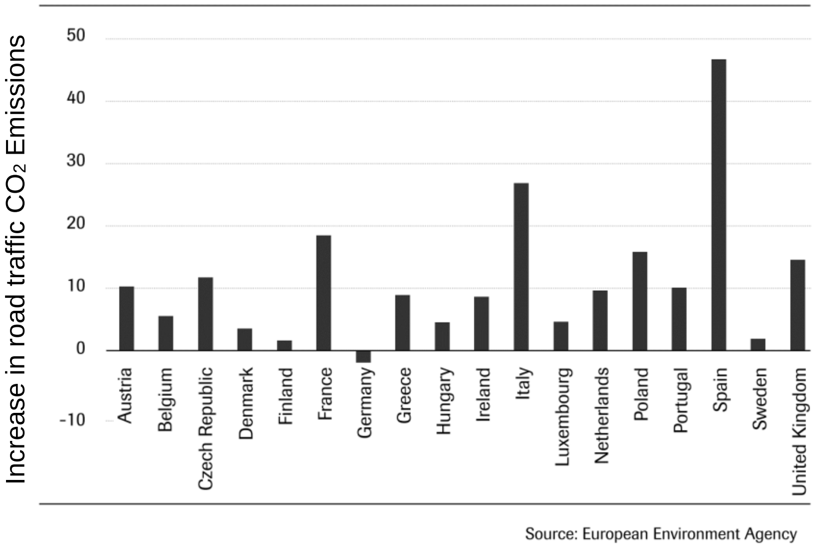

Source: European Environment Agency

Figure 2.1: Increase in road traffic CO_2-emissions in the EU from 1990 to 2006 [VDA09].

In general, composite materials consist of a combination of two (or more) materials of different natures aiming to obtain a material with better performance characteristics than the composite constituents separately [Ash05, Ber99]. Composite materials can be categorized according to their structure as listed in **Figure 2.2**. The particle reinforced composites are common for reinforcing metallic matrices with hard particles, such as the MMC (metal matrix composite) aiming at, for instance, increasing their strength and wear resistance. However, fiber-reinforced composites are normally based on polymeric matrices to offer e.g. higher stiffness. The fiber material can be carbon, glass, or even metallic ones. Structural sandwiches are of lamellar structure with a number of bonded layers that is the focus of the current study.

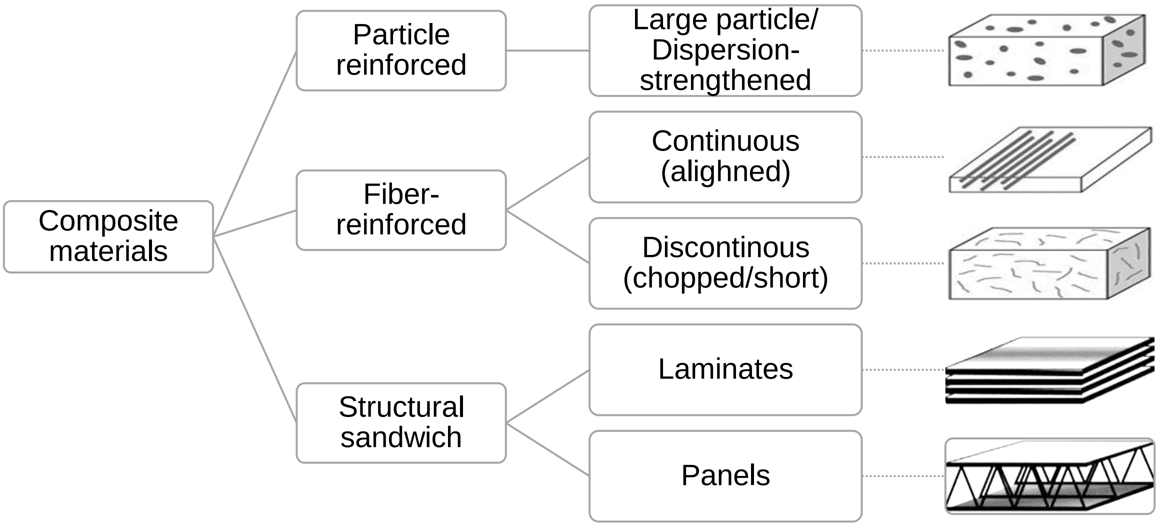

Figure 2.2: Types of composite materials [Ash03].

2.1. Hybrid laminates

The MPM-laminates were developed to gain numerous advantages like weight saving, high rigidity combined with higher strength to weight ratio, high load carrying capacity, increased fatigue life, crack growth and fracture toughness characteristics and improved thermal and acoustical insulation (vibration damping).

Despite these advantages, some challenges are necessary to overcome to give durable sandwich laminates during:

1. The metal/polymer adhesion (different surface energies, thermal, physical properties),
2. Forming (optimized skin/core stacking and interface shearing to avoid delamination), and
3. Joining, machining and recycling (thermal degradation and dimensional distortion) [Hay94, Kim97].

The basic structure of sandwich laminates is described in **Figure 2.3**. They always consist of three constituents, as listed below:

1. Facing or skin layers, which are relatively thin and possess high strength. This layer will convey the loads and absorb most of the forming energy.
2. Enclosed core layer(s), which is (are) relatively thick and light and has a sufficient stiffness in a direction normal to the faces of the panel in order to stabilize the skin sheets [Dav01].
3. The interface between the skin and the core layers, which should be improved to avoid the forming defects, such as delamination and wrinkling.

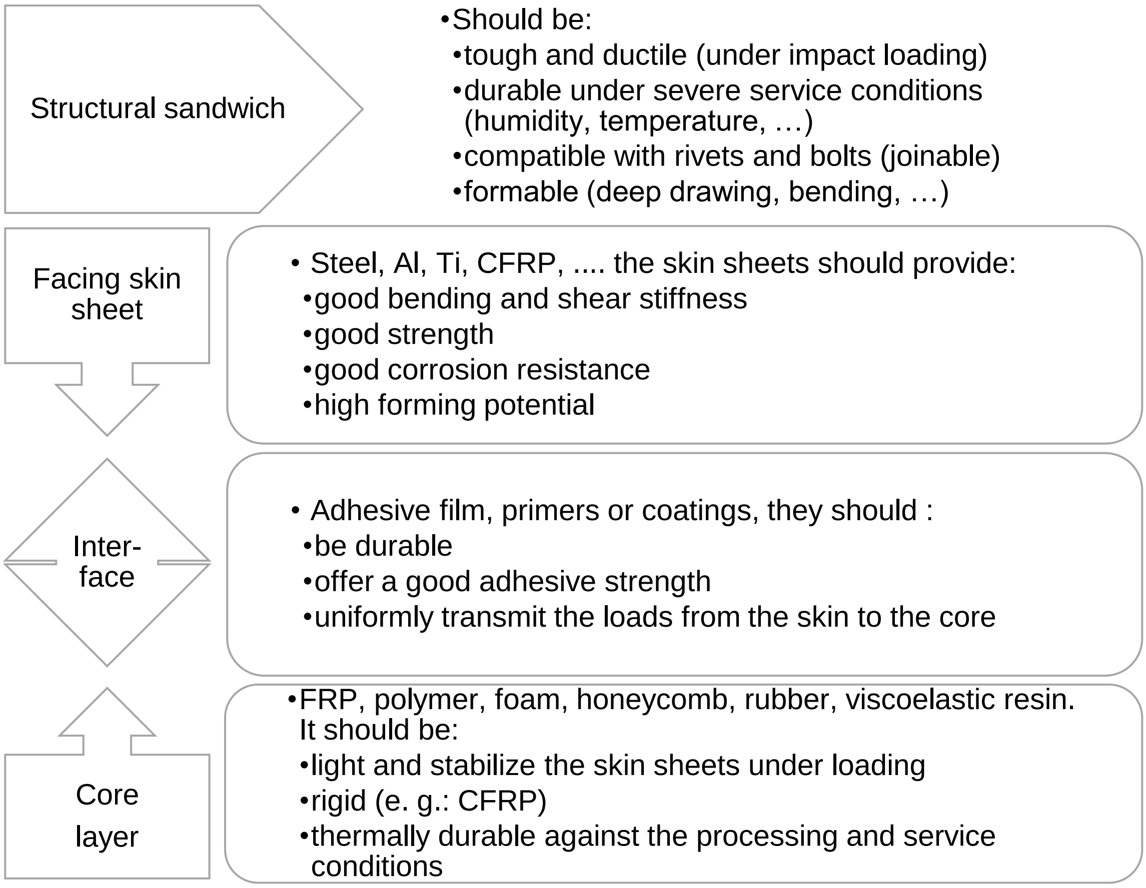

- Should be:
  - tough and ductile (under impact loading)
  - durable under severe service conditions (humidity, temperature, …)
  - compatible with rivets and bolts (joinable)
  - formable (deep drawing, bending, …)

- Steel, Al, Ti, CFRP, ... the skin sheets should provide:
  - good bending and shear stiffness
  - good strength
  - good corrosion resistance
  - high forming potential

- Adhesive film, primers or coatings, they should :
  - be durable
  - offer a good adhesive strength
  - uniformly transmit the loads from the skin to the core

- FRP, polymer, foam, honeycomb, rubber, viscoelastic resin. It should be:
  - light and stabilize the skin sheets under loading
  - rigid (e. g.: CFRP)
  - thermally durable against the processing and service conditions

Figure 2.3: An overview of the sandwich system components and their basic features or rather the requirements [Dav01, Kim97].

MPM-laminates are classified according to the type and relative thickness of the core in respect to the total laminate thickness as shown in **Figure 2.4**. Firstly, the fiber reinforced core is applied in Fiber Metal Laminates (FML's), where a fiber reinforced bondline or core is introduced between the metallic layers, such as HTCL®, ARALL®, GLARE® and Hybrix™, as listed in **Table 2.1**. This core contains brittle fibers (glass or carbon) in a thermoset matrix (mostly epoxy resin), therefore these systems exhibit a poor forming potential. Aiming at improving the ductility of the FML's, thermoplastic matrices were applied like PP, PA and PET, such as CAPAAL® and CAPET® [Sch15, Tek15, Wie11]. In other MPM, the brittle fibers were replaced by thermoplastic fibers, such as Al/SRPP (self-reinforced PP matrix with PP fibers)/Al [Car09, Rey07].

Conversely, combinations of bare thermoplastic polymers with metals offer a high forming potential and the possibility to produce semi-finished MPM to be shaped into complex geometries afterward. The latter type of laminates is the one concerned in this study. These laminates can be classified into two categories according to the core/skin thickness ratio [Hay94, Kim97]:

1. Sound damping laminates with thickness ratio less than 20%, such as Bondal® (core thickness ≤50µm) and,

2. Low-density laminates with thickness ratio about 40–60%, such as Alucobond®, Usilight®, Hylite®, Steelite® and Litecor® (core thickness 0.3–2.0 mm).

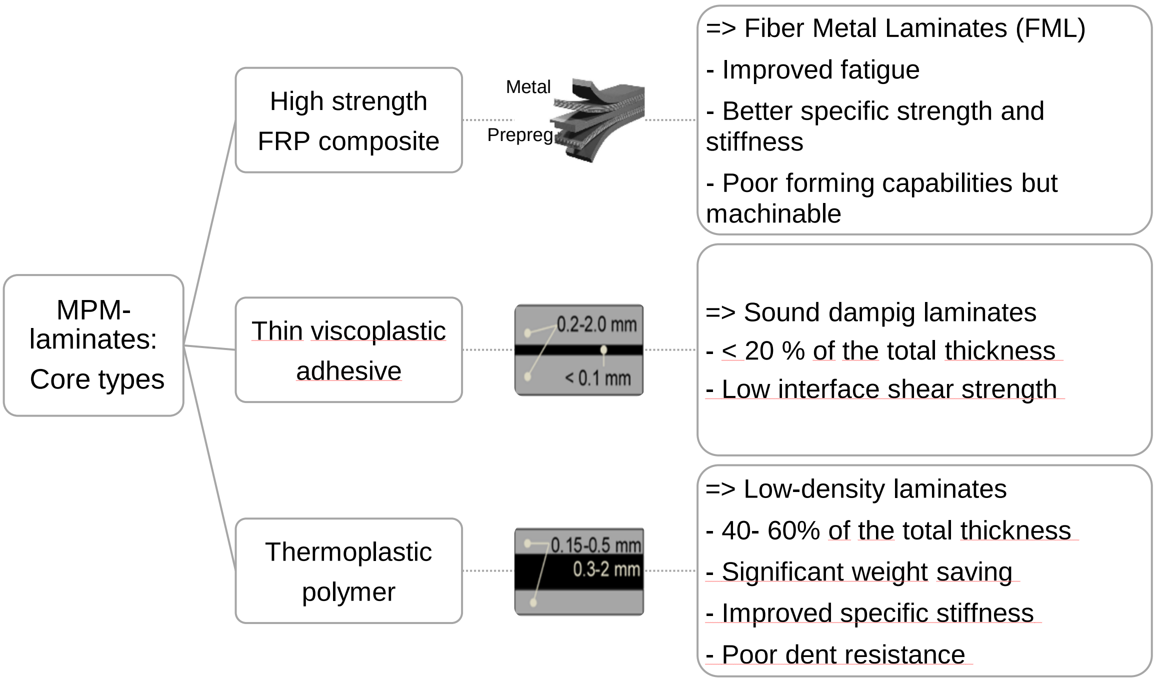

Figure 2.4: Classification of MPM-laminates according to the core type/features [Hay94, Kim97].

Table 2.1: Some commercial MPM-laminates – in an alphabetic order.

Designation	Skin sheet	Core layer	Reference
Alucobond®	Al	PE	[3A15b]
ARALL®	Al	Aramid-reinforced polymer	[Joh98]
Bondal®	Steel	Viscoelastic adhesive	[Thy09a, Thy14b]
CAPAAL®	Al	Carbon-fiber reinforced PA6	[Wie11]
CAPET®	Ti	Carbon-fiber reinforced PEEK	[Wie11]
GLARE®	Al	Glass-fiber reinforced polymer	[Bot06, Sch93]
HTCL®	Ti	Carbon-fiber reinforced polymer	[Joh96]
Hybrix™	Al or steel	Micro-fibrous reinforced adhesive	[Lam15a, Mar13]
Hylite®	Al	PP	[Bur05, Huf08]
Litecor®	Steel	PE-PA	[Thy12, Thy14d]
Steelite®	Steel	PP	[Boe97, Gow06, Gow07]
Usilight®	Steel	PP, PP/PE	[Dun06]

2.2. Metal/polymer joining

In principle, there are three common methods for joining materials and parts thereof metal/polymer joints [Mes04]: mechanical joining, adhesive bonding and welding, as well as combined joining methods (adhesive bonding combined with mechanical fastening or welding). Mechanical fastening and welding result in spot-like metal/polymer joints, however adhesive bonding is applied for a continuous joining over the whole metal/polymer contact area. Adhesive joining is the joining technique used in this study. Therefore, this part covers this method focusing of the surface preparation, behaviour of the joints under loading and evaluation the service life durability. Furthermore, a brief over the other joining methods is given.

2.2.1. Adhesive bonding

Adhesive bonding is adequate when the joints are subjected mainly to shear loading. Adhesive joints are performed over standard steps, which are:

1. Surface preparation/pretreatment by degreasing,
2. Applying the adhesive agent and clamping the adherends and
3. Applying joining parameters (pressure, temperature, time, etc.).

This joining method offers some advantages compared to mechanical fastening and welding [Ama09, Hab09b]:

1. The ability of bonding dissimilar materials with low and homogeneous stress distribution,
2. Improvement of the fatigue resistance,
3. Good surface finishing and sealing,
4. Joining of very thin materials is possible (flexibility) and
5. The most important advantage is the relatively low processing temperature (curing) which can match the thermal properties of polymers.

However, there are some disadvantages:

1. Limited disassembling,
2. Good surface preparation is required,
3. Resistant mainly to shear loading but weak under peel conditions,
4. Bond failure during application is difficult to be predicted due the uncertainty in forecasting its long-term durability,
5. Temperature sensitivity (thermal and environmental degradation),
6. Production time penalty (for curing), and
7. Special handling (hazardous chemicals and solvents).

The adhesion can be interpreted with the help of different theories in addition to the mechanical interlocking, such as the physical (polarization, electrostatic or diffusion theories), thermodynamic interactions (thermodynamic theory) or the chemical bonds (chemisorption theory). Further information can be found in [Bro09].

2.2.1.1. Surface treatment prior to metal/polymer adhesion

To achieve or even improve the metal/polymer bonding, various surface preparation and treatment methods can be applied, as summarized in **Figure 2.5**. The surface treatment can be accomplished mechanically, chemically, or physically.

Mechanical treatment is performed to introduce grooves/pins (macro-scale) in order to increase the anchorage probabilities [Häl13, Nes14a, Nes14b, Nes16, Ucs10, Wie11]; like sand blasting, brushing, grinding. It was found that the surfaces roughness plays an important role on the adhesion quality, however no specific correlation could be defined.

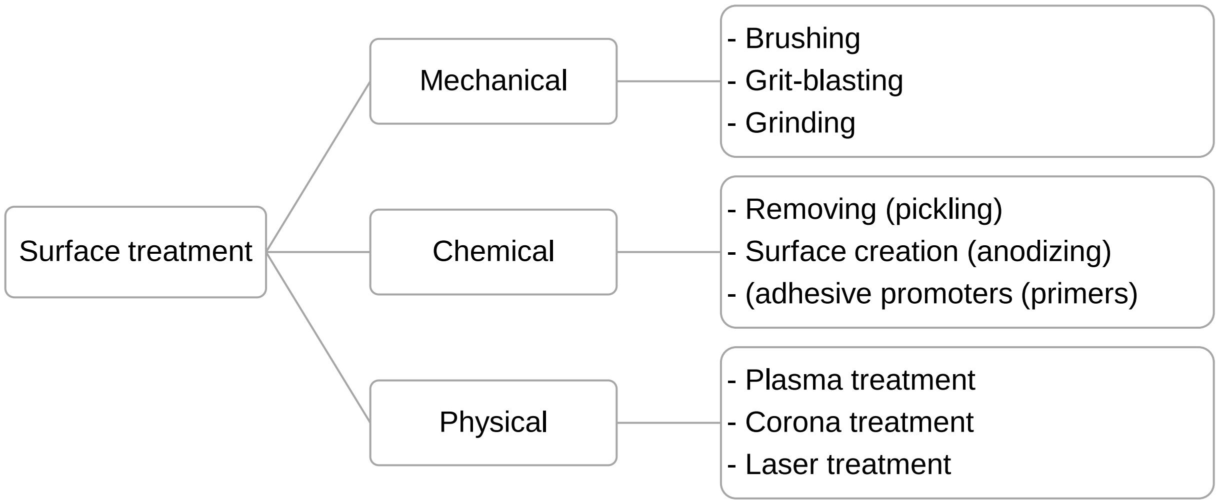

Figure 2.5: Surface treatment methods [Bro09].

Chemical treatment is applied to create chemical bonds at the interface between the adherends. It can be performed by electrochemical etching [Häl13], acidic or basic anodisation and introducing adhesive promoters [Sch13, Vel05, Wu14] or epoxy resins [Fra11, Sha14, Sok11b]. It was found that the surface treatments can provide a significant improvement of the bonding quality and failure mechanism. For instance, the adhesive strength of steel/CFR-PA66 joints can be improved from 12 MPa to 16 MPa by polishing the steel, followed by etching in 10%-HCl [Vel05].

Physical treatment aims at creating a certain surface topography by laser treatment [Ber12, Rod14, Sch13, Sch14] or cleaning/activating the adherend surfaces by plasma or corona treatment to create polar groups, by which the bonding is possible [Cha10, Hir12, Lis93, Man14, Sok11a]. Therefore, it can be named as chemo-physical treatments. The topography produced by laser treatment led to an outstanding improvement of the adhesion strength. For instance, not only the lap shear strength after laser treatment of Ti/PEEK/Ti was increased from 50 MPa to 80 MPa but also the strength loss after hydrothermal aging was less. A loss of about 20% of the laser treated surfaces against about 40% of the ground condition [Sch13].

After applying the proper surface treatment routes, the sandwich laminates can be produced in a sheet-like form by applying different techniques like hot pressing [Kim13, Sic14], adhesive bonding, liquid molding or continuous lamination by e.g. coil coating Bondal® [Asn00, Jan13, Kar97]. Moreover, recent developments focus on producing a finished product by combining the adhesion and forming steps of FML, for instance, hat profiles of steel/prepreg [Fra11, Lau11] and B-pillars composed of steel and CFR-PP, PA and PET [Gro12, Gro13, Sta14]. Moreover, steel/CFR-PA6 and GFR-PA6 hybrid laminates are produced with the help of different surface treatments and hot melt adhesive agents, such as Vestamelt® (Evonik Industries AG) [Sch15], followed by creating roof-rack as a demonstrator.

In the current study, preparing the surfaces by degreasing (with acetone) and applying a compatible adhesive agent was sufficient to deliver good bonding qualities, therefore, there was no need for applying sophisticated surface treatments. Some cases, like the oiled hot-dip galvanized steels (seen part 3.3.2), required a special preparation like grinding with sand soap and cleaning with acetone, due to their as-received inappropriate surface condition in terms of the contact angles. The lap shear strength increased accordingly from 9.5 MPa to 12 MPa after this treatment.

2.2.1.2. Durability assessment of adhesive joints

In many applications, the metal/polymer interfaces are subjected to harsh, cyclic environmental service conditions. Therefore, it is necessary to carry out the life assessment of the bonded laminates by considering their future application conditions. In addition to testing the effect of the actual service conditions, some specific service conditions can be regulated by standards and codes, such as the salt spray test and others [Bro09]. This assessment can be performed through experimental procedures by comparing the characteristic mechanical and physical properties before and after a given period of aging. To reduce the testing time, there is a strong demand for accelerating the aging by cutting down the duration required for natural exposure or real service conditions tests. Therefore, testing following accelerated aging will generally form the basis of predictions of service lives. Such accelerated testing can be applied to the actual joint geometry as well as standardized specimens.

Water, humidity or salt solution belong to the commonest application environments. Aggressive environments can cause an irreversible deterioration of the mechanical characteristics of a joint. Such aggressive media enter the bondline via diffusion processes or capillary attraction along existing microcracks in the polymer or at the interface. This is considered to be the most frequent cause of poor durability of bonded joints; particularly if the adherent material is inorganic (e.g. metal or glass). The deterioration depends on [Bro09]:

1. The type and intensity of the external influences (such as climate, environment and mechanical stresses),
2. The quality of the manufacturing process, and
3. The surface pretreatment prior to bonding.

The following list of testing conditions may serve to suggest accelerating aging cycles as being both applicable and relevant to the major mechanisms of degradation:

1. Outdoor weathering “Natural aging” in the normal atmosphere (humidity and temperature) for longer time, e. g. one year.
2. Exposure to moisture. Aging in climate chambers at 95% relative humidity (no condensation on the surface of the specimen) and 60°C or 80°C for 300–1000 h, depending on the intended application.
3. Exposure to water or other liquids at 40–80°C for typically 500–1500 h, depending on the intended application. In the following, the main humidity-induced, damage mechanisms are discussed:
    a. Plasticization of the adhesive polymer by uptaking water. This process is partly reversible upon redrying and generally results in a cohesive failure within the bondline.
    b. Formation of oxides on metals due to the diffusion of water into the interface, weakening the bonding interface.
    c. Degradation of the adhesive bondline is accelerated under elevated temperature and high humidity and eventually test loading conditions.
    d. Bondline corrosion, particularly in metal/metal bondlines, in case if the unprotected edges of the adherents are subjected to regularly aerated water that can contain corrosive substances, such as chloride or sulfate ions. This becomes more severe for dissimilar metallic joints due to the electrochemical potential difference.
4. Corrosion in chlorine environment: Standard cabinets for corrosion testing create a salt spray environment at 35°C. Exposure times typically range from 300 to 500 h, depending on the intended application.
5. Aging at elevated temperatures depending on the intended application: Aging at elevated temperatures (80–120°C) in the absence of moisture especially promotes oxidation, embrittlement and thermal degradation.
6. Accelerated thermal aging under cyclic change of temperature include the freeze–warm transition to examine the detrimental effect of water penetration and icing. Temperatures typically span from -20 to 80°C with 95% relative

humidity (during the warm period of the cycles) or even water. It is noteworthy that thermal stresses can be induced due to the rapid transitions between high and low-temperature limits.

From the previous list, some selected regimes were applied in the current study like natural aging (type 1), cyclic aging in humid atmosphere (type 2 and 6) as well as water (type 3 and 6).

2.2.1.3. Behaviour of the metal/polymer joints under shear loading

In the context of the adhesion evaluation of multilayer systems, various shear test assemblies are utilized; therefrom the single lap shear test is one of the commonest testing setups as shown schematically for its specimen in **Figure 2.6** and **Figure 2.7**.

The overall mechanical strength of the adhesive bonded joint is, in its majority, dependent on [Bro05]:

1. The adhesive properties (strength and ductility).
2. The joint configuration also plays an important role.
3. The type of the adherends (the metal or polymer layer) in terms of their surface condition, thickness and mechanical properties).
4. The adhesion process (thermoset- or thermoplastic- based adhesive agent and the bonding parameters: time, temperature and pressure).

The adhesive shear stress distribution in an overlap-bonded joint is uneven, where the edges will experience the loading peak values, while the central regions will be less affected, as shown in **Figure 2.6**. Accordingly, bending moments and peel rather than pure shear can take place. In this figure, the symmetry of the joined materials (1 and 2) in terms of the elastic modulus (E) is considered. In the case of symmetric material couple ($E_1 = E_2$), such as joining two metallic or polymer layers with an adhesive agent, the distribution of the shear strength is equal on the edges of the joint. However, for asymmetric joints, such as a single metal/polymer joint with an adhesive agent ($E_1 > E_2$), the stiffer material side (material 1) shows lower shear stress. Based on that, the softer side can be plastically deformed and subsequently fail according to the acting force. Moreover, the nature (elastic or elastic/plastic flow behaviour) of the adhesive joint plays an important role. For the elastic adhesives, failure occurs at lower shear displacements and additionally the peak shear force regions are located at the edge of the overlapped area, as shown in **Figure 2.6-a)**. However, the maximum shear stress is located away from these edges in the case of the elastic/plastic adhesive layer, as shown in **Figure 2.6-b)**. As can be seen, the edges are subjected to plastic deformation and the central regions are still elastic. This fact can be transferred to the behaviour of the asymmetrical joints, where the weaker, softer, or even the thinner material in the joint will be plastically deformed and may fail. Therefore, the joint dimensions should be designed to keep the skin sheets in the elastic deformation, not only for precise evaluation of the adhesion strength, but also for the real application of the adhesive lap joints.

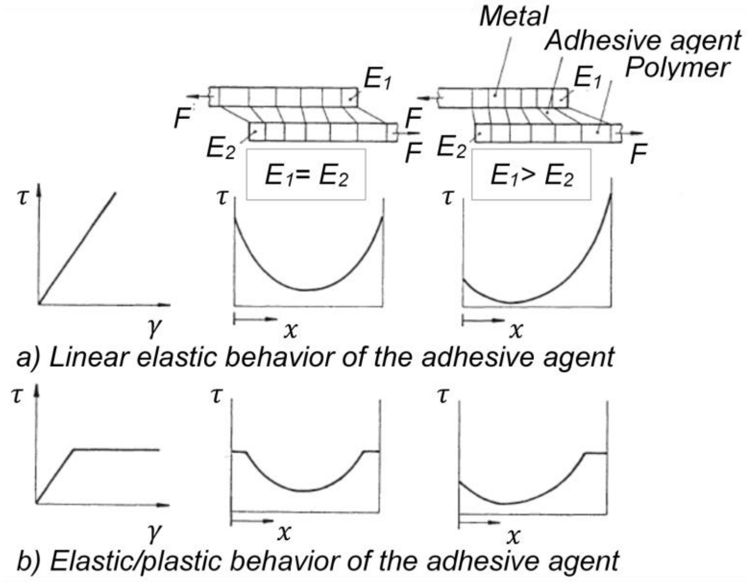

Figure 2.6: Shear stress distribution based on the mechanical behaviour of the adhesive agent and the adherends as well for a) elastic and b) elastic/plastic behaviours [Bro05].

The joint dimension can be expressed in terms of the overlapping length (L_{OV}) and width b. The dependency of the shear force on the shear stress and the geometrical parameters namely b and L_{OV} is shown in Eq. **(2.1)**. The overlapping width has no remarkable influence of the stress distribution of the skin sheet, as with wider specimens, the resistance of the skin sheet is directly increased [Sic14]. However L_{OV} plays a major role in determining the stress condition and accordingly the expected failure mechanism (shearing delamination or skin sheet cracking) [Bro05]. The effect of L_{OV} was studied in numerous studies, for instance, where this value should be optimized to avoid cracking of the skin sheets as well as to deliver the maximum adhesive strength [Nut08, Sic14]. In principle, the acting shear force is compared to the force at which plastic deformation of the skin sheet takes place, i.e. at the yield strength.

Shear force → $$F_{shear} = \tau \times L_{OV} \times b \qquad \textbf{(2.1)}$$

τ is the expected shear strength of the joint. In case of cohesive failure, τ corresponds to the maximum shear strength of the core layer.

In the case of $L_{OV} = L_{OV-1}$, as shown in Eq. **(2.2)** and **Figure 2.7**, a low shear force is acting and, therefore, pure shear stress is dominant at the metal/polymer interface. Accordingly, the skin metal sheet is not subjected to plastic deformation (below YS). Increasing the overlapping length to L_{OV-2}, the optimum overlapping length (L_{OV-Op})

[AST00b] is reached, where the shearing force balances the onset plastic deformation force, as expressed in Eq. **(2.3)**. If the overlapping length is further increased to L_{OV-3}, there is a higher tendency of the skin sheet to cracking when the acting force reaches the rupture force; which is corresponding to the tensile strength (UTS) of the skin sheets, as shown in Eq.**(2.4)**.

Pure shearing→
$$L_{OV-1} < L_{OV-Op} \qquad F_{shear} < F_{YS} \tag{2.2}$$

Optimum overlapping→
$$L_{OV-2} = L_{OV-Op} \qquad \begin{gathered} F_{shear} = F_{YS} \\ F_{YS} = YS \times t_{skin} \times b \\ L_{OV-Op} = (YS \times t_{skin})/\tau \end{gathered} \tag{2.3}$$

Skin sheet cracking→
$$L_{OV-3} > L_{OV-Op} \qquad F_{shear} \geq F_{UTS} \tag{2.4}$$

The recommended L_{OV} is roughly 12.5 mm in most of the standards, such as ASTM D3165 [AST00b], DIN 53281 [DIN06] and others. Therein, thicker skin sheets are required to avoid the cracking or even an onset of the plastic deformation, for instance, starting from 1.5 mm steel sheets to ensure L_{OV} = 12 mm.

Another approach can be applied for metallic skin sheets considering their thicknesses following: $L_{OV} \approx 10 \times t_{skin}$ [Hab09a]. Moreover, the recommended L_{OV} for thin aluminum skin sheets in [Nut08] is 2–5 mm to ensure shearing and no cracking.

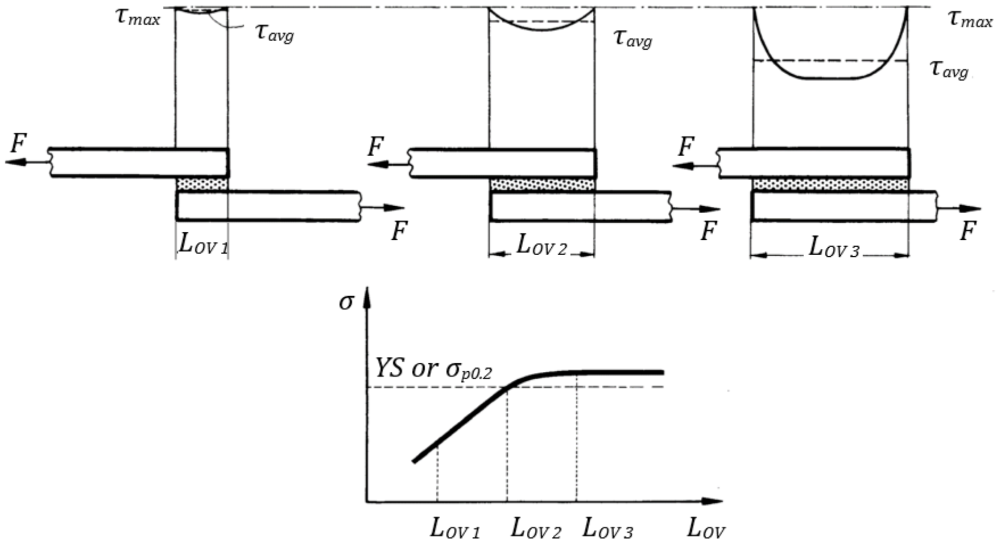

Figure 2.7: Stress development over the skin sheet in correlation to the overlapping length (L_{OV}) the yield strength limit [Bro89, Hab09a].

2.2.2. Other metal/polymer joining methods

Mechanical fastening depends on interlocking of the mechanical forces between the metallic and polymer layers using fasteners attachments, such as riveting, clinching, screwing and bolting (see **Figure 2.8**). Some key advantages of mechanical fastening are [Ama09]:

1. The ability for disassembling; limited for plastic deformation interlocking like metal/metal clinching,
2. Easy technology, machinery, repair and inspection,
3. Joining of dissimilar materials, and
4. Simple surface preparation and cleaning.

On the other hand, disadvantages are:

1. Increased stress concentration,
2. Joint loss due to creep, moisture, hole edges cracking and stress relaxation,
3. Residual stresses (in the case of joining plastics and metallic partners), and
4. Weight penalty at the joined area die to the attached fasteners.

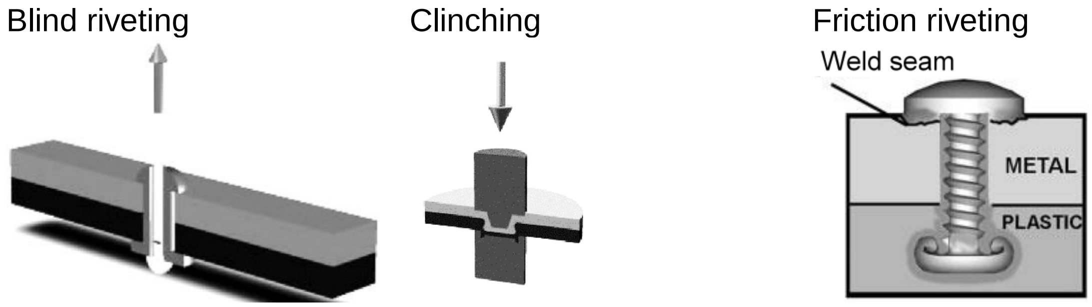

Figure 2.8: Some metal/polymer mechanical fastening methods [Ama09].

Direct metal/polymer welding by conventional methods, which require high heat input like shielded metal arc welding and others, is not, so far, useful due to the significant difference in the thermal properties between them [Ama09, Kah14, Lam15b]. However, recently developed welding techniques are more feasible, such as ultrasonic welding, laser welding and friction spot welding [Ama09, End02, Kah14, Nes13].

2.3. Mechanical properties of the MPM-laminates

The tensile test is one of the main evaluation methods used to characterize and specify the mechanical and forming potential of materials. In this part, an overview of some terms that are frequently mentioned in this work will be given. **Figure 2.9** shows typical engineering ($S - e$) and true ($\sigma - \varepsilon$) stress–strains curves, which can be estimated using the equation set Eqs. **(2.5)**–**(2.7)**. The main relevant properties from this test are the yield strength (YS or $R_{p0.2}$) and the tensile strength (UTS or R_m) at which the uniform strain (e_u) is determined, as well. Moreover, the strain at failure (e_f) is one of the characteristic values.

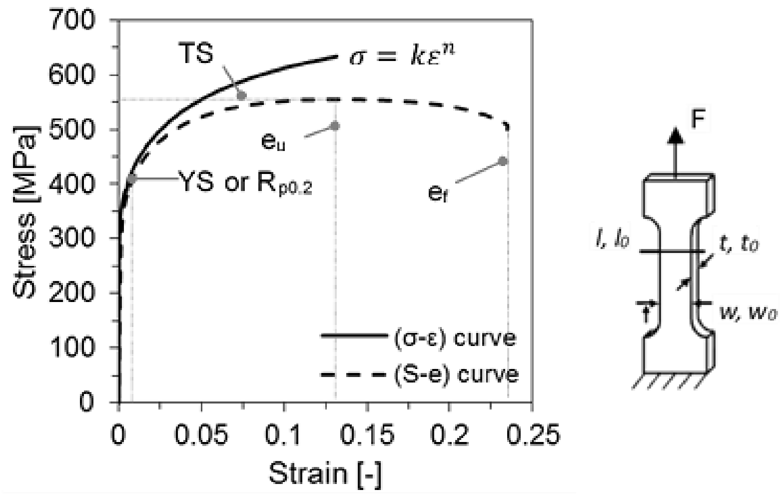

$$e = \frac{l - l_0}{l_0}$$

$$S = \frac{F}{A_0} \tag{2.5}$$

$$\sigma = S(1 + e) \tag{2.6}$$

$$\varepsilon = ln(1 + e) = ln\,\frac{l}{l_0} \tag{2.7}$$

Figure 2.9: Typical engineering and true stress–strain curves of steel with the corresponding conversion equations.

From the power law equation Eq. **(2.8)**, the plastic behaviour of the material can be described in terms of the strain-hardening index (n) and the strength coefficient (K) at ($\varepsilon = 1$) [Mar02]. The n and K values are important for expecting and describing the formability of materials. Therefore, for a successful forming operation (such as deep drawing), these values should be sufficiently large to guarantee a reasonable strengthening behaviour, but not be so high as to require excessive forces to accomplish the forming processes or initiation of undesirable cracking [Alt12]. The n value can be estimated according to Reihle, as in Eq. **(2.9)** [Doe10].

$$\sigma = K\varepsilon^n \tag{2.8}$$

$$n = \varepsilon_u = \ln(1 + e_u) \tag{2.9}$$

Anisotropy or the plastic strain ratio r value is a measure of plastic anisotropy in sheet materials and is defined as the instantaneous ratio of true width strain (ε_w) to true thickness strain (ε_t) during the plastic deformation in a tensile test, as expressed in Eq. **(2.10)**. Good forming potential is expected with higher r values (≥ 1) where the material thinning is minimized [Alt12]. The average or normal plastic anisotropy (R) can be determined to express the average anisotropy over the different direction of the material, as described in Eq. **(2.11)**. Moreover, the affinity of the material to earing under drawing can be indicated through the planar anisotropy Δr, as expressed in Eq. **(2.12)**. If $\Delta r = 0$, no earing is expected; if ($\Delta r > 0$), earing occurs in the 0° and 90° respect to the rolling direction. However, if ($\Delta r < 0$), earing occurs in the 45° direction. Normally the n and r values are estimated according to [DIN14b, DIN14a].

$$r = \frac{\varepsilon_w}{\varepsilon_t} \tag{2.10}$$

$$\mathrm{R} = \frac{r_{0^\circ} + 2r_{45^\circ} + r_{90^\circ}}{4} \tag{2.11}$$

$$\Delta r = \frac{r_{0^\circ} - 2r_{45^\circ} + r_{90^\circ}}{4} \tag{2.12}$$

2.3.1. Mechanical properties of laminated systems

The mechanical properties of composite materials – such as laminated or continuous-fibrous systems can be estimated (**Figure 2.10-a)**) under:

1. Tangential loading: following the so-called “Voigt structure” or the rule of mixtures (ROM) (Eq. **(2.13)**). This is applicable for the elastic modulus (E), yield (YS) and ultimate tensile strength (UTS), density (ρ) of composite “c” systems based on the volume fraction “f” of its constituents “1 & 2.” It is noteworthy that not all the properties follow this rule under tensile loading, such as e_f, because the MPM failure depends on the ductility of the individual skin/core layers. In the case of the thermoplastic cores, the skin sheets convey the loads and fail first and the whole MPM as a result. However, in case of the brittle FRP cores, the MPM fail when the FRP reach its failure conditions.
2. Transverse loading: E can be estimated for the so-called “Reuss structure” as shown in **Figure 2.10-b)** following Eq. **(2.14)** [Bol14, Che93].

a) Tangential loading “Voigt structure”

b) Transverse loading “Reuss structure.”

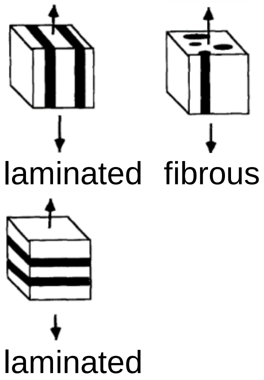

→
$$\begin{gathered} E_c = f_1.E_1 + f_2.E_2 \\ YS_c = f_1.YS_1 + f_2.YS_2 \\ UTS_c = f_1.UTS_1 + f_2.\mathrm{U}TS_2 \\ \rho_c = f_1.\rho_1 + f_2.\rho_2 \end{gathered} \tag{2.13}$$

→
$$\frac{1}{E_c} = \frac{f_1}{E_1} + \frac{f_2}{E_2} \tag{2.14}$$

Figure 2.10: Laminated and fibrous a) Voigt structure and b) Reuss structure [Bol14, Che93].

The mechanical properties of numerous MPM-laminated systems can be found in the literature. The tensile forces of the sandwich laminates can be estimated by summing the forces for the single layers, as shown in Eq. **(2.15)**. Good agreement between the estimated and the experimental results was found for symmetric Hylite® and others, as described in [Har16c, Jas12, Neu06].

$$F_{MPM} = F_{skin-1} + F_{core} + F_{skin-2} \tag{2.15}$$

In case of thermoplastic cores, $F_{core} \ll F_{skin}$, so Eq. **(2.16)** and **(2.17)** can be applied for symmetric and asymmetric MPM-laminates, as follow:

Symmetric MPM→ $$F_{MPM} = 2 \times F_{Skin} \tag{2.16}$$

Asymmetric MPM→ $$F_{MPM} = F_{skin-1} + F_{skin-2} \tag{2.17}$$

The properties of the core layer affect the ductility of the laminated sheets. A ductile behaviour of FML based on aluminium skin sheets and SRPP (self-reinforced PP) core, which consists of thermoplastic PP fibers in a thermoplastic PP matrix, such as reported in [Car09, Rey07]. However, by reinforcing the PP core with glass fibers instead of PP fibers, the ductility was significantly reduced. Moreover, the effect of the strain rate, in the range between 10^{-4} and 10^{-1} s^{-1}, on the mechanical behaviour of SRPP-FML was studied [Mck07]; an increase of the mechanical properties (E, YS and UTS) was found with increasing the testing rate. The effect of the testing rate and temperature on the stress–strain development of Hylite® and Usilite® was investigated in [Jas12, Neu06].

Moreover, the MPM production conditions have a significant effect on changing the strengthening behaviour of the metallic skin sheets especially the Al ones. It was found in [Gra13] after applying the production conditions (temperature, pressure and holding time) for Al/CFR-PA laminates that there a substantial reduction not only in the strength from 275 down to 200 MPa took place, but also in the strain at failure from 22 down to 12%. The FML composed of a Ti-alloy and carbon fiber-reinforced PEEK [Cor04, Cor06] were investigated at different stacking and volume fraction of the carbon fibers; good matching with ROM was verified, as well as for other laminated systems [Ash05, Bol14, Che93, Har14b, Hin03].

The effect of corona surface treatment of the polymeric core on the mechanical properties in 316L/PP-PE/316L sandwich laminates were studied in [Car10, Sok12]. They reported minor improvement of the tensile properties. Moreover, varying the direction of the skin sheets in respect to the rolling direction in the same laminate was studied to control the anisotropic behaviour of the skin sheets. A significant effect of varying the adhesive layer properties on the mechanical properties was found [Sat14, Sat15]. Within the studied material combinations, it was stated that increasing the hardener content results in improving the formability. Furthermore, the mechanical properties of various commercial sandwich laminates are presented in [Nut08]. The effect of introducing stiffening beads into laminates on the mechanical behaviour was investigated by [Bol14]. He showed that the strength values were improved with deeper beads. The temperature dissipation during tensile test of sandwich sheets based on deep-drawable and stainless steel grades was investigated by [Buh14] to indicate the temperature inhomogeneity over the specimen length. Temperature differences of approx. 15 K were found between the specimen center and its sides.

2.4. Forming of the MPM-laminates

Due to the inhomogeneous material behaviour of the MPM-laminates over thickness, it is necessary to analyse their forming behaviour under different loading conditions. Therefore, this part will handle the available literature about the laminates forming and the corresponding theoretical background of these forming operations. The formability of commercial MPM is investigated, such as Hylite®, Litecor®, Bondal®, Usilite® and others in [Bol14, Jas12, Neu06, Nut08]. Various sheet forming processes of the MPM were investigated, such as bending, deep drawing, stretching evaluation, shear and forming limit curve (FLC) determination.

2.4.1. Fundamentals of local strain measurements

It is necessary to determine the resulting strains after the different forming processes in order to characterize the forming operations/parameters (e.g. lubrication, forming rates, etc.) and to determine the tendency of the components to failure when compared to the corresponding FLC [Doe10]. In this study, the strains were determined using the photogrammetry concept. Photogrammetry is a 3D coordinate measurement technique that is widely accepted in industrial applications based on the triangulation principles. Therefore, a series of photographs of the measured object are taken from numerous angles to recreate the 3D coordinates with many different views of each target. Later, these photographs are processed and analysed using the DIC technique with the help of high speed processors [McG05]. Some factors that affect the quality of a photogrammetric quality include the resolution of the captured images, camera calibration, angles between captured photos and redundancy in the appearance of object appearing in multiple.

This method depends on creating a particular grid pattern (e.g. dots or squares) on the surface. After forming, the distortion of the pattern is determined. An example for uniform deformation, assuming volume consistency, is shown in **Figure 2.11-a)** and **-b)** [Mar02]. If the non-deformed sheet with initial thickness t_0 is marked with a grid of dots of initial diameter d_0, then during deformation, the grid will deform to be ellipses of major and minor axes d_1 and d_2, respectively, as shown in **Figure 2.11-b)**. Based on that and assuming volume constancy, the three principle strains namely major (ε_1), minor (ε_2) and thickness strain (ε_3) can be determined following Eq. **(2.18)**. An example of (ε_1) distribution over the inner side of a deep-drawn cup based on a dot-pattern is shown in **Figure 2.11-c)**. It is noteworthy that ε_3 is estimated based on ε_1 and ε_2, which can deviate from real thickness measurements obtained, for instance, by the metallographic methods. This deviation between metallographic and photogrammetric methods can be ignored for monolithic sheets. However, a significant difference can arise in case of laminated systems due to the existing soft polymeric core. One of the study objectives it to define this difference.

$$\begin{gathered}\varepsilon_1 = ln\frac{d_1}{d_0};\;\; \varepsilon_2 = ln\frac{d_2}{d_0};\;\; \varepsilon_3 = ln\frac{t}{t_0}\\ \varepsilon_1 + \varepsilon_2 + \varepsilon_3 = 0\\ \alpha = \frac{\varepsilon_2}{\varepsilon_1} \rightarrow \varepsilon_2 = \alpha.\varepsilon_1\\ \varepsilon_3 = -(\varepsilon_1 + \varepsilon_2) = -(1+\alpha).\varepsilon_1\\ t = t_0.e^{\varepsilon_3} = t_0.e^{(-(1+\alpha)\varepsilon_1)}\end{gathered} \tag{2.18}$$

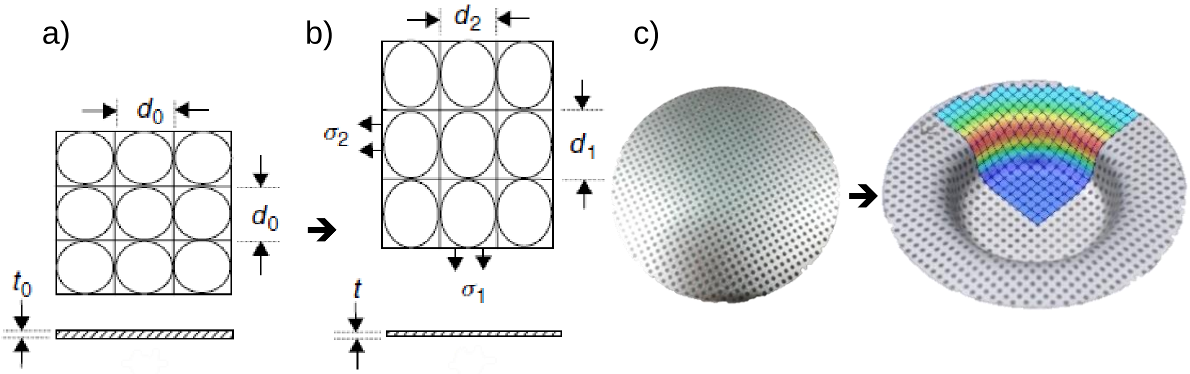

Figure 2.11: a) Determination of the principal strains of circular grid pattern [Mar02] a) before and b) after deformation, in addition to c) major strain (ε_1) distribution over the inner skin sheet of deep drawn cup (1 mm$^{\varnothing}$ dot-pattern with 2 mm center to center distance).

2.4.1. Forming limit curve determination

The forming limit curve, also flow limit curve (FLC) is an empirically derived curve showing the major/minor (ε_1– ε_2) strain levels in a surface beyond which localized through-thickness thinning (necking) and subsequent failure occurs during the deformation of a metallic sheet [AST08], as shown in **Figure 2.12**. In a FLC diagram, different load conditions are presented. FLC determination was firstly developed in the 60's by Keeler and Goodwin [Doe10, Kee65]; Keeler developed the minimum and maximum strains in the stretching region, where biaxial strains are dominant, i.e. the right part ($\varepsilon_1 = \varepsilon_2$). However, Goodwin developed later the deep drawing part (the left part: $\varepsilon_1 = -2.\varepsilon_2$). The forming condition is considered safe if the forming strains are located below the FLC. However, localized necking (close to failure) takes place when the strains meet the FLC. Moreover, beyond the FLC, failure occurs. Normally, the FLC is determined using a semi-spherical punch at a defined displacement rate for different specimen widths aiming at creating different strain paths (**Figure 2.12**). The metal sheet is monitored with a DIC system while testing. The strain path of the specimen or rather the FLC level is significantly influenced by various parameters: a) material-related: thickness and its mechanical properties (n and r values and strength) and b) process-related: lubrication, testing rate, blank holding force and its geometry, punch geometry, blank size, die radius and temperature.

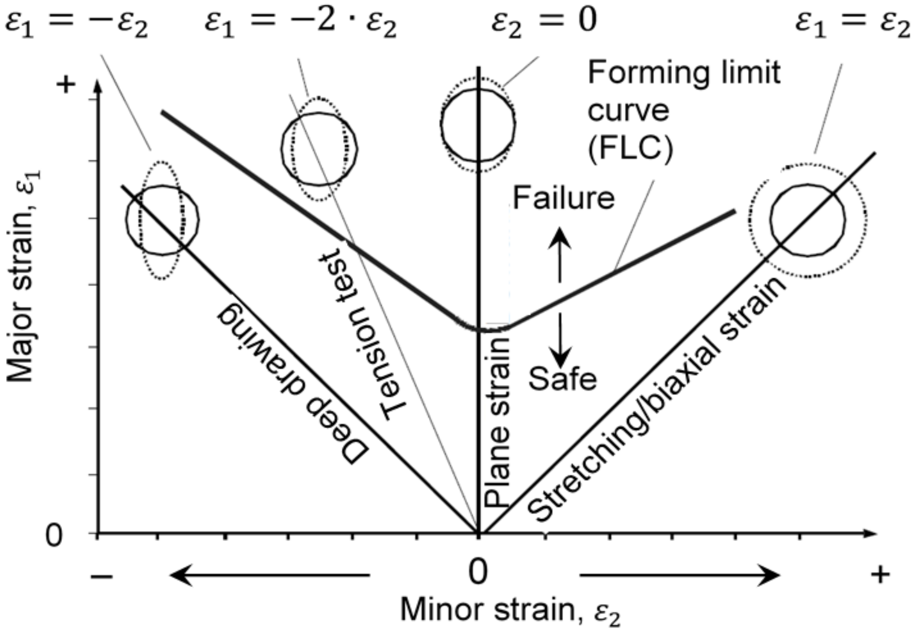

Figure 2.12: Illustration of the FLC curve showing the different strain ($\varepsilon_1 - \varepsilon_2$) regions [Doe10].

The FLC strains can be approximated based on the initial sheet thickness (t) and the strain-hardening exponent (n) of the material according to Keeler-Brazier equations [Pal12], as expressed in Eqs. **(2.19)**, **(2.20)** and **(2.21)**.

Plane strain
$$FLD_0^{true} = \ln\left[1 + (23.3 + 14.13t) \cdot \frac{n}{0.21}\right]; n \leq 0.21 \qquad \textbf{(2.19)}$$

Tensile strain
$$\varepsilon_1 = FLD_0^{true} - \varepsilon_2;\ \varepsilon_2 < 0 \qquad \textbf{(2.20)}$$

Biaxial strain
$$\varepsilon_1 = \ln[0.6(exp(\varepsilon_2) - 1)] + exp(FLD_0^{true});\ \varepsilon_2 > 0 \qquad \textbf{(2.21)}$$

Different experimental methods were developed for precise detection of the localized necking, such as the time-dependent or the ISO standard methods (ISO 12004-2) [Hor14, Mer10, Mer14]. In this regard, one of the aims of this thesis is to study the applicability of these different methods on the used SPS laminates and finally to recommend the most appropriate method.

2.4.1.1. FLC of laminated systems

Due to its importance, the FLC of different MPM-laminates compared to their monolithic skin sheets was determined in some publications. The mechanical and FLC curves of different thickness AA5052/PE/AA5052 namely 1.5 mm (0.5/0.5/0.5), 2.0 (0.5/1.0/0.5) and 3.0 mm (0.5/2.0/0.5) were studied and compared with the used monolithic 0.5 mm thick Al-alloy skin sheet. It was found that the FLC level (in y-axis or the major strain) is improved as well as the elongation at failure with increasing the core thickness [Liu13b, Liu13a]. Moreover, the FLC level can be improved with increasing the Al/PE adhesive strength [Liu12]. Another approach is presented in [Par13] for Al(A3105)/PP/Al(A3105) laminates, where the FLC level decreases with increasing the core thickness. However, increasing the temperature to 60°C decreases the FLC level of Al/PP/Al laminates due to softening [Wei07]. The conflicting effect of the core thickness on the FLC level can be attributed to the mechanical behaviour of the core layer and metal/polymer adhesion quality and additionally the softening behaviour of the skin sheets, especially the Al ones as a result of the production conditions (temperature, time and pressure), as reported by [Gra13]. In this context, PE offers a better strain behaviour compared to PP under creep and fatigue conditions [Ali13]. It was even concluded that when using a polymeric core with a higher n value, the formability of the MPM can be improved [Kim03]. The stretch-drawing behaviour of FML composed of some Al/SRPP/Al and Al/GFR-PP/Al laminates was investigated considering the effect of the preheat temperature and blank holder force. A significant effect of these parameters on the failure type, either wrinkling or cracking, as well as the dome height at cracking was stated [Gre06]. Moreover, the strain development at different regions of the stretch-drawn blanks with temperature and blank holder force is presented in [Kal12]. It is shown that increasing the blank holder force increases the major strain values. Increasing the temperature can lead to decrease the FLC level, where the adhesive layer melts and hence leads to sliding of the layers over each other. Melting of the adhesive layer took place, where a 50 µm thick hot-melt polypropylene adhesive was applied at the metal/PP interface. However, at lower temperature, the FML layers are intact and behave as one thick layer.

2.4.2. Deep drawing

Deep drawing is a widely-applied process in sheet metal forming for numerous applications. In principle, a hollow cup is formed by forcing a flat blank (e.g. symmetric round cup drawing is shown in **Figure 2.13**) into a die using a punch with the help of a certain blank holder force (F_{BH}) to control the sheet flow as well as to avoid wrinkling [DIN09b, Kar12]. In deep drawing, the punch force is transmitted indirectly to the drawing zone (blank holder/die) through the cup sidewall.

Figure 2.14-a) shows **v**arious deformation modes arising during deep drawing [Kar12], which can be expressed in terms of the ratio ($\varepsilon_2/\varepsilon_1$) as shown in **Figure 2.14-b)** [Mar02]. The flange (A–C) is subjected to thickening due to the acting axial compression, radial tension and circumferential compression. However, bending and friction conditions are dominant at the die and punch corner radii (C–D and E–F). Failure is more probable at zone (E–F) due to localized necking. Moreover, the flat cup bottom (F–G) is subjected to equal-biaxial tensile strains close to zero, however uniaxial radial tension is dominant at the sidewall (D–E).

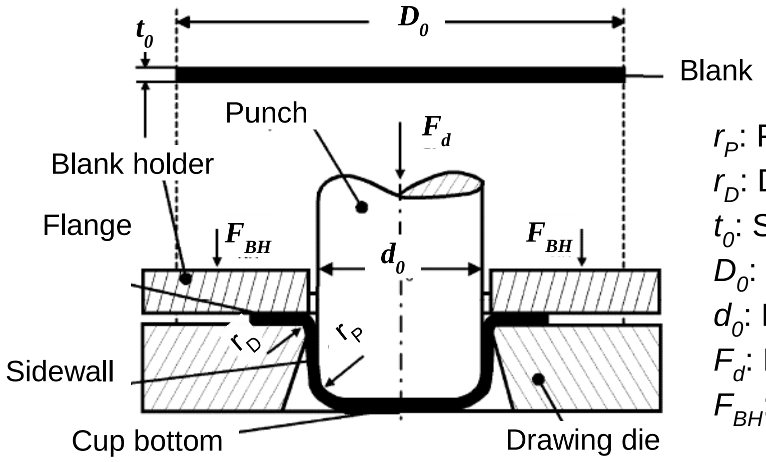

r_P: Punch corner radius
r_D: Drawing die corner radius
t_0: Sheet thickness
D_0: Blank Ø
d_0: Punch Ø
F_d: Drawing force
F_{BH}: Blank holding force

Figure 2.13: Illustration of a simple deep drawing arrangement [Doe10].

The deep drawability is expressed generally in terms of the drawing ratio, $ß_0$, as given in Eq. **(2.22)**.

Symmetric circular geometry → $ß_0 = {D_0}/{d_0}$

Other geometries → $ß_0 = \sqrt{{A_{blank}}/{A_{punch}}}$ **(2.22)**

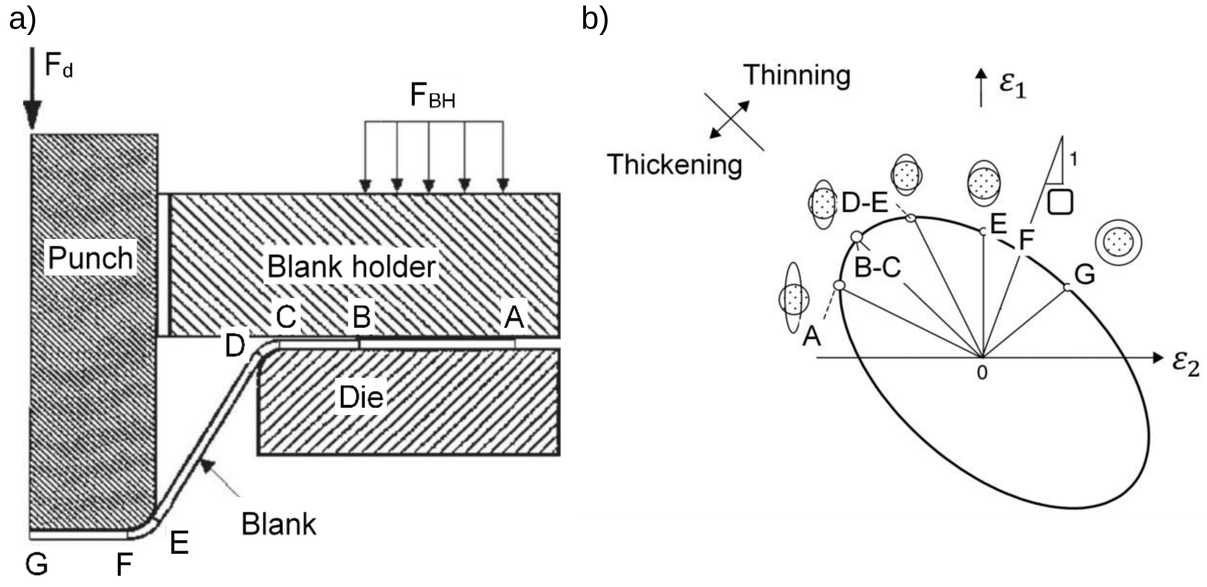

Figure 2.14: a) Schematic illustration of the different cup zone under loading and b) deformation modes in terms of the minor/major strain ratio [Kar12, Mar02].

The maximum drawing ratio at the optimum drawing parameters is expressed as the limiting draw ratio (LDR) or $ß_{0,\max}$ as depicted in **Figure 2.15** at the optimum F_{BH}. Wrinkling or cracking are expected at lower or extremely higher F_{BH}, respectively. In actual cases, $ß_{0,\max}$ can reach 2–2.2 for steel qualities, however a theoretical value of 2.7 is given for a non-strain-hardening material, in which the flow stress do not change with the drawing process [Mar02].

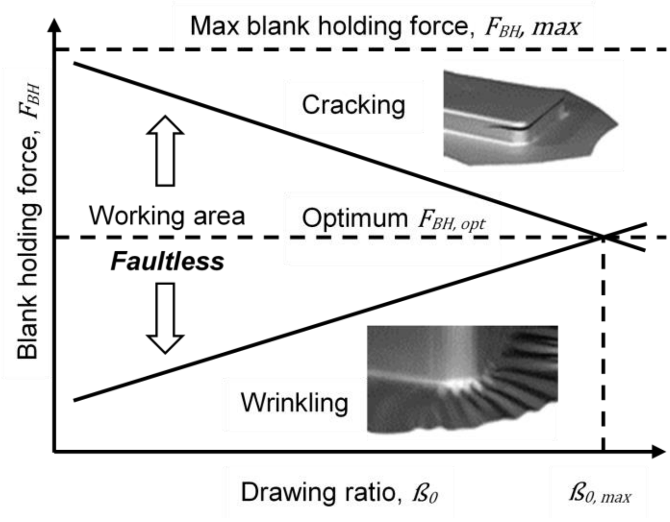

Figure 2.15: Deep drawing working area [Doe10].

The deep drawability is affected by several parameters as shown in **Figure 2.16** [Doe10, Kar12] to be optimized to deliver a reliable faultless drawn cup. Lubrication thickness and quality affect the drawing ratio and the strain distribution significantly over the cup surface [Yan10].

Generally, the required F_{BH} is often determined by 'trial and error' through a series of experiments prior to the actual deep drawing process. The optimum conditions are mostly dependent on the expertise of the investigator [Bol05]. Moreover, F_{BH} can be even estimated based on analytical/empirical approaches as shown in Eq. **(2.23)**, for instance, according to Siebel [Sie55] for axial symmetric as well as rectangular geometries [Doe10, Kar12, Lan95] as follow:

$$F_{BH} = A_{BH} \times 10^{-3} \times c \left[(ß_0 - 1)^3 + \frac{0.005 D_0}{t_0} \right] \times \mathrm{U}TS \qquad \textbf{(2.23)}$$

where A_{BH} is the area of the blank under the blank holder and c is an empirical factor (ranging from 2 to 3).

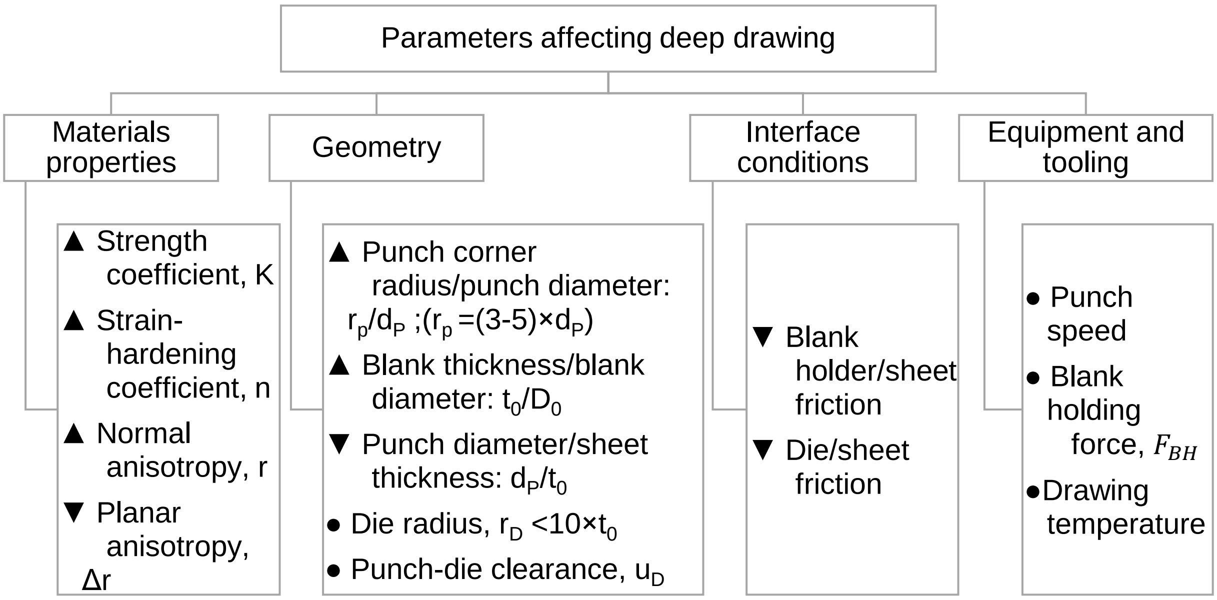

Figure 2.16: Main parameters affecting the deep drawability [Doe10, Kar12]; ▼, ▲, ●: mean that the drawability is improved if these parameters are decreased (▼), increased (▲) or adjusted (●).

2.4.2.1. Drawing force prediction

The instantaneous drawing force F_d is required to deform the sheet and overcome the friction of the blank with the die and blank holder in addition to the bending over the die corner radius, as expressed in Eq. **(2.24)**. In this regard the maximum drawing force, $F_{d,max}$ can be calculated according to Siebel [Sie55], as in Eq. **(2.25)**, at the corresponding flange diameter, $d_{F,max}$.

Siebel (general form)

$$F_{d,total} = F_{Deformation} + F_{Friction} + \mathrm{F}_{Bending} = F_{id} + (F_F + F_D) + F_B \tag{2.24}$$

$$F_{d,\text{total}} = \pi d_m t_0 \left[\underbrace{e^{\mu\pi/2}}_{F_{d,D}} \underbrace{1.1\,\sigma_{f,m,I}\,ln\left(\frac{d_F}{d_m}\right)}_{F_{d,id}} + \underbrace{\frac{2\mu F_{BH}}{\pi d_F t_0}}_{F_{d,F}} + \underbrace{\sigma_{f,m,II}\frac{t_0}{2r_D}}_{F_{d,B}}\right] \tag{2.25}$$

$$F_{d,max} \rightarrow\ d_F = d_{F,max} \approx 0.77\,D_0$$

where:

d:	instantaneous flange diameter, however
$d_{F,max}$:	flange diameter at the maximum drawing force
$F_{d,max}$:	maximum drawing force
$F_{d,D}$:	force increase due to the friction at the drawing die;
$F_{d,id}$:	ideal deformation load;
$F_{d,F}$:	force increase due to the friction at the flange with the blank holder and drawing die
$F_{d,B}$:	load necessary for bending the sheet around the die radius
$\sigma_{f,m,I}$:	mean flow stresses in the region A-C (**Figure 2.14**)
$\sigma_{f,m,II}$:	mean flow stresses in the region C-D (**Figure 2.14**)
µ:	friction coefficient; depends on the lubrication system (0.01–0.15);
d_m:	mean sidewall diameter $d_m = d_0 + t_0$.

Other simple approaches were suggested by Siebel and others, Eqs. **(2.26)** and **(2.27)**, considering the deep drawing efficiency η [Sie55] or tabulated correction factor k [Rom71], respectively. However, Eq. **(2.25)** is the best equation for calculating the drawing load because it considers all the load components. Moreover, it can predict F_d instantaneously, i.e. at each cup height.

Siebel (simple form):

$$F_{d,max} = \pi d_m t_0 \left[1.1\,\frac{\sigma_f}{\eta}\left(ln\frac{D_0}{d_0} - 0.25\right)\right], \qquad \sigma_f \approx 1.3\,\mathrm{U}TS, \qquad \eta = 0.5 - 0.79 \tag{2.26}$$

Romanowski:

$$F_{d,max} = \pi d_0 t_0\ UTS\ k \tag{2.27}$$

The efficiency η depends mainly on geometrical and lubrications conditions of the drawing operation. It can range from 0.5 up to 0.79 [Kar12, Lan95]. η can be determined from the ratio between the ideal deformation force, $F_{d,id}$ and the total drawing force, $F_{d,tot}$, as expressed in Eq. **(2.28)**.

$$\eta = \frac{F_{d,id}}{F_{d,tot}} \tag{2.28}$$

Theoretically cracking occurs when the drawing force exceeds the necking condition, as expressed in Eq. **(2.29)**:

$$F_{cracking} = a_c\, \pi\, d_{\mathrm{m}}\, t_0\, \mathrm{U}TS \qquad \textbf{(2.29)}$$

where a_c is the cracking factor: for steel, it ranges between 1.05 and 1.55.

The LDR value ($\text{ß}_{0,\max}$) can be roughly estimated according to Eqs. **(2.30)** [Kar12], **(2.31)** [Lan95], or **(2.32)** [Sat15].

$$\ln \text{ß}_{0,\max} = \eta \sqrt{(\mathrm{R}+1)/2} \qquad \textbf{(2.30)}$$

$$\ln \text{ß}_{0,\max} = \left(\frac{\eta}{1.1}\right)^{1/(\mathrm{n}+1)} (\mathrm{n}+1) \qquad \textbf{(2.31)}$$

$$\text{ß}_{0,\max} = \sqrt{\mathrm{e}^{(1+\mathrm{n})[2\eta \mathrm{e}^{-\mathrm{n}} - \mathrm{e}^{\mu\pi/2\mathrm{t}\cdot r_d}\sqrt{(1+\mathrm{R})/2\, -\, 4\mu\sqrt{(1+2\mathrm{R})/[2(1+\mathrm{R})]}}]} + \mathrm{e}^{2\mathrm{n}\sqrt{(1+\mathrm{R})/2}} - 1} \qquad \textbf{(2.32)}$$

For calculating the drawing force at each cup height (h), the geometrical correlation between the instantaneous flange diameter d and h is expressed based on the original blank diameter D_0 in Eq. **(2.33)** [Lan95].

$$\begin{aligned} D_0 &= \sqrt{d_0^2 + 4dh} \\ h &= \frac{1}{4d}\left(D_0^2 - d_0^2\right) \end{aligned} \qquad \textbf{(2.33)}$$

2.4.2.2. Deep drawing of laminated systems

Deep drawing of thin-cored MPM-laminates, namely Bondal®, was investigated using circular geometries showing the accompanying defects [Bol14]. Moreover, an attempt to increase its stiffness was proposed by introducing stiffening beads. It was found that the core shear stress acting on the interface between the skin and the core layers and the bending/unbending are responsible for the laminates failure under deep drawing [Moh05]. The shearing of the core layer depends mainly on the thickness and properties of the skin sheets in addition to the geometrical factors. A summary of the deep drawability of sound damping laminates is described by [Kim97]. The drawability decreased with increasing the adhesive layer thickness between the two skin sheets. This is because due to the stress condition of the laminate skins. Additionally, drawing force are required with increasing the adhesive thickness due to the higher rigidity for thicker laminates.

Moreover, some defects were found in the fibrous composite core in e.g. 1.5–2.0 mm thick steel/GFR-PA/steel sandwich laminates after deep drawing at an elevated temperature, such as fiber cracks, wrinkling and thickness irregularities [Han12, Tek15]. Therefore, further interpretation, development and improvement of these structures are still a need. Similar defects were reported in [Bol13, Bol14] after deep drawing of different geometries of steel/aramid fiber reinforced core/steel laminates at RT (room temperature) at varied core thicknesses. The deep drawability or forming of profiles, such as B-pillars, of metal/FRP/metal laminates can be carried out stepwise to minimize the arising defects by drawing the metals skins separately and then achieving the metal/core adhesion at optimized temperature/pressure/time/textile design [Gro12, Sta15]. Moreover, wrinkling severity and drawing force relation with blank diameter, laminate thickness, blank holder force (F_{BH}) and temperature for Al/PP/Al as well as Al/GFR-PP/Al laminates was studied. In this study it is shown that higher temperature and F_{BH} reduce wrinkling, however, faultless drawing was not possible under the studied parameters [Raj15]. Well drawn cups were reached of 0.5 mm thick Al skin in Al/PP/Al with $ß_{0,max}$ values of 1.8, 1.7 and 1.67 for core thickness of 0.2, 0.5 and 1.0 mm, respectively [Par10]. Increasing the temperature increases the possibility of wrinkling [Wei07] because of the softening of the core and hot melt adhesive layers.

Besides the investigations of MPM-laminates, the deep drawing behaviour of sheet metal laminates, such as steel/steel [Che06], Al/Cu [Che06, Tse10] steel/brass laminates [Atr13] and the springback after draw-bending of two-ply steel/Al laminates [Hin03] was investigated. The results show that forming forces and springback are strongly affected by the strength difference between the component layers, the relative position of the strong/weak layers and the thickness ratio of each layer.

2.5. Locally reinforced MPM-laminates

After producing the semi-finished MPM-laminates, there might be the need to join them for the final applications. The joining operations can be mechanical (riveting, clinching or bolting), thermal (welding), chemical (using adhesive agents like glue) or a combination of the methods. Joining the MPM-laminates is still a challenge due to the difficulties of the polymeric core layer. The core layer is:

1. Electrically insulating (hinders the welding processes),
2. Mechanically elastic and soft (it can lead to dimensional distortion), and
3. Thermally unstable especially at the high processing and service temperatures like welding and coating operations.

However, joining can be achieved after adapting the joining areas. Some joining methods of multilayer materials are summarized in [Ama09, Huf96]. The joining process can be accomplished directly by friction stir welding [Che09] after adjusting the heat input parameters like the rotation speed and pressure (**Figure 2.17-a)**). Some attempts on direct laser welding were performed on low-density laminates like e.g. Steelite® and 316L/PP-PE/316L [Gow07, Pal06]. The corrosion resistance of laser welded low-density laminates based on 316L skin sheets and PP-PE core showed no deterioration compared to the reference (unwelded) laminates [Pal06]. Other joining methods were applied like self-pierce riveting of Al sheets with Hylite as well [Pic07], wherein the drawbacks (springback, non-uniform deformation) of the polymeric core are described.

Various approaches were developed to overcome the joining drawbacks of the MPM-laminates by adapting the joint:

1. Hot pressing the welding zone for the resistance spot welding (RSW). So, the polymer core is locally removed and hence facilitates the electrical conductivity. This method can be applied for sound damping, e.g. Bondal® [Thy09a] (**Figure 2.17-b)**) as well as the low-density laminates, e.g. Litecor® [Lau14] (**Figure 2.17-c)**).
2. Inserting plug holes in the joining points in one of the joined work-pieces, so the wire electrode can be melted and fill the plug with the help of shielding gas, i.e. gas metal arc welding [Fon13].
3. Local-substituting the core layer with metallic reinforcement (RE) in the joint area, so the electrical conductivity and improved coupling efficiency can be achieved as well as reduced indentation effect [Cam09, Fin03, Fin13, Pal06, Pat13, Per11, Sok12]. The bearing strength and the indentation behaviour of the locally reinforced MPM-laminates under bolting with different moments were investigated, where the indentation was enhanced [Cam09, Pal11].

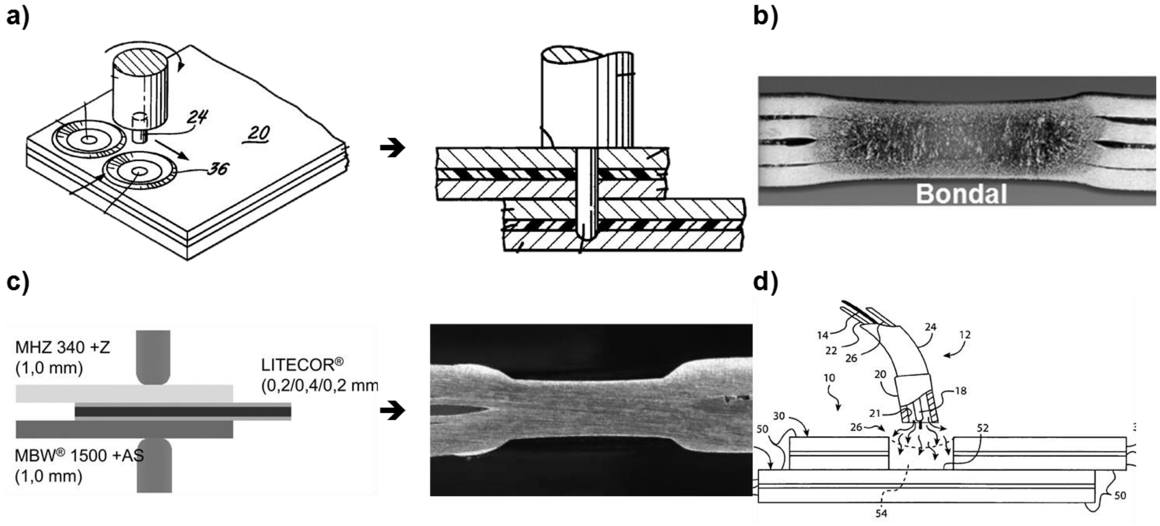

Figure 2.17: Welding possibility of MPM-laminates: a) friction stir welding [Che09], b) and c) resistance spot welding [Lau14, Thy09a] and d) gas metal arc welding [Fon13].

Based on the thickness and the number of the laminate layers or rather the core structure, the RE's can be single-layered in the case of relatively thin MPM (0.8–3 mm) [Pal11, Pat13, Sok12] or multilayered in case of joining CFRP laminates (3–18 mm thick) with other joint couples [Fin03, Fin03, Per11].

The solution approach of the single-layered reinforced MPM-laminates is the one applied in the current study. However, this approach faces a number of drawbacks [Har17]:

1. The development of an automated production scheme for inserting the inlays during the laminate production in-line, preferably by rolling. In this regard, a concept for a continuous production by rolling of weldable band-like MPM-laminates, containing a locally treated polymer core with conducting elements to ensure the electrical conductivity, is patented by [Pat13].
2. The location of the reinforced regions should be monitored/recognized during/after shaping the formable reinforced laminates. This point has been studied by [Pal11, Sok12]; predicting the location of the RE's after forming and their influence on the forming limits is the main focus. However, there is a need to study further parameters on the forming limit of these reinforced laminates like varied mechanical and geometrical properties of the MPM-laminates
3. The interface at the RE edge - between the RE and the neighbour core layer - has a significant effect on creating stress concentration regions that can accelerate failure during processing and application. This point was handled in [Fin13, Fle12] by creating different overlapping regions between the inserts and the neighbour core, as shown in **Figure 2.18**.

The production of metal/CFRP hybrid laminates using RTM in one-step represents the main research proposal of LiA, LWF and LTM Paderborn University [Zin15]. Other laminate structures cores were locally reinforced, for instance, PVC foam with local inserts of Plywood (Butt or scarf form) [Boz05] or with a honeycomb core [Kim08, Lim11, Son08].

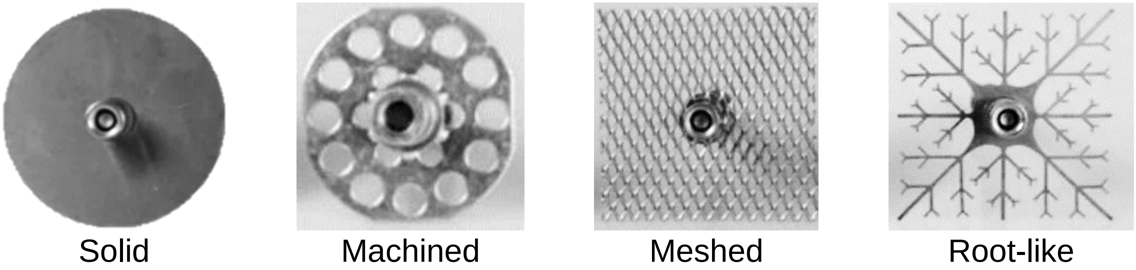

Figure 2.18: Different reinforcement structures to manipulate the interface with the adjacent core layer [Fle12].

3. Characterization of non-reinforced MPM-laminates

In this chapter, the main characteristic values of the MPM-laminates and the monomaterials are determined, that will help interpreting and predicting their forming potential. For this purpose, the necessary experimental methodology is depicted in **Figure 3.1**. Firstly, the used materials, i.e. skin, core and adhesive layers, are specified and the purpose of their selection is given. Afterwards, the MPM-laminate production scheme is described. The metal/polymer interface properties are evaluated by means of single lap shear and peel testing, where the failure surfaces are examined as well. Additionally, the metal/polymer interface durability is evaluated by subjecting the sandwich laminates to natural and accelerated environmental conditions. Also, the mechanical behaviour was characterized in terms of the tensile properties. Finally, the formability limits were investigated by the determination of the FLC of some monolithic sheets and their MPM-laminates. Therefore, the output of this chapter is an extensive description of the metal/polymer interface, forming-related mechanical properties and suitable FLC curves in order to interpret and monitor the later sheet forming processes.

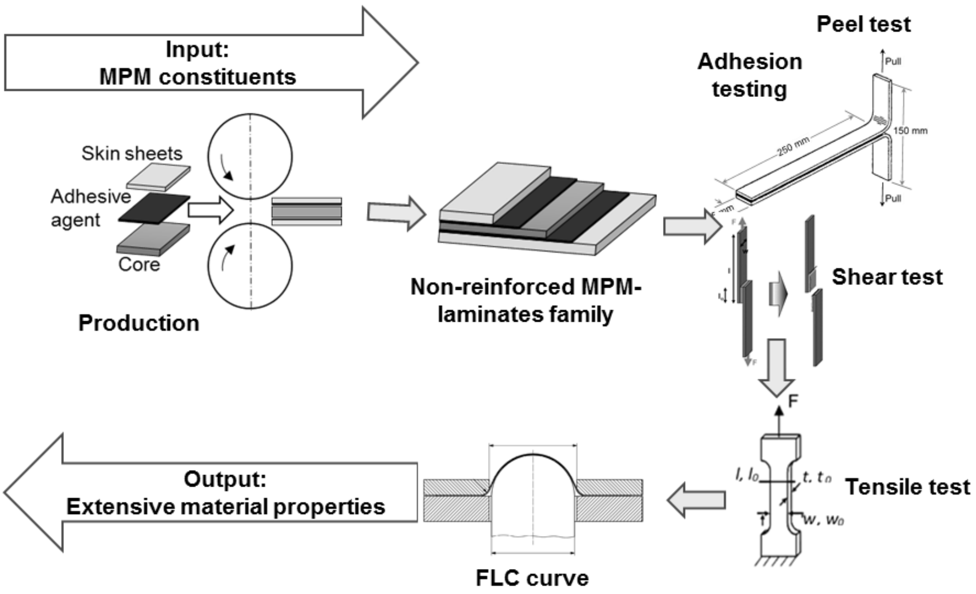

Figure 3.1: Characterization methodology of the monomaterials and the MPM-laminates.

3.1. Materials

Different grades of metallic sheets were utilized as the MPM-laminate skin sheets, namely steel, aluminium and titanium ones, focusing on different applications. However, a PP-PE thermoplastic copolymer was used as core layer. Different thicknesses of the skin and core layers were considered. The adhesion was achieved with the aid of an epoxy resin. The goal of including various sheet metallic grades as skin sheets is to characterize and interpret the mechanical behaviour of the various symmetric and asymmetric MPM-laminates in respect to the reference monolithic skin sheets. “Symmetric MPM-laminate” means that the used two skin sheets are identical in thickness and grade. However, in the asymmetric ones, skin sheets of the same grade but in different thicknesses are used for tailoring three- as well as five-layered SPS. Moreover, different steel grades can be combined in such asymmetric laminates. Another aim of coupling different steel grades in a single laminate is to gain the advantage of each grade to deliver good corrosion resistance, forming potential, better specific mechanical properties and cost-efficiency. In this case, there is a need to characterize the mechanical and forming properties of these asymmetric laminates from both sides in order to determine the forming limits.

3.1.1. Metallic skin sheets

Table 3.1 gives an overview of the used skin sheets and their notations being used in the thesis.

Table 3.1: Specification and notation of the used metallic skin sheets.

Skin sheet	Notation	Grade	t, [mm]	Surface condition
Deep drawable steel	DD1	TS245	0.49	Sn-coated
		TS245	0.24	
	DD2	TH470	0.49	
Dual-phase steel	DP	HCT500XD+z100	0.52	Galvanized
Stainless steel	SS	316L	0.5	-
Aluminium	Al	EN AW-3003	0.3	-
Titanium	Ti	Titanium Grade 1	0.5	-

Following is a brief description of the used four steel grades and their chemical composition (see **Table 3.2**):

1. A deep-drawing (DD) quality namely the Tinplate® grade TS 245 (EU 1.0372 grade supplied by thyssenkrupp-Rasselstein GmbH, [Eur16, Mar10]). This grade is a high corrosion resistant, electrolytic Sn-coated steel delivered in two thicknesses; 0.49 and 0.24 mm.
2. Another high strength DD grade TH470 was involved in order to study the effect the mechanical properties of the skin sheets on the forming potential of the

SPS-laminates. A further application of it is the production of asymmetric SPS-laminates composed of two dissimilar steel grades aiming at controlling the strength and the forming properties in respect to each steel grade.

3. Furthermore, a hot-dip galvanized dual-phase (DP) steel grade was utilized HCT500XD+z100 (EU 1.0939 grade, Salzgitter Flachstahl GmbH [Mar10]), , with a thickness of 0.52 mm.
4. The fourth steel type is a low carbon austenitic stainless steel, the EN 1.4404 / AISI 316L, with a thickness of 0.5 mm. This grade possesses superior mechanical properties and high corrosion resistance; however, the price/kg can limit their applications in various engineering fields.

Aluminium skin sheets in a thickness of 0.3 mm was used to verify the production scheme for other metallic skin sheets besides the steel ones with different surface properties and to ensure the ROM. Additionally to enable using the tailored MPM-laminates for biomedical applications, a 0.5 mm thick titanium grade 1 was used in addition to the 316L one.

Table 3.2: The chemical composition of the used steels in wt%. NA: not available

Grade	t [mm]	C	Mn	Al	N	S	P	Si	Cr	Ni	Mo
DD1	0.49	0.06	0.32	0.03	0.01	0.01	0.01	0.01	0.04	0.01	<0.00
	0.24	0.03	0.22	0.03	0.01	0.01	0.01	0.01	0.04	0.02	0.00
DD2	0.49	0.06	0.28	0.03	0.01	0.01	0.01	0.01	0.04	0.01	0.00
DP	0.52	0.1	1.5	0.05	NA	0.01	0.05	0.15	0.04	NA	0.04
SS	0.5	0.03	2.0	NA	NA	0.03	0.05	0.75	16-18	10-13	2.0-2.5

3.1.2. Polymer core layer

The polymer core used for this study is a polypropylene-polyethylene (PP-PE) polyolefin foil in a thickness of 0.2, 0.3 and 0.6 mm. PP-PE blend represent 80% and the rest is talc, rutile and barite. More details can be found in [Lan06, Sok12]. For thicker core layers, the available layers are laid up and molten together to deliver the required thickness, namely 1.0 and 2.0 mm. Heating or rather melting and cooling in the sheet-like form has no remarkable effect on the mechanical properties of the foils. It was found that the maximum tensile strength is reduced from (29±1) MPa for the as-received condition to (27±1) MPa after preheating the polymer at 260° and tested at RT.

The polyolefin (PP and PE) are chemically inert [Ari94], thus leading to difficulties achieving adhesion between them and the metal without applying appropriate surface pre-treatments like using compatible adhesive agents. In the case of achieving a good adhesion strength between the metal and PP-PE layers, a good forming potential of the produced MPM-laminates can be achieved due to the superior ductility of this polymer at RT (low T_g value). **Table 3.3** summarizes the main properties of the copolymer.

Table 3.3: Physical and mechanical properties of the core layer (PP-PE copolymer).

Property	Unit	Value
Density	$g.cm^{-3}$	0.920
Poisson's ratio	-	0.45
T_m	°C	~157
T_g	°C	-17
UTS	MPa	29
E	GPa	1.45
e_f	%	200-400

3.1.3. Adhesive agent

In this study, the one-component epoxy resin Köratac FL201 was used (Kömmerling Chemische Fabrik GmbH) to achieve the metal/polymer bonding. Its main technical data are illustrated in **Table 3.4**, as delivered from the supplier. The peak metal temperature (PMT), at which the metallic skin sheet should be preheated in order to perform the metal/polymer adhesion [Jan13], ranges between 220 and 240°C.

Table 3.4: Technical data for the adhesive agent (Köratac FL201).

Property	Unit	Value
Density of adhesive	$g.cm^{-3}$	0.96
Density of solvent	$g.cm^{-3}$	0.92
Solvent content	%	69
Wet layer thickness	µm	35
Dry layer thickness	µm	10
Peak metal temperature (PMT)	°C	220–240

3.2. MPM-laminate production

The different MPM-laminates were produced through roll bonding, as shown in **Figure 3.2**, using the principle of the so-called coil coating technology, described in [Jan13, Thy09a]. This method was adapted to lab scale by [Lan06, Sok12].

The production process consists of the following steps:

1. Degreasing and cleaning the steel skins and the polymer foil using acetone.
2. Spreading the resin over the steel sheet using a spread roll to give a wet layer thickness of ~35 µm and subsequently a dry adhesive layer thickness of ~10 µm after drying/curing.

3. Heating up the coated steel sheet with the adhesive layer to (260 ±2) °C for 3 min to reach the PMT. The polymer foil is softened by warming it up to (120 ±2) °C for 3 min.
4. Laying-up the coated steel sheet with the polymer layer and rolling in a soft rubber casing to avoid heat loss and spread load, giving a half sandwich. It is noteworthy that negligible rolling pressure was applied to avoid thickness reduction of the polymer core.
5. Producing the complete MPM-laminate by repeating point 2 and 3 for the second skin sheet then rolling with the half sandwich as in step 4.

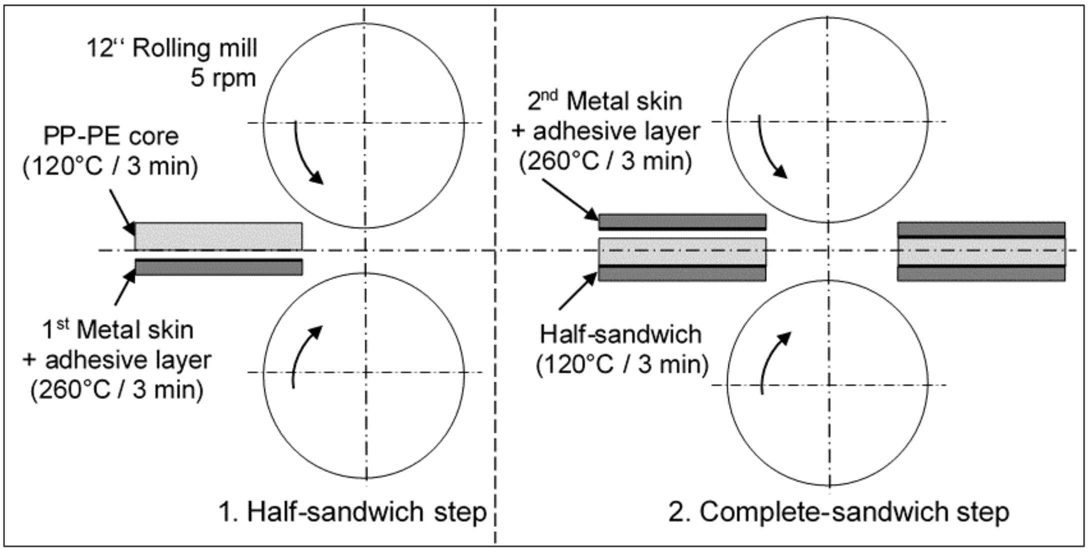

Figure 3.2: Illustration of the MPM-laminate production scheme.

A scaling approach is proposed for reliable and efficient characterization methodology, as described in **Figure 3.3**. This scaling is achieved as follow:

1. Monomaterials: metals and core layers
2. Sheet metal laminates: joined metal/metal laminates with a commercial adhesive.
3. Unjoined MPM-laminates: three-layered MPM-laminate without adhesion to study the effect of the interface strength.
4. Normal, joined, symmetric MPM-laminates with varied core and skin layer thicknesses
5. Different asymmetric MPM-laminates: based on dissimilar skin layer thickness or grade in the same laminates and additionally five-layered ones.

For this purpose, different MPM-laminate configurations were produced with various skin/core thicknesses using the previously described production scheme. **Table 3.5** gives an overview of the produced laminates, their thicknesses ratios and their notation. For simplification, these notations will be utilized for the rest of the study.

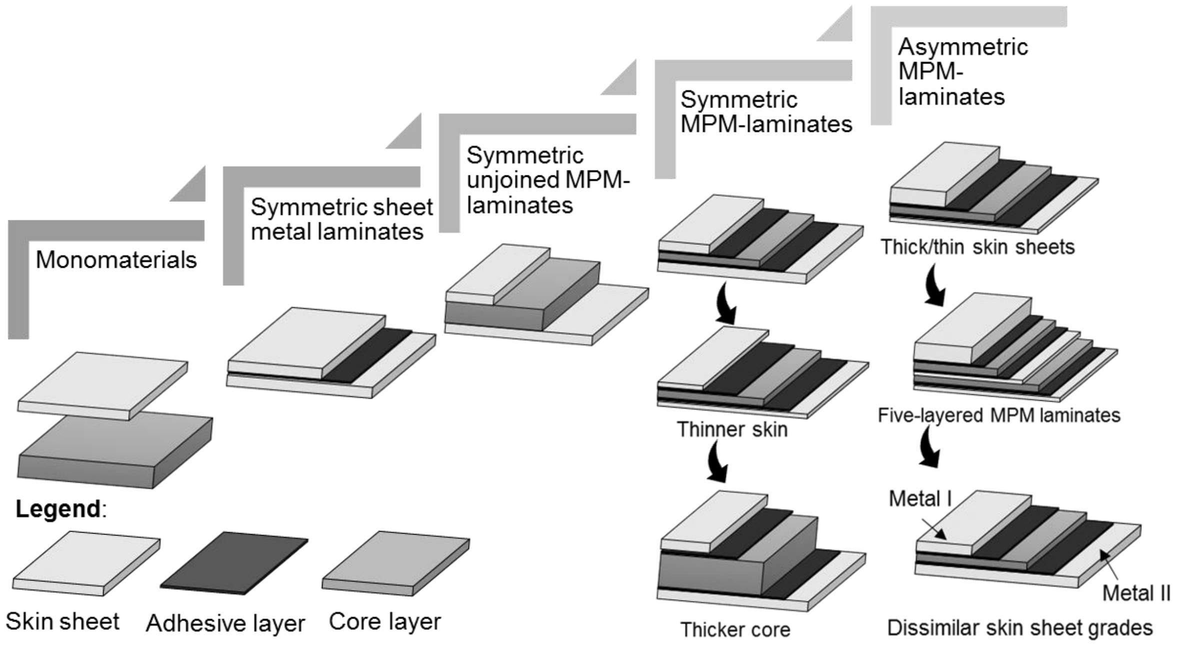

Figure 3.3: The scaling approach starting from the monomaterials to variable laminar configurations for reliable and efficient material characterization.

3.3. Evaluation of the metal/polymer adhesion

In this part, the quality of the steel/polymer interface is evaluated in order to verify that the adhesive strength is enough for a successful forming operation. This evaluation is necessary because the interface shear strength is significant for improving the forming limits as well as minimizing the forming defects, such as wrinkling and delamination or interlaminar shearing. The adhesive quality was determined in terms of the shear strength and the peel resistance. Moreover, the kind of failure between the layers was identified, whether adhesive, cohesive or mixed. Furthermore, the service life durability was assessed by different hydrothermal aging regimes.

Table 3.5: MPM-laminates with their notations showing the reason for tailoring each laminates structure.

Notation	Thickness distribution of the MPM-laminates layers [mm]			t_{MPM} [mm]	f_c
	Skin	Core	Skin		
	TS245	PP-PE	TS245		
Effect of the core thickness at constant skin sheet thickness (0.49 mm)					
DD1 0.49/0/0	0.49	0	0	0.49	-
DD1 0.49/0/0.49	0.49	0	0.49	0.98	0.1
DD1 0.49/0.3/0.49	0.49	0.3	0.49	1.28	0.23
DD1 0.49/0.6/0.49	0.49	0.6	0.49	1.58	0.38
DD1 0.49/1.0/0.49	0.49	1.0	0.49	1.98	0.51
DD1 0.49/2.0/0.49	0.49	2.0	0.49	2.98	0.67
Effect of the core thickness using the same steel grade (DD1) but thinner (0.24 mm)					
DD1 0.24/0/0	0.24	0	0	0.24	-
DD1 0.24/0.3/0.24	0.24	0.3	0.24	0.78	0.38
DD1 0.24/0.6/0.24	0.24	0.6	0.24	1.08	0.55
Effect of the sandwich symmetry of the same steel grade with varying the core thickness (0.3 and 0.6 mm)					
DD1 0.49/0.6/0.24	0.49	0.6	0.24	1.33	0.45
DD1 0.49/0.3/0.24	0.49	0.3	0.24	1.03	0.29
Effect of the number of layers (5-layered sandwich) in comparison with 3-layered ones keeping the same *f*-value of 0.38					
DD1 0.49/0.3/0.24/0.3/0.24	0.49	0.3 (2^{X})	0.24 (2^{X})	1.57	0.38
Effect of the steel grade maintaining the same thickness and f_c = 0.38					
	TH470	PP-PE	TH470		
DD2 0.49/0/0	0.49	0	0	0.49	-
DD2 0.49/0/0.49	0.49	0	0.49		0.1
DD2 0.49/0.6/0.49	0.49	0.6	0.49	1.58	0.38
	HCT500XD	PP-PE	HCT500XD		
DP 0.52/0/0	0.52	0	0	0.52	-
DP 0.52/0/0.52	0.52	0	0.52		0.1
DP 0.52/0.6/0.52	0.52	0.6	0.52	1.64	0.37
	316L	PP-PE	316L		
SS 0.5/0/0	0.5	0	0	0.50	-
SS 0.5/0/0.5	0.5	0	0.5	0.50	0.1
SS 0.5/0.6/0.5	0.5	0.6	0.5	1.60	0.38
	Ti Gr. 1	PP-PE	Ti Gr. 1		
Ti 0.5/0/0	0.5	0	0	0.50	-
Ti 0.5/0.6/0.5	0.5	0.6	0.5	1.60	0.38
	Al	PP-PE	Al		
Al 0.3/0/0	0.3	0	0	0.30	-
Al 0.3/0.6/0.3	0.3	0.6	0.3	1.20	0.5
Effect of the MPM-laminate symmetry utilizing different steel grades at constant core thickness of 0.6 mm or constant f_c = 0.38					
DD1/0.6/DD2	0.49	0.6	0.49	1.58	0.38
DD1/0.6/DP	0.49	0.6	0.52	1.61	0.37
DD1/0.6/SS	0.49	0.6	0.5	1.59	0.38

^{X}: number of layers

3.3.1. Durability assessment of the metal/polymer interface

The MPM-laminates were subjected to selected hydrothermal aging environments. The aim was to analyse the aging behaviour and to determine the loss of the bond strength in correspondence with the aging period. The applied aging regimes are:

1. One year natural aging at room conditions (23±3) °C.
2. Three different accelerated cycling regimes using a climatic chamber, where one cycles each regime is described in **Figure 3.4**):
   a. +50/-20°C: (+50°C/12h)–(-20°C/12h) in water for 28 cycles,
   b. +70/-20°C: (+70°C/12h)–(-20°C/12h) in water for 7 cycles, and
   c. VW P1200: (+80°C/4h)–(-40°C/4h) in 80% rel. humidity or the so-called “climate change test” for 20 cycles [Bro05].

The single lap shear as well as the T-peel finished specimens were subjected to the test medium in a not-sealed condition, which allows the test medium to reach the metal/polymer interface easily.

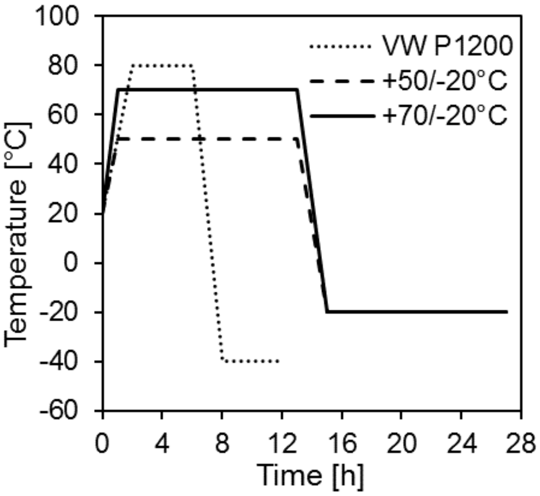

Figure 3.4: Hydrothermal aging regimes (one cycle/each regime is shown).

3.3.2. Single lap shear testing

For an accurate measurement of lap shear strength, the maximum overlapping length should not overstep the optimum L_{OV-Op} following Eq. **(2.3)** to avoid cracking of the skin sheets. Therefore, intending to approximate the L_{OV}, the shear strength of the polymer core is required to be considered in this equation. For that, it was assumed that the shear failure would take place in the core itself, i.e. cohesive failure. In this regard, the shear strength of the polymer was evaluated at the Institute of Applied Mechanics, TU Clausthal using a modified three-rail shear testing setup. The value of maximum shear strength (τ) of the PP-PE foil, at a testing rate of 0.01 mm/s (0.6 mm/min), was 13 MPa, as shown in **Figure 3.5** [Sgu15].

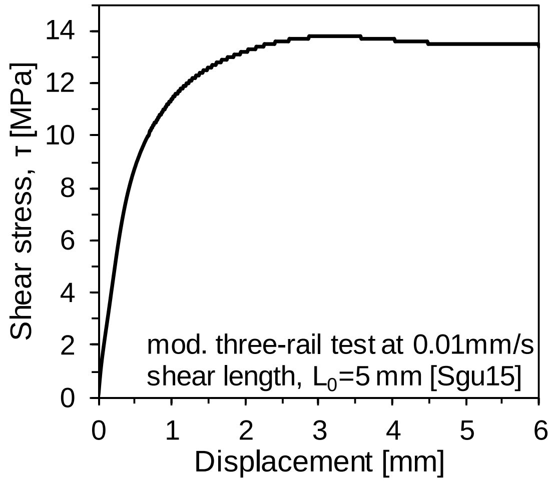

Figure 3.5: Shear test with a modified three-rail testing tool of a 0.6 mm PP-PE foil at room temperature with a shearing rate of 0.01 mm/s [Sgu15].

The L_{OV} is more critical for thin and weak skin sheets. The L_{OV} estimations are summarized in **Table 3.6**. Therefore, to maintain a constant L_{OV} for all the specimens, the thin skin sheet, namely the 0.24 mm DD1 grade, is the determinant for that estimation. Accordingly, it was safe to perform the shear test with an overlapping length of 5 mm, where the yielding force is relatively close to the maximum shear force of the 0.24 mm sheet.

Table 3.6: Effect of the overlapping length on the adhesion strength considering the tendency of the skin sheets to plastic deformation based on their YS values.

SPS laminate	L_{OV} [mm]	YS [MPa]	F_{YS} [N]	τ_{max} [MPa]	F_{shear} [N]
DD1 0.24/0.6/0.24	5.0	225	1350	9.6±1.2	1200±150
DD1 0.49/0.6/0.49	12.5	218	2670	12.2±1.5	3897±469
	5.0			11.2±0.8	1425±103
DP 0.52/0.6/0.52	12.5	362	4706	9.28±1.2	3165±398
	5.0			9.7±0.7	1258±82

Subsequently, the adhesive strength of the laminates was determined according to ASTM 3165, using the specimen dimensions illustrated in **Figure 3.6**, with a displacement rate of 1 mm/min. A groove of 6 mm width, going through the layers until reaching the opposite skin layer, was machined from both sides defining the overlapped area. The test specimens were prepared in this way to ensure axial loading and avoid bending moments, as far as possible. At least, five test specimens were used for each laminate combination; each specimen was cut from different production cycles to consider individual deviations. The maximum lap shear strength (in MPa) of the bond was calculated by dividing the maximal force reached by the overlapped surface area (L_{OV}×25 mm^2).

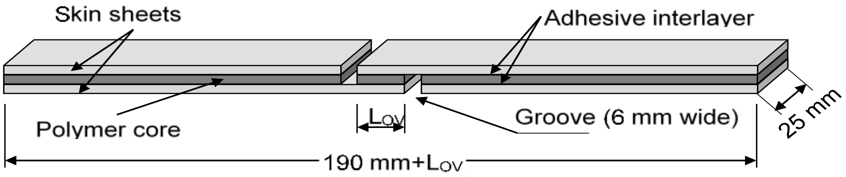

Figure 3.6: Single lap shear test specimen.

It can be stated from **Table 3.6** and **Figure 3.7-a)** that the shear force changes linearly with L_{OV} but the adhesion strength does not change remarkably. It can be even observed from **Table 3.6** that for stronger and thicker skin sheets, such as the DP 0.52 mm grade, the test can be carried out at larger L_{OV} values (>12.5 mm), where the shear force is still far away from the yielding force. The progress of the shear stress–displacement is different according to the L_{OV} value, as shown in **Figure 3.7-b)**. The longer the overlapping length is, the higher is the displacement until reaching the point of complete delamination or, in this case, complete shearing of the polymer. Regardless the L_{OV} value, cohesive failure in the core layer took place, as observed from the failure surfaces **Figure 3.7-b)**. It is noteworthy that the cohesive failure took place after simple surface preparation, i.e. degreasing with acetone, therefore no complex surface treatments were necessary for the tinned DD1 and DD2 grades.

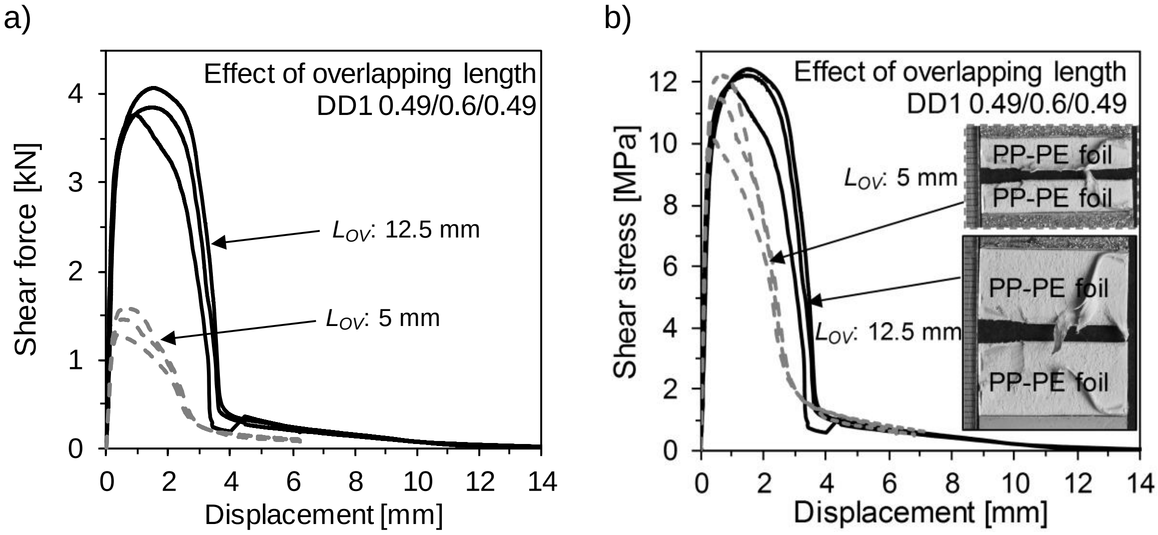

Figure 3.7: Effect of the overlapping length (L_{OV}) on the shear behaviour regarding a) the shear force and b) strength for DD1 0.49/0.6/0.49 (three test specimens each).

The strain distribution over the skin sheets during the shear test at the area close to the lap joint was monitored with the DIC system to determine the strain extent and the tendency of the skin sheets to cracking and bending in terms of the out-of-plane displacement. **Figure 3.8-a)** shows the progress of the shear stress–displacement of a SPS with thin skin sheets (0.24 mm) and a 0.6 mm core. This combination was chosen to be studied in details due to the expected surface strains. The von-Mises strain (in %) mapping and the out-of-plane displacement (in mm) are depicted in **Figure 3.8-a)** at:

1. Point 1 at the maximum shear stress, and
2. Point 2 close to the final metal/polymer delamination, i.e. at the end of the stress–displacement progress.

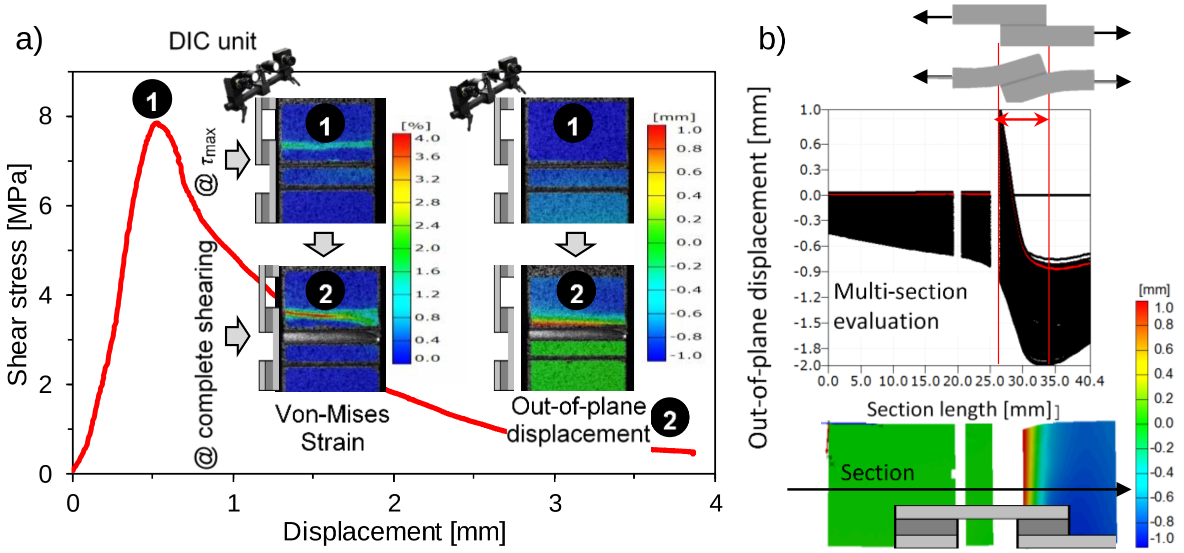

Figure 3.8: a) Von Mises strain distribution and the out-of-plane displacement results at the maximum lap shear strength (point 1) and close to complete shearing (point 2) of the overlapped area, monitored by the DIC system for the DD1 0.24/0.6/0.24 and b) the progress of the out-of-plane displacement over the test progress by means of multi-section evaluation.

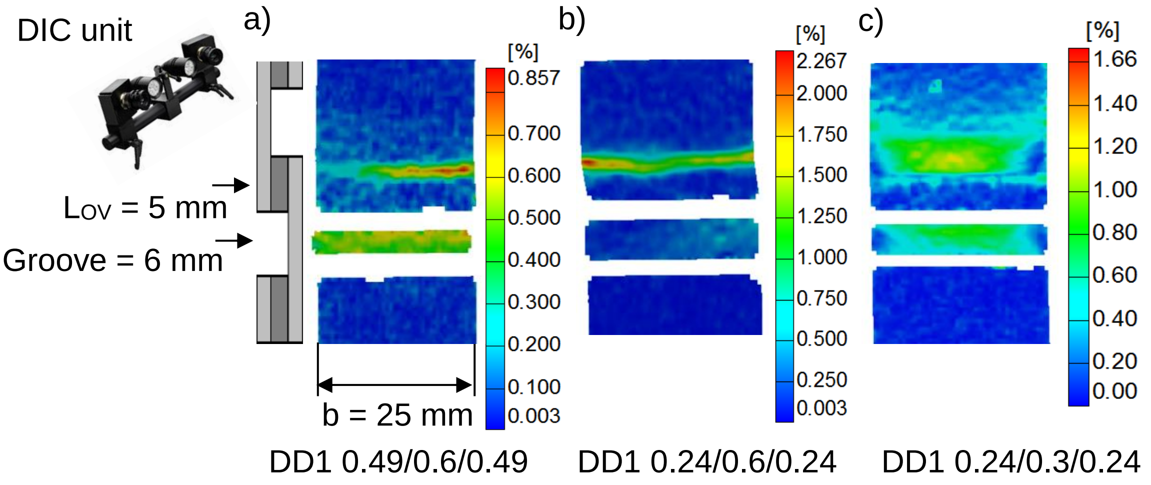

DD1 0.49/0.6/0.49 DD1 0.24/0.6/0.24 DD1 0.24/0.3/0.24

Figure 3.9: Von Mises strain distribution at the maximum lap shear strength value (point 1 in **Figure 3.8**) of the skin sheets close to the overlapped area for three DD1-combinations; a) 0.49/0.6/0.49, b) 0.24/0.6/0.24 and c) 0.24/0.3/0.24 evaluated by photogrammetry analysis.

It can be observed that at the maximum shear stress at shear displacement of 0.5 mm, a negligible out-of-plane displacement took place, additionally only 1 % strain was found at the boundary of the overlapped area. With further shear displacement up to 4 mm, remarkable bending deformation occurred that led to about 2 mm out-of-plane shift at 4 % strain at the edges. This shifting is very clear with the time-steps of the shear test as shown from the multi-section evaluation in **Figure 3.8-b)**. The obtained strain values are still away from the limiting strains, at which cracking could take place.

In order to consider the geometrical parameters, i.e. the skin/core thicknesses on behaviour of the overlapped area, **Figure 3.9** shows three DD1 based SPS conditions: 0.49/0.6/0.49, 0.24/0.3/0.24 and 0.24/0.6/0.24. In all cases, there was a localized straining in the single skin sheet close to the lap joint. These strains differ according to the SPS structure. Minor changes were attained for the thicker skin sheet (0.49 mm), as shown in **Figure 3.9-a)**. However, for the thinner ones, the strain values are higher. These strain values are dependent on the core thickness. For thicker cores (0.6 mm), higher strains were obtained in respect to the 0.3 mm core because of the longer displacement-potential provided by the thicker core until delamination (**Figure 3.9-b)**). As a result, bending deformation is most likely for the thinner skin sheets. While the thicker skin sheets come closest to a purely shear loading, the thinner skin sheets have a combined state of shear and large peel stresses, which in turn produce a different state of stress in the adhesive bond than the thicker ones [Rod12, Tom01].

As mentioned in part 3.2, the PP-PE core layer is preheated to 120°C before adhesion. This step can be performed easily, in the lab scale, for the 0.6 mm polymer thickness. However, thinner layer (0.3 mm) tended to roll up during heating in the furnace, which complicated its handling and therefore there is a need to determine the effect of the preheating on the bond quality. In this regard, the effect of the polymer preheating was studied for the DD1 0.49/0.6/0.49. The effect of preheating in terms of the shear stress-displacement is shown in **Figure 3.10**. Here, the preheating effect was carried out on the 0.6 mm core thickness because it was not possible to perform those experiments with the 0.3 mm one. It can be observed, that the maximum shear strength in the case of skipping the preheating was slightly lower than that one of the preheated ones: a proper preheating improves the adhesion between the polymer and the adhesive layer. Consequently, a mixed cohesive/adhesive failure mode occurred, instead of the pure cohesive mode while preheating. As a result, the shear displacement is reduced at delamination. Further results for different laminates showing the effect of the polymer preheating are listed in **Table 3.7**. Accordingly, it can be stated that preheating has a minor influence on the maximum shear strength value at which delamination initiates, but significant impact on the failure mode and shear displacement until complete failure.

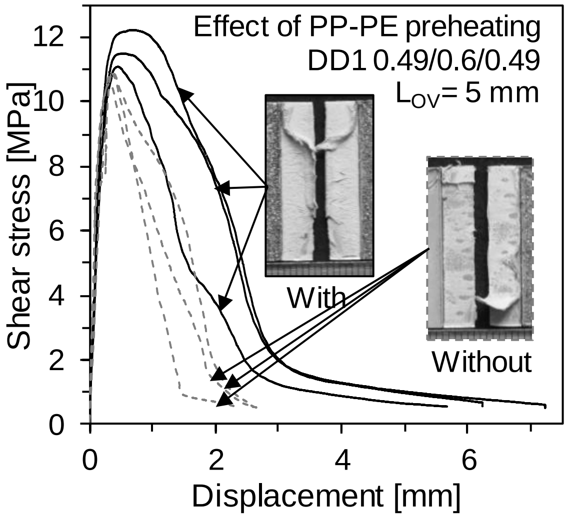

Figure 3.10: Effect of the polymer preheating on the shear stress–displacement progress for DD1 0.49/0.6/0.49 (three specimens each).

Table 3.7: Effect of preheating the PP-PE layer and aging on the lap shear strength.

SPS laminate	PP-PE preheating	Average lap shear strength [MPa]				
		Before aging	After aging			
			Natural aging (one year)	+50/-20°C 7 cycles	VW P 1200	
					One cycle	10 cycles
DD1 0.49/0.6/0.49	with	11.2±0.8	11.8±0.3	11.7±0.8	11.2±1.8	10.4±1.6
DD1 0.24/0.6/0.24		10.6±1.7	10.0±0.9	8.9±1.0	10.1±0.6	9.3±0.5
DD1 0.24/0.6/0.24	without	10.5±0.9	9.7±1.7	-	9.6±1.4	7.8±2.9
DD1 0.24/0.3/0.24		10.8±1.4	13.2±1.1	10.5±0.7	12.8±0.7*	12.1±1.1
DD1 0.49/0.6/0.49		10.8±0.2	-	11.4±1.2	-	-
DD1 0.49/0.3/0.49		9.2±0.8	-	10.0±2.8	-	-

*: skin sheet cracking, -: not tested

The effect of different aging regimes – see part 3.3.1 – on the lap shear strength are depicted for selected aging times for DD1 0.49/0.6/0.49 in **Figure 3.11**. The results for all the tested conditions are listed in **Table 3.7**. The results are statistically evaluated using the median and the average values of the individual results. The median value is primarily applied for skewed distributions where there is a significant deviation/scattering of the data set, like the present case. Median values in such cases deliver better indication than the arithmetic average [von05]. Firstly, the results showed no remarkable effect of the natural aging condition after one year on the adhesion strength where the failure surfaces are still cohesive ones like of the reference condition. Secondly, in the case of water aging for 28 cycles (~700 h) following the +50°C/-20°C regime, there was likewise no remarkable deterioration effect on the lap shear strength, but a slight improvement was observed, as shown in **Figure 3.11-a)**.

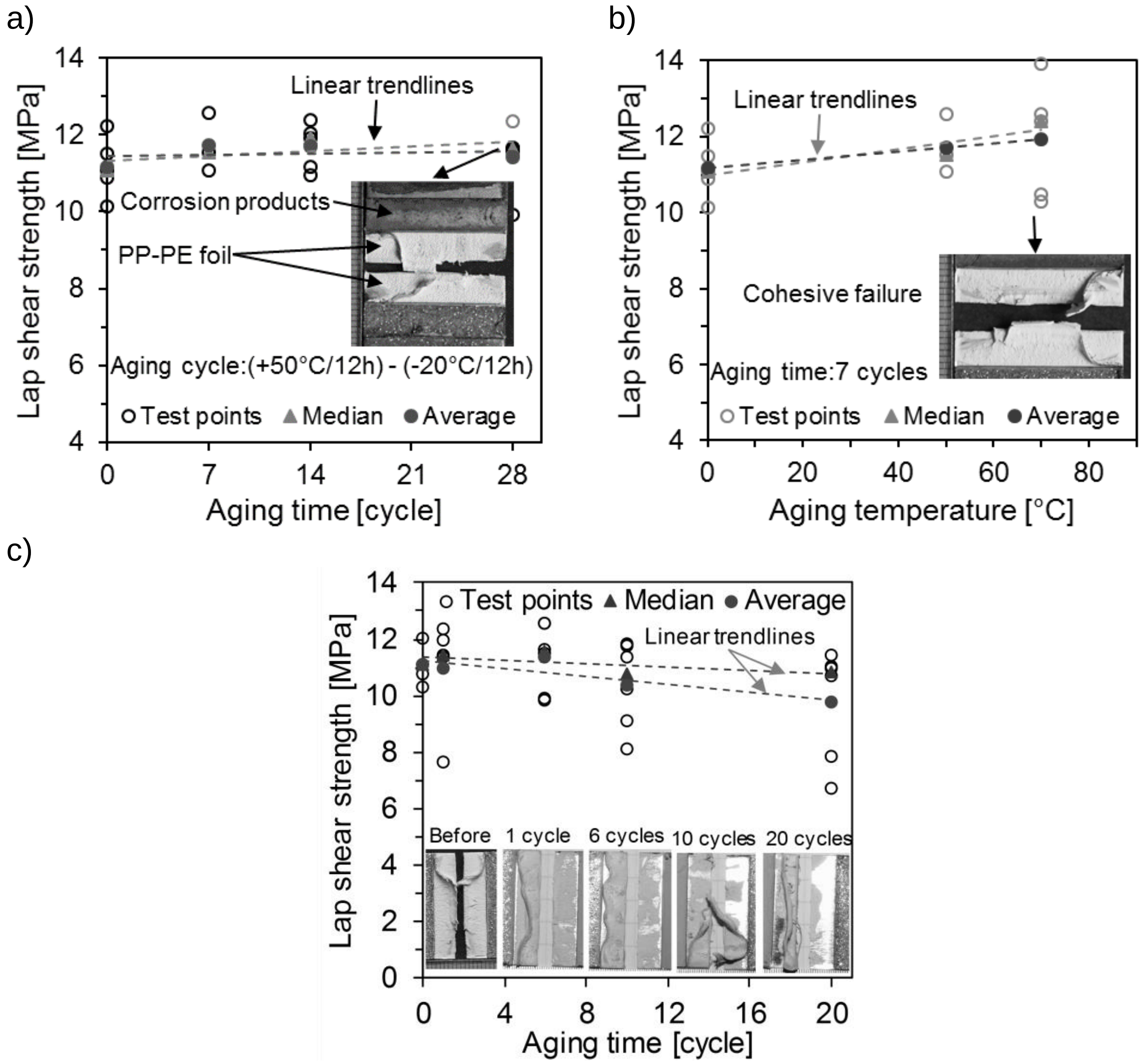

Figure 3.11: Effect of the different aging regimes on the adhesion strength of DD1 0.49/0.6/0.49: a) aging regime +50/-20°C at different aging periods, b) effect of gaining temperature for 7 cycles and c) aging according to VW P1200.

In principle, the aging conditions can attack one or more of the bond constituents, either the polymeric core or the metallic skin sheet or adhesive layer (here an epoxy resin), which can lead to the likely degradation of the metal/polymer shear strength. Firstly, due to the hydrophobic nature of the used polyolefin core, there is no chance for water absorption, therefore the mechanical properties i.e. the shear strength of the core were not influenced [Ash08, Den10]. Secondly, the applied conditions had no remarkable influence on the mechanical properties of the metallic sheets, however corrosion products, brown areas, were detected in the vicinity of the overlapped area, see **Figure 3.11-a)**. The effect of the aging medium on the epoxy resin is medium-dependent. In this case of water immersion, even considering the icing effect at -20°C, the water uptake of the epoxy resin could lead to its plasticization effect which lead to reduction of the T_g. This effect is ordinarily reversible once the water is removed. Moreover, when increasing the aging temperature from 50 to 70°C, as shown in

Figure 3.11-b), the average value of the lap shear strength was not negatively influenced.

The aging results following the VW P1200 standard until 20 cycles (240 h) are depicted in **Figure 3.11-c)**. In this case, the results based on the median evaluation are diverging from the ones based on the average ones, due to significant scattering. In both cases, median and average, the shear strength decreased gradually with the increasing of the aging time. In this regard, the failure type, as shown **Figure 3.11-c)**, changed from pure cohesive failure before aging to a mixed adhesive/cohesive one; the cohesive region decreased with increasing the aging period. Moreover, the steel/epoxy interface is attacked by the humid atmosphere leading to uncovering the steel surface, see 10 and 20 cycles. Exposure of the epoxy resin bonds to humid environments at elevated temperatures can produce irreversible effects, which can be attributed to the chemical degradation of the polymer/resin interface. This causes an increase of the internal voids of the entangling polymer chain, promoting as a consequence the chain expansion and the microcracks formation into the polymer matrix [Cos05].

The lap shear strength was likewise evaluated for the laminates, which combine dissimilar steel grades as skin sheets, as depicted in **Figure 3.12**. All of these laminates were produced following the standard preparation procedure, as described in part 0. It can be seen that the DD1 steels showed better adhesion qualities compared to the DP grade (galvanized) and the SS ones. These differences can be confirmed with the help of the lap shear strength values and additionally the failure surface. In the case of the SS and DP based sandwiches, failure took place at the polymer/epoxy interface, as shown clearly in **Figure 3.12**. These results were correlated to the roughness values as well as the contact angles to interpret these differences, as summarized in **Table 3.8**. The contact angles were measured with distilled water at RT with an optical lab contact angle measuring instrument OCA 15 plus (Dataphysics Instruments GmbH) at the Institute of Non-Metallic Materials, TU Clausthal. Additionally, the surface roughness was measured with a tactile roughness tester HOMMEL ETAMIC W10 (PCE Instruments) at the Institute of Metallurgy. The characteristic results, namely the R_a (the average surface roughness) and R_z (the maximum height of the roughness profile) values, were determined. Although the SS grade surface exhibited low contact angle, its high smoothness, very low roughness value, led to a weaker adhesion strength. Consequently, adhesive failure resulted at the polymer/epoxy interface, in addition to the epoxy/SS interface, as observed from the partially uncovered steel surface. In this regard, some successful attempts to improve the SS/PP-PE adhesion strength were performed by plasma- and corona-treatment [Sok12], where the lap shear and peel strength values were with 20% as a result of the significant improvement of the contact angle, as shown in **Table 3.8**.

Table 3.8: Roughness and contact angle values of the used steel sheets after acetone cleaning (five measurements each).

Steel grade	Thickness [mm]	Roughness		Contact angle [°]
		R_a [µm]	R_z [µm]	
DD1 (tinned)	0.49	0.2±0.05	1.4±0.5	83±3
	0.24	1.0±0.1	5.3±0.5	78±2
DD2 (tinned)	0.49	0.2±0.05	2.0±1.0	84±2
DP (galvanized)	0.52	1.2±0.1	7.7+0.3	103±2
SS	0.5	0.1±0.05	0.7±0.3	69±2
SS (PT) [Sok12]	0.5	-	-	29±1
SS (CT) [Sok12]	0.5	-	-	27±1
PT: Plasma treatment, CT: Corona treatment				

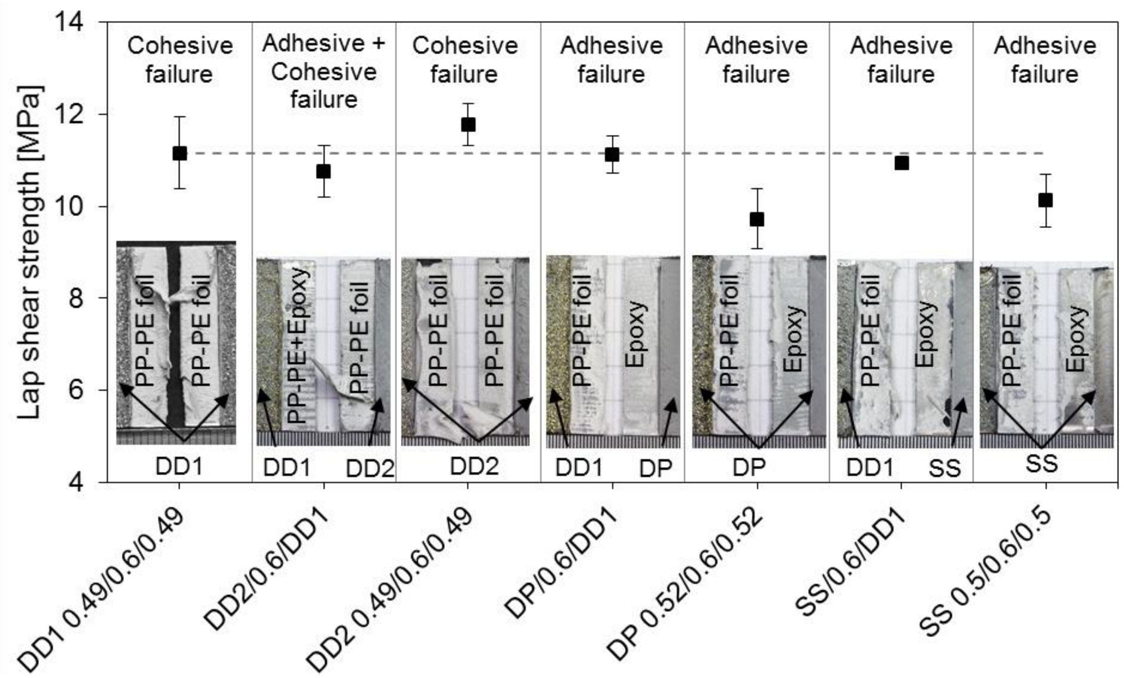

Figure 3.12: Lap shear strength and failure surface of the laminates combining dissimilar steel grades (at least three test specimens each).

Adhesive failure type was observed for the hot-dip galvanized DP grade SPS laminate, where it possesses higher roughness values, but simultaneously higher contact angles. The surface properties of the oiled hot-dip galvanized steel were improved by cleaning with sand soap, where the lap shear strength was increased from 9.5 MPa up to 12 MPa [Pal16]. With combining the SS and DP grades with the DD1 grade (tinned) in the asymmetric SPS laminates, such as SS/0.6/DD1 or DP/0.6/DD1, the lap shear strength values are the same like for the symmetric DD1 SPS laminates. Furthermore, the DD2 based SPS laminate showed the same adhesion strength and cohesive failure type like the DD1 grade, as both the DD1 and DD2 are Sn-coated and possess the same surface properties (contact angles and roughness). In summary, the adhesion strength and failure type of the symmetric and asymmetric laminates depend on the surface properties of the bond constitutes. However, due to using the same adhesive agent, the differences were only about 10%.

3.3.3. T-peel testing

The adhesion strength was determined using the T-peel test to quantify the tearing resistance of the bondline or rather the polymeric core. The peel strength determined with a given adhesive bond configuration may not necessarily be applied to others, i.e. it provides commonly qualitative characteristic values [Bro09]. That's because the peel resistance depends not only on the properties of the adhesive used but also on the specimen geometry, the rate of peeling, the surface conditions and the deformation behaviour of the adherends.

The peel test was performed at RT according to ASTM D1876 [AST00a] using a universal testing machine with 254 mm/min testing speed. The geometry of the test specimen is shown in **Figure 3.13-a)**. Minimum five test specimens were considered. The peeling displacement was set to be 250 mm for a specimen width of 25 mm. In this case, the average peel strength (in N/mm) is the characteristic value to express the peel resistance. This term can be determined from the mean peeling load, F_{avg}, per unit width (25 mm) as shown in **Figure 3.13-b)**. However, the peel initiation resistance refers to the maximum peel force per unit width. The peel quality can be expressed regarding the peel work in Joule, which is determined by the area under the curve, i.e. $W_{peel} = F_{avg} \times peel\ displacement$, as illustrated in **Figure 3.13-b).** To assess the reproducibility of the results, the peel-progress of two types of laminates is shown in **Figure 3.13-c)**.

The thickness of the SPS laminates layers showed a significant role on the peel resistance, as shown in **Figure 3.13-c)** and **Table 3.9**; the thicker SPS constituents showed higher peel resistance due to the higher stiffness of the thicker layers. Moreover, the DD1 0.49/0.6/0.49 showed an excellent average peel resistance (~10 N/mm), which is much better than the required specifications of the automotive industry, which is between 1 and 5 N/mm depending on the use of the component [Gau06]. In this regard, the peel resistance of the current SPS laminates are comparable or even better than some commercial products (see **Figure 3.13-d)**) like Bondal®, Litecor® that can reach 7-10 N/mm according to patent (EP 1651432 B1), Hylite®/Corus (Al/PP/Al) and Usilight®/Arcelor (DC04/PP/DC04) that can reach 5 N/mm [Nut08] for non-standard specimens at 100 mm/min peeling rate. The effect of the peeling rate was also studied. It is clearly observable from **Table 3.9** that the higher the testing rate, the higher is the peel resistance, matching the strain rate sensitivity results in [Sgu15].

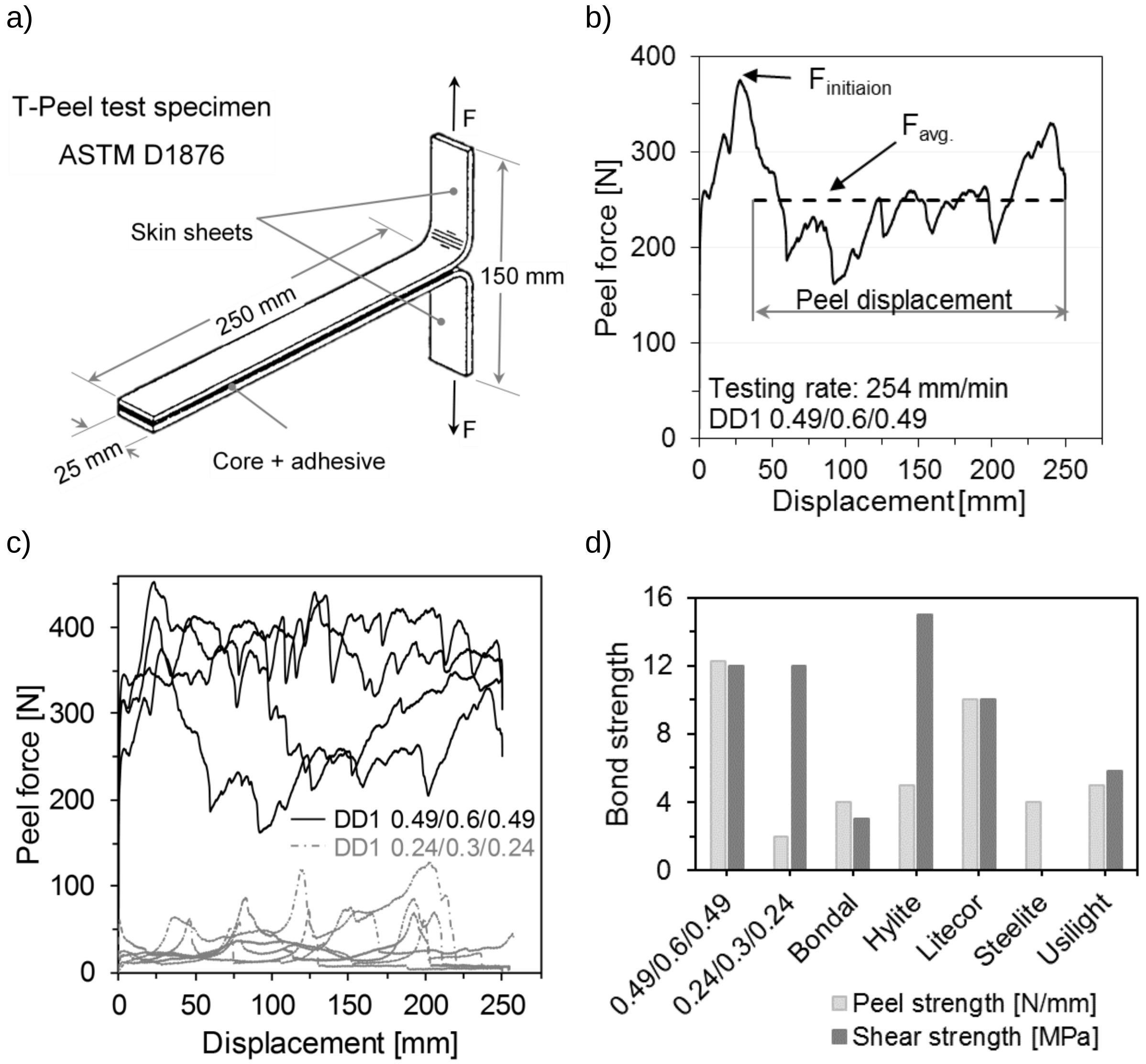

Figure 3.13: a) T-peel test specimen according to ASTM D 1876, b) peel force–displacement progress of DD1 049/0.6/0.49 and its comparison with DD 0.24/0.3/0.24 for some test specimens to show the reproducibility c). d) Comparison of some commercial laminates to the current ones (the corresponding units can be found in the legend).

Table 3.9: T-peel results before and after aging for seven cycles following the +50°C/-20°C regime.

SPS laminate	Testing rate [mm/min]	Peel strength [N/mm]				Peel work [Joule]	
		Before aging		After aging		Before aging	After aging
		Max.	Average	Max.	Average		
DD1 0.49/0.6/0.49	254	16±1	12±3.0	15±1	11±2.1	73±14	66±13
	25.4	9±1	8±0.5	10±1	8±0.9	56±10	54±7
DD1 0.24/0.3/0.24	254	3±1	1.5±0.5	4±1	1.5±1	7±1	7±2

The service life durability of the peel specimens was even evaluated after aging in water following the regime (+70/-20°C for seven cycles); the peel resistance was not negatively affected (**Table 3.9**). It can be observed that the DD1 0.49/0.6/0.49 showed a repeatedly cohesive fracture surface before and after aging, as shown in **Figure 3.14-a)**. On the contrary, the fracture surface of the thinner SPS DD1 0.24/0.3/0.24 (**Figure 3.14-b)**) is mostly adhesive at the interface between the epoxy resin and the core. The reason for that is the combined effect of the low thickness and the absence of preheating the 0.3 mm core. This confirms the obtained results showing the effect of polymer core preheating in part 3.3.2.

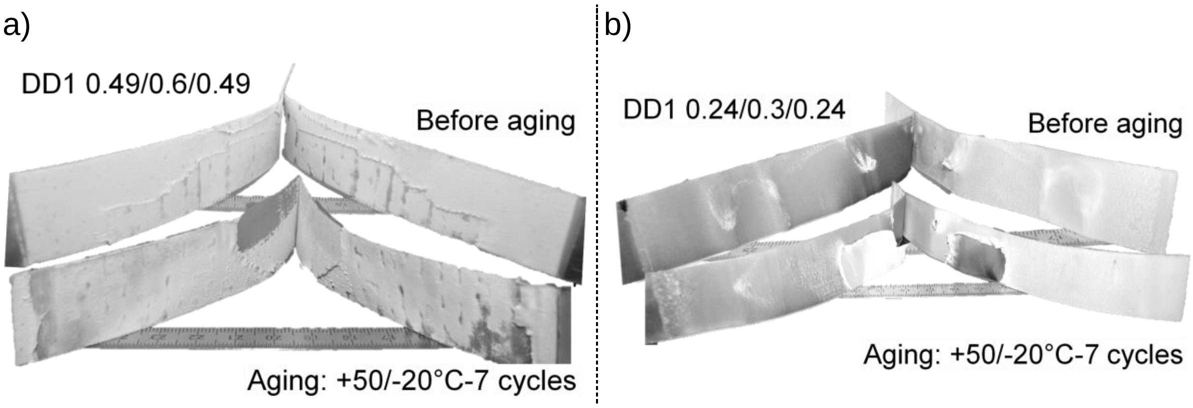

Figure 3.14: Fracture surface after peeling before and after aging (+50/-20°C regime for seven cycles) for: a) DD1 0.49/0.6/0.49 and b) DD1 0.24/0.3/0.24.

3.4. Determination of the mechanical properties

In this part, the mechanical properties, especially the ones related to the forming behaviour of the different metallic sheets and their MPM-laminates, are evaluated. It is aimed to determine:

1. The global tensile properties like the yield strength, ultimate tensile strength, elastic modulus, strength coefficient, strain hardening exponent, anisotropy, uniform strain and strain at failure.
2. The local properties, such as the major and minor strains following the strain path in addition to the thinning rate in the failure position.

In order to interpret the effect of tailoring different sandwich configurations, the mechanical properties were intensively investigated considering the scaling approach (see **Figure 3.3**) for the MPM-laminates listed in **Table 3.5**. In addition to that, a fundamental evaluation of the anisotropy behaviour of the steel sheets was carried out, due to its expected influence on the forming potential and the failure causes. The effect of the core thickness on the mechanical properties was characterized. Moreover, the effect of combining dissimilar steel grades in asymmetric MPM-laminates on their mechanical properties was investigated aiming to define rules for calculating their behaviour under these changing conditions.

3.4.1. Tensile test procedure

The mechanical properties were determined via tensile testing according to DIN 50114 [DIN80] on test specimens as shown in **Figure 3.15-a)**, with a constant strain rate of 0.005 s^{-1}. The tensile test specimen was monitored from one side with the DIC system “GOM-Aramis”, as shown from the illustrative test setup in **Figure 3.15-b)**.

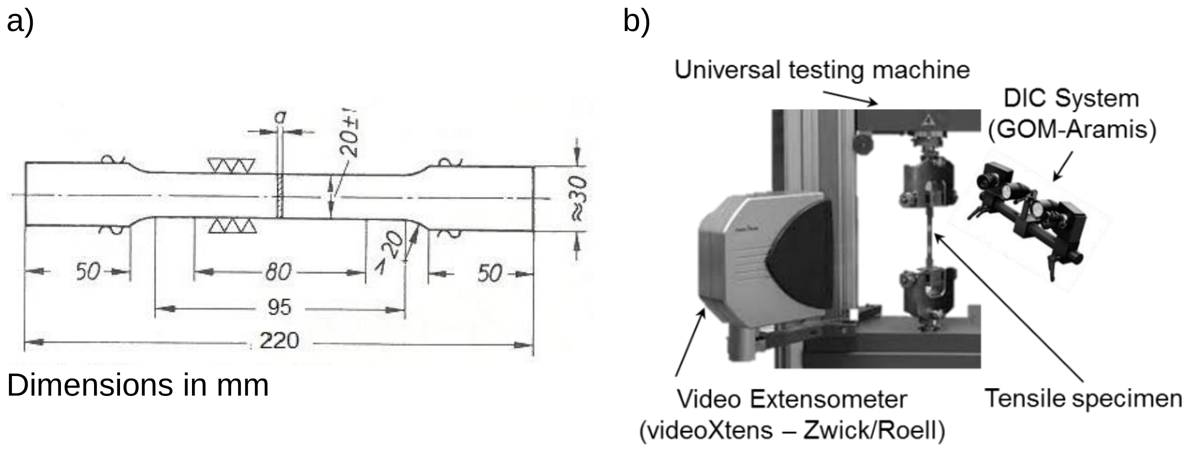

Figure 3.15: a) Tensile test specimen according to DIN 50114 and b) the test setup by monitoring the specimen with two optical strain measuring systems: Video extensometer and DIC unit.

The DIC system was used basically due to its accurate measurement, where a higher number of facets can be evaluated on the same surface area of the specimen, in addition to the possibility to determine the instantaneous strain distribution. The mechanical properties in terms of the stress–strain curves can be synchronized with the strain mapping in the different test stages through transferring the force–elongation signals from the universal testing machine to the DIC unit through AD channels then applying the script “tt_eval_v630_reve.scriptar” [GOM14]. On the other side of the specimen, global extension of the gauge length was measured by the non-contact video extensometer (Zwick), the so-called “videoXtens extensometer” [Zwi15].

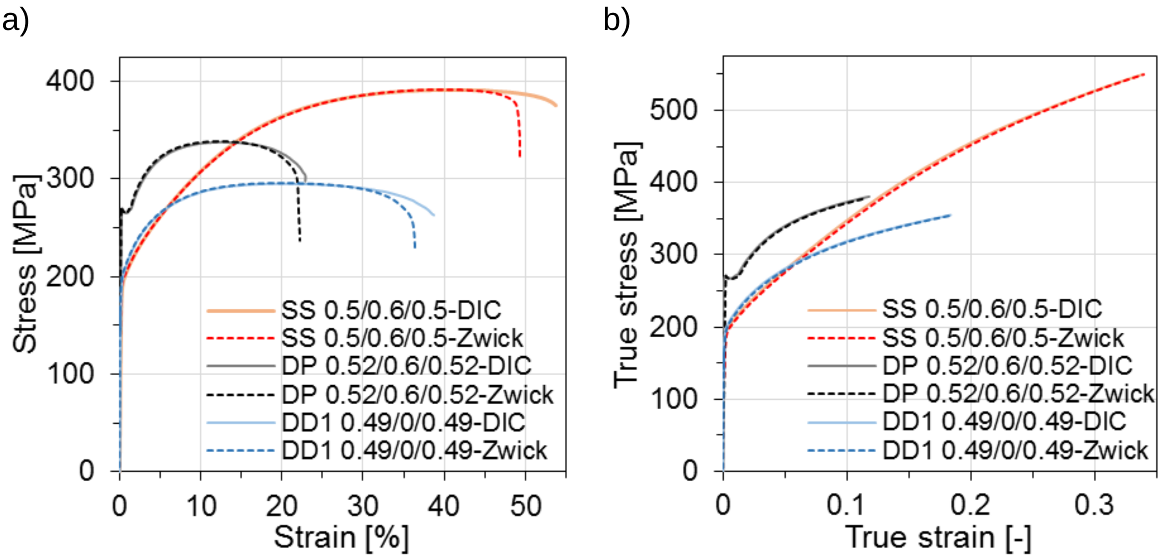

Figure 3.16: Comparison of a) the engineering and b) true stress-strain curves of some specimens obtained by the DIC and Zwick systems.

It is noteworthy in this context that the measuring range of the DIC system, the gauge length is 68 mm; which is less than the standard one considered in Zwick, i.e. 80 mm. Therefore, the elongation at failure (e_f %) measured by DIC is slightly higher than the ones measured by Zwick with about 2-5 %. This can be observed from the engineering stress–strain curves in **Figure 3.16-a)**, where the curves of the two methods are coincident until shortly before failure. Furthermore, the true curves, which are essential for interpreting the forming potential, are identical, see **Figure 3.16-b)**. Based on this, the global mechanical properties (E, YS, UTS, e_u, e_f and n values) were determined according to DIN ISO 10275 [DIN14b] using the Zwick video extensometer to keep the results comparable with the standard conditions. However, the r value was calculated with the DIC system as the DIC system can measure the strain in width more accurately in respect to the video extensometer.

For the local strain evaluation, the forming limit strains (major (ε_1) and minor (ε_2) strains) of the different laminates under uniaxial tensile loading were determined. An illustrative example showing the progress of the surface strains in correlation with the stress-strain curve is shown in **Figure 3.17-a)**. For this purpose, the strain paths from the beginning of the tensile test over the specimen surface in failure position were determined by the DIC system. These paths include ε_1, ε_2, thickness reduction ε_t (calculated assuming volume consistency: $\varepsilon_t = -\varepsilon_3 = (\varepsilon_1 + \varepsilon_2)$) and the thinning rate $(d\varepsilon_t/d\ time)$, as shown in **Figure 3.17-b)**.

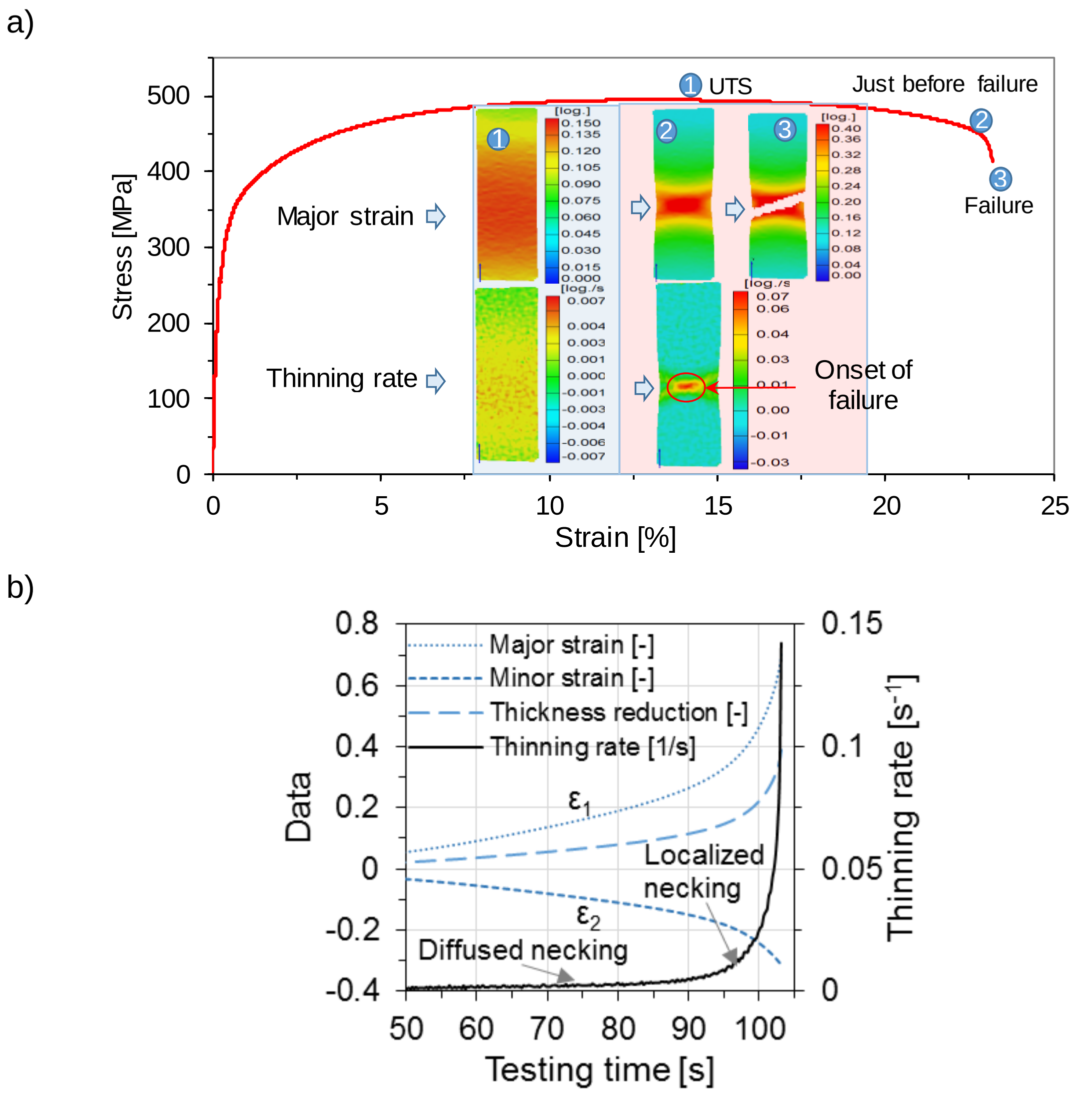

Figure 3.17: a) The progress of the thinning rate and major strain distribution photographs in the tensile specimen along the stress-strain curve and b) strain and thinning rate paths in respect to the testing time in the area of localized necking until failure.

The failure position can be recognized from the thinning rate mapping in the stage just before failure, as shown in **Figure 3.17-a)**. In this position, the strain paths in respect to the testing time or the tensile elongation ΔL can be presented as shown in **Figure 3.17-b)**. It is observed that the strain distribution is uniform up to UTS which is called the diffused necking, however localized necking takes place in the stages close to failure, which can be recognized from graphs and curves by the thinning rate and major strain. The limiting strains were set in the stage just before failure. So, the strain paths of ε1, ε2 and the thinning rate will be compared for the examined MPM-laminates and the metallic materials. The importance of this thinning rate is to identify the onset of the localized necking to show the instability and failure conditions. For instance, the limiting strains (ε1, ε2) of some laminates – especially the one based on the same skin sheet and varied core thicknesses – are identical, so in this case with the help of the thinning rate curves, a differentiation method between them can be possible. This method is the concept of the time-dependent method for determining the forming limit curve, which will be intensively illustrated later in part 3.5.

3.4.2. Anisotropy evaluation

To predict and interpret the forming behaviour of the MPM-laminates, such as earing under deep drawing or springback under bending conditions, it is necessary to know the mechanical anisotropy of the monolithic steel sheets. The anisotropy investigations were carried out on some metallic sheets to follow their influence on the forming potential when combined to laminates, namely the steel grade DD1 with its two thicknesses (0.24 and 0.49 mm) and SS one at 0, 45 and 90° directions to RD (rolling direction). The true stress–stain curves of the DD1 grade under these conditions shown in **Figure 3.18-a)**. It can be observed that the strength level of the 0.49 mm sheet curves is slightly higher than that of the thinner sheet. The mechanical properties of both thicknesses are listed in **Table 3.10**.

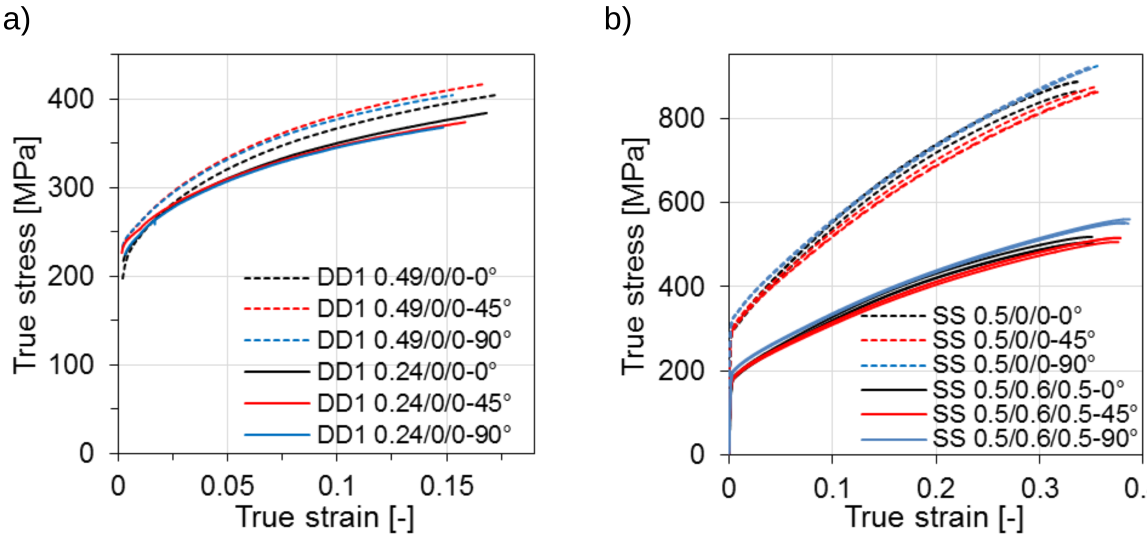

Figure 3.18: Mechanical anisotropy evaluation of the a) DD1 and b) SS one in terms of the true stress-strain diagrams at the different angles to the rolling direction.

Primarily, the chemical segregation and/or thermomechanical working lead to orientation-dependent crystallographic texture and grain structure. For the 0.49 mm sheet, it was found that the 45° direction showed higher YS and UTS values but lower n and r values compared to the 0° and 90° ones. However, the 0° and 90° directions are quite similar and provide better forming-related values. For the 0.24 mm grade, there was a lower difference between the different directions, i.e. mostly isotropic. This may be attributed to the reduced carbon content (see **Table 3.2**), which helps make the steel more isotropic and uniform structure [Joo13]. Although the r or rather the R values of the DD1 0.49 mm grade is higher than that of the 0.24 mm one, the Δr value of the 0.24 mm grade is less and very small. Therefore, earing in the DD1 0.24 mm grade during deep drawing is unlikely. However, the higher positive Δr value of the DD1 0.49 mm means that earing in 0° and 90° is probable. In conclusion, the DD1 grade with 0.24 mm provided a more isotropic behaviour compared to the 0.49 mm one. As expected, the mechanical anisotropic behaviour of the skin sheet is dominant even after creating the MPM-laminates, as can be shown for the SS 0.5 mm grade and the SS 0.5/0.6/0.5, see **Figure 3.18-b)** [Har14b].

Table 3.10: Mechanical anisotropy results of the DD1 steel grade (four specimens each).

Steel DD1	θ [°]	E [GPa]	YS [MPa]	UTS [MPa]	K [MPa]	e_u [%]	e_f [%]	n [-]	r [-]	R [-]	Δr [-]
0.49 mm	0	191±4	219±10	345±3	536±6	19±1	30±1	0.18	1.75	1.74	0.19
	45	203±8	240±5	359±5	582±6	18±1	27±0	0.18	1.50		
	90	205±12	227±11	343±4	549±2	17±1	28±1	0.18	2.03		
0.24 mm	0	197±3	225±5	327±5	527±3	18±1	28±1	0.17	1.55	1.67	0.04
	45	195±7	236±3	322±5	511±5	17±1	28±1	0.16	1.63		
	90	195±9	226±3	317±4	500±5	17±1	30±3	0.16	1.87		

3.4.3. Effect of the core thickness

In this part, the effect of the core thickness on the mechanical properties is determined for the MPM-laminates of the DD1 grade (0.49 and 0.24 mm) with varying core thicknesses of 0.3, 0.6, 1.0 and 2.0 mm. In addition to that, the combination DD1 0.49/0/0.49, as a sheet metal laminate, was investigated, where the two steel sheets of the same thickness (0.49 mm) were glued together with ~ 0.1 mm EPX^{TM} adhesive DP490.

The relation between the mechanical properties and the core thickness is represented by true stress-strain curves in **Figure 3.19-a)** and summarized in **Table 3.11**. With increasing core thickness, the mechanical properties decrease following ROM. Moreover, the forming related parameters decrease, i.e. the n, e_u and r values. The strengthening parameters in terms of the n value decreased with increasing the f_c due to the negative contribution of the soft core on the strengthening behaviour. Also, the r values ($\varepsilon_t/\varepsilon_w$) of the MPM-laminates were lower compared to the ones of the monolithic steels (see **Table 3.11**) due to the higher thickness strain (ε_t) as a result of the additional thinning contribution of the soft polymeric core compared to the width straining (ε_w).

The measured results were verified with the estimated ones according to ROM based on the mechanical properties of the monomaterials, as shown in **Figure 3.19-b)**. Beside the flow curves of the monomaterials (DD1 and PP-PE), three laminates are shown:

1. The sheet metal laminate: DD1 0.49/0/0.49.
2. Normal, joined, MPM-laminate containing 0.6 mm core: DD1 0.49/0.6/0.49.
3. Unjoined MPM-laminate: DD1 0.49/0.6/0.49-unjoined.

The estimated curves according to the ROM show an excellent agreement with the measured ones [Har14a]. Moreover, no remarkable changes in the strain at failure (e_f), between the monolithic steel sheets and the MPM-laminates, were found, which can be attributed to the strong dominance of the skin steel sheets: they convey the load and fail first. However, the polymeric core showed further straining after failure of the skins at a low level of stress. The results stated no delamination during tensile testing. Further examples on the applicability of ROM at different skin/core thicknesses are shown in **Figure 3.19-c)** focusing on the YS and UTS. In summary, it can be stated that the ROM is applicable for these laminates and other skin/core thickness combinations as well.

Table 3.11: Mechanical properties based on the core thickness in rolling direction (four specimens each).

Steel DD1	Core [mm]	f_c [-]	E [GPa]	YS [MPa]	UTS [MPa]	K [MPa]	e_u [%]	e_f [%]	n [-]	r [-]	ε_2 [-]	ε_1 [-]
0.49 mm	-	-	191±4	219±10	345±3	536±6	19	30	0.18	1.75	-0.37	0.77
	0.1	0.1	173±5	196±3	297±2	485±3	19	32	0.18	1.74	-0.37	0.79
	0.3	0.23	148±4	171±2	262±3	418±3	17	30	0.17	1.71	-0.37	0.83
	0.6	0.38	118±3	142±7	215±1	337±1	16	29	0.16	1.72	-0.37	0.86
	1.0	0.51	87±3	112±2	168±3	262±3	16	28	0.15	1.67	-0.37	0.83
	2.0	0.67	55±5	88±4	128±1	194±1	14	28	0.14	1.62	-0.37	0.83
0.24 mm	-	-	197±3	225±5	327±5	527±3	18	28	0.17	1.55	-0.29	0.59
	0.3	0.38	128±2	137±2	209±1	327±3	16	28	0.15	1.50	-0.31	0.72

Further investigations on the strain evolution on the surface of the MPM-laminates in the failure position were carried out to correlate the deterioration effect of the mechanical properties, especially the forming-related ones, to the failure strains (ε_1–ε_2). **Figure 3.19-d)** shows the progress of ε_1–ε_2 strain path from the tensile test start until just before failure for the different core thickness SPS laminates. The thin DD1 grade 0.24 mm and its laminates show lower forming limits compared to the thicker ones. Moreover, the different paths of the laminates based on the DD1 (0.49 mm) show minor differences with increasing core thickness, because the forming limits of the laminates are nearly the same as for the single skin sheets facing the DIC system. Moreover, the thinning rates in dependence on the tensile extension, as shown **Figure**

3.19-d), are very close as they are based on the same steel grade with almost the same e$_u$ (see **Table 3.11**). It can be concluded that although most of the mechanical properties decrease with increasing the core thickness under uniaxial tensile loading, the failure strains show no remarkable differences and depend only on the forming properties of the skin sheet. -

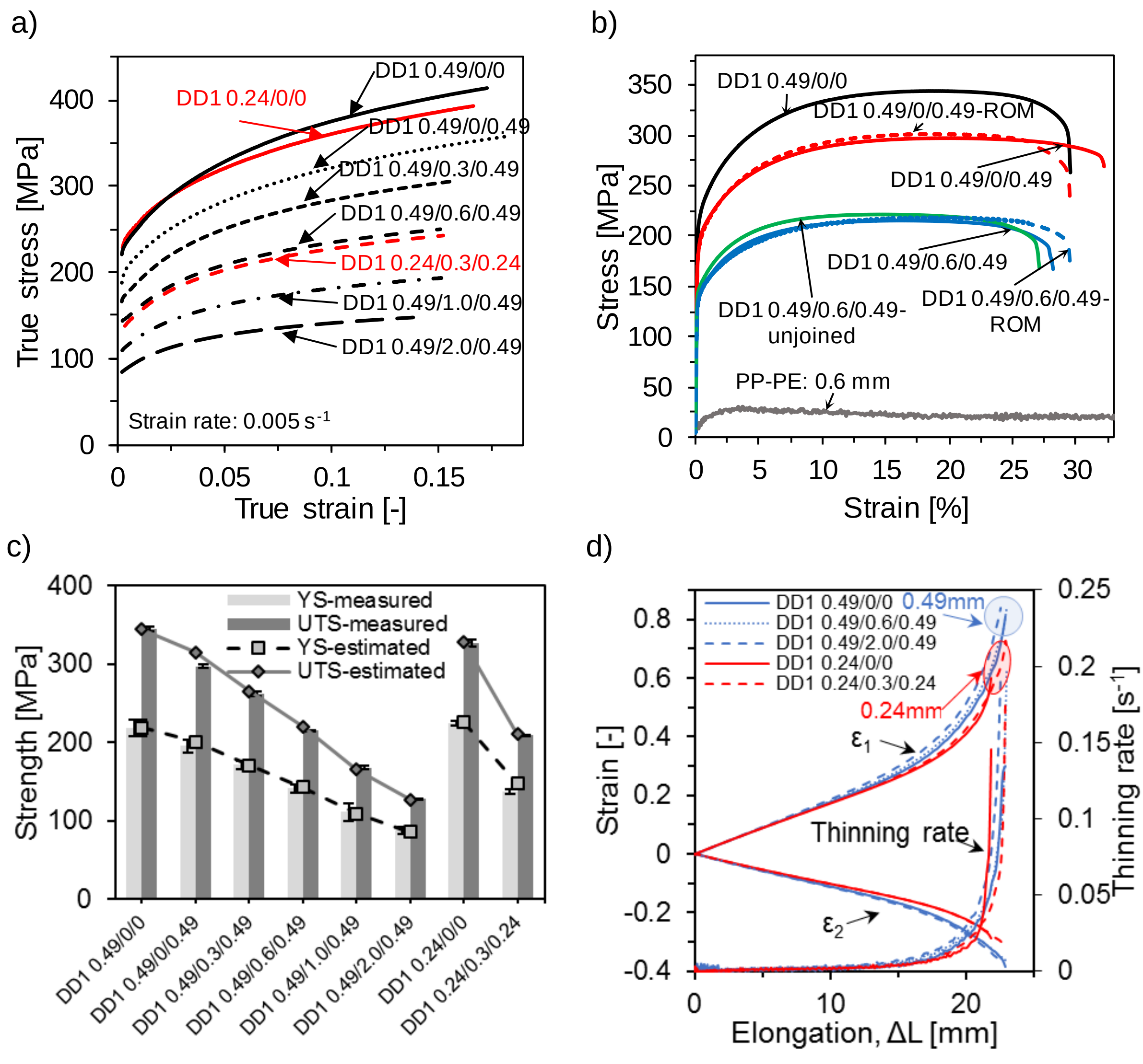

Figure 3.19: a) True stress–strain diagram at various skin/core thicknesses, b) verification of the ROM for three MPM-laminate configurations, c) comparison of the measured YS and UTS with the estimated ones according to ROM, d) ε_1–ε_2 strain paths and thinning rate progress for symmetric laminates based on the DD1 grade at constant strain rate of 0.005 s^{-1}.

The obtained mechanical properties of the different thickness laminates were sorted according to the lightweight material index (E/ρ) – which is to be maximized under tensile loading [Ash05] – with respect to the specific strength (UTS/ρ), as shown in **Figure 3.20-a)**. It can be observed that up to 0.5 volume fraction of the steels, i.e. DD1 0.49/1.0/0.49, the MPM-laminate can reach comparable specific properties to the monolithic metal. However, when applying another material index namely the $E^{1/3}/\rho$ (see **Figure 3.20-b)**), where its maximizing is favourable for the bending conditions. In this case, increasing the core thickness leads to a significant improvement of this index due to the increased bending stiffness that depends mainly on the sheet thickness following: $(EI = E\,(b \times t^3/12)$ at the same area weight, i.e. $\rho \times t$ (in kg/m^2). However, increasing the core thickness will show, as expected, other forming limits during shaping. Therefore, a balance between maximizing the material indices and the forming limits should be realized.

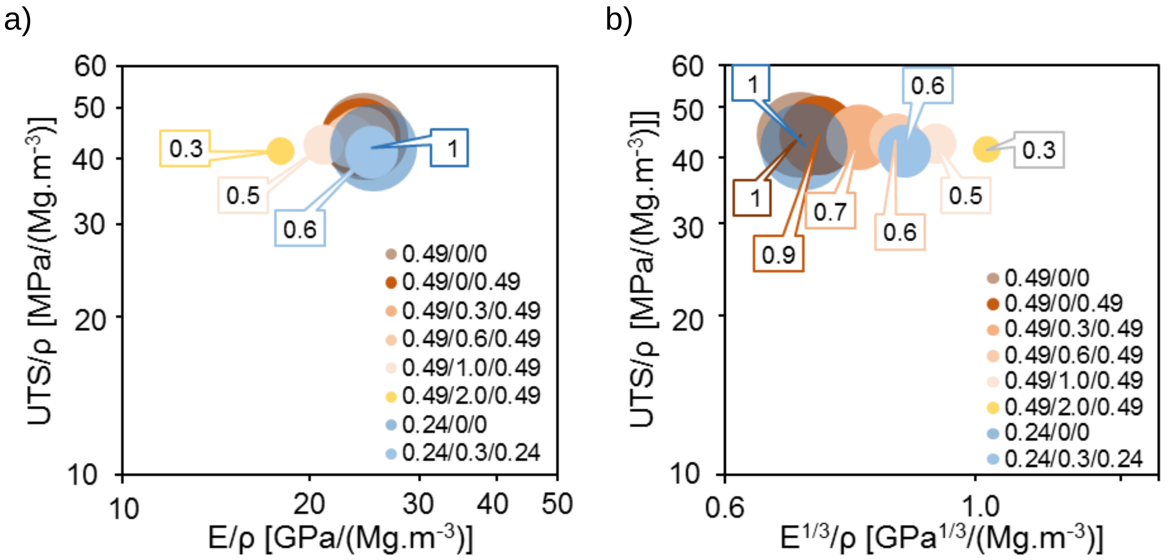

Figure 3.20: Applying the a) E/ρ and b) $E^{1/3}/\rho$ material indices of different skin/core thickness ratios in respect to the specific strength (UTS/ρ). The values in the legend boxes and the balloon diameters represent the volume fraction of the steel ($1–f_c$). The data are plotted in log–log scale.

3.4.4. Effect of the laminate configuration

In this part, the effect of the MPM-laminate configurations on the mechanical properties is presented considering the influence of:

1. The number of layers and adhesion at a constant polymer content (f_c) using the same steel grade.
2. Combining different skin thickness in the same laminate.
3. Using dissimilar steel grades in the same laminate with a constant f_c.

The different steel thicknesses/grades are subjected alternatively to the Zwick/DIC measuring systems, as illustrated in **Figure 3.15**. For instance, for the asymmetric laminate DD1 0.49/0.6/0.24(Zwick), the 0.24 mm side is monitored with the Zwick system and simultaneously the other side (0.49 mm) with the DIC one. **Figure 3.21** shows a comparison of different laminate configurations based on the DD1 steel grade and their corresponding results are listed in **Table 3.12**. Firstly, the effect of adhesion can be shown by comparing the normal DD1 0.49/0.6/0.49 with the unjoined one:

“unjoined” means the three SPS layers are cut to the tensile specimen sizes and tested together without adhesion. It can be observed, that the global and local mechanical properties of the unjoined and normal laminates are very close, however the n and r values of the unjoined SPS laminates were slightly higher than the joined ones. The r value of the unjoined one is much closer to the one of the monolithic steel sheet but the n value is smaller. This result could be attributed to the softening effect of the polymer core.

Table 3.12: Results summary of the effect of the various SPS configurations based on the DD1 steel grade (four specimens each).

Steel DD1	E [GPa]	YS [MPa]	UTS [MPa]	K [MPa]	e_u [%]	e_f [%]	n [-]	r [-]	ε_2 [-]	ε_1 [-]
0.49/0.6/0.49	118±3	142±7	215±1	337	16	29	0.16	1.72	-0.37	0.86
0.49/0.6/0.49-unjoined	126±7	144±1	221±1	358	19	36	0.17	1.77	-0.37	0.83
0.49/0.6/0.24(DIC)	121±4	130±4	196±2	307	18	36	0.16	1.46	-0.31	0.69
0.49(DIC)/0.6/0.24	123±2	128±3	193±2	311	18	36	0.16	1.73	-0.36	0.79
0.49/0.3/0.24/0.3/0.24(DIC)	121±1	144±1	212±1	334	17	34	0.16	1.42	-0.31	0.71
0.49(DIC)/0.3/0.24/0.3/0.24	126±3	145±1	212±2	333	17	35	0.16	1.81	-0.35	0.76
0.24/0.3/0.24	128±2	137±2	209±1	327	16	28	0.15	1.50	-0.31	0.72

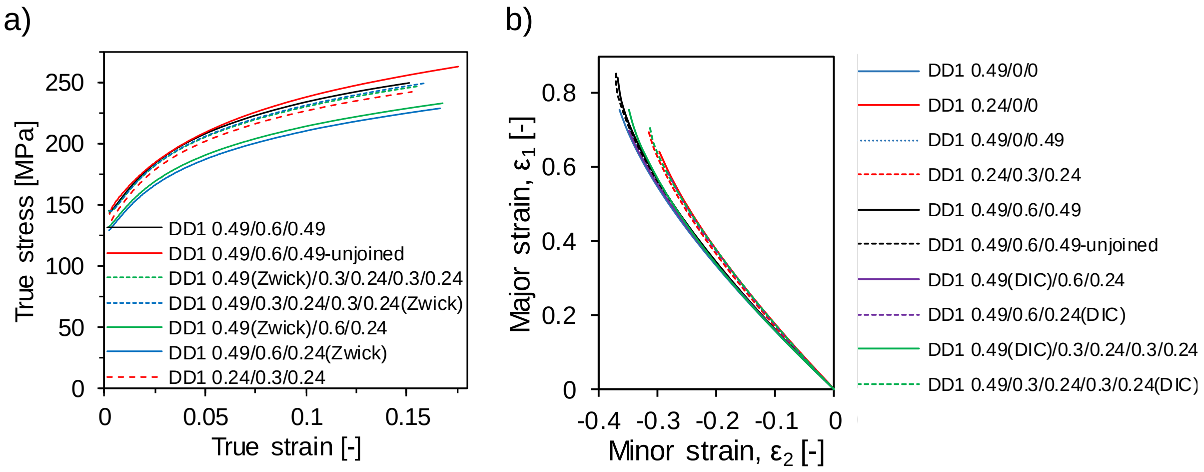

Figure 3.21: a) True stress–strain curves and b) ε_1–ε_2 strain paths for different asymmetric laminate configurations based on the DD1 grade with its two thicknesses 0.24 and 0.49 mm.

3.4.4.1. Asymmetric laminates with varied thicknesses and number of layers

The effect of combining different steel thicknesses can be presented with the combination: DD1 0.49(Zwick)/0.6/0.24 and DD1 0.49/0.6/0.24(Zwick). The advantage of using thick/thin skin sheet combination is, besides using different metal/surface properties, providing a good forming potential – in the case of designing the thick layer in the region of higher tensile strains – together with an enhanced weight saving contribution with a polymer content (f_c = 0.45), which means that the mechanical properties are lower compared to the other SPS laminates with $f_c = 0.38$. Most of the mechanical properties of both asymmetric combinations are identical. However, the r value is different, as it is inherent with the metal sheet: the r value of the 0.49 mm side facing the DIC camera is 1.77, but 1.46 for the 0.24 mm side. These r values are approximately the same of their monolithic steels.

The five-layered laminate is tailored to reinforce the core against mechanical joining, such as bolting or riveting, in addition to improving their fatigue and bending properties. However, production of such multilayer SPS is more difficult: it requires on lab scale four steps instead of two ones in the case of the three-layered laminates. The flow curves of two asymmetric five-layered laminates are shown in **Figure 3.21-a)**. A similar behaviour is found as for the three-layered one, where the 0.24 mm side exhibited a lower r value. It was found that the three-layered laminate (DD1 0.49/0.6/0.49) exhibited the same strength values of the five-layered one (0.49/0.3/0.24/0.3/0.24) at the same f_c value of 0.38. Yet, the limiting ε_1–ε_2 strain values depend on the skin sheet facing the DIC system as explained earlier.

It can be stated from the strain paths of different asymmetric laminates – based on the DD1 grade, as shown in **Figure 3.21-b)** – that the limiting strains under tensile loading conditions depend primarily on the ε_1–ε_2 values of the single skin sheets, regardless the laminate structure (symmetric, five- or three-layered asymmetric laminates), core thickness and interlaminar adhesive strength (the joined vs. the normal laminate).

3.4.4.2. Symmetric laminates with different metallic skin sheets

To show the differences between the used metallic sheets and their sandwich laminates, **Figure 3.22-a)** shows the corresponding engineering stress-strain curves for the laminates based on the various steel grades at $f_c = 0.38$, i.e. SS, DD1, DD2 and DP. Based on **Figure 3.22**, the forming-related values, such as r, n and K values were determined in different strain ranges between YS and UTS. This range for DD1, DD2, DP and SS are 5–10%, 4–6%, 5–15% and 5–20%, respectively. However, **Figure 3.22-b)** depicts other metallic skin sheets, i.e. Al and Ti. In principle, the sandwich laminates exhibit the same flow behaviour of their skins but, of course, with lower strength values following the ROM.

The stainless steel (SS) and the titanium (Ti) sheets show the highest e_f values. These materials were considered in this study due to their significant contribution for biomedical applications. The goal of tailoring sandwich materials based on them is to design the mechanical properties by varying the volume fraction of the polymer and the sandwich structure to come closer to the ones of the human bone [Har14c]. Grade DD1, with its two thicknesses, shows moderate strength and strain values with outstanding forming-related properties. However, DD2 grade shows higher strength with a limited strain capacity. Therefore, it was thought if a SPS to combine both, DD1 and DD2, gaining both advantages; this approach is discussed in detail in the next part (3.4.4.3).

The as-received (AR) Al sheets and their laminates showed a strongly limited e_f, therefore they were annealed at 400°C/1 h. A significant improvement of e_f from 6% to 25% but with a sharp drop of the strength from 190 to 120 MPa. Additionally, the production regime (260°/3 min) showed a further improvement of the e_f with about 5%, as can be observed by comparing the e_f of the Al sheets with that of their laminates (Al 0.3/0.6/0.3), both in the as-received and annealed conditions.

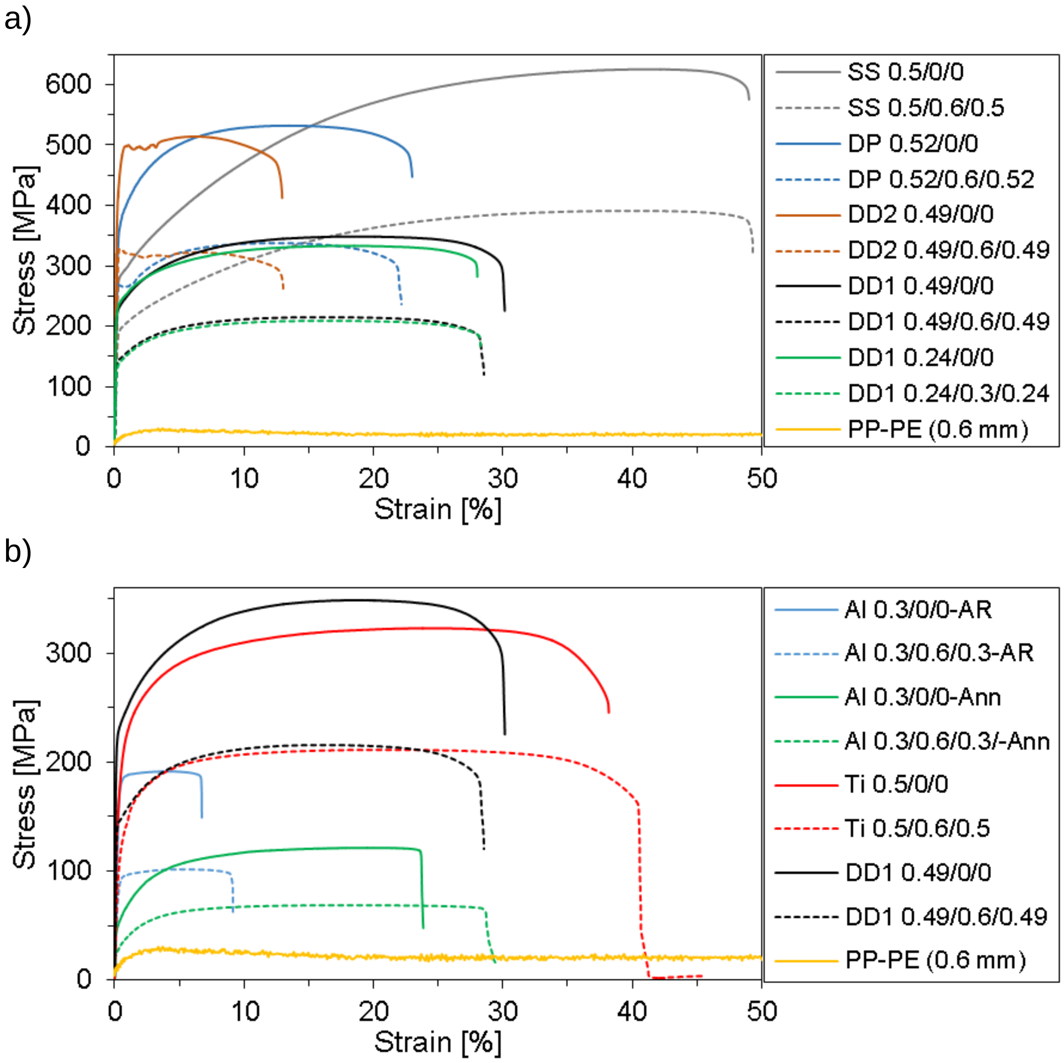

Figure 3.22: Stress–strain curves of the laminates based on: a) the steel and b) the other metallic skin sheets. AR: as-received, Ann: after annealing at 400°C/1h.

3.4.4.3. Asymmetric laminates with dissimilar skin sheet grades

The effect of combining dissimilar steel grades to form asymmetric SPS laminates was performed by combining the three steel grades SS, DP and DD2 with the DD1 one. Their mechanical properties and true stress–strain diagrams are given in **Figure 3.23** and listed in **Table 3.13**. It is clear that the stress–strain flow curves of the asymmetric laminates are located between the one of the symmetric laminates of each steel grade, see **Figure 3.23-a)**, **-d)** and **-g)**.

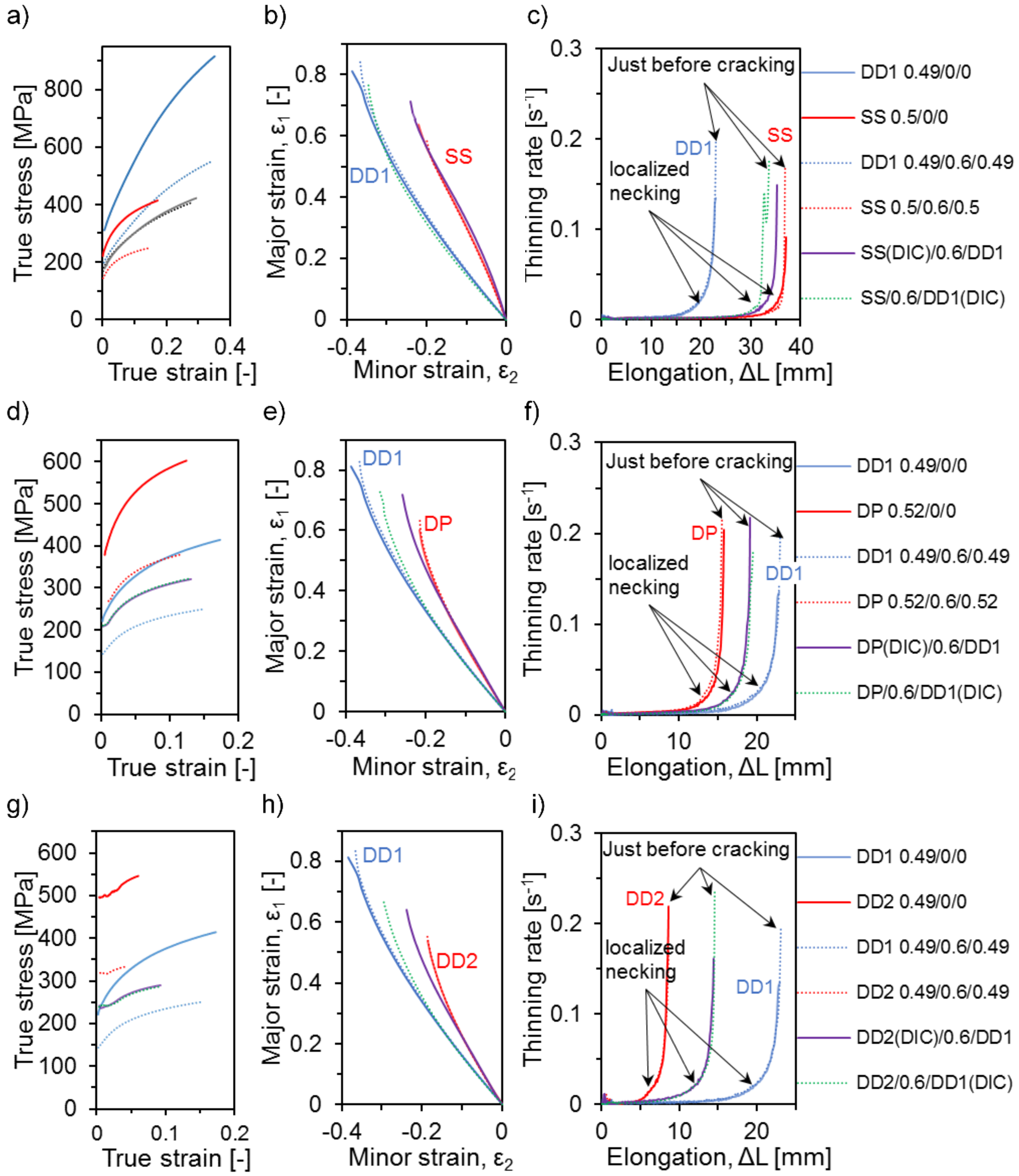

Figure 3.23: True stress–strain curves, ε_1–ε_2 paths and the thinning rate–elongation progresses for the asymmetric SPS laminates at $f_c = 0.38$ composed of dissimilar steel grades in the same laminate: one side is constantly the DD1 and other side is the a)–c) SS, d)–f) DP and g)–i) DD2 grades.

As can be observed, the mechanical properties can be approximated for such asymmetric SPS laminates by applying the ROM for the strength-related properties like YS, UTS, K and E as shown, e.g. for YS, in Eq. **(3.1)**. Good matching was reached when comparing the measured and the approximated results for all the asymmetric variants, see **Figure 3.24**. Accordingly, the strength of all the asymmetric laminates are higher than that of the symmetric DD1 one (DD1 0.49/0.6/0.49) because the strength of the coupled three steels grades (SS, DP and DD2) are higher compared to the DD1 one.

YS, UTS, E, K ➔ $$YS_{asymmetric} = (f.YS)_{Skin\#1} + (f.YS)_{Core} + (f.YS)_{Skin\#2} \tag{3.1}$$

e_u, e_f, ε_1, ε_2 ➔ $$e_{u-asymmetric} = \frac{e_{u-Skin\#1} + e_{u-Skin\#2}}{2} \tag{3.2}$$

However, the strain-related properties can be estimated by the mean value of the two skin sheets as shown, e.g. for e_u, in Eq. **(3.2)** [Har16c, Sat15]. This can be clearly observed from the ε_1–ε_2 strain paths (**Figure 3.23-b)**, **-e)** and **-h)**) and thinning rate progresses (**Figure 3.23-c)**, **-f)** and **-i)**) of the various asymmetric laminates, where the forming limits are located between the coupled dissimilar skin sheets. The corresponding limiting strains (ε_1–ε_2) just before failure are listed in **Table 3.13**. Yet, the r and n values could not be estimated following these approaches, i.e. Eqs. **(3.1)** or **(3.2)**.

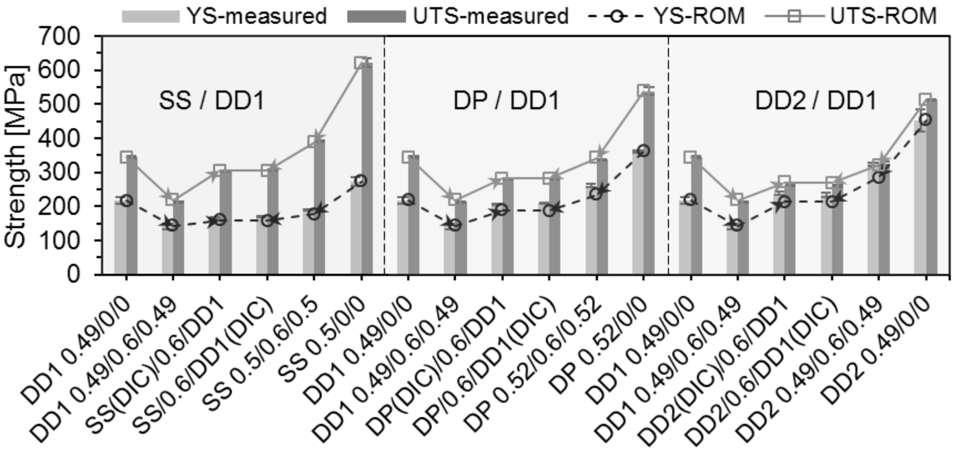

Figure 3.24: Verification of ROM for the asymmetric SPS laminates.

The behaviour of the SS/DD1 combinations are shown in **Figure 3.23-a) – -c)**. Due to the higher n and e_u values of the SS grade, the localized necking of SS and its SPS laminates take place at higher elongation (about 38 mm). However, the ε_1–ε_2 progress of the SS combinations show lower forming limits due to their limited r-value. By combining the SS and DD1 grades, the thinning rate progress of the SS/DD1 laminates is located between that of each skin sheet but much closer to the SS curve, see **Figure 3.23-c)**. So, Eq. **(3.2)** cannot predict the e_u value in a good way due to the remarkable strength and ductility difference between the two steel grades. The two skin sheets behave independently until reaching the necking of DD1, then a combined progress can be observed. The SS side in the asymmetric SPS shows later necking, at higher elongation, than the DD1 side in the same SPS.

Table 3.13: The mechanical properties for the SPS-laminates containing different steel grades (four specimens each).

SPS	E [GPa]	YS [MPa]	UTS [MPa]	K [MPa]	e_u [%]	e_f [%]	n [-]	r [-]	ε_2 [-]	ε_1 [-]
DD1 0.49/0/0	191±4	219±10	345±3	536±6	19	30	0.18	1.75	-0.37	0.77
DD1 0.49/0/0.49	173±5	196±3	297±2	485±3	19	32	0.18	1.74	-0.37	0.79
DD1 0.49/0.6/0.49	118±3	142±7	215±1	337±1	16	29	0.16	1.72	-0.37	0.86
SS 0.5/0/0	188±7	274±13	621±13	1191±10	41	49	0.33	0.41	-0.20	0.58
SS 0.5/0/0.5	152±7	258±4	545±7	1017±15	40	48	0.33	0.42	-0.20	0.58
SS 0.5/0.6/0.5	121±5	191±1	392±1	723±4	40	49	0.31	0.44	-0.17	0.48
SS(DIC)/0.6/DD1	120±2	168±1	305±1	760±80	47	35	0.48	0.32	-0.24	0.71
SS/0.6/DD1(DIC)	123±1	170±2	307±1	535±7	43	32	0.25	2.22	-0.35	0.75
DP 0.52/0/0	206±9	362±4	538±11	831±10	13	23	0.15	0.89	-0.21	0.55
DP 0.52/0/0.52	192±9	301±30	482±9	755±14	11	23	0.15	0.88	-0.21	0.54
DP 0.52/0.6/0.52	122±7	262±5	337±1	525±2	12	22	0.11	0.89	-0.21	0.58
DP(DIC)/0.6/DD1	134±9	209±1	281±1	425±1	14	26	0.15	0.78	-0.25	0.65
DP/0.6/DD1(DIC)	131±7	211±1	284±1	422±1	14	27	0.15	1.94	-0.30	0.63
DD2 0.49/0/0	210±3	453±33	514±1	669±3	6	13	0.07	0.99	-0.18	0.50
DD2 0.49/0/0.49	173±8	428±3	442±1	568±4	6	12	0.07	0.96	-0.18	0.53
DD2 0.49/0.6/0.49	133±2	324±5	326±5	389±2	3	13	0.05	0.99	-0.19	0.55
DD2(DIC)/0.6/DD1	120±5	238±5	262±2	378±5	10	22	0.11	0.92	-0.23	0.60
DD2/0.6/DD1(DIC)	115±10	234±5	260±2	381±1	10	22	0.11	1.97	-0.29	0.65

Figure 3.23-d) – -f) show the behaviour of the DP/DD1 combinations. Due to their lower formability in terms of the r value, as stated before in **Table 3.13**, the ε_1–ε_2 limits of the DP and SPS laminates are lower than the ones of the DD1. The forming limit of the DP/DD1 asymmetric SPS laminates is improved compared to the DP symmetric ones. By observing the thinning rate progress of both the DP(DIC)/0.6/DD1 and DP/0.6/DD1(DIC), the start of their localized necking takes place at the same elongation, i.e. Eq. **(3.2)** is applicable.

Furthermore, **Figure 3.23-g) – -i)** show the flow behaviour of the DD2/DD1 combinations. The forming limits of the DD2 grade was significantly improved in the DD2/DD1 laminates in terms of the limiting strains, elongation at the localized necking and e_f. For the strain estimation, Eq. **(3.2)** is applicable.

After performing the tensile test of the asymmetric laminates containing dissimilar skin sheet properties, repeatable visual macroscopic distortion or rather curvature of all specimens was found. This distortion can be characterized in terms of out-of-plane displacement (in z-direction) out of the xy-plane. **Figure 3.25** shows an example of this effect and the corresponding xyz-coordinates. The maximum displacement is z-axis is located in the center which leads to a curved specimen contour around the y-axis. In order to evaluate these displacements and their correlation with the stetting (staking) configuration of the asymmetric laminates, linear sections in the specimen width (x-axis) were evaluated in the stage just before failure. It was found, that the symmetric DD1 0.49/0.6/0.49 showed approximately a constant (negative) shifting distance of ~ 0.25 mm over the specimen width, which indicates uniform necking (thickness reduction) through the specimen width. However, the two sides of the asymmetric laminates showed different displacements from the specimen edge to the center: one side becomes a concave-like due to the positive out-of-plane displacement (>0) and the other side, of course, is convex-like due to the opposite negative displacement. It was observed that constantly the DD1 grade, in all studied asymmetric laminates, shows a concave surface. Furthermore, it was found that the displacement degree depends on the strength difference between the two steel layers. Based on the current results, the higher the strength difference is, the higher is that displacement, i.e. the convex (red area) / concave (blue area) displacements on the SS, DP or DD2 / DD1 sides are 1.3, 0.6 and 0.5 mm, respectively. Such curvature led to changing the strain in width straining ε_w that can consequently affect the r value of each side, as observed from the listed values in **Table 3.13**.

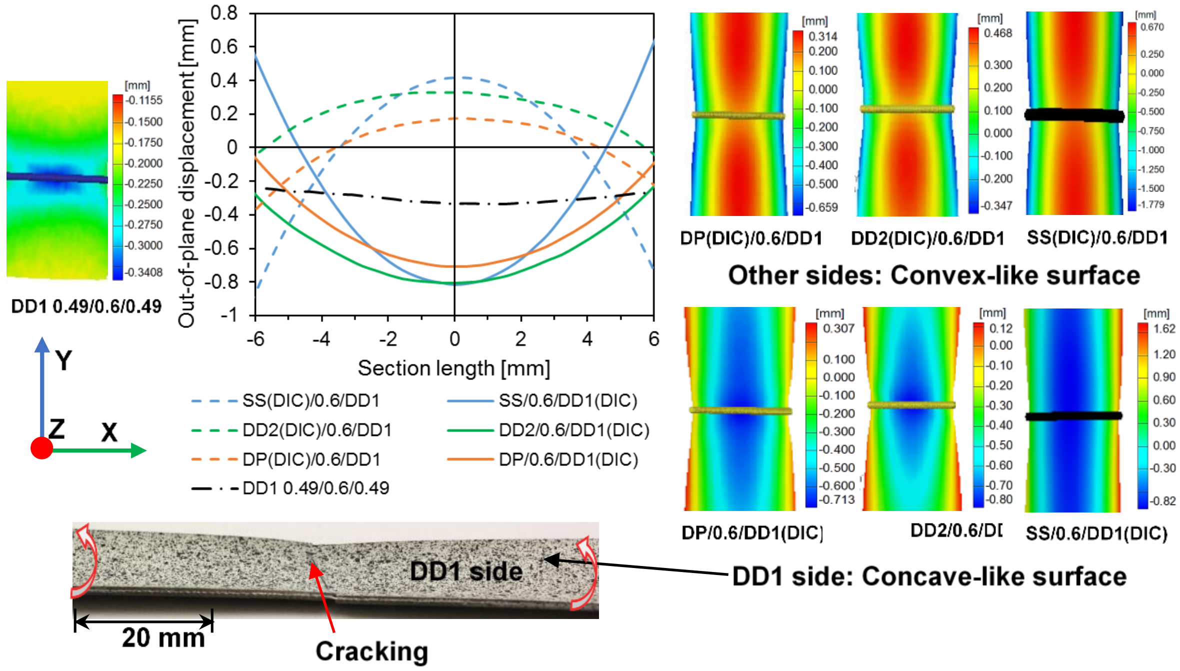

Figure 3.25: Curvature of the tensile specimen plane in z-direction over the specimen width by combining the steel grade DD1 with the other grades (SS, DP and DD2) [Har16c].

3.5. Determination of the forming limit curves

Due to the significance of the FLC curves for determining the tendency of the sheet metal as well as SPS laminates to failure under defined stress conditions, FLCs were determined for the steel sheets – for instance, steel grade DD1 with its two thicknesses 0.49 and 0.24 mm – and their SPS-laminates with different core thicknesses. Different FLC determination methodologies were applied to find out the most relevant one for the sandwich materials.

3.5.1. Test procedure

FLC curves were determined for the monolithic steels as well as the SPS-laminates according to DIN 12004-2 [DIN09a] using a 75 mm$^{\varnothing}$ semispherical punch and 180 mm$^{\varnothing}$ blank. The punch displacement rate was set to 1.5 mm/s. A blank holder force of 100 kN was applied in order to prevent sliding (drawing) of the blank. In order to stimulate different stress conditions or rather failure strains (biaxial, plane and tensile/drawing strain conditions), the test blanks were cut into seven sizes with different widths: 180, 140, 100, 90, 80, 50 and 20 mm. The FLC test setup and specimen geometry are shown in **Figure 3.26-a)** and **-b)**, respectively. **Figure 3.26-c)** shows the lubrication system that was set to ensure minimum friction between the punch and the blank to deliver a central cracking, as can be observed from the failed blanks after the test in **Figure 3.26-d)**. The limiting strains progress is monitored with the DIC system with an imaging rate of 15 Hz.

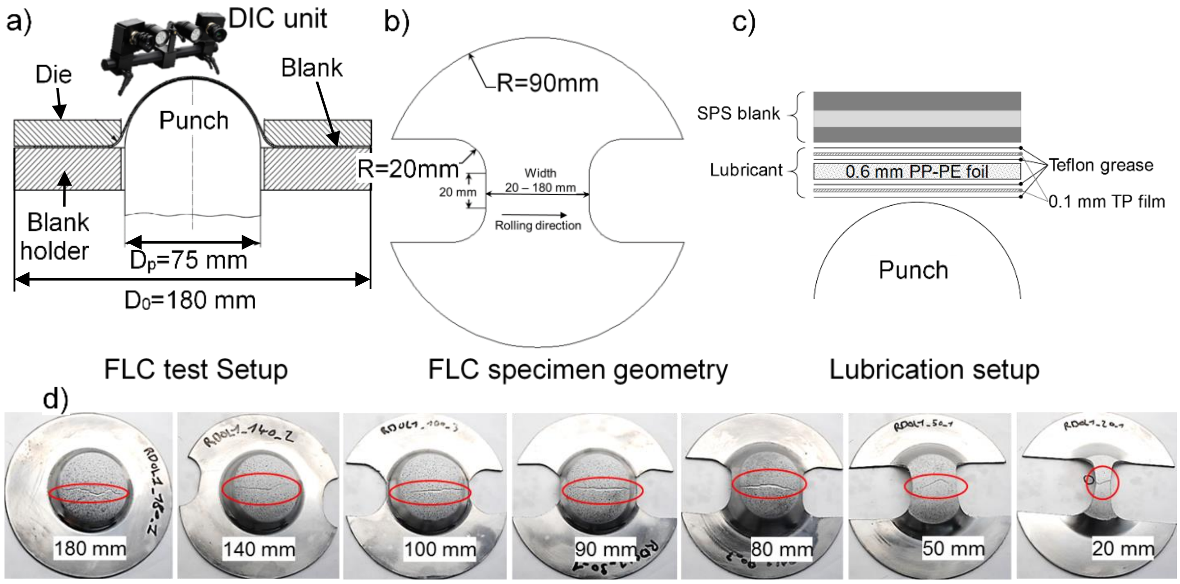

FLC test Setup FLC specimen geometry Lubrication setup

Figure 3.26: a) FLC test setup and b) the corresponding test specimen geometry in addition to c) the lubrication setup (TP: thermoplastic film) and d) the middle crack of the used seven specimen cuts after the test.

The FLC strains were determined based on different approaches:

1. The section maximum values just before failure.
2. The standard section method (ISO 12004).
3. The time-dependent method, particularly the linear best-fit concept [Mer10, Mer14, Vol11].

The first two approaches depend on creating a number of sections – in this case five, as shown in **Figure 3.27-a)** – in the stage just before failure. However, the third one depends on following the area at which failure takes place from the beginning of the punch displacement until failure. This area is recognized from the thinning rate distribution in the stage before failure, as shown in **Figure 3.27-b)**.

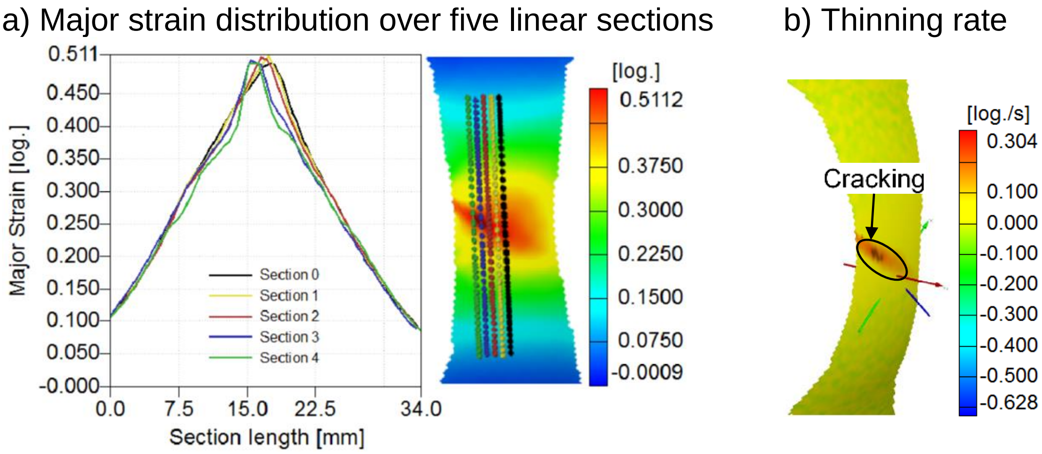
a) Major strain distribution over five linear sections
b) Thinning rate

Figure 3.27: 20 mm wide DD1 0.24/0/0 specimen just before failure showing a) the five sections used in the section method and b) the highest thinning rate region at which failure initiates.

An example explaining the realization of the previous approaches is shown in **Figure 3.28**. In this example, a 20 mm wide specimen of DD1 0.24/0/0 is presented, i.e. the sample is subjected to tensile stresses that gives $\varepsilon_1 = -2 \times \varepsilon_2$ and evaluated by the three approaches, as shown in **Figure 3.28-a)**, **-b)** and **-c)**. The maximum values in the evaluation sections are the limiting strain for the section maximum approach (method 1), where in this case $\varepsilon_1 = 0.67$ and $\varepsilon_2 = –0.32$ as shown in **Figure 3.28-a)**. However, the standard section method ISO 12004 (method 2) depends on generating fitting lines for the major and minor strain progress over these sections in order to predict the limiting strains as shown in **Figure 3.28-b)**. The limiting strains in this case are: $\varepsilon_1 = 0.51$ and $\varepsilon_2 = –0.27$. Moreover, the limiting strains according to the time-dependent method (method 3) based on the best line fit approach were determined by plotting fitting lines for the stable to the unstable thinning rate progresses to define the transition zone as shown in **Figure 3.28-c)**. The major–minor strains at the intersection between the fitting lines represent the limiting strains: in this case $\varepsilon_1 = 0.56$ and $\varepsilon_2 = –0.29$.

a) Tensile strains: Section maximum

b) Tensile strains: Section ISO 12004

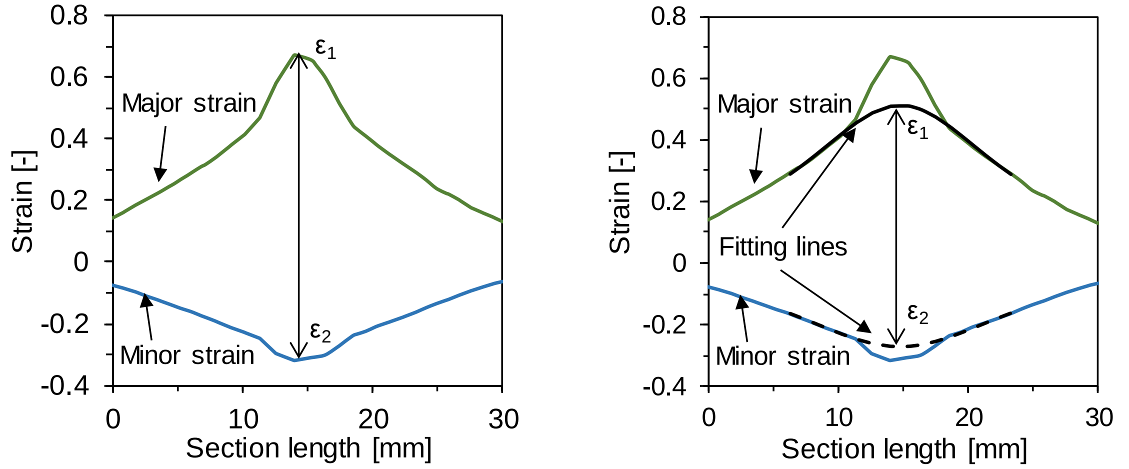

c) Tensile strains: Line fit method

d) Biaxial strains: Section ISO 12004

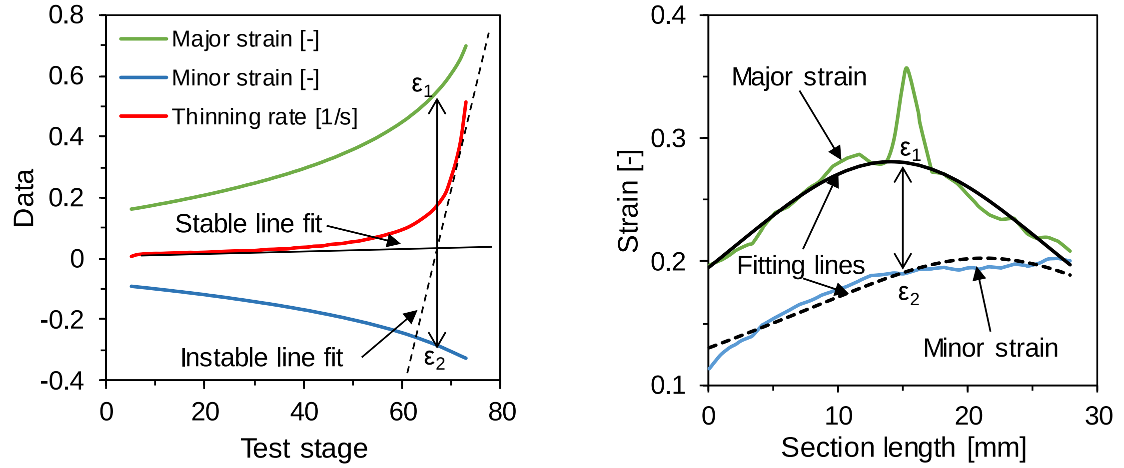

Figure 3.28: Limiting strains determination for DD1 0.24/0/0 under tensile condition according to the: a) section maximum, b) standard section method (ISO 12004) and c) time-dependent method based on best line fit approach, however d) is a plane strain condition evaluated by the section method.

An example of the FLC determined by the before mentioned methods is shown in **Figure 3.29** for the DD1 0.49/2.0/0.49. Firstly, the section-maximum method describes the limiting strains just before failure (after necking) which is in reality a very late prediction. Therefore, it is not a convenient method and no longer applicable to detect the forming limits. The differences between ISO 12004 and the line fit method are ignorable in the tension/drawing region (left side). However, they become significant starting from the plane strain condition (in the center at $\varepsilon_2 = 0$) to the biaxial one (the right side at $\varepsilon_1 = \varepsilon_2$). The reason for that is those fitting lines (method 2) in the tensile region (**Figure 3.28-b)**) are closer to the necking strains. However, the fitting lines in biaxial condition, ISO 12004, get farther from the necking values, clearly shown in (**Figure 3.28-d)**).

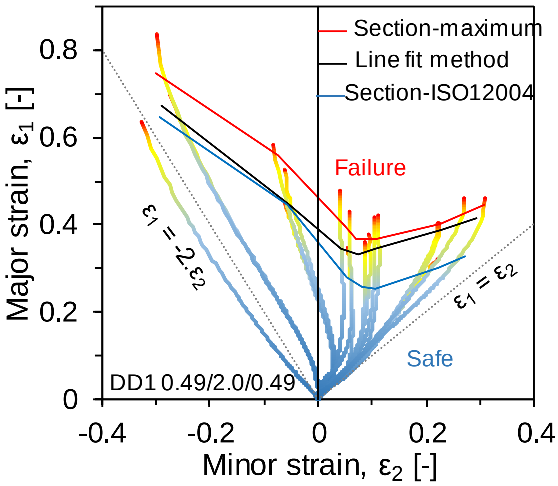

Figure 3.29: FLC determination of DD1 0.49/2.0/0.49 with the different methods overlapped with different strain paths.

3.5.2. Results and verification examples

Firstly, the different FLC determination methods were evaluated and verified with some SPS laminates under different loading conditions especially bending, stretching and tensile loading. Afterwards, the most suitable method is then selected and recommended for the used laminates.

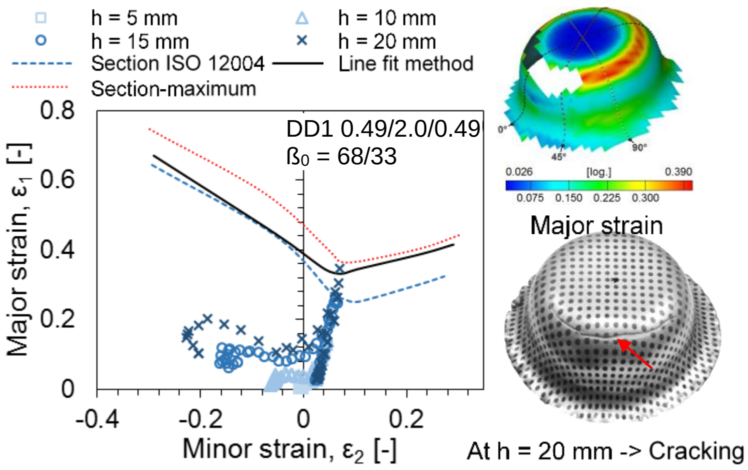

Figure 3.30: Comparing the strain progress of deep drawn cups at different cup heights with the different FLC determinations methods for DD1 0.49/2.0/0.49.

The first verification example is for deep drawing of DD1 0.49/2.0/0.49 with $ß_0 = 68/33$ at different cup heights (h), as shown in **Figure 3.30**. Cracking took place at the punch rounding at h = 20 mm; where a mixed biaxial and bending conditions exist. Comparing the strain progress at h = 15 mm it was found that the strains of the cup surface meet the FLC obtained by the ISO 12004 section method. However, there is no visible failure. It can be stated that the ISO 12004 predicts failure earlier. However, the line fit method met the failure condition of the drawn cup at h = 20 mm.

Deep drawing of DD1 0.24/0.3/0.24 with $ß_0$= 180/75 results in failure at h = 35 mm in the cup sidewall, not at the punch edge, as usually happen, as shown in **Figure 3.31**. Cracking in the sidewall took place due to the low thickness of the skin sheet (0.24 mm) that cannot withstand the radial tensile stresses. As a result, the ε_1–ε_2 strain points of the drawn cup meet the FLC curves determined by both the line-fit and the ISO 12004 section methods in the left side, i.e. where tensile conditions are dominant. In this condition, it can be stated that if failure takes place under tensile conditions, both of the ISO 12004 and line-fit methods predict failure in a proper way.

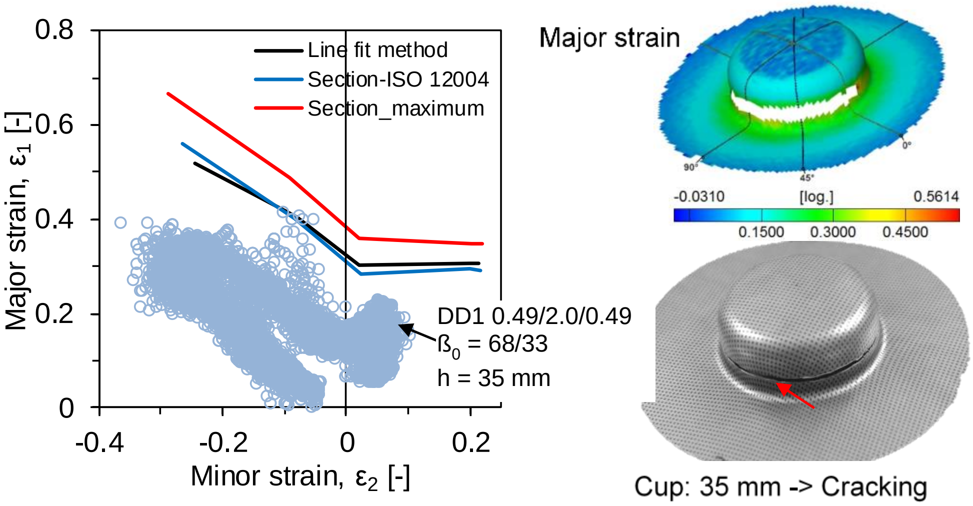

Figure 3.31: Verification of the strain progress of deep drawn cups with different FLC determinations methods for DD1 0.24/0.3/0.24 under tensile failure for $ß_0$=180/75.

A further verification example is failure of DD1 0.49/2.0/0.49 under bending condition. In this case, a bending specimen of 100×60×3 mm^3 was tested with 3 $mm^{Ø}$ punch diameter: failure took place at an angle α = 68.5°, see **Figure 3.32**.

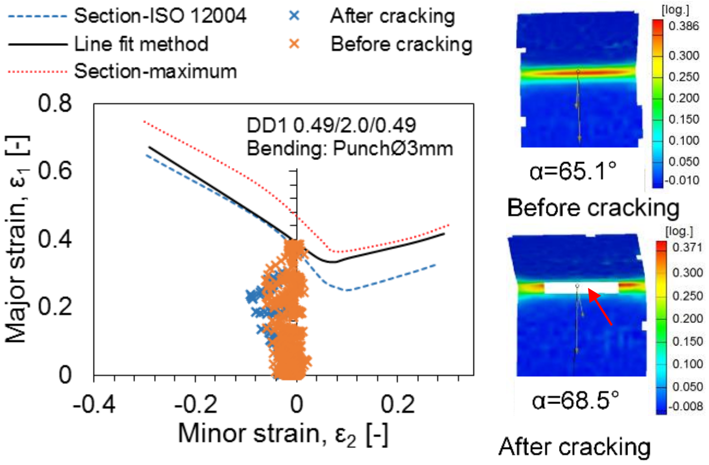

Figure 3.32: Verification of bending failure of DD1 0.49/2.0/0.49 with different FLC determinations methods.

When plotting the strain data at failure of the bent specimen, no reasonable representation was found because the strain points in the crack region were missing as the dot-pattern was not continuous any more, see the graph of the failed specimen in **Figure 3.32**. Therefore, there was a need to plot the data just before failure, for instance at an angle of about 65°: it can be observed that the strain progress meets the plane strain condition in the FLC curve ($\varepsilon_2 = 0$), where both the ISO 12004 and the line fit method coincide. Accordingly, it can be stated that in the case of plane strain loading both approaches are reliable. Concluding, the time-dependent method is the best fitting method to detect the limiting strains, therefore it was used in the further investigation.

The effect of the skin sheet thickness on the FLC level is shown in **Figure 3.33-a)**. Although both sheets (0.49 and 0.24 mm) possess nearby the same mechanical properties, the thicker skin sheet (0.49 mm) showed a higher FLC level (in y axis).This is due to the significant influence of the sheet metal thickness on the FLC level as stated in [Pal12, Sem90], in addition to the differences in the chemical compositions of both steel sheets.

The FLC curves of three SPS laminates based on the DD1 grade are shown in **Figure 3.33-b)**. It can be observed that the SPS based on the thicker steel are higher than that of the 0.24 mm one, following **Figure 3.33-a)**. Moreover, when increasing the core thickness from 0.6 to 2.0 mm, the level of the FLC curve decreases. This difference can be attributed to the higher stress level acting on the outer skin sheet with increased core thickness [Har14a].

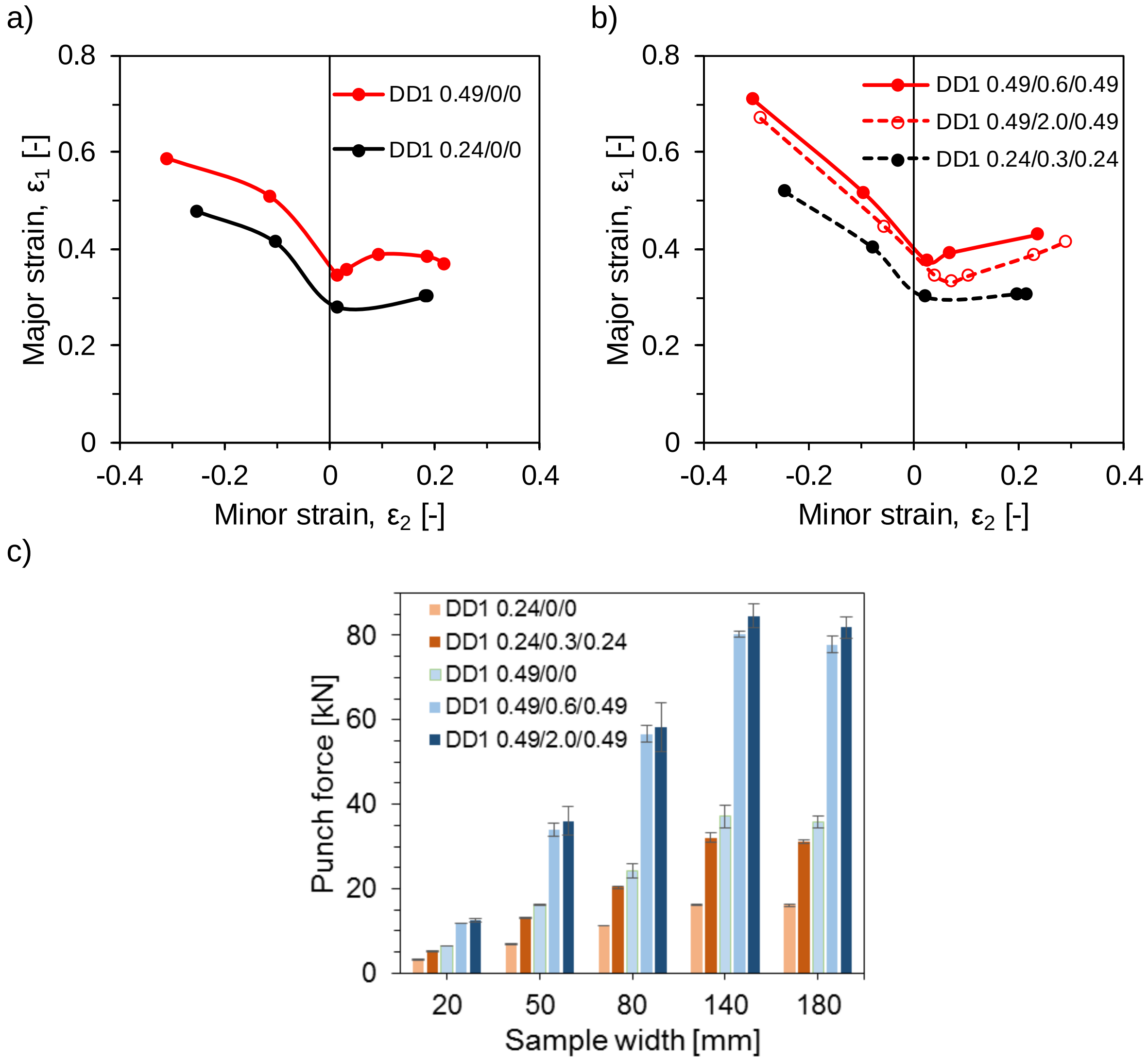

Figure 3.33: a) FLC curves determined by the time-dependent method for the steel sheets and b) their SPS combinations in addition to c) the corresponding maximum drawing forces at the different specimen widths.

Additionally, as stated in the mechanical properties part, with increasing the core thickness, the forming related parameters, such as the n and r values (**Table 3.11**) decrease indicating a restricted forming potential. Some similar effects regarding Al/PP/Al laminates were reported in [Par13]. However, contradictory findings for Al/PE/Al were stated in [Liu13a]. Moreover, the skin and core thickness has a remarkable effect on the maximum punch force as shown in **Figure 3.33-c)**. The thicker is the core and the skin sheet, the higher is the maximum drawing force.

3.6. Summary and conclusions

Based on the systematic methodology proposed for characterizing the metal/polymer adhesion properties, the flow behaviour and forming limits of the monolithic materials and their MPM-laminates, it was possible to derive the following conclusions:

1. The applied production methodology enabled a full-flexibility of bonding arbitrary metallic sheets with different surface properties (steel, aluminium, titanium sheets) with a polyolefin core using a compatible epoxy resin and the continuous coil coating technology.
2. The adhesion results showed cohesive failure in the tinned steel sheets and no complicated surface pre-treatments were required (only acetone degreasing). However, the different surface condition of the other metallic sheets led to a mixed adhesive/cohesive failure mode and a slightly reduced adhesion strength to about 9 MPa compared the 12 MPa for the tinned steel grades. The oiled galvanized steels should be additionally cleaned, for instance, mechanically by grinding and degreasing with acetone to enable a better adhesion. In this case the lap shear strength increased from 9.5 MPa up to 12 MPa after cleaning with sand soap and later with acetone.
3. Although the overlapped length in the single lap shear test was optimized, following empirical equations, bending moments were arisen at the end of the shear stress–displacement progress that led to peeling (out-of-place displacement) in addition to the shearing conditions. This displacement depends on the skin/core thicknesses: significant displacement was found for thin skin sheet (0.24 mm) and becomes clearer with thicker cores.
4. The durability investigation in water lead to no remarkable deterioration of the shear strength even considering icing being reversible after drying the specimens. However, aging in a humid atmosphere showed an irreversible effect, as the vapor particles attacks the steel/epoxy resin interface leading to a gradual decrement of the shear strength with 10% after 20 cycles aging. In general, the adhesion quality is satisfactory to deliver delamination-free forming operations, which is the current case.
5. The obtained correlations regarding the mechanical properties of the monolithic materials with their MPM-laminates verified the applicability of ROM to estimate the strength-related properties, like E, YS, UTS and K, for both symmetric and asymmetric MPM-laminates. The forming-related properties like the n and r values are lower for the MPM-laminates than the ones of the skin sheets but the correlation with the core thickness could not be analytically defined.
6. Under uniaxial tensile loading, the forming limits of the skin sheets depend mainly on the ones for the single skin sheets, as these limits of the MPM-

laminates are very close to their skin sheets: thicker skins result in better forming limits.

7. The forming limits can be tailored by designing MPM-laminates that contain dissimilar skin sheets. Good example is the DD2 / DD1 laminate, where the strain at failure for the DD2 steel sheet as well the DD2 laminates was improved from 13 to be 22%. The strain-related properties, like e_f, e_u, ε_1 and ε_2, for the asymmetric laminates can by calculated from the mean values of the two skin sheets.
8. Different FLC determination methods were applied to define the suitable one for the MPM-laminates. The time-dependent method was the one recommended with the help of some verification examples under different loading conditions.
9. The FLC level depends mainly on the skin sheet thickness and their properties. Increasing the core thickness led to a slight decrement of its level.

Based on these characteristic properties, a successful forming operation, at least free of delamination, can be achieved. However, a balance between the lightweight potential – in terms of increasing the core volume fraction – and the MPM-laminate stacking and thickness of its constitutes should be reached for a successful forming operation, as illustrated in **Figure 3.34**.

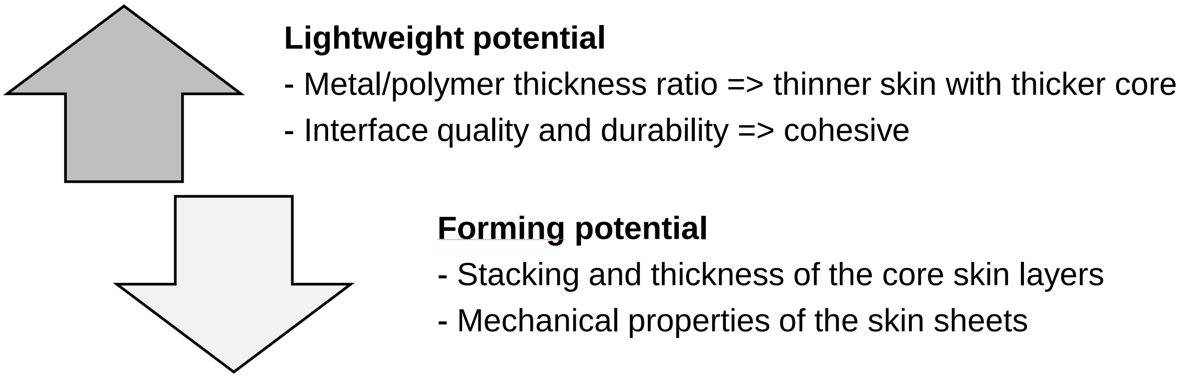

Lightweight potential
- Metal/polymer thickness ratio => thinner skin with thicker core
- Interface quality and durability => cohesive

Forming potential
- Stacking and thickness of the core skin layers
- Mechanical properties of the skin sheets

Figure 3.34: Some factors affecting the successful forming processes of MPM-laminates.

This page intentionally left blank

4. Forming behaviour of the non-reinforced MPM-laminates

Deep drawing is an operation, where the test blank is subjected to forming under compressive and tensile conditions transforming a sheet metal blank into 3D geometry in a single working stroke of the press [Sch98]. Unlike in deep drawing, in stretch forming, a free sheet metal flow of the outer blank area is suppressed as the sheet is fixed by a blank holder. The forming process takes place in the punch region with a reduction in thickness of the sheet. Pure stretch drawing is a forming process conducted under tensile stresses. Both forming processes were applied on the MPM-laminates aiming at defining their working window considering various compositions, properties and thicknesses.

4.1. Deep drawing

The deep drawability of the monolithic steel sheets and their MPM-laminates were investigated. Firstly, the optimum lubrication method to provide good surface finish and faultless cupping was investigated. Moreover, the maximum deep drawing ratio ($ß_{0,max}$) and the optimum blank holder force ($F_{BH,Op}$) for the different laminates were determined and correlated to their mechanical properties. The development of the drawing process in terms of strains and drawing forces was performed by means of stepwise drawing (five steps) until cracking or complete drawing. Moreover, the deep drawability of the symmetric and asymmetric SPS configurations in respect to the forming punch was characterized considering different skin/core thicknesses, steel grades and the number of layers. The impact of the inherent anisotropy in the monolithic sheets of the strain distribution under deep drawing was investigated. Also, the effect of the interlaminar shear strength was considered. The strain distribution was determined using the DIC technique and compared with metallographic evaluation for verification.

4.1.1. Experimental procedure

Firstly, three lubrication conditions were investigated to select the appropriate one delivering good forming and surface properties, as follow:

1. Dry (D): without lubrication.
2. Lubricant film (LF): using a traditional lubricant (SKF LGMT-3 grease).

3. Thermoplastic foil (TF): using a 0.1 mm foil that ensures a continuous separating layer due to its outstanding ductility.

Figure 4.1 illustrates an example of using these conditions on DD1 0.49/0.3/0.49. Drawing without lubrication resulted, as expected, in an early cup-bottom cracking due to high friction conditions between the blank and the drawing tools, see **Figure 4.1-a)**. Using a traditional lubricant led to a good cup, but the surface finish was not satisfactory especially if a dot-pattern was used for the photogrammetry (**Figure 4.1-b)**). However, using the TF condition produced a good surface finish and lower drawing forces were required (**Figure 4.1-c)** and **-d)**). Nevertheless, due to the reduced friction condition of TF, F_{BH} should be slightly increased to avoid wrinkling and deliver a faultless cup. Accordingly, the better cup could be produced by increasing F_{BH} from 9 to 20 kN as shown in **Figure 4.1-c)** and **-d)**, respectively. Therefore, deep drawing with TF was favoured and chosen to be applied for the subsequent investigations.

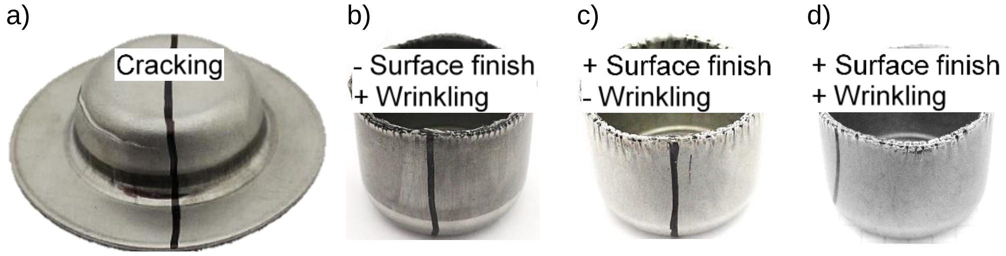

Without lubrication
F_{BH} :9 kN
$F_{d,max}$:43±1 kN

Lubricant film
F_{BH} :9 kN
$F_{d,max}$:40±1 kN

Thermoplastic foil
F_{BH} :9 kN
$F_{d,max}$:35±1 kN

Thermoplastic foil
F_{BH} :20 kN
$F_{d,max}$:34±1 kN

Figure 4.1: Effect of the lubrication condition on the deep-drawability and quality of the drawn cup of DD1 0.49/0.3/0.49 at ß$_0$ = 68/33 (+: good, -: poor).

Further drawability investigations were carried out to determine the working areas (as illustrated in **Figure 2.13**) of the different used steel grades and their laminates. The aim was to specify the drawing defects in terms of varying F_{BH} (5–100 kN) and ß$_0$ (1.6–2.4) and even how the drawability of the steels is affected by creating sandwich laminates based on them. Finally, the working area of MPM-laminates – based on different metallic skin sheets – could be determined. The aim here is to correlate the previously obtained mechanical properties with their drawability. The effect of the core thickness on the boundaries of the faultless cup working area was investigated as well. In this regard, a flat cylindrical punch (d_0 = 33 mm) with a punch corner radius r_P = 4.5 mm was utilized. The used die dimensions for the different thicknesses are summarized in **Table 4.1**. The ratio of the gap size between the punch and the inner diameter of the drawing die to the blank thickness corresponds to 1.2–1.4. The drawing speed was kept constant at 0.5 mm/s.

Table 4.1: Drawing die dimensions and the corresponding allowances.

SPS-laminate	t_{SPS} [mm]	r_D [mm]	D_D* [mm]	Gap size**[mm]	Gap size/t_{SPS}
DD1 0.49/0/0	0.49	2.75	34.2	0.6	1.2
DD1 0.49/0/0.49	0.98	2.75	35.9	1.5	1.4
DD1 0.49/0.3/0.49	1.28	2.75	36.8	1. 9	1.4
DD1 0.49/0.6/0.49	1.58	3.5	37.3	2.1	1.3
DD1 0.49/1.0/0.49	1.98	3.5	38.5	2.8	1.4
DD1 0.49/2.0/0.49	2.98	5.5	40.9	3.9	1.3
DD1 0.24/0/0	0.24	2.75	33.7	0.3	1.4

*:D_D: the inner diameter of the drawing die, **: Gap size = $(D_D\text{-}d_0)/2$, d_0: punch diameter = 33 mm

Furthermore, stepwise drawability of the steel grade DD1 (0.49 and 0.24 mm) in addition to its laminates with different skin/core thickness combinations was carried out, where the stacking of the SPS layers was considered (**Figure 4.2**), too. In this case, ß$_0$ = 68/33 was chosen with variable F_{BH} based on the blank properties. In this regard, the strain distribution over the outer and inner skin sheet surfaces was evaluated using photogrammetry in the five drawing steps: 5, 10, 15, 20 mm and until complete drawing or cracking. For photogrammetry, a dot-pattern (1 mm$^{\varnothing}$ point with 2 mm center to center distance) was etched on the metallic surfaces electrochemically, see **Figure 2.11-c)**. As mentioned before, a thermoplastic film was used as lubricant to preserve this pattern from friction damage while shaping.

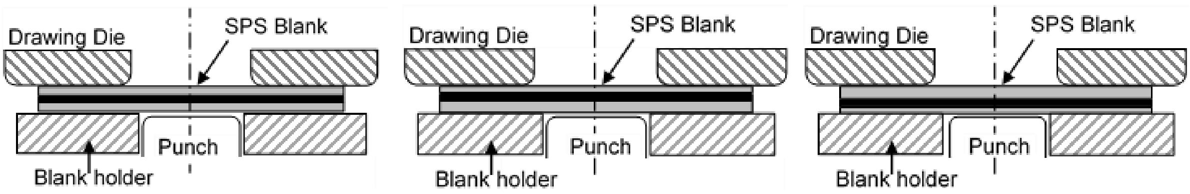

Symmetric laminate DD1 0.49/0.6/0.49 | Punch/thick/thin skin stacking DD1 0.49*/0.6/0.24 | Punch/thin/thick skin stacking DD1 0.49/0.6/0.24*

Figure 4.2: Different stacking configurations in respect to the drawing punch. *: refers to the skin sheet in contact with the punch.

4.1.2. Determination of the working area

Firstly, the working limits were determined for the steel skin sheets considering the resulting defects. The different regions are shown for the steel sheet DD1, i.e. DD1 0.49/0/0 in **Figure 4.3-a)**. Four regions can be defined:

1. Edge wrinkling (EW) is expected at low F_{BH}; longer EW takes place for completely drawn cups at higher drawing ratios, for instance at ß$_0$ = 2.34.
2. Complete drawing (CD) or faultless drawing: with the optimum F_{BH} of 25 kN, the max drawing ratio is ß$_{0,max}$ = 2.28.

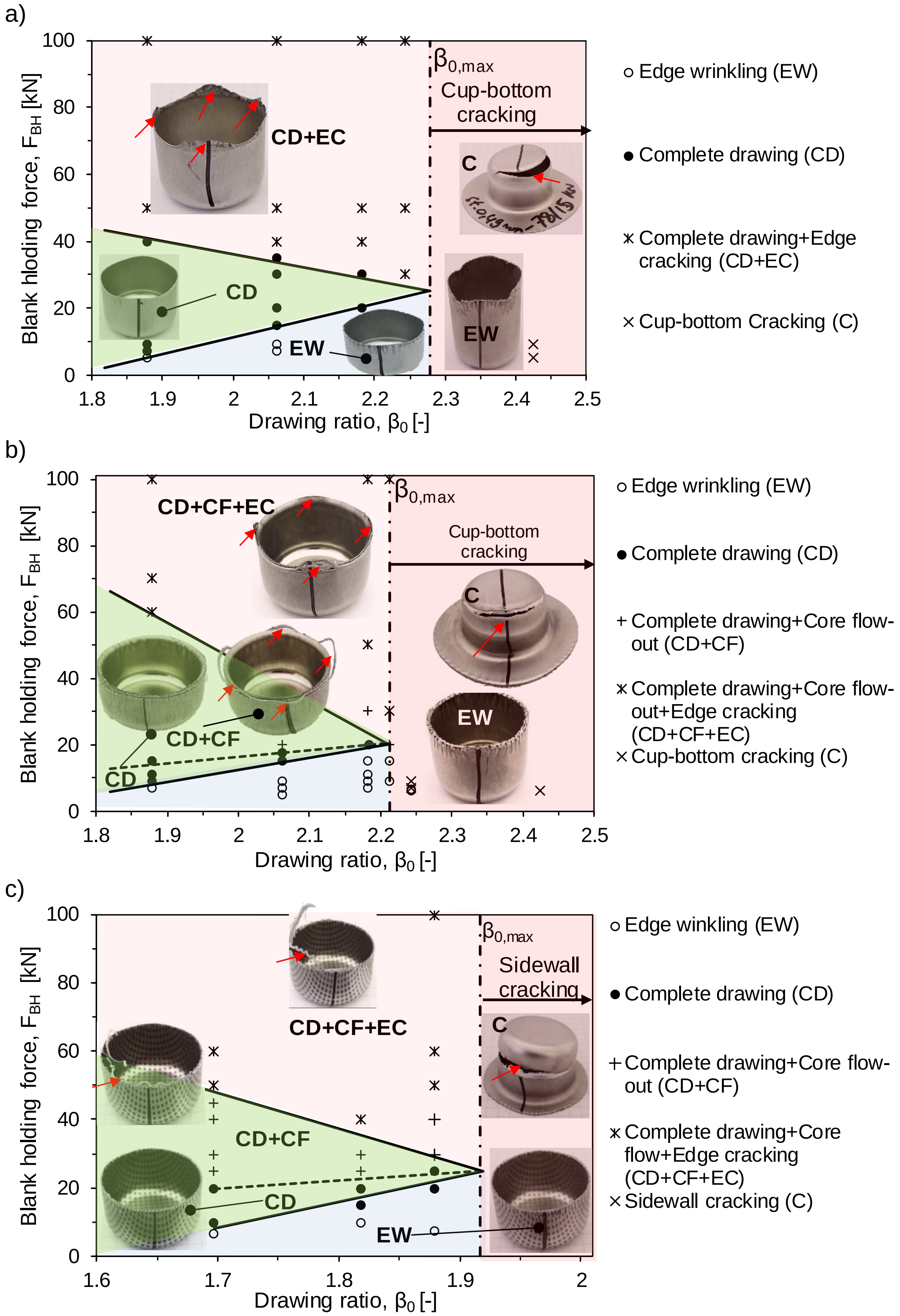

Figure 4.3: Deep drawability working areas for: a) the steel sheet DD1 0.49/0/0, b) DD1 0.49/0.3/0.49 and c) DD1 0.24/0.3/0.24. Green-shaded region represents the working area, i.e. CD for monolithic steels and CD+(CD+CF) for the MPM laminates.

3. At the end of the drawing stroke, when applying higher F_{BH} values (> 40 kN), edge cracking (EC) in the earing regions of the complete drawn cup takes place, denoted as (CD+EC).
4. Cup-bottom cracking (C) occurs at $ß_0 > ß_{0,max}$ at higher F_{BH}. The drawn cup exhibits neither cup-bottom cracking nor sidewall cracking until reaching $ß_{0,max}$, alike the traditional diagrams (**Figure 2.15**). This can be attributed to:
    a. The good lubrication conditions.
    b. The limited F_{BH} of the used Erichsen sheet testing machine (100 kN).

   Based on these regions, the working area can be defined, where no wrinkling, cup-bottom or cup-edge cracking could be found, i.e. the green-shaded one. However, unavoidable earing was found in 0° and 90° directions to RD due to the anisotropic behaviour of the steel sheets.

Like for the steel sheets, the working areas for some laminates were determined, as shown in **Figure 4.3-b)** and **-c)** for thicker skin SPS (DD1 0.49/0.3/0.49) and a thinner skin one (DD1 0.24/0.3/0.24), respectively. In comparison to the behaviour of the steel sheets in **Figure 4.3-a)**, different drawing defects in such multilayer laminates under deep drawing can occur because of three possible effects, like delamination, as illustrated in **Figure 4.4**:

1. High-tension stresses at the outer skin which can lead to cracking.
2. Compressive stresses acting on the inner skin that can lead to wrinkling with a higher degree than the outer one. Additionally, compressive stresses at the flange can lead to core thickening and subsequently core flow-out.
3. Shear stresses at the cup edges that can lead to shifting between the skin sheets.

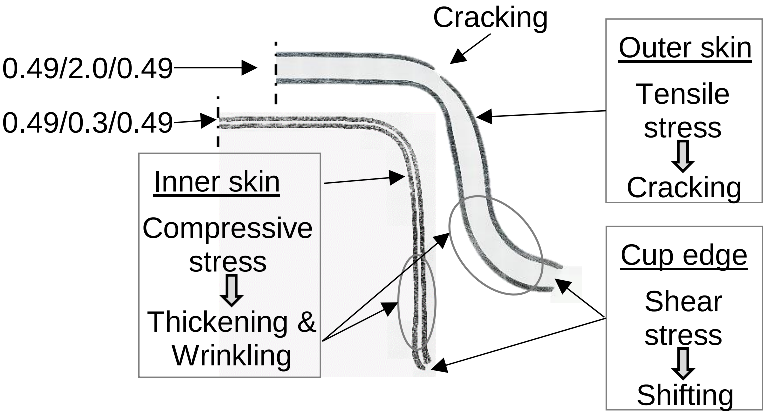

Figure 4.4: Possible defect sources of MPM-laminates drawn cups.

The common defects between the steel sheet and the SPS-laminate are: cup-bottom cracking (C), complete drawing (CD) and edge wrinkling (EW). Additional defects were found at the drawn cup edge when applying high F_{BH}, like:

1. Completely drawn cup (CD) with limited core flow-out (CF) was found mainly at the earing edges (CD+CF). CF takes place as a result of the higher blank holding forces acting on the cup flange, where core thickening normally occurs, as shown in **Figure 4.4**.

   For the MPM-laminates, faultless drawing is defined for a cup free of edge cracking, edge wrinkling, core flow-out and cup-bottom cracking. Moreover, no cup-bottom cracking was found until reaching $ß_{0,max}$ = 2.21, which is slightly less than for the steel. So, CD and CD+CF can be considered as the working area of the MPM-laminates, where no cracking of the metallic skin sheet is observable.
2. At higher F_{BH} (50–100 kN), besides CF, the earing edges are subjected to edge cracking (EC) similar to that of the steel sheets: (CD+CF+EC).

The working area of thin-skin sheet SPS (0.24 mm), i.e. DD1 0.24/0.3/0.24 is depicted in **Figure 4.3-c)**. In this case, the defects found in **Figure 4.3-b)** are repeated. However, sidewall cracking was found instead of cup-bottom cracking for thicker skin SPS (0.49 mm) after reaching $ß_{0,max}$. As mentioned before, thinner sheets, or in this case SPS that contain thinner skin sheets, are more sensitive to cracking especially in the sidewall, as expressed in Eq. **(2.29)**.

A comparison of the working areas of some DD1-laminates is shown in **Figure 4.5-a)**. It can be observed that with increasing the core thickness (0.3, 0.6 and 2.0 mm) with the same steel grade DD1 (0.49 mm), the $ß_{0,max}$ values decrease directly.

There is no significant effect of the core thickness on the optimum F_{BH}. However, at the same $ß_0$, slightly higher F_{BH} is required for drawing the MPM-laminates in respect to the one required for the single steel sheet to enable delivering good cups, see **Figure 4.5-a)**. With thicker core laminates, the tendency of shearing the skin sheets is higher, i.e. for the DD1 0.49/2.0/0.49, such shearing is unavoidable even for good cups at very low $ß_0$ (50/33), as shown in **Figure 4.5-c)**. This led to a significant restriction of the working area; green shaded in **Figure 4.5-a)**. Furthermore, the degree of wrinkling increases with $ß_0$ and it is much clearer in the inner skin sheet as a result of the compressive stresses, see **Figure 4.4**. On the other side, for thinner cored DD1 laminates, very limited defects at the same drawing conditions (F_{BH} and $ß_0$) were found, as shown in **Figure 4.5-b)**. Although both of the DD1 0.49/0.6/0.49 and DD1 0.24/0.3/0.24 have the same strength and consisting the same f_c, $ß_{0,max}$ is clearly reduced for thinner SPS to 1.92. This is due to the thickness effect on reducing the forming potential and the less r values in respect to the thicker skin sheet.

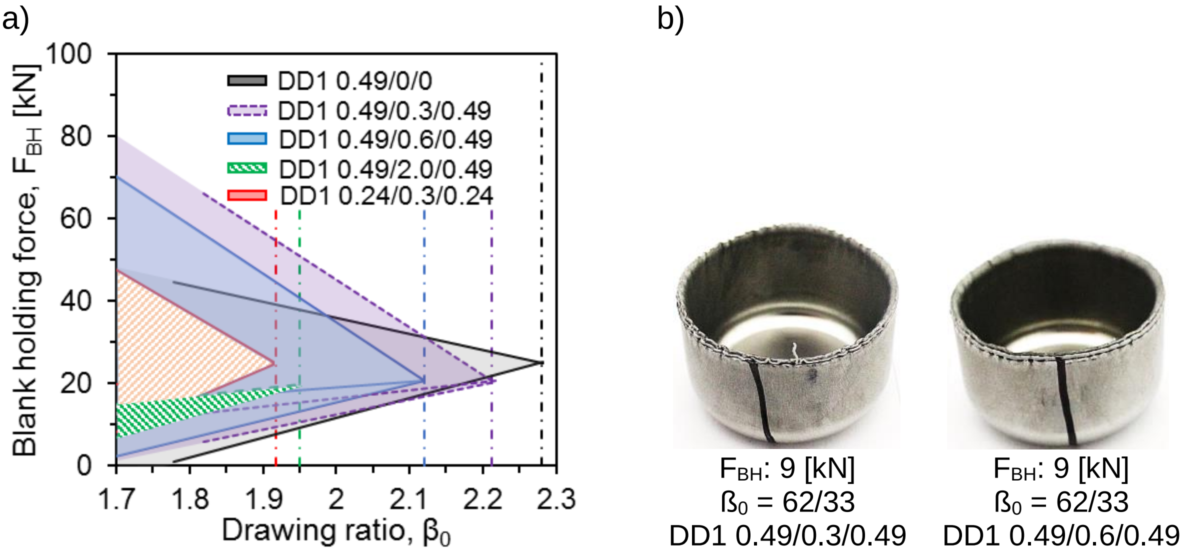

F_{BH}: 9 [kN]
ß$_0$ = 62/33
DD1 0.49/0.3/0.49

F_{BH}: 9 [kN]
ß$_0$ = 62/33
DD1 0.49/0.6/0.49

c) DD1 0.49/2.0/0.49

F_{BH}: 7 [kN] ß$_0$=50/33

F_{BH}: 7 [kN] ß$_0$=56/33

F_{BH}: 7 [kN]

F_{BH}: 60 [kN] ß$_0$=62/33

F_{BH}: 100 [kN]

Figure 4.5: a) The working areas of some DD1 laminates with different skin/core thickness ratios and b) skin sheets shearing, core flow-out and wrinkling of thin-cored DD1 laminates in comparison to c) thicker-cored ones, i.e. DD1 0.49/2.0/0.49 at different F_{BH} and ß$_0$.

The defects arising in the drawn cups at different drawing ratios and thicknesses can be interpreted in terms of the forced–punch displacement behaviour. **Figure 4.6-a)** shows the effect of the core thickness on the maximum drawing force at different ß$_0$ and core thicknesses. The drawing forces of the SPS with 0.3 and 0.6 mm core thickness are quite similar and equal approximately twice the F_d of their monolithic steel sheet. However, for the SPS with 2.0 mm core thickness, F_d is reduced significantly at the same ß$_0$ and F_{BH}. This can be attributed to the low strength values of this SPS and additionally due to the large separation with the soft thick (2 mm) core between the two skin sheets that can accordingly reduce the punch forces.

The obvious shear behaviour of the DD1 0.49/2.0/0.49 illustrated in **Figure 4.5-c)** can be recognized from the drawing force–displacement curve at F_{BH} = 60 kN in respect to other DD1-laminates with lower core thicknesses of 0.3 and 0.6 mm, as presented in **Figure 4.6-b)**. It can be observed from the behaviour of the DD1 0.49/2.0/0.49 that F_d drops in the middle of the stroke due to the significant core flow-out leading to a local thinning in these regions. At the end of the punch stroke and due to the skin sheets shearing, there are two maxima, each for one skin sheet.

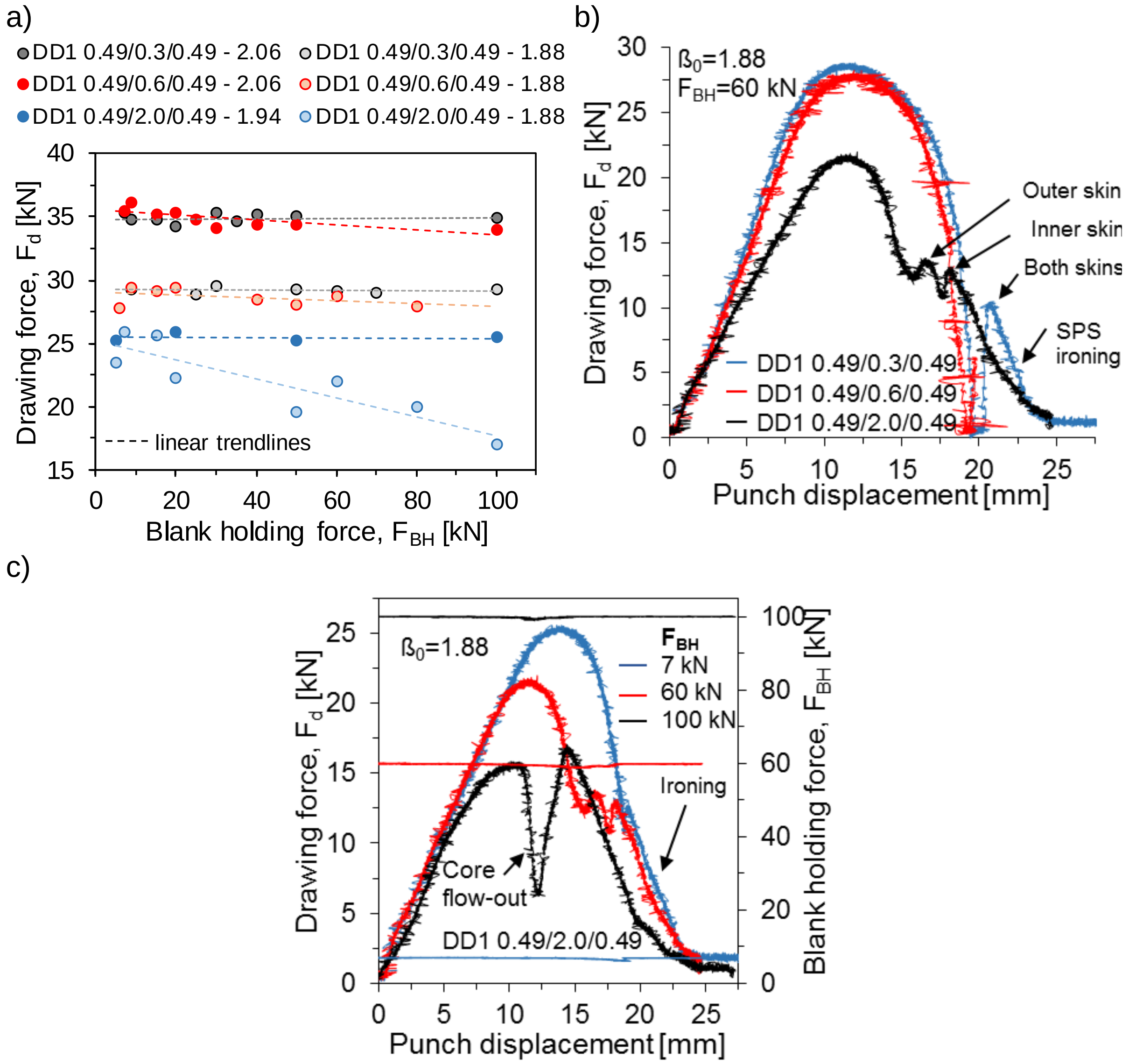

Figure 4.6: a) Maximum drawing force in dependence on the drawing ratio ($ß_0$) and F_{BH} for the DD1-laminates at different core thicknesses (0.3, 0.6 and 2.0 mm) and b) their drawing force-displacement progress at constant $ß_0$ (1.88) and F_{BH} (60 kN) and c) focusing of the thicker core DD1-laminates (DD1 0.49/2.0/0.49) at $ß_0$ of 1.88 at different F_{BH}. The legend DD1 0.49/0.3/0.49 - 2.06 in a) means that the DD1 0.49/0.3/0.49 is drawn at $ß_0$ = 2.06.

The outer skin sheet starts drawing followed by the inner one. This can be seen clearly from **Figure 4.5-c)**, where the outer skin sheet is shorter than the inner one. At the very end of the stroke, the whole SPS is subjected to ironing. This behaviour is not remarkable for thinner cores, but ironing is consistently acting at the stroke end. It is likewise overserved from **Figure 4.6-a)** that with increasing F_{BH} for the DD1 0.49/2.0/0.49 at $ß_0$ = 62/33 = 1.88, F_d gradually decreases. This result can be clarified through the drawing force–displacement given in **Figure 4.6-c)** and the drawn cups images **Figure 4.5-c)** at F_{BH} = 7, 60 and 100 [kN]. At F_{BH} = 100 kN, F_d drops significantly from ~ 16 to ~ 6 kN at a cup height h = 10 mm due to the core flow-out and accordingly the uneven F_{BH} distribution. It was repeatedly found that at the end of the stroke a core ring of about 5 mm in width was cut and separated from the cup edges.

The working areas of different SPS laminates containing different steel grades (DP and DD2) in addition to the DD1 at the same f_c are illustrated in **Figure 4.7-a)**. The $ß_{0,max}$ of the single steels (DD2 and DP) are relatively good and comparable to the DD1 grade, however when combined in the form of three-layered SPS with $f_c = 0.38$, the tendency of $ß_{0,max}$ to decrease is higher than for the DD1 laminates, as illustrated from the slope of the linear trendlines in **Figure 4.7-b)**. This is due to the significant different in the r value between them and the DD1 one. Furthermore, the lower r value combined with the higher strength of the DD2 and DP steels, the optimum F_{BH} for them are considerably higher compared to the DD1 grade, as illustrated in **Figure 4.7-c)**. With lower r values, higher F_{BH} values are required to avoid wrinkling, where thickening of the flange is more likely [Lan95].

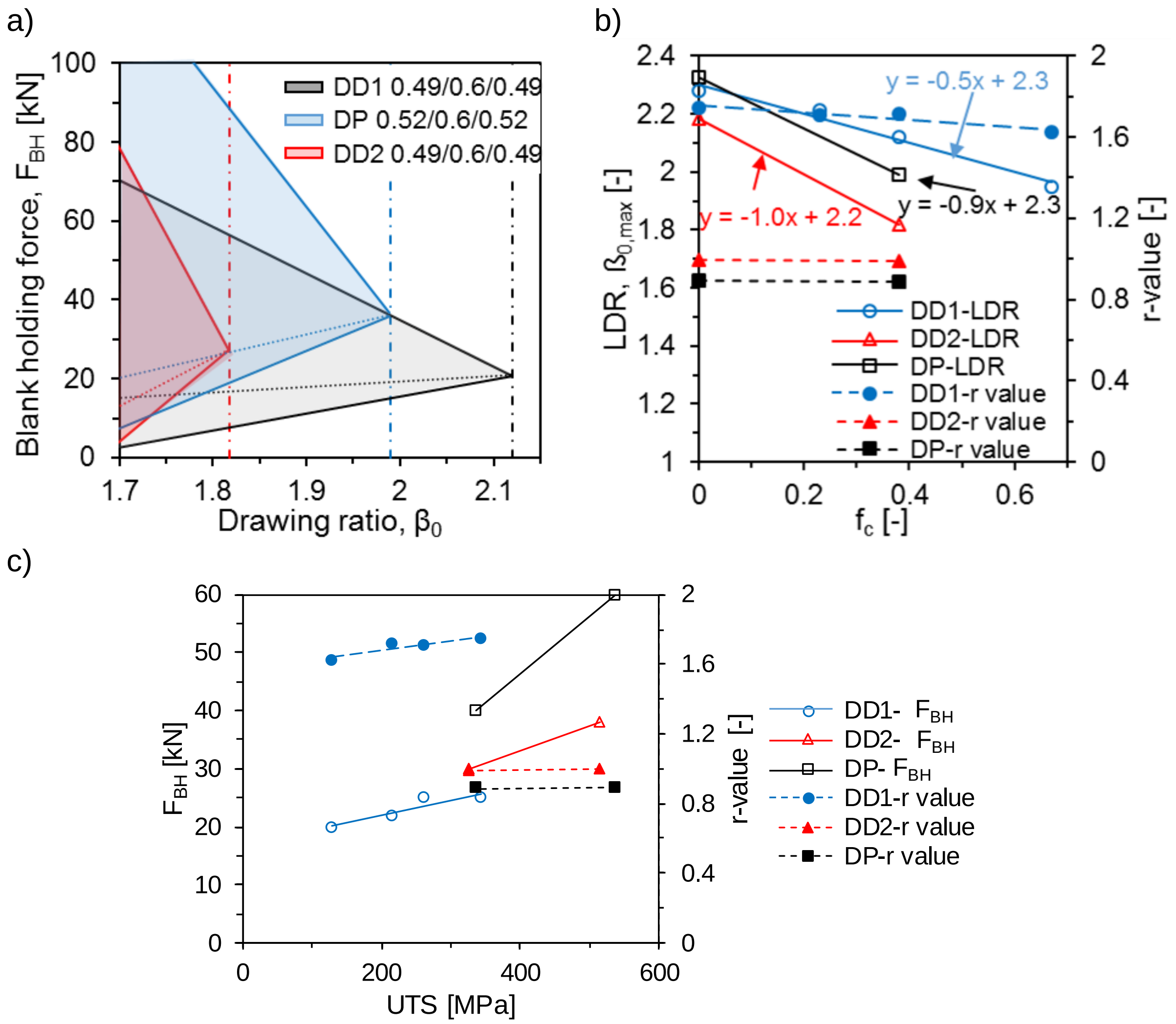

Figure 4.7: a) The working areas of SPS laminates based on different steel grades at $f_c = 0.38$ in addition to b) the correlation with their r values and the resulting $ß_{0,max}$ and with c) UTS and F_{BH} values.

The effect of the steel grade on F_d in terms of F_{BH} and ß_0 at constant f_c is presented in **Figure 4.8**. As expected, the higher strength SPS requires a higher F_d at the same F_{BH} and ß_0 (**Figure 4.8-c)**. Moreover, no remarkable change of the F_d with increasing F_{BH} was found (**Figure 4.8-b)**, attributed to the low friction condition between the blank and the drawing tools (blank holder, die as well as the punch) using the thermoplastic film lubricant.

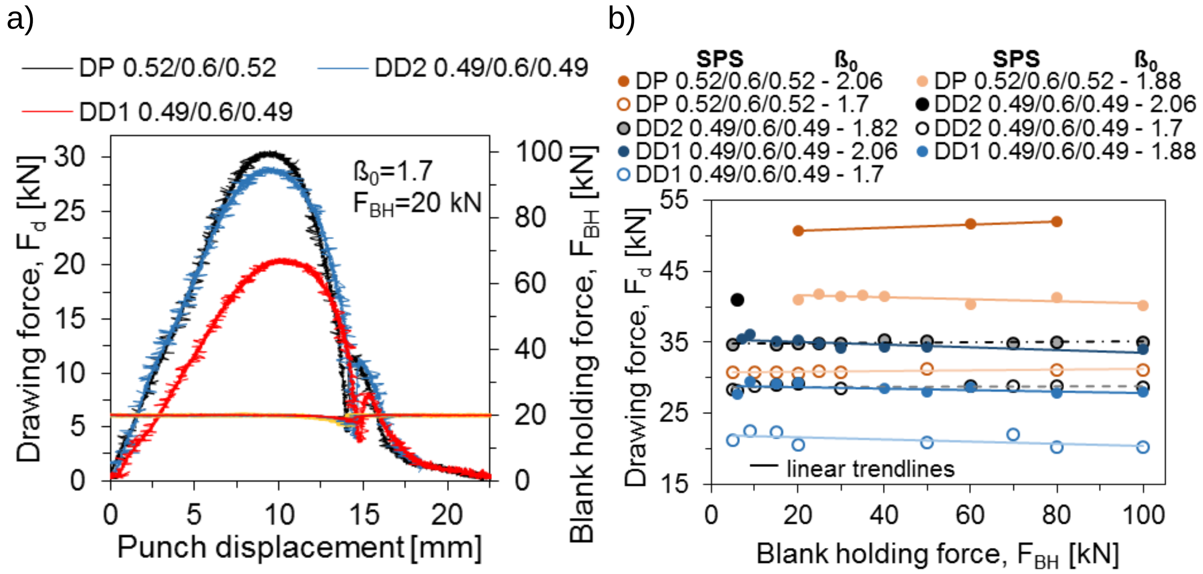

Figure 4.8: a) The drawing force – displacement progress of SPS laminates based on different steel grades at $\text{ß}_0 = 1.7$ and $F_{BH} = 20$ kN and b) the corresponding maximum drawing force based on varied ß_0 and F_{BH}.

4.1.3. Prediction of the drawing force and the limiting drawing ratio (LDR)

It is essential to examine whether the available analytical and empirical approaches for the metallic sheets are applicable for the current multilayered materials. Therefore, the applicability of some approaches described earlier in part 2.4.2 was examined.

4.1.3.1. Drawing force prediction

The total drawing force F_d, is measured experimentally by the Erichsen cupping machine and then compared with the estimated ones according to the following approaches:

1. Cracking force was estimated according to Eq. **(2.29)** as the higher limit the material can withstand before cracking. The correction factor $a_c = 1.05$ was applied to indicate the affinity of the SPS sheets and steels to cracking following the guidelines of [Lan95].
2. The general Siebel form described in Eqs. **(2.24)** and **(2.25)**: $\mu = 0.05$ was assumed [Lan95]. The advantage of this approach is that it can approximate the F_d instantaneously during the drawing process, i.e. at varied cup height.

3. The simplified Siebel approach given in Eq. **(2.26)**. A drawing efficiency η = 0.7 was applied [Lan95].
4. Romanowski approach **(2.27)**. Based on the tabulated data of the k factor in [Rom71], k = 1 was chosen.
5. The summation approach. F_d equals the summation of the single F_d of the SPS constituents at the same cup height. Eq. **(2.15)** stands for the summation form for three-layered SPS. In this condition, each layer is separately deep drawn and then the sum of the three-layer forces represents F_d for such SPS. Nutzmann [Nut08] studied this assumption and reported 10–20% deviation from the experimental results.

Figure 4.9 shows the comparison of the $F_{d,max}$ results of some SPS laminates estimated with the previously introduced approaches in respect to the experimental results. **Table 4.2** gives an overview of $F_{d,max}$ of all the studied SPSs determined by these approaches and the experiments. The difference between the experiment and the estimation is evaluated in $\Delta F_{d,max}$ % according to Eq. **(4.1)**.

$$\Delta \mathrm{F}_{d,max}\,[\%] = 100 \cdot \frac{F_{d,max}^{Estimated} - F_{d,max}^{Experiment}}{F_{d,max}^{Experiment}} \qquad \mathbf{(4.1)}$$

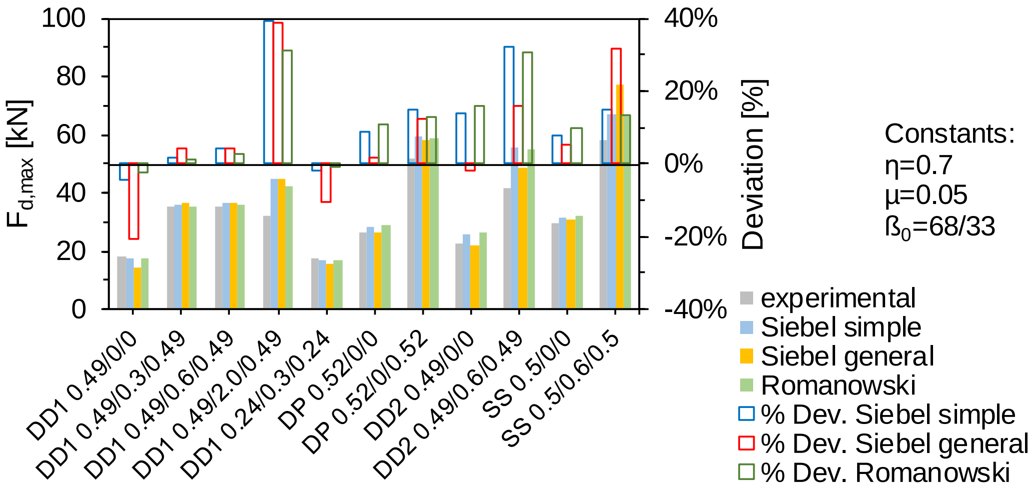

Figure 4.9: Comparison of the deep drawing force of various SPS configurations based on experimental and theoretical approaches.

It can be primarily observed that the SPS based on DD1 grade show lower F_d values than the other steels (DP, DD2 and SS) fundamentally due to the strength difference. Moreover, when considering the asymmetric SPS that compose two steel grades like the DD1*/0.6/DP and DD1/0.6/DP*, F_d of these SPS are equal and their values are intermediate between the F_d of their symmetric SPS.

Table 4.2: Comparison of the experimental drawing force at h = 15 mm with the determined ones following the previously mentioned approaches at $ß_0$ = 68/33. The values in round brackets represent $\Delta F_{d,max}$ % following Eq. **(4.1)**.

SPS-laminate	F_{BH} [kN]	Maximum drawing force, $F_{d,max}$ [kN]**					$F_{cracking}$ Eq. **(2.29)**
		Exp.	Summation Eq. **(2.15)**	Siebel		Romanowski	
				General form	Simple form		
DD1-laminates							
0.49/0/0	15	18±1	18 (0)	14 (-21)	17 (-4)	18 (-2)	19
0.49/0/0.49	10	34±1	36 (6)	33 (-2)	33 (-2)	33 (-2)	36
0.49/0.3/0.49	10	35±1	38 (8)	37 (4)	36 (2)	36 (1)	39
0.49/0.6/0.49	10	35±1	39 (10)	37 (4)	37 (4)	36 (3)	40
0.49/1.0/0.49	9	35±1	40 (16)	49 (41)	41 (19)	40 (15)	45
0.49/2.0/0.49	8	32±1	43 (33)	45 (39)	45 (39)	42 (31)	49
0.49/0.6/0.49-unjoined	10	32±1	39 (20)	37 (14)	37 (14)	36 (12)	40
0.49*/0.6/0.24	9	26±1	31 (18)	27 (4)	27 (4)	27 (4)	30
0.49/0.6/0.24*	9	26±1	31 (18)	28 (6)	28 (6)	27 (5)	30
0.49*/0.3/0.24/0.3/0.24	10	33±1	42 (25)	36 (7)	37 (11)	35 (5)	39
0.49/0.3/0.24/0.3/0.24*	10	33±1	42 (26)	36 (8)	37 (13)	35 (7)	39
0.24/0/0	9	10±1	10 (0)	8 (-20)	8 (-21)	8 (-19)	9
0.24/0.3/0.24	7	17±1	22 (27)	17 (-2)	17 (-2)	17 (-1)	18
SS-laminates							
0.5/0/0	20	29±1	30 (0)	31 (5)	32 (8)	32 (10)	34
0.5/0/0.5	30	60±1	59 (-2)	70 (16)	62 (4)	62 (4)	67
0.5/0.6/0.5	25	58±1	62 (5)	77 (32)	67 (15)	66 (13)	73
SS/0.6/DD1*	25	47±1	50(8)	76 (64)	52 (12)	52 (11)	57
SS*/0.6/DD1	25	46±1	50 (8)	59 (27)	53 (14)	52 (12)	57
DP-laminates							
0.52/0/0	60	26±1	26 (0)	27 (2)	28.4 (9)	29 (11)	31
0.52/0/0.52	30	53±1	52 (-1)	55 (5)	57 (8)	57 (8)	62
0.52/0.6/0.52	25	52±1	55 (6)	58 (12)	60 (15)	59 (13)	65
DP/0.6/DD1*	10	43±1	47 (10)	48 (13)	49 (14)	48 (13)	53
DP*/0.6/DD1	10	43±1	47 (10)	48 (12)	49 (15)	49 (14)	54
DD2-laminates							
0.49/0/0	40	23±1	23 (0)	22 (-2)	26 (14)	26 (16)	28
0.49/0/0.49	30	45±1	45 (0)	45 (0)	49 (10)	50 (10)	54
0.49/0.6/0.49	10	42±1	48 (14)	49 (16)	56 (32)	55 (30)	60
DD2/0.6/DD1*	10	37±1	43 (18)	43 (18)	45 (22)	44 (20)	49
DD2*/0.6/DD1	10	40±1	43 (9)	44 (10)	44 (12)	44 (10)	48
PP-PE: 0.3 mm	8	2± 1	2 (0)	2 (-5)	1 (-55)	1 (-55)	1
PP-PE: 0.6 mm	8	3±1	3 (0)	3 (-10)	2 (-38)	2 (-31)	2

*: The steel side in contact with the drawing punch, +: these SPS cracked at ~ 8 mm

: The values in round brackets represent $\Delta F_{d,max}$ [%] following Eq. **(4.1). For instance, 14 (-21) means that the drawing force is 14 kN with a $\Delta F_{d,max}$ % of -21%.

Based on **Table 4.2** and **Figure 4.9**, the summation approach of the SPS is the closest to their experimental results because it considers the summation of the experimental drawing forces for each separate layer. Based on the Siebel theoretical estimation of F_d, higher deviation takes place. The deviation sources can be: 1) The assumed μ and η values, 2) These approaches assume homogenous monolithic sheet materials, not three-layered ones.

In addition to the evaluation of $F_{d,max}$ in **Table 4.2** and **Figure 4.9**, it is essential to examine applicability of those approaches for the whole drawing force–punch stroke progresses. **Figure 4.10-a)** presents the results for DD1 0.49/0/0 and DD1 0.49/0.6/0.49 at $\text{ß}_0 = 68/33$ and $F_{BH} = 15$ kN that are determined by:

1. Experiment.
2. Siebel general form.
3. The summation approach.

The force progress according to Siebel is very different at the beginning with the experimental ones for both the steel sheet and the SPS laminate. This is because the Siebel approach ignores the elastic deformation. However, the force progress according to the summation approach, that is based on the experimental F_d for each layer, presents good matching with the experimental data.

Figure 4.10-b) shows the dependence of $F_{d,max}$, on F_{BH}, obtained by experiment and by the Siebel approach for three examples: one monolithic steel and two SPS with 0.3 and 0.6 mm core thickness. Normally, with increasing the F_{BH}, the drawing force was expected to increase like what happened according to Siebel, but the experimental data showed no increase. Accordingly, the $F_{d,max}$ difference between the experimental and approximated results increased with increasing the F_{BH} for the SPS laminates.

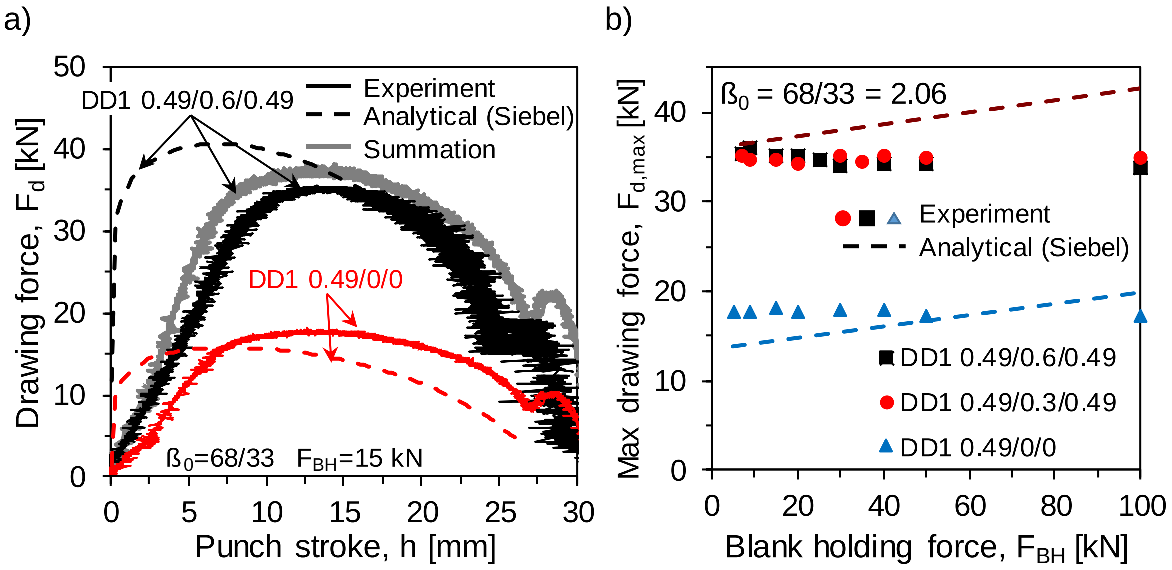

Figure 4.10: a) Comparing the drawing force progress based on two approaches (summation and Siebel) with the experimental ones and b) comparing $F_{d,max}$ at different F_{BH} obtained experimentally to the ones estimated by Siebel.

4.1.3.2. LDR prediction

Furthermore, the obtained LDR ($\text{ß}_{0,max}$) values from the experiments were compared with the ones estimated according to three analytical approaches [Lan95, Sat15], as described in Eqs. **(2.30)–(2.32)**. Normally, these approaches estimate the LDR of metallic sheets based on the friction coefficient (μ), deep drawing efficiency (η), average anisotropy (R) and strain hardening exponent (n). In **Figure 4.11**, the LDRs for different laminates are presented based on different skin/core layers' thicknesses and material properties using η = 0.7 and μ = 0.05 following [Lan95].

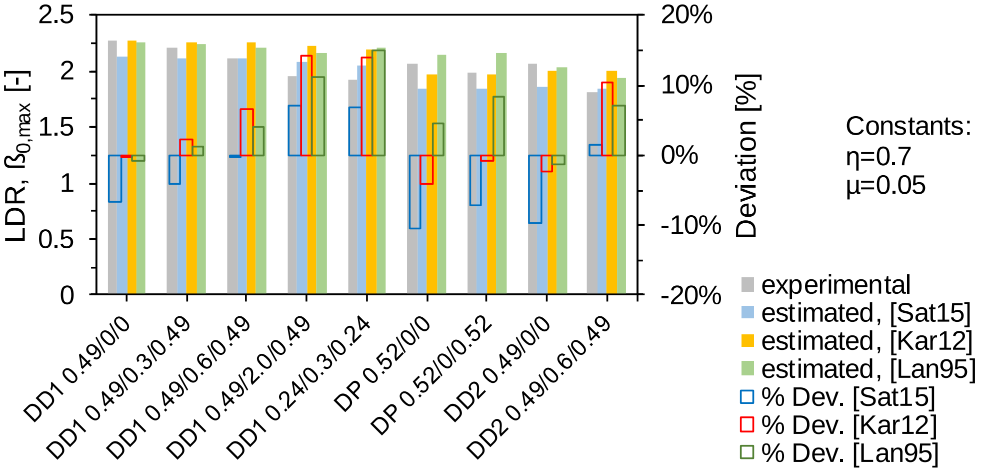

Figure 4.11: Experimental LDR values of some SPS compared to the calculated ones according to [Lan95, Sat15].

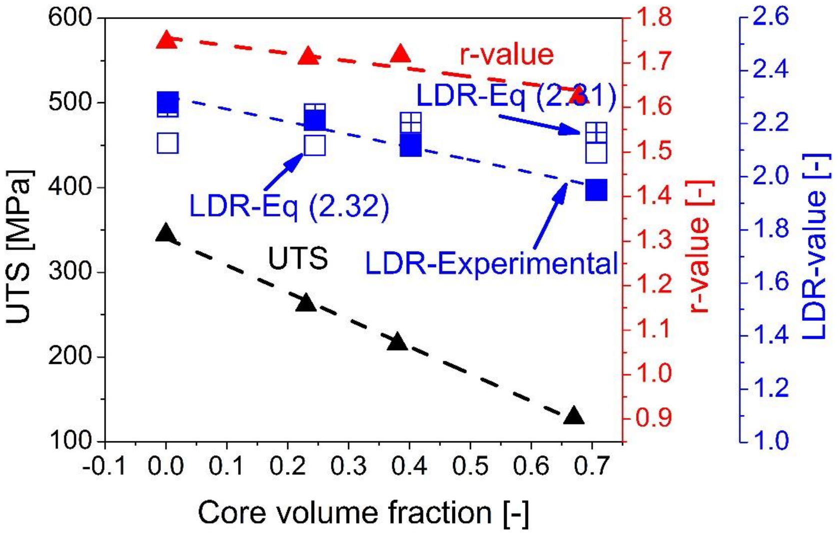

Figure 4.12: Correlating the mechanical properties of the DD1-laminates to the experimental and estimated LDR values according to [Lan95, Sat15].

The difference between the experimental and estimated results are expressed in terms of their LDR deviation (in %), as expressed in Eq. **(4.2)**. The results show a quite good agreement between the estimated and the experimental results with a deviation value ranging from -11% to 15%. Although these approaches are mainly applied for monolithic sheets, a deviation was found for the used monolithic steels.

$$\mathrm{LDR-Deviation}\ [\%] = 100 \cdot \frac{\mathrm{LDR_{estimated}} - \mathrm{LDR_{experiment}}}{\mathrm{LDR_{experiment}}} \qquad \textbf{(4.2)}$$

Furthermore, **Figure 4.13** shows a general correlation between LDR and the mechanical properties of DD-laminates at different core volume fractions. With increasing the contribution of the polymeric core up to 0.67, the strength of the SPS linearly following ROM decreases and additionally the r value. Accordingly, the LDR decrease. Comparing the experimental LDR values to the estimated ones according to Eq. **(2.31)** [Lan95] and Eq. **(2.32)** [Sat15], good agreement could be found up to a core volume fraction of about 0.5. Based on that, the previously mentioned approaches, initially for the metallic sheets, can be used for estimating LDR for the current multilayer formable sandwich laminates.

4.1.4. Stepwise drawing

In order to interpret the change of the deep drawability in terms of the skin/core thicknesses and therewith the skin sheet properties, development of the strain distribution over the skin sheets surfaces during deep drawing had been analysed through stepwise drawing. In general, five drawing steps were applied namely 5, 10, 15, 20 mm and finally complete drawing or until cracking at constant drawing ratio, i.e. $ß_0$ = 2.06 (68/33).

The force–displacement progress for the five drawing steps is exemplary illustrated in **Figure 4.13** for DD1 0.49/0.6/0.49. It can be stated that the curves of the drawing steps follow the one-step run. After studying the five-successive steps, there is a need to study the thickness reduction of the laminates layers by means of metallographic investigation and photogrammetrical ones at a certain common stage. This stage was chosen at the cup height that corresponds to the maximum drawing force, $F_{d,max}$. For $ß_0$ = 68/33, the cup height h for the fully-drawn step is ~ 26 mm matching the geometrical estimation in Eq. **(2.33)**. In addition, the $F_{d,max}$ was found in the third drawing step, i.e. at h = 15 mm, which means that the flange diameter D ~51.4 mm and accordingly D/D_0 equals = 51.4/68 = 0.76, which matches the empirical assumption in Eq. **(2.25)**, where $F_{d,max}$ takes place at D/D_0 ~ 0.77. Therefore, the cup height of 15 mm was chosen for the further investigations of evaluating the local strain distribution and thickness reduction.

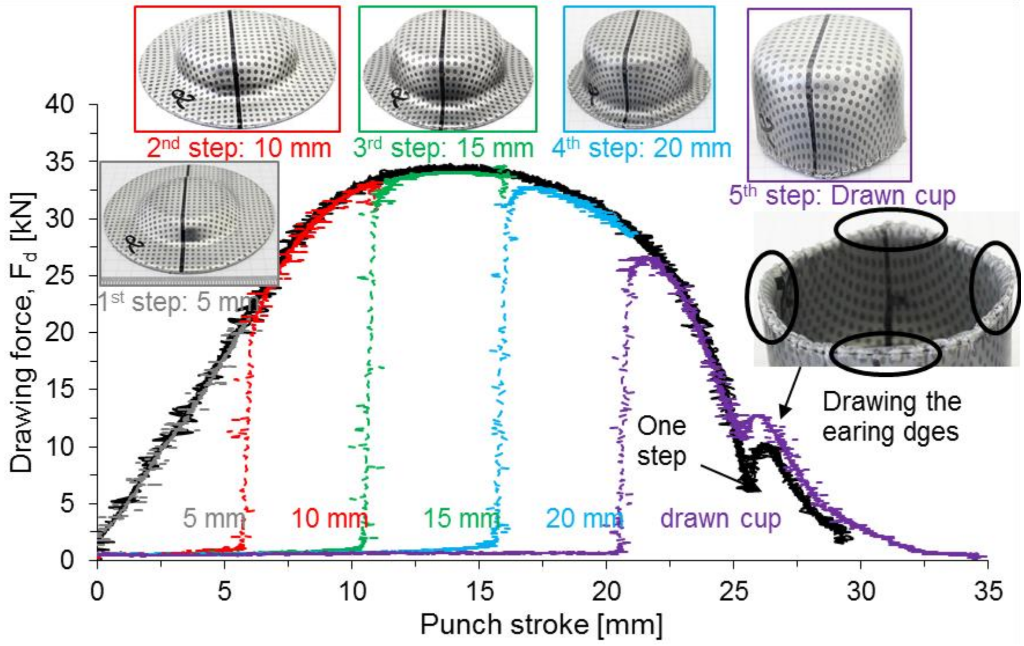

Figure 4.13: Punch force–displacement progress for the five drawing steps for DD1 0.49/0.6/0.49 in respect to the one-step drawing (black line).

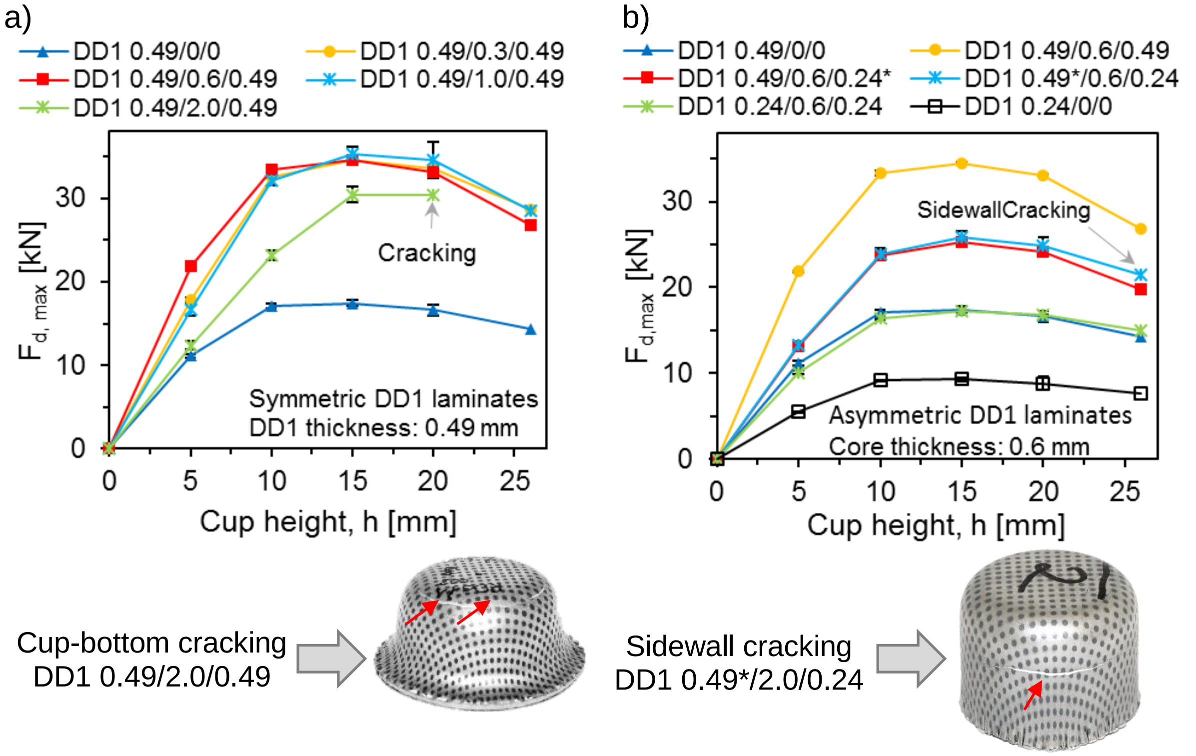

Figure 4.14. Drawing force in dependence on the cup height at varied: a) core thickness at constant skin sheet thickness (0.49 mm) and b) skin sheet stacking configuration at constant core thickness (0.6 mm). * refers to the skin sheet in contact with the punch (three specimens evaluated) [Har14a].

The $F_{d,max}$ at each drawing step is presented in terms of h in **Figure 4.14**. The effect of the core thickness on the drawing force at constant skin thickness of 0.49 mm is depicted in **Figure 4.14-a)**. No remarkable effect of the core thickness on the drawing force for the core thicknesses of 0.3, 0.6 and 1.0 mm at the five tested steps, i.e. until f_c of ~ 0.5 can be stated. However, for the thicker core of 2.0 mm, the drawing force decreases significantly as previously described in part 4.1.2. Additionally, the DD1 0.49/2.0/0.49 cracks in an earlier stage at a height h = 20 mm. Nevertheless, it can be stated that good drawability is expected up to 50 % core volume fraction.

The effect of varying the skin thickness and the stacking conditions with respect to the punch at a constant core thickness of 0.6 mm is shown in **Figure 4.14-b)**. The core thickness showed minor effects on $F_{d,max}$, i.e. the steel sheet DD1 0.49/0/0 required the same force like DD1 0.24/0.6/0.24 and, additionally, the thicker laminate (DD1 0.49/0.6/0.49) required as double as the DD1 0.24/0.6/0.24, as expected. Moreover, no remarkable differences in $F_{d,max}$ were found for the asymmetric DD1 laminates at the two possible stacking conditions: i.e. for DD1 0.49*/0.6/0.24 and DD1 0.49/0.6/0.24. Despite the similar $F_{d,max}$ of the two asymmetric laminates, the stacking of the skin/core layers affects the crack initiation on the outer skin sheets. When the thinner sheet (0.24 mm) is set to be the outer skin sheet (not in contact with the punch), cracking in the sidewall took place during the last drawing step (h > 20 mm), However the thicker one (0.49 mm) shows no cracking. It can be stated, that the laminate stacking and core thickness, up to $f_c = 0.5$, have an ignorable influence on F_d. However, the steel thickness and strength are the dominant factors.

The strains over the SPS, as well as the steel sheets (0.49 and 0.24 mm), were determined using photogrammetry for the successive drawing steps. Firstly, the major strain distribution over the outer and inner sides of the steel sheet DD1 0.49/0/0 is illustrated in **Figure 4.15** by the strain images and the radial section in RD (0°). The figure is divided into two parts; the left represents the outer side and the right for the inner one for the successive drawing steps. Although it is a mono-steel layer, each side behaves slightly different. Regarding the outer side: the maximum major strain is firstly occurred at the punch rounding at h = 5 mm and then gradually moves to the die rounding region (h ≥ 20 mm) through the sidewall (h = 10–15 mm). However, the maximum major strain values over the inner side are always located at the die rounding. As a result of the bending/unbending at the die corner, the inner side shows higher strain values due to the dominant tensile stresses. The strain distribution in the different direction in respect to the rolling direction is described in part: 4.1.5.2.

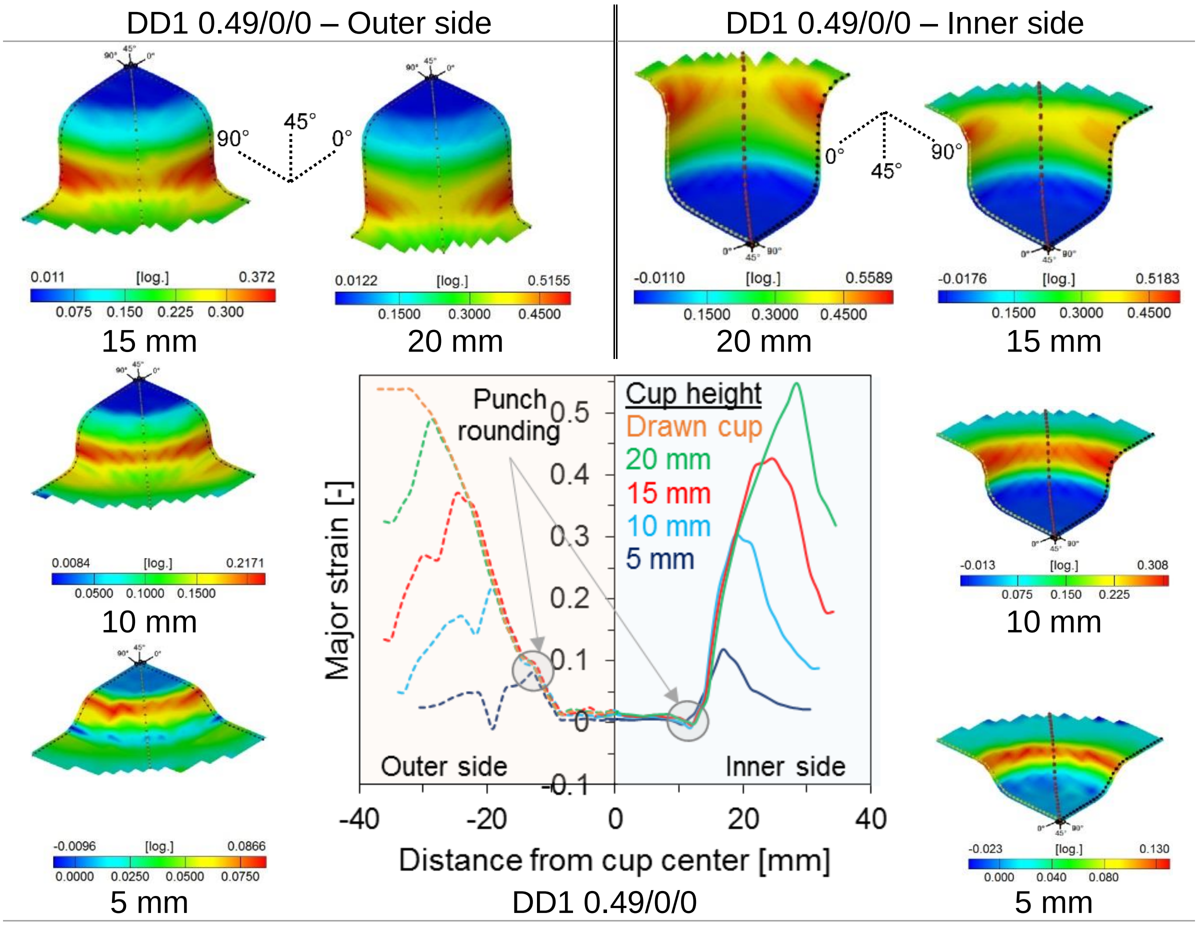

Figure 4.15: Major strain distribution over the outer (left side) and the inner sides (right side) of the monolithic steel sheet DD1 0.49/0/0 for a quarter of the cup.

The major strain distribution was even compared between two SPSs at different core thickness to interpret the tendency of thicker core SPS laminates to cracking. A comparison of the major strain distribution over the outer skin for DD1 0.49/0.6/0.49 and DD1 0.49/2.0/0.49 at the successive cup heights is shown in **Figure 4.16**. For the 0.6 mm core SPS, the maximum major strain is located firstly at the punch rounding and then moves to the direction of the die rounding. However, the maximum major strain value of the 2.0 mm core SPS is permanently located at the punch rounding, regardless the cup height, until cracking at h = 20 mm. It is also observed that the major strain at the die rounding region of DD1 0.49/0.6/0.49 is significantly higher than that of DD1 0.49/2.0/0.49, but this region is not critical as it is away from the failure condition.

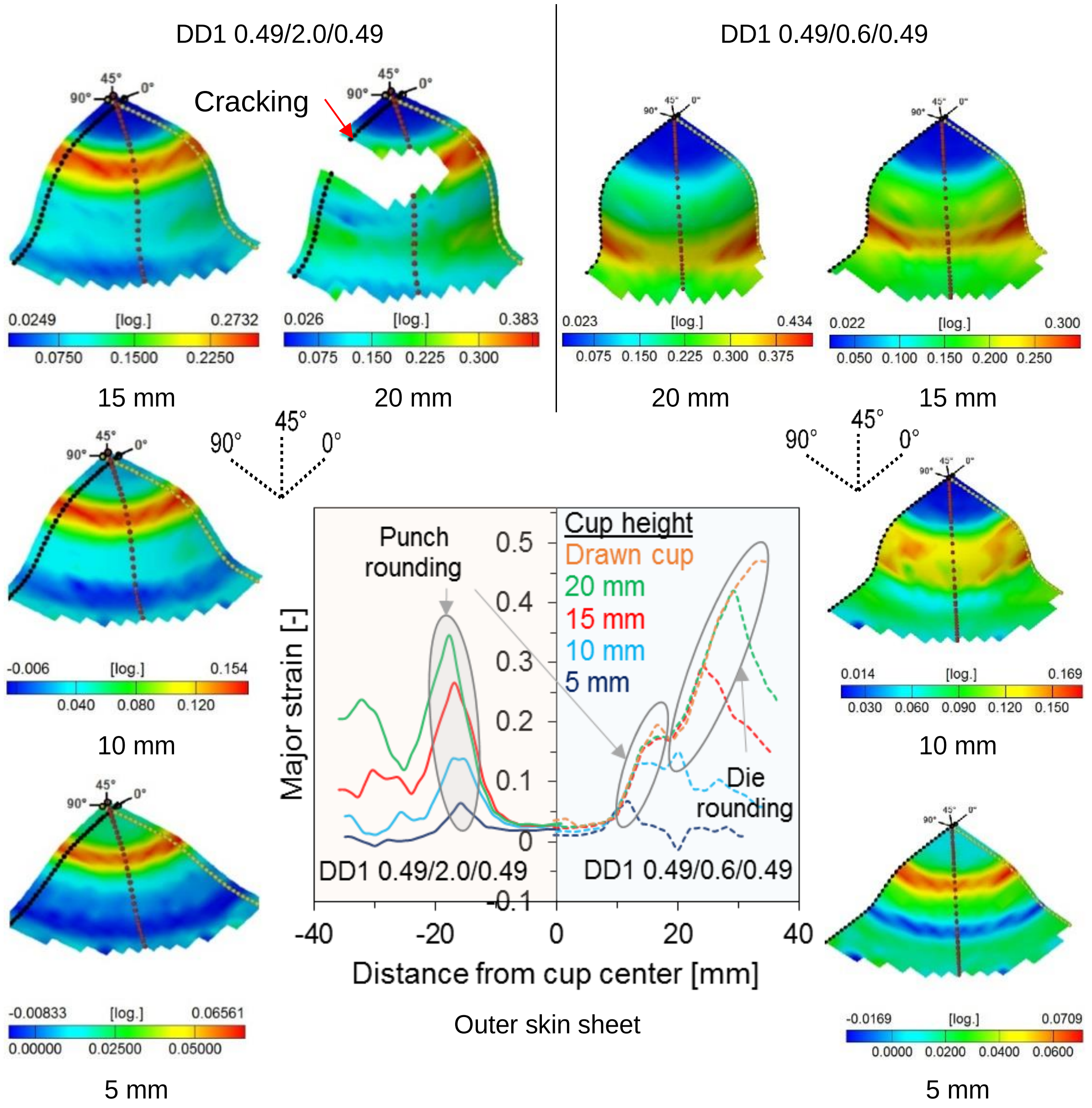

Figure 4.16: Major strain distribution over the outer skin sheet of two SPS at different core thickness: DD1 0.49/2.0/0.49 (left side) and DD1 0.49/0.6/0.49 (right side) at the successive cup heights for a quarter of the cup.

This significant difference can be clarified by comparing the thickness reduction progress in a radial section in RD (**Figure 4.17-a)**). The higher thickness reduction of the 2.0 mm core SPS can be attributed to the localized thinning of the thicker core at the punch rounding. The tendency of the cup regions to cracking can be determined by comparing the ε_1–ε_2 strain points over the outer skin sheet with the FLC curve of DD1 0.49/2.0/0.49 as shown in **Figure 4.17-b)**. The maximum major strain values at the punch rounding were additionally evaluated and compared to the lowest value of the FLC (%) following: $\Delta\varepsilon\% = 100.(\varepsilon_{SPS} - \varepsilon_{FLC})/\varepsilon_{FLC}$. The Δε% result in dependence with the cup height is presented in **Figure 4.18**. Negative Δε% indicates safe conditions where the strain values do not reach the critical FLC level. However, the positive ones mean that the FLC level is exceeded. These Δε% becomes more positive with increasing cup height. All the studied SPSs are safe until the complete drawing step up to a core thickness of 1.0 mm, i.e. 50% core volume fraction. It was found that only DD1 0.49/2.0/0.49 exceeded the FLC curve, which corresponds to the cracking case.

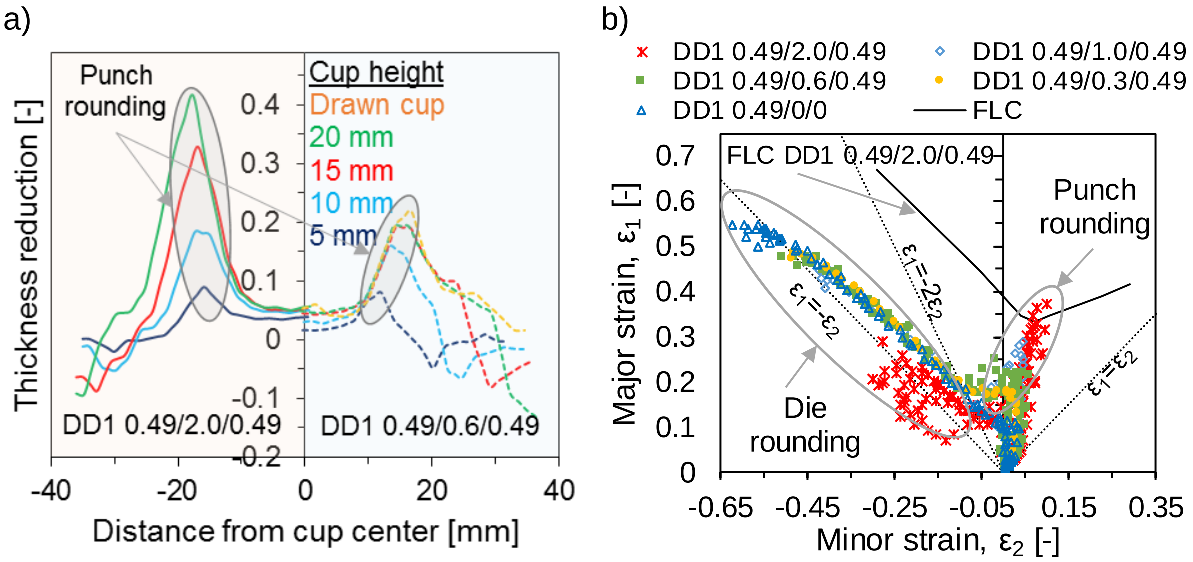

Figure 4.17: a) Comparison of the thickness reduction distribution over a radial section in RD at the successive cup heights for DD1 0.49/2.0/0.49 (left side) and DD1 0.49/2.0/0.49 (right side), b) overlapping the ε_1–ε_2 strain points at the different core thicknesses on the FLC at the last drawing step.

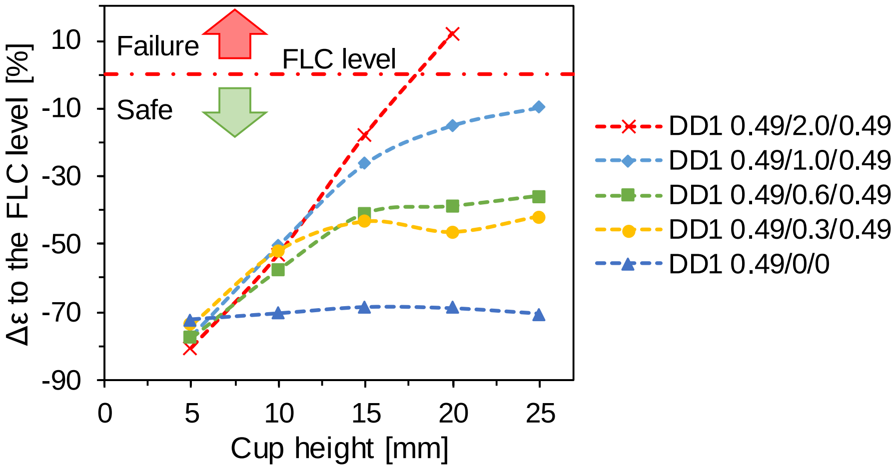

Figure 4.18: The extent of the maximum major strains at the punch rounding to the FLC level by means of Δε% in dependence on the cup height.

A comparison of the major strain distribution over the inner surface of the two SPS containing 0.6 and 2.0 mm core thick at the different cup heights is shown in **Figure 4.19**. The SPS with 0.6 mm core showed higher major strain at the die rounding. That is primarily correlated to the SPS thickness and strength that lead to using different drawing die dimensions and holding forces following Eq. **(2.23)** as given **Table 4.1**. For thinner sheets, smaller r_d are used, that can lead to increase the stain level at that radius comparing to thicker sheets following: $r_d = 0.035 \times [50 + (D_0 - d_0)] \times \sqrt{t}$ [Tsc77]. In this regard, the DD1 0.49/0.6/0.49 is drawn with lower r_d = 3.5 mm and higher F_{BH} = 15 kN compared to r_d = 5.5 mm and F_{BH} = 8 kN for the DD1 0.49/2.0/0.49 (**Table 4.1**). Nevertheless, failure is not expected to initiate in the inner skin sheet of the SPS laminate as can be shown in **Figure 4.20-a),** because the punch supports and stabilizes the inner skin and conveys the load to the outer skin through the core.

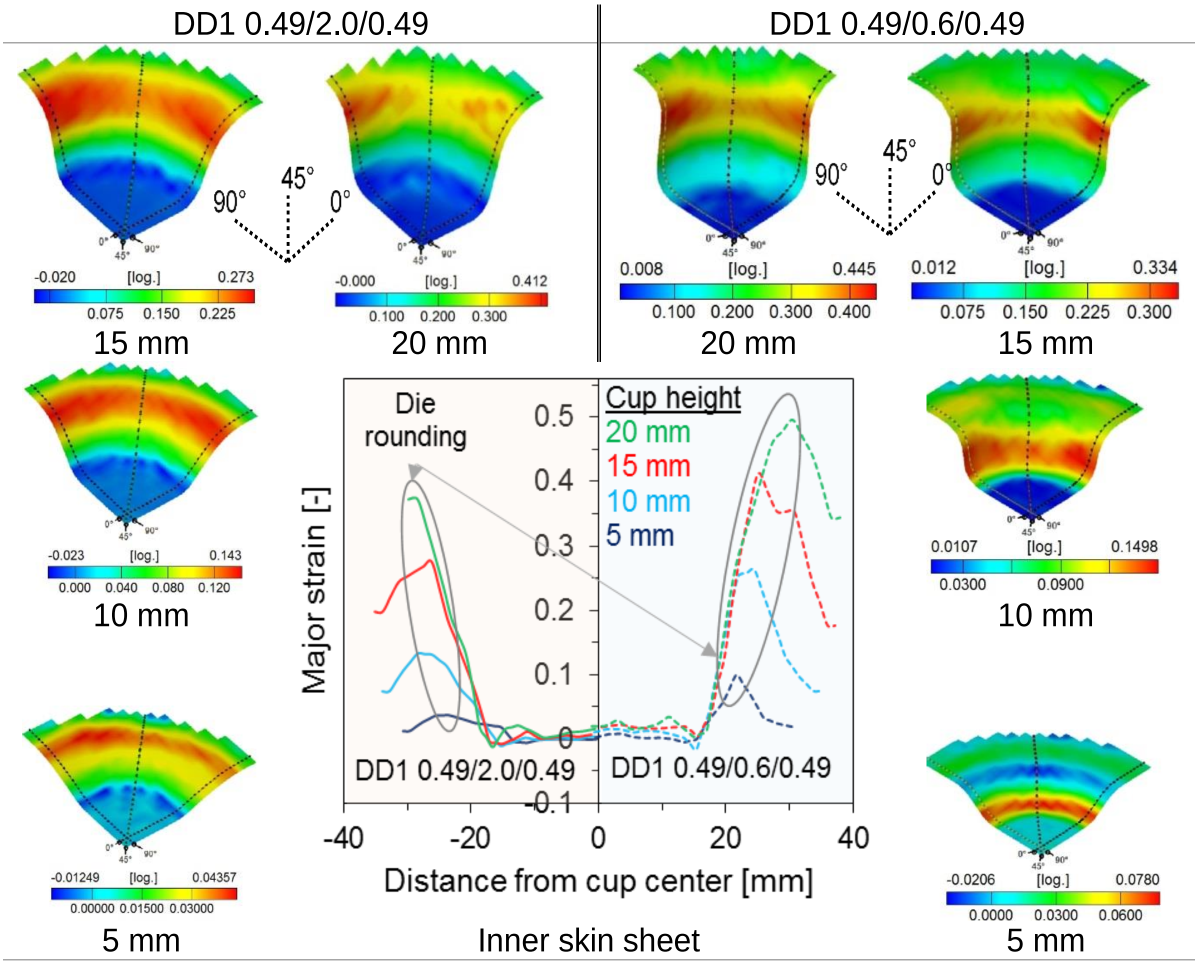

Figure 4.19: Comparison of the major strain distribution over the inner skin sheet between DD1 0.49/2.0/0.49 (left side) and DD1 0.49/0.6/0.49 (right side) for a quarter of the cup.

A comparison of the thickness reduction along a radial section in RD for the different core SPS is depicted in **Figure 4.20-b)** for the final drawing stage (either complete drawing or cracking). The thickness reduction path is affected significantly by the core thickness at constant skin thicknesses. The thicker is the core, the higher is the thickness reduction until cracking of the 2.0 mm core SPS is reached. The main difference is located at the punch rounding region where necking mostly takes place.

These findings were emphasized by the summary of the thickness reduction values for the varied core thicknesses at the successive drawing heights, as shown in **Figure 4.20-c)**. **Figure 4.20-d)** shows the effect of the SPS configuration in terms of the progress of the thickness reduction with a constant core thickness. When the thinner skin sheet is not in contact with the punch, a higher thickness reduction results and the SPS is prone to cracking at the cup sidewall. When the stacking is reversed, the outer thicker tends to crack later and still being under the safe forming conditions. It can be stated that the best stacking condition for different skin thicknesses is to position the thicker sheet at the outer layer if the forming limits should be maximized.

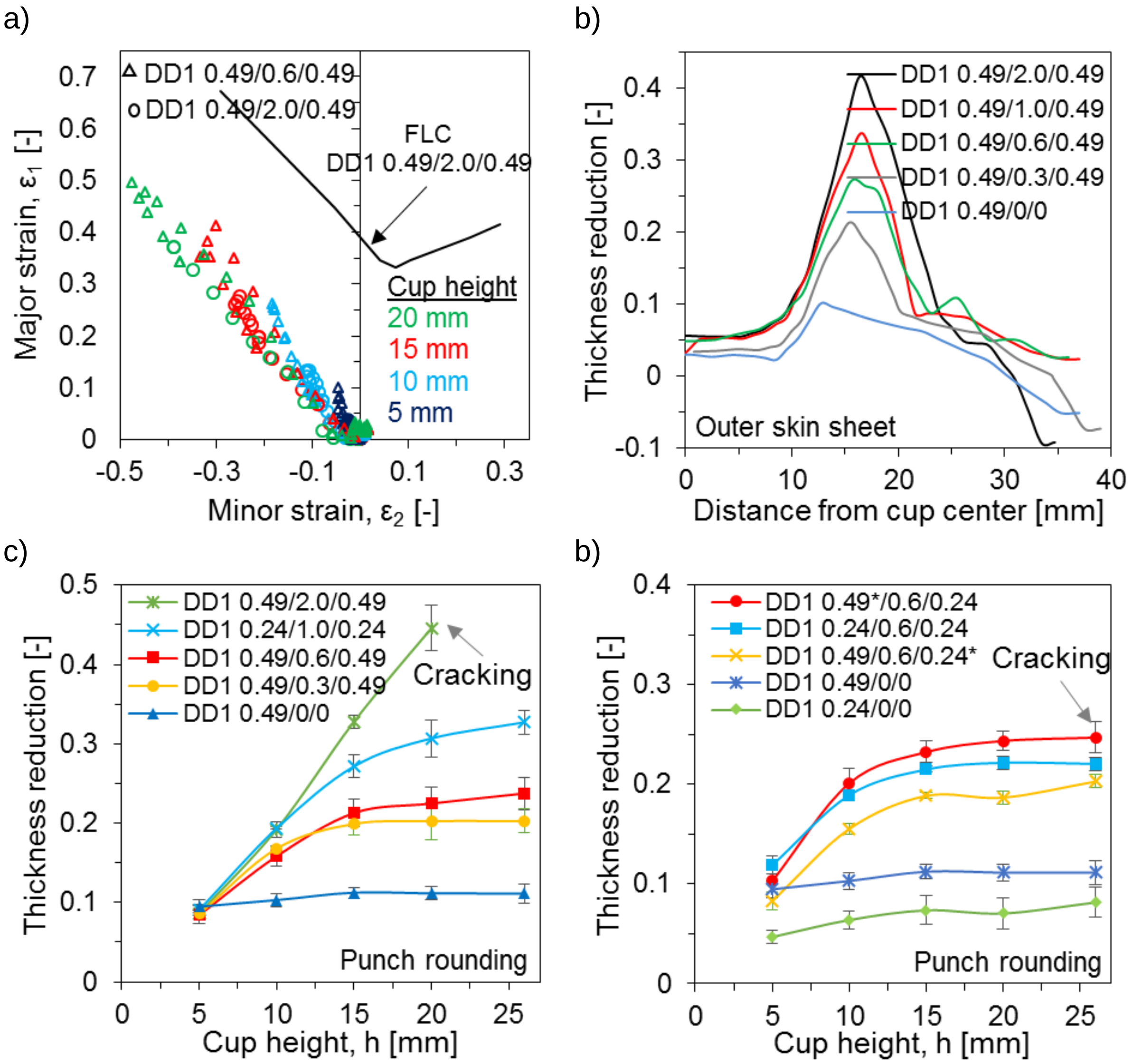

Figure 4.20. a) ε_1–ε_2 strain points over the inner skin at core thicknesses 0.6 and 2.0 mm in respect to the FLC at the different cup heights, b) comparison of the thickness reduction over the radial section in RD at the last drawing step obtained by photogrammetry and c) summary of the maximum thickness reduction obtained at the punch corner rounding for all drawing steps and d) the effect of the SPS configuration at constant core thickness of 0.6 mm.

4.1.5. Strain analysis

The aim of this part is to investigate the effect of the SPS symmetry and mechanical properties, as listed in **Table 3.5**, on the surface strains obtained by photogrammetry. In this context, a certain drawing ratio and cup height were selected to perform the deep drawing, i.e. $ß_0 = 2.06$ (68/33) at h = 15 mm. At this cup height, the $F_{d,max}$ is reached and most of the tested materials exhibit no cracking. After drawing, the strain distribution – especially the thickness reduction – is evaluated in a radial section in RD. The 15-mm cup was then prepared for metallographic investigations by LOM in order to measure the thickness reduction along the same section measured before by photogrammetry. The cup was fixed in a transparent epoxy resin, left for curing, cut in RD, captured with LOM and finally the single layers were measured. The advantage of metallographic method is to evaluate the thickness reduction of the core layer, which cannot be reached by photogrammetric investigation. The strain analysis is performed for the materials following the proposed scaling approach as a systematic methodology for the desired fundamental correlations.

4.1.5.1. Monolithic steels

Firstly, the strain and thinning distribution of the monolithic steels – obtained by photogrammetry – at h = 15 mm over a section in RD is shown in **Figure 4.21**. **Figure 4.21-a)** shows the (ε_1–ε_2) strain points for the outer surface of the five steel sheets used in the study. This distribution can be correlated to their mechanical properties (part 3.4.4) to interpret their affinity to stretching or thinning. At the die rounding, where the tensile stresses are dominating, the major strain value can be directly correlated to the n value; this is depicted in **Figure 4.21-b)**. With higher n value, the tendency to straining of the different steels is lower at the same cup height. Based on that, the DD2 grade is strained much higher than the other grades and the SS grade was the lowest. Between the DD2 and SS grades, the DD1 and DP are located due to their moderate n value.

However, the thickness reduction distribution over the same section shows that the highest reduction values are located at the punch edge rounding (**Figure 4.21-c)**), where the plane strain condition is dominant. It was found that, the SS grade show the highest thinning tendency. However, the high n value of the SS grade can delay its failure. The other steels exhibit approximately equal stretching behaviour as they possess r value ≥ 1. This result can be correlated or rather confirmed with the r values ($\varepsilon_w/\varepsilon_t$) as shown in **Figure 4.21-d)**

Furthermore, the distribution of the major and minor strain distribution over the inner surfaces of the steel sheets are depicted in **Figure 8.1-a)**, which show the same order as for the outer ones. Additionally, the comparison of the strains over the inner and outer surfaces are depicted in **Figure 8.1-b)** for SS 0.5/0/0: the minor strain progress in the inner and the outer sides is quite the same. However, the major strain is different: at the punch edge, the outer layer shows higher strains but at the die edge, the inner skin shows higher major strains due to the difference in tensile stresses acting on both sides. The 3D strain images of the 15 mm drawn cups of the steels are shown in **Figure 8.1-c)**. It was difficult to normalize the legend bar of the outer and inner surface strain images due to the significant strain differences. However, it was normalized for all the inner and outer surfaces separately.

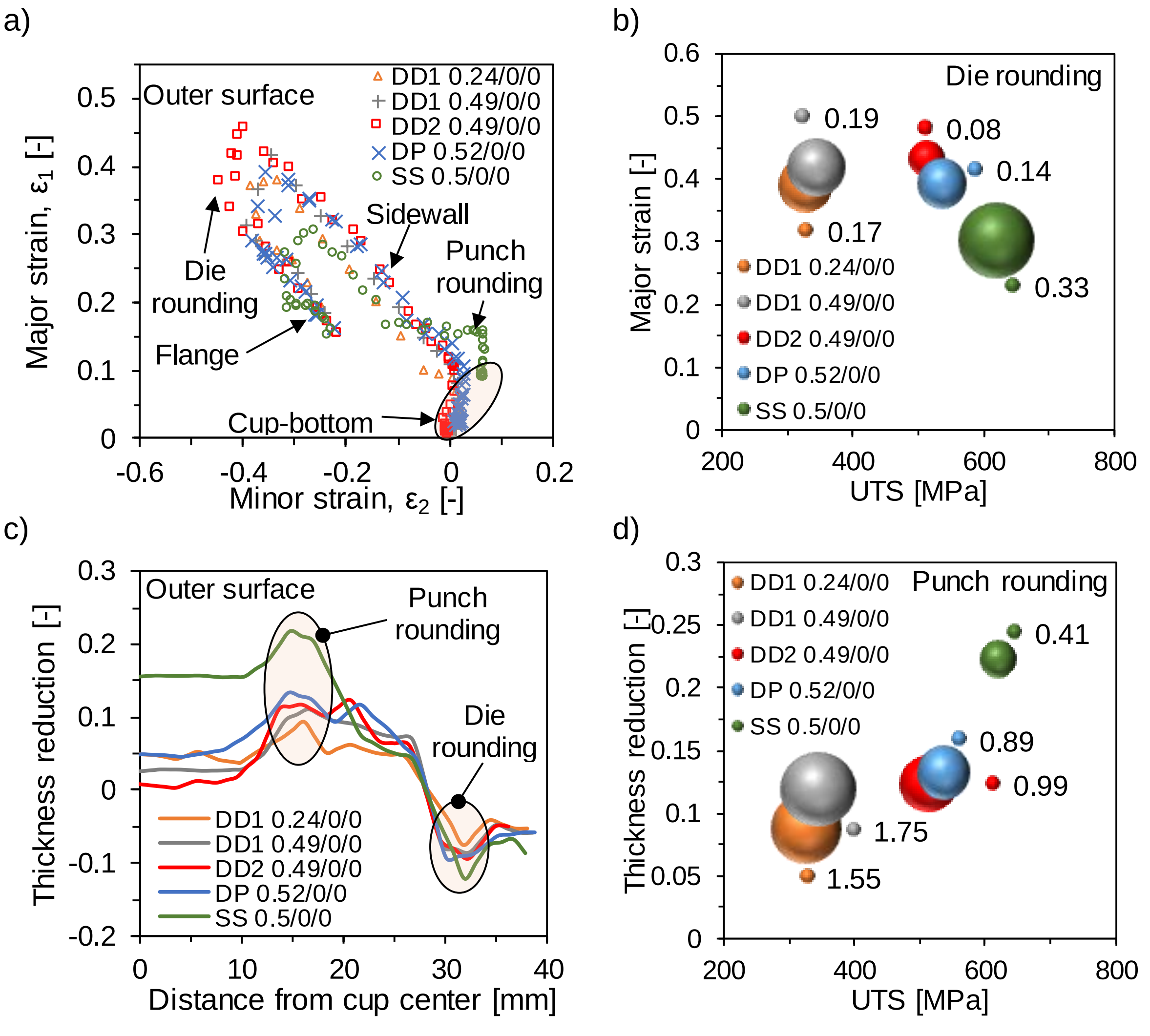

Figure 4.21: a) Major–minor strain distributions over a section in RD of the outer surface and b) a correlation of the maximum major strain the die rounding with the n and UTS values of the different mono-steel sheets (the balloon size and label correspond to the n value), in addition to c) the thickness reduction over the same section and d) the correlation of the maximum thickness reduction values at the punch rounding with the r and UTS values (the balloon size and label correspond to the r value).

4.1.5.2. Anisotropy evaluation

Evaluating the anisotropic strain behaviour over the drawn cups as a result of the mechanical anisotropy, determined earlier in part 3.4.2, is necessary for predicting the flow behaviour and the subsequent failure conditions. Additionally, to examine whether the anisotropy of the monolithic steel sheets is affected by creating the SPS under deep drawing. **Figure 4.22** depicts the major strain distribution in the three radial sections 0°, 45° and 90° respect to RD for two steel grades and their SPS laminates namely the SS and DD1 (0.49 mm) and a further example is shown for the DD1 (0.24 mm) in **Figure 8.2**.

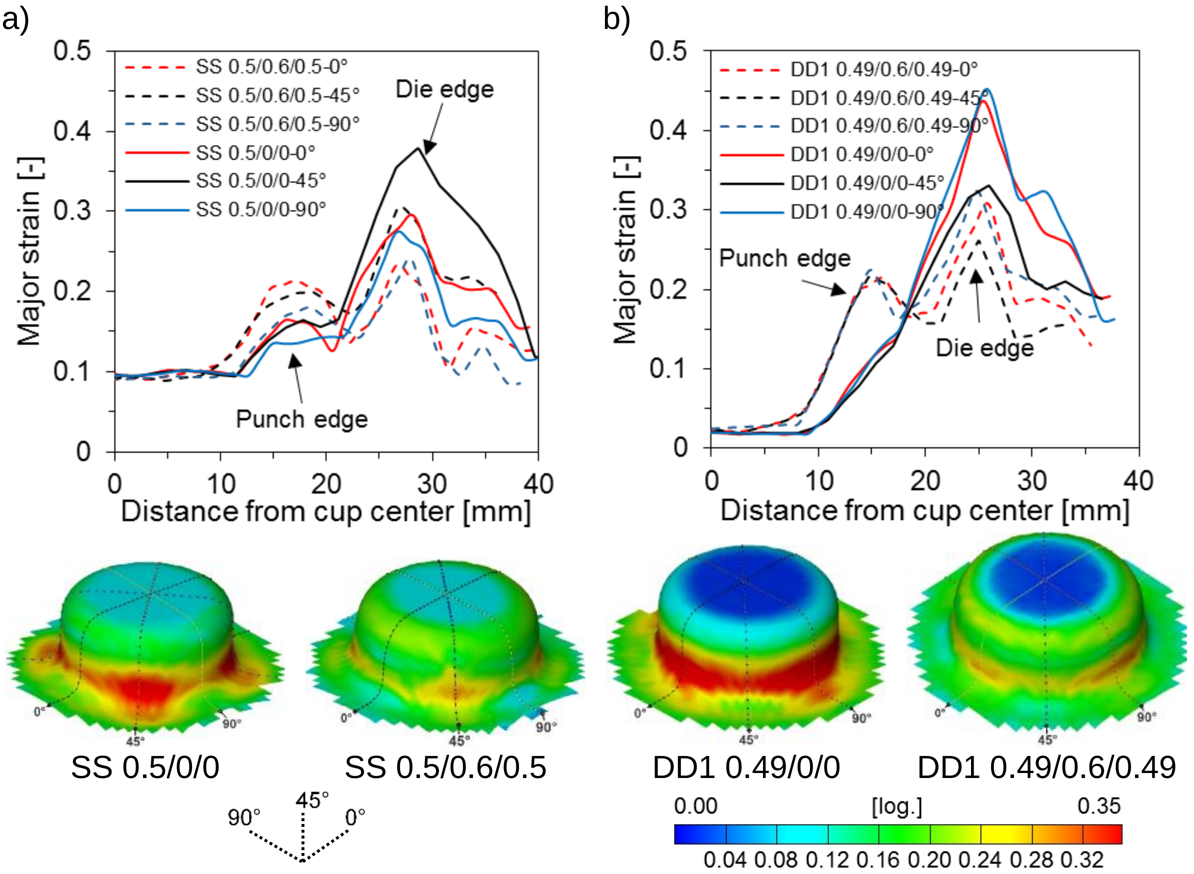

Figure 4.22: Anisotropic major strain distribution of the steel sheets and their SPS in 0°, 45° and 90° to RD with their strain images at h = 15 mm for: a) SS (0.5 mm), b) DD1 (0.49 mm) and c) DD1 (0.24 mm) grades.

For the SS grade, it can be observed that the 0° and 45° directions exhibit higher strain values than the 90° one at the die edge. This is simply correlated to the mechanical properties: the 90° direction has the highest strength and strengthening properties. As expected, the same effect is dominating for the SS 0.5/0.6/0.5 laminate. Moreover, the SPS exhibited higher strains at the punch edge than the steel sheets. For the SPS, the 0° direction showed the highest strain levels at the punch edge i.e. cracking is more probable in this direction, which was confirmed by experiments. The DD1 grade (0.49 mm) shows a different behaviour, where the 0° and 90° are similar and show higher strain than the 45° one. On the other side, the DD1 (0.24 mm) showed most likely isotropic behaviour as well as its SPS (DD1 0.24/0.3/0.24). It can be stated that the anisotropic behaviour of the symmetric SPS remains the same as their original steel sheets. However, the strain distribution is different along the radial sections; it increased at the punch edge and decreased at the die edge due to the reduced strengthening behaviour of the SPS.

4.1.5.3. Effect of the metal/polymer adhesion

Figure 4.23 shows the effect of the adhesion between the layers in the three-layered SPS on the strain distribution at h = 15 mm. The unjoined SPS are composed of two DD1 0.49 mm skin sheets (inner and outer) and 0.6 mm core layer without an adhesive agent. Therefore, each of outer and inner skin sheets has two surfaces (inner and outer) that can be evaluated by photogrammetry. In this case, the dot-pattern was introduced on all metallic surfaces. **Figure 4.23-a)** shows a schematic illustration of the different surfaces in the unjoined SPS.

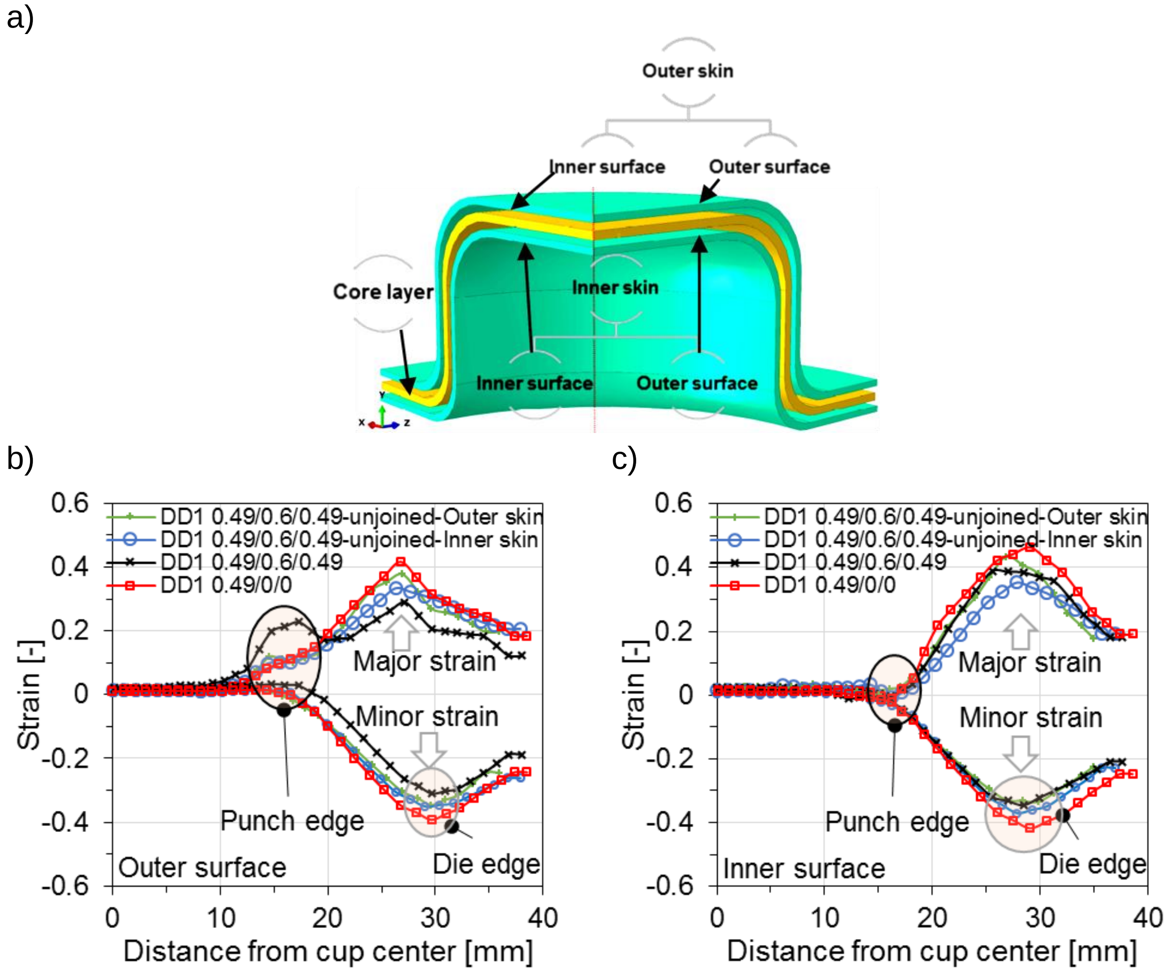

Figure 4.23: Effect of the adhesion between the SPS layers on the strain distribution of the different surfaces at h = 15 mm as illustrated in a) compared to their steel sheets and the joined SPS over the b) outer and c) inner surfaces.

The major strain distribution over the outer surface of the inner and outer skin sheets are shown by means of radial sections in **Figure 4.23-b)** and **-c)** and images in **Figure 8.3**. At the punch edge, the two skin sheets of the unjoined SPS behave like the monolithic steel. However, at the die edge, the unjoined SPS skin sheets shows lower strains than the monolithic steel sheet (DD1 0.49/0/0), where the skin sheets are free to shear and additionally the unjoined core layer acts as an extra lubrication foil between them. When comparing the joined SPS to the unjoined one, the outer surface of the joined SPS exhibits higher strain at the punch edge. In the case of the joined SPS, the SPS behaves as a joint 1.6 mm thick sheet due to the enough interlaminar shear stress between the SPS layers which hinders the delamination. Accordingly, the joined SPS is more susceptible to cracking. The same order can be found for the major and minor strains over the inner skin surfaces (**Figure 4.23-b)**).

4.1.5.4. Effect of the core thickness

In this part, the thickness measurements were carried out basically with metallographic methods by LOM of the DD1-laminates at h = 15 mm. in this case, one direction to RD was evaluated, i.e. the 0° one. Assuming the symmetry of the used circular cup in respect to its center over this section, half sections were metallographically prepared and evaluated as shown in **Figure 4.24-a)**. Different core thicknesses (0–2.0 mm) were considered with the DD1 (0.49 mm) grade. The total thickness of the SPS layers is presented in **Figure 4.24-b)** by summing the measured thickness of each layer.

The thickness reduction of the SPSs in dependence on the core thickness can be described based on the different regions of the cup. In the cup-bottom: the SPSs and the steel show insignificant thinning region: a thickness reduction of about 0.04 can be reached as a result of the biaxial stretching. At the punch edge: the thinning becomes significant due to the plane strain conditions. Moreover, the extent of the thinning at the punch edge is dependent on the core thickness. For the monolithic steel sheet, slight thickness variation over the different cup regions ca be observed: a thickness reduction of ~ 0.05 can be reached. On the contrary, the SPS show significant thickness variation: the higher the core thickness is, the higher is the thinning tendency at the punch edge, even in monolithic steel sheet. For instance, a thickness reduction of ~ 0.75 mm took place for the DD1 0.49/2.0/0.49, see **Figure 4.24-b)**. Furthermore, the die edge zone shows lower thinning values than the punch edge, where drawing conditions are dominating. The flange regions show a thickening where a thickness reduction of -0.05 can be reached. This thickness behaviour is already described in the literature [Alt12].

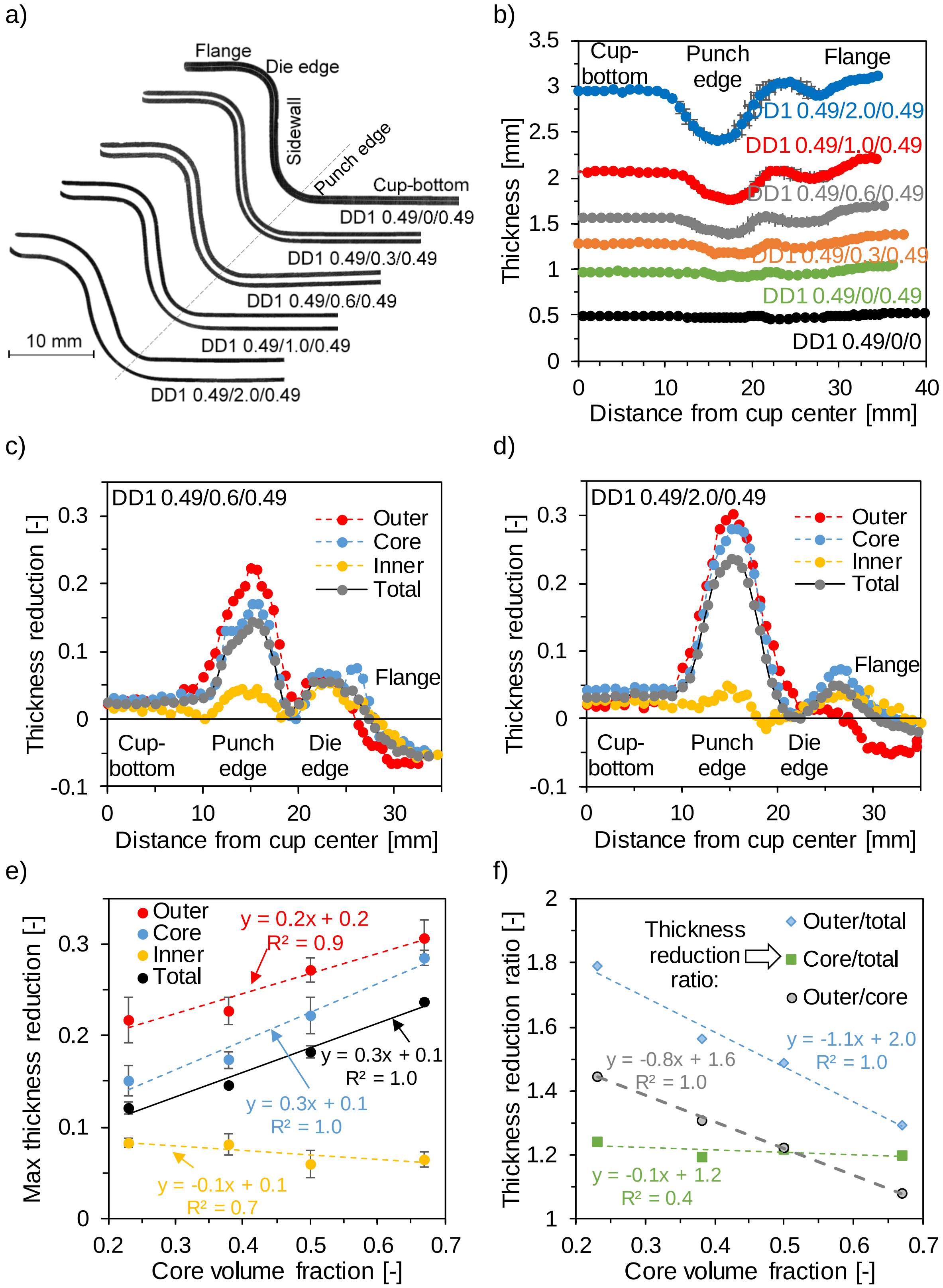

Figure 4.24: a) Metallographic cup sections in RD for the DD1-laminates at h = 15 mm, b) their the total thicknesses, in addition to two examples showing the thickness reduction progress in the inner, outer, core layers and total values for c) 0.6 mm and d) 2.0 mm core thicknesses measured by metallography and correlating the core volume fraction to e) the maximum thickness reduction at the punch rounding and f) thickness reduction ratios.

Figure 4.24-c) and **-d)** depict a comparison of the thickness reduction progress of each layer of the SPS (the outer, core and inner layers in addition to the total reduction) for two core thicknesses, i.e. 0.6 and 2.0 mm to show the relative behaviour of the layers and their contribution in the total thickness reduction. In both cases, the outer skin sheet shows the highest thinning behaviour, then the core layer and the least thinning occurred for the inner skin sheet.

Based on the section evaluation, the maximum thickness reduction at the punch edge was chosen to characterize the differences between the SPSs, as presented in **Figure 4.24-e)**. Regardless the core thickness, the inner skin sheet shows the same thickness reduction progress. However, a linear trendline describing the increase of the thickness reduction of the core and outer layers can be stated. The gradient of these trendlines (core and outer layers) are slightly different: the core layer tends to thin with a higher rate than the outer one. Based on the thinning of the three layers, a direct linear proportion of the total thickness reduction in dependence on the core volume fraction or rather the core thickness is given.

The correlation between the thickness reduction of the single SPS layers in respect to the core volume fraction is depicted in **Figure 4.24-f)**. With higher core volume fraction, the ratio between the thickness reduction of the core to the total one (core/total) remains unchanged i.e. the tendency of the SPS to thinning is the same as of the core layer. However, the thickness reduction ratio of the outer layer to the total SPS (outer/total) is linearly reduced. Likely is the behaviour of the outer/core thickness reduction ratio.

Based on the scaling approach proposed in **Figure 3.3**, a comparison between the major strain distribution over the outer surfaces of the sheet metal laminates (steel/resin/steel) with the monolithic steels and the SPS with 0.6 mm core thickness, i.e. steel/polymer/steel is shown in **Figure 8.4**. The tendency to failure is higher in the case of the SPS, however the probability of the interlaminar shearing and delamination in the sheet metal laminates is significant, as described previously in [Buh14].

4.1.5.5. Effect of the symmetry and the number of layers

The effect of the number of layers and the symmetry of the DD1-laminates on the strain distribution under deep drawing at h = 15 mm is depicted through the metallographic section in **Figure 8.5**. In general, the thickness of the SPS layers is fairly the same except at the punch edge, where remarkable thickness reduction took place, see **Figure 4.25**. Additionally, no delamination took place even for the five-layered laminates in the flange regions, where thickening of the core normally occurs due to the polymer flow-out effect.

Furthermore, **Figure 4.25** depicts the thickness reduction distribution over some asymmetric SPSs determined by photogrammetry. Because the five-layered SPS are thicker than the other asymmetric three-layered ones, i.e. 1.57 mm (DD1 0.49/0.3/0.24/0.3/0.24) vs. 1.35 mm (DD1 0.49/0.6/0.24) or 1.03 mm (DD1 0.49/0.3/0.24), higher thickness reduction at the punch edge took place. Moreover, by comparing the five-layered SPS, when the thicker steel sheet in contact with the punch, the thinner one on the other side exhibits higher thickness reduction. This occurred for the asymmetric three-layered SPS, as well.

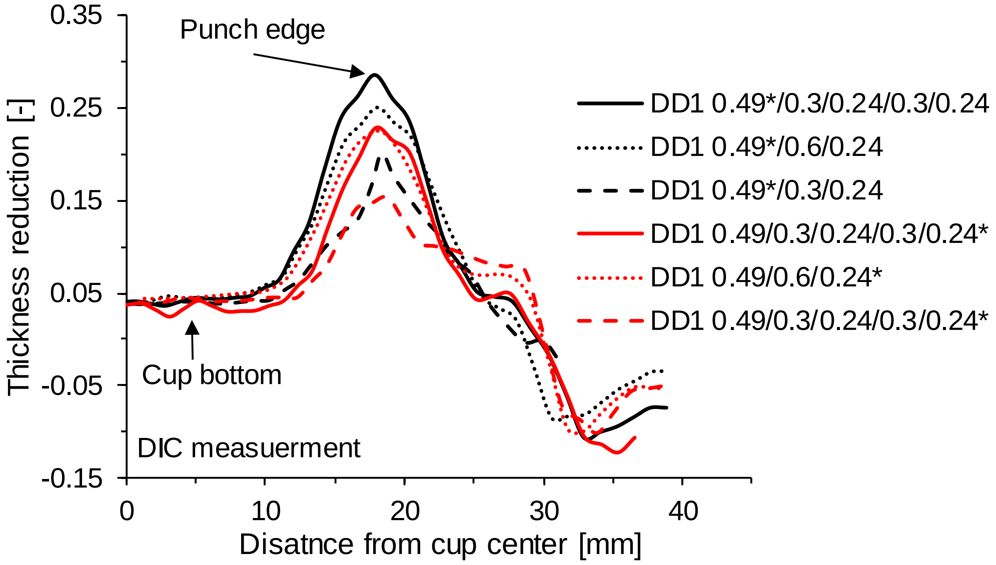

Figure 4.25: Effect of the SPS symmetry and the number of on the thickness reduction determined by photogrammetry. *: refers to the skin sheet in contact with the punch.

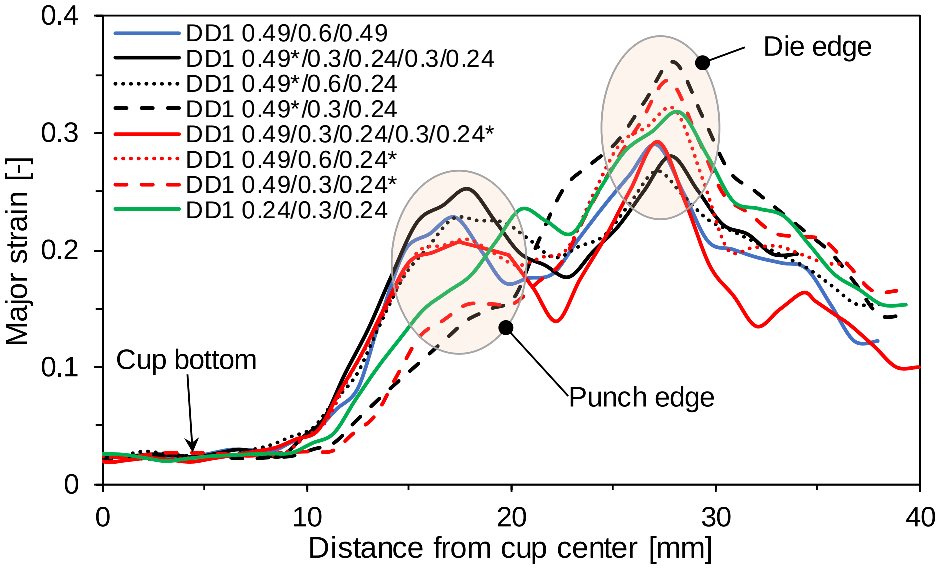

Figure 4.26: Major strain distribution for the drawn cups shown in **Figure 8.6** showing the effect of the symmetry and number of layers determined by photogrammetry. *: refers to the skin sheet in contact with the punch.

The major strain distribution confirms this tendency, as shown in **Figure 4.26**, where the major strain is higher at the punch edge, which indicates higher cracking probabilities. Furthermore, if the thickness of the five-layer SPS (1.57 mm: DD1 0.49/0.3/0.24/0.24/0.24) is the same as the three-layered one (1.58 mm: DD1 0.49/0.6/0.49), the major strain progress is very close if the thicker skin sheet 0.49 mm is the outer one, i.e. DD1 0.49/0.3/0.24/0.24/0.24*. The effect of the core thickness in the asymmetric SPS is the same as for the symmetric ones, as shown in **Figure 4.26**. This can be seen by comparing DD1 0.49/0.3/0.24 with DD1 0.49/0.6/0.3, where the major strain at the punch edge increased from 0.15 up to 0.2.

The first example showing the effect of different asymmetric SPS containing dissimilar steel skin sheets on the strain distribution is exhibited in **Figure 4.27**.

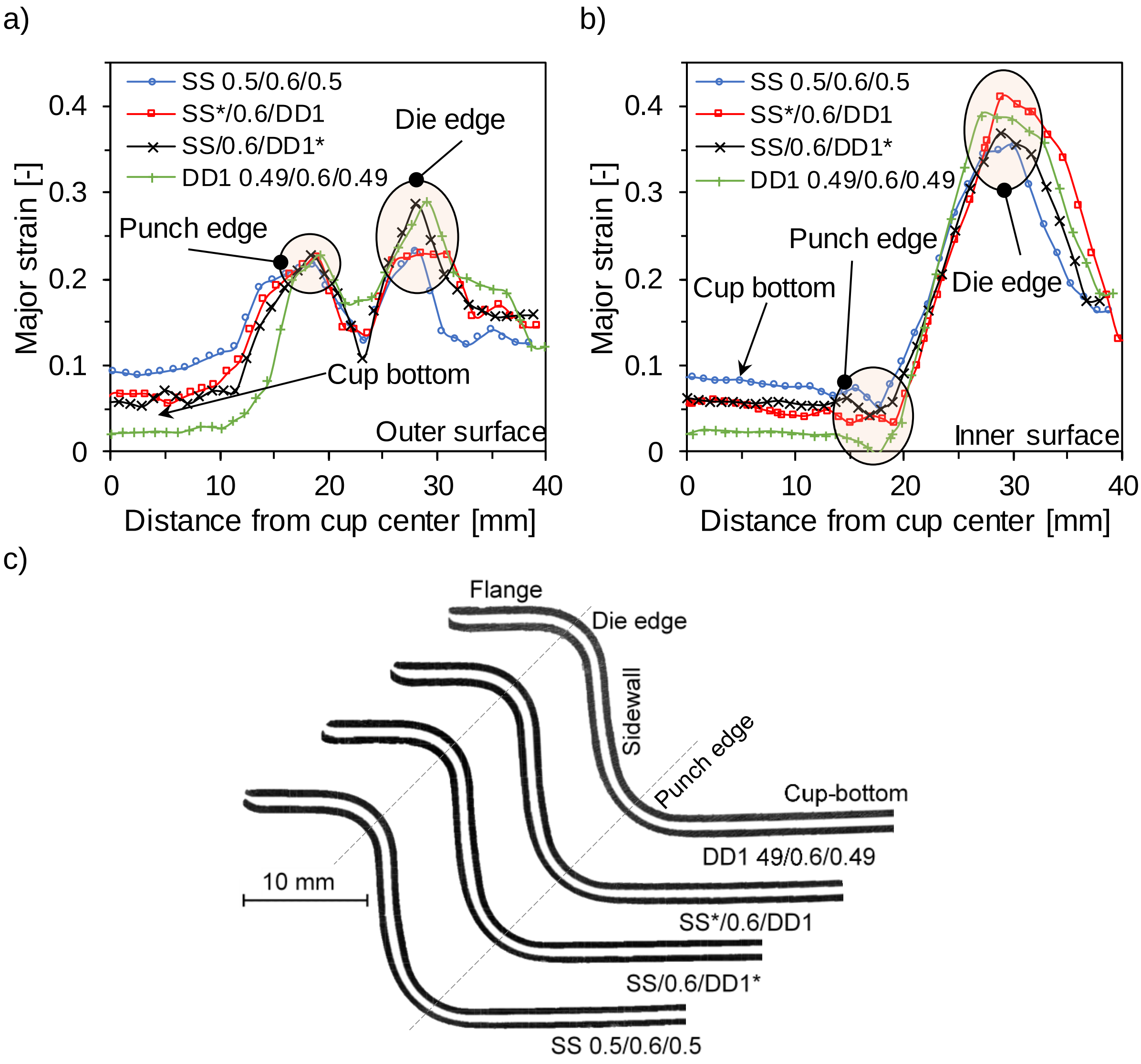

Figure 4.27: Effect of the SPS symmetry based on SS and DD1 steel grades on the major strain distribution in the a) outer and b) inner surfaces in addition to c) their metallographic cross sections at h = 15 mm. *: refers to the skin sheet in contact with the punch.

In this case, the SS is combined with the DD1 grade. In this figure, four SPS combinations are presented: two symmetric SPS and two asymmetric ones. The advantage of coupling these two steels together, is to provide better corrosion resistance in the side of the SS-grade and the other side of the DD1 grade provides the formability and reduce the material cost. The difference in the major strain distribution is clear in the cup-bottom region. The SS-based SPS laminates exhibited higher strain values due to the lower r value of the monolithic SS-steel sheet as discussed in part 3.4.4. This difference is observed for the outer and inner skin sheets, as depicted in **Figure 4.27-a)** and **-b)**, respectively. The strain path for both the asymmetric SPS laminates are located between the symmetric ones, which confirm the mechanical properties. Furthermore, the corresponding photogrammetric images of the asymmetric SPS containing SS and DD1 are depicted in **Figure 8.7** for the outer and inner surfaces, respectively. Additionally, the metallographic sections in **Figure 4.27-c)** show drawn cups free of defects, regardless the combined steel skin sheets.

The advantage of coupling different steel grades becomes clear analysing the combination of DD2 grade with the DD1 one. The DD2 grade exhibits a higher strength but a limited forming potential. Also, the tailored SPS stacking plays an important role to overcome the reduced formability of the DD2. The deep drawability of the DD2 based SPS is poor failing at h ~ 8 mm. Replacing one DD2 skin sheet by a DD1 one of same thickness, the formability was significantly improved, as shown in **Figure 4.28** and **Figure 8.8**. When the DD1 was located in contact with the punch (DD2/0.6/DD1*), the cup height was improved to reach $h \approx 11$ mm. Therefore, a drawing step – before cracking – was chosen for further investigations to match all the DD2 based SPS, i.e. at h = 5 mm. However, when the DD2 was in contact with the punch, i.e. DD2*/0.6/DD1, completely drawn cups could be reached. These results can be further interpreted from major strain sections shown in **Figure 4.28** at h = 5 mm. In the case of DD2 being the outer skin sheet (the symmetric DD2 0.49/0.6/0.49 and the asymmetric DD2/0.6/DD1*), the major strain progresses are very similar. However, in the case of the DD1 as the outer sheet (the symmetric DD1 0.49/0.6/0.49 and the asymmetric DD2*/0.6/DD1 SPS), higher strains can be reached over the outer and inner surfaces and therewith a higher cup height of 15 mm.

The coupling of the DD1 and DP is shown in **Figure 4.29**. In this case, the DP possesses higher strength than the DD1. However, its formability with r = 1, n = 1.15 is good enough but less than that of the DD1 one. Therefore, the asymmetric SPS based on them showed good forming potential and ignorable differences appeared. Higher strain results when the DP is located as the outer skin sheet, as shown in **Figure 4.29** and **Figure 8.9** for the outer surface. However, the inner surface is fairly similar for both asymmetric combinations.

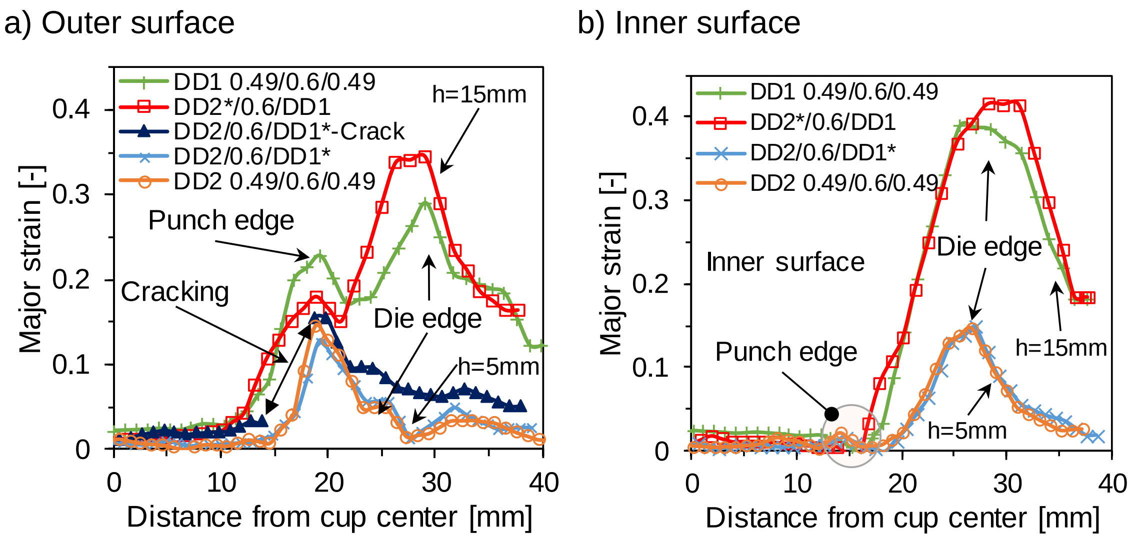

Figure 4.28: Effect of the SPS symmetry based on DD2 and DD1 steel grades on the major strain progresses of the a) outer and b) inner surfaces. *: refers to the skin sheet in contact with the punch.

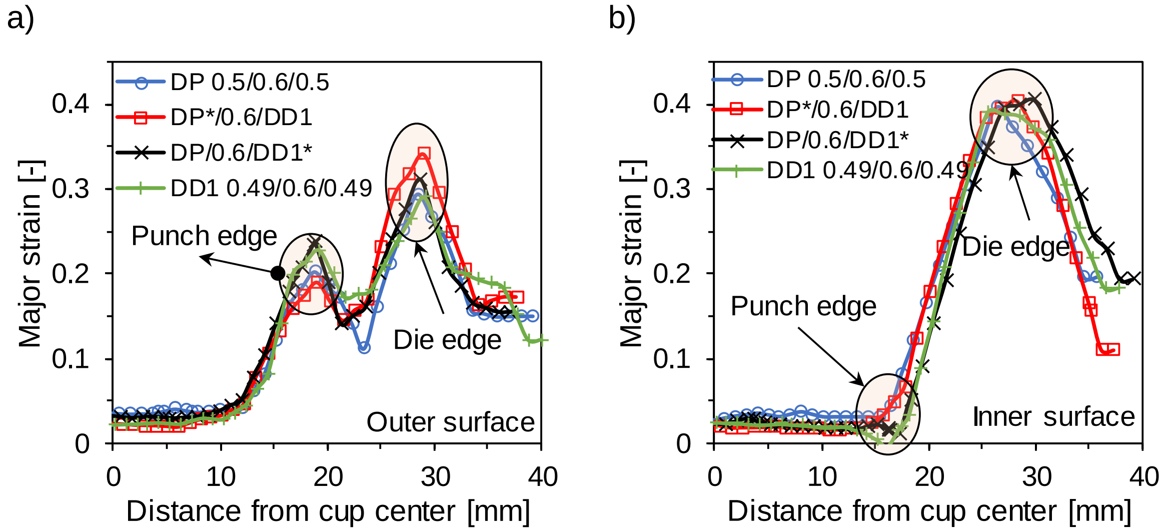

Figure 4.29: Effect of the SPS symmetry based on the DP and DD1 steel grades on the major strain distribution in the a) outer and b) inner surfaces for the drawn cups in **Figure 8.9**. *: refers to the skin sheet in contact with the punch.

4.2. Stretch forming

In this section, different SPS combinations were evaluated under stretch forming conditions using a 33 mm$^{\varnothing}$ semi-spherical punch and a 0.5 mm/s displacement rate, whereby the blank was rigidly clamped at the edges with a given blank holding force (60–100 kN) to avoid sliding/drawing of the blank. The aim is to determine the forming potential under biaxial stretching load conditions. The formability is expressed in terms of the dome height (the punch stroke until visible cracking of the outer surface) of the drawn blanks and the maximum drawing forces. Moreover, the strains or rather the major–minor strain points over the outer skin surface were evaluated by photogrammetry before and after cracking. Furthermore, the thickness distribution of the three-layered SPS was evaluated by LOM.

4.2.1. Effect of the core thickness

The effect of the core thickness on the maximum drawing force and the dome height at different core thicknesses with a constant skin thickness of DD1 grade of 0.49 mm is shown in **Figure 4.30-a)**. The dome height reached the level of the monolithic steel in all cases and was not strongly affected by increasing the core thickness as the formability depends mainly of the thickness and mechanical properties of the outer skin sheet. However, the drawing force remains constant up to core thickness of 1.0 mm which corresponds to $f_c = 0.5$. For the thicker core (2.0 mm), the drawing force decreased due to the higher content of the soft polymeric core that leads to a significant reduction in the strengthening behaviour of such thick-cored SPS in terms of the strain hardening exponent (n). These results match the previous deep drawing behaviour.

This correlation can be further clarified by analysing the strains over the outer and inner surfaces of the skin sheets. The thickness reduction, determined by photogrammetry, of the inner and outer surfaces through a section in RD after the visible cracking of the outer skin layer is depicted in **Figure 4.30-b)**. It can be clearly observed that cracking of the thicker core SPS occurred at low thickness reduction values, i.e. the cracking conditions were reduced. This is attributed to the higher tensile stress at the outer surface with a thicker core layer, see **Figure 4.30-c)**.

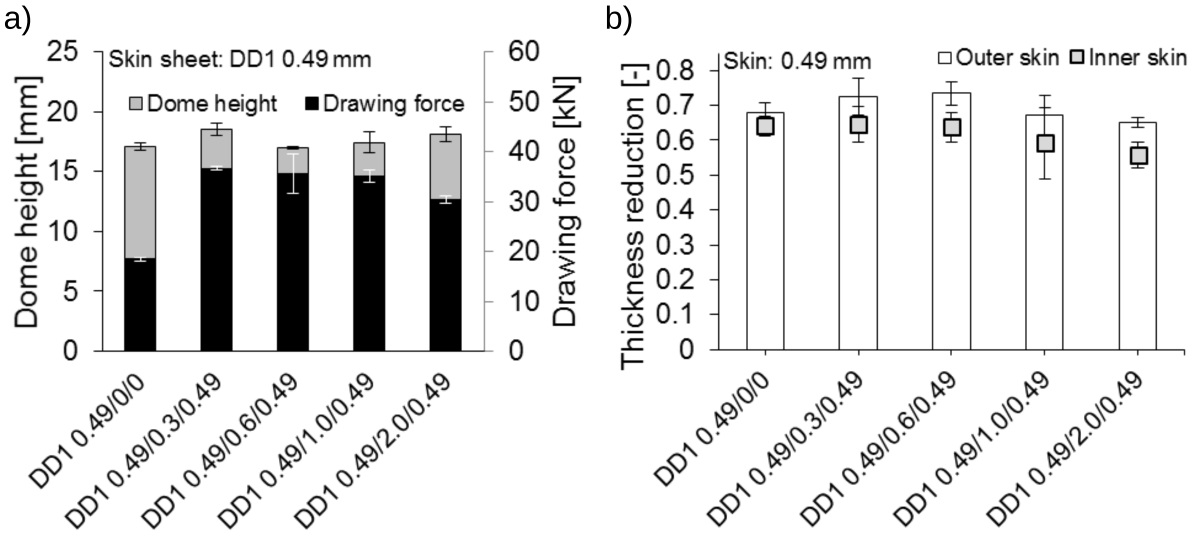

c) Thickness reduction distribution just before cracking

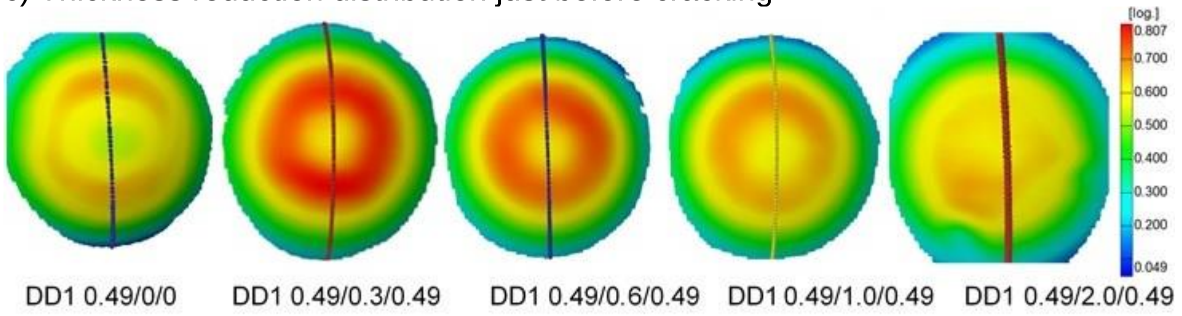

Figure 4.30: a) Illustration of the stretch-drawing potential of the SPS based on the steel grade DD1 by varying the core thickness in terms of dome height and maximum drawing force and b) the maximum thickness reduction over the inner and outer skin layers and c) its distribution over the outer skin sheet just before the visible cracking obtained by the Aramis system.

The ε_1–ε_2 strain points directly before and after cracking of the outer skin layer are presented in **Figure 4.31**. The thicker the core layer is, the lower are the limiting strains [Har16b]. By comparing the outer skin with the inner one, lower thickness reduction occurred on the inner one. Moreover, cracking of the inner skin sheet of the SPS, i.e. continuous cracking, was unlikely with thicker cores; the inner skin was kept safe without cracking for the core thickness =1.0 and 2.0 mm ($f_c \geq 0.5$) as shown from the metallographic sections in **Figure 4.32-a)**. These findings were emphasized comparing the major–minor strain points in the inner and outer surfaces with the corresponding FLC curve. Two conditions were selected:

1. DD1 0.49/0.6/0.49 with cracking in the inner layer, see **Figure 4.32-b)**.
2. DD1 0.49/2.0/0.49 with a safe inner layer, see **Figure 4.32-c)**, where its strain values did not intersect the FLC.

The behaviour of the inner skin sheet at thicker core layer is a featured point to provide a safer application to avoid leakage if being applied in containers.

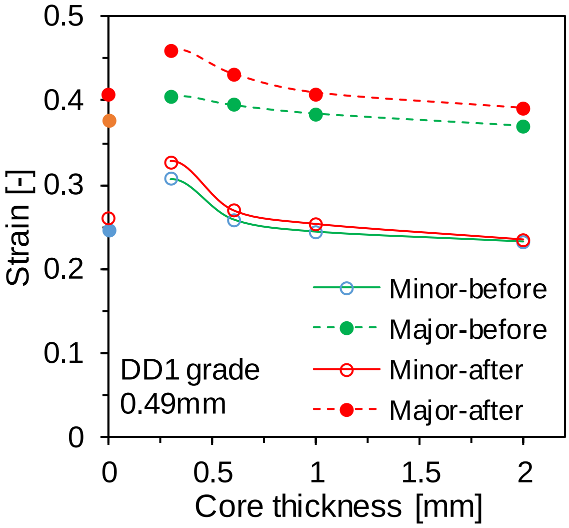

Figure 4.31: The limiting strains before and after cracking of different core thickness DD1 SPS (three specimens each).

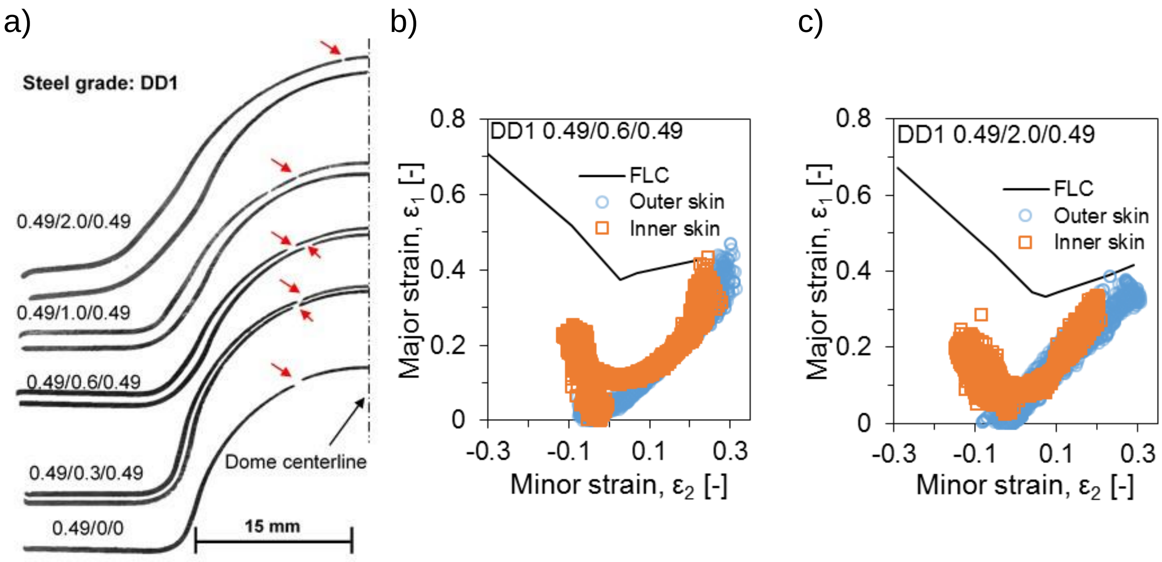

Figure 4.32: a) Stretched domes over a section in RD of different core thickness SPS, b) comparison of the minor–major strain values over the inner and outer skin layers in case of continuous cracking (from the outer skin sheet to the inner one including the core) and c) safe inner layer.

4.2.2. Effect of SPS symmetry

The effect of using different thickness of the skin sheet in the same SPS to give different layers stacking in respect to the forming punch is presented in **Figure 4.33-a)**. In this case, the SPS are based on the DD1 grade in 0.49 and 0.24 mm at constant core thickness of 0.6 mm. Firstly, the symmetric SPS containing thicker skin sheets, e.g. the DD1 0.49/0.6/0.49 shows, as expected, a higher dome height as well as drawing force in respect to the DD1 0.24/0.6/0.24. The asymmetric SPS containing both skin thicknesses (0.24 and 0.49 mm) exhibits an intermediate behaviour.

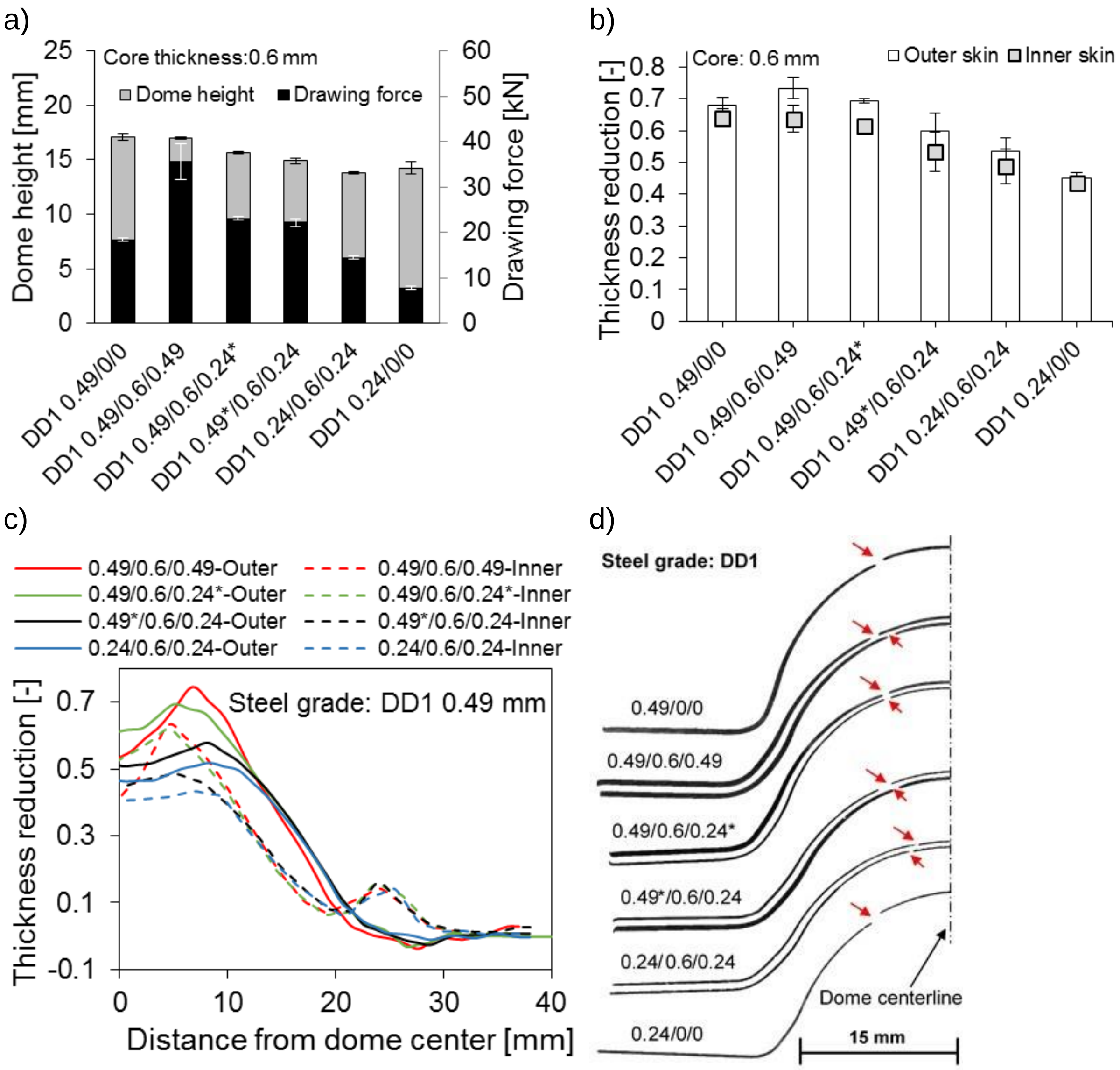

e) Thickness reduction distribution just before failure over the outer skin sheet

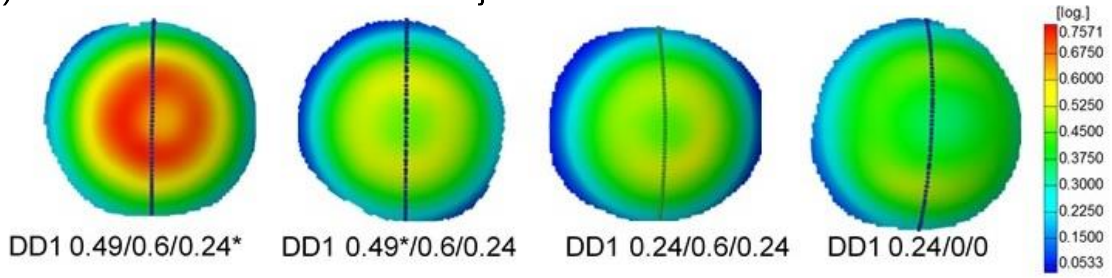

Figure 4.33: a) Maximum drawing force and dome height for different asymmetric SPS configurations at constant core thickness of 0.6 mm and b) the maximum thickness reduction over the outer and inner surfaces obtained by photogrammetry from thickness reduction progress in c), d) the metallographic sections in addition to e) the thickness reduction images just before failure. *: refers to the skin sheet in contact with the punch.

The effect of the SPS stacking (location of the specific skin sheet to the punch as shown previously in **Figure 4.2**) is demonstrated in **Figure 4.33-a)** with the help of 0.49/0.6/0.24* and 0.49*/0.6/0.24. If the thicker sheet is the outer one (not in contact with the punch), a better forming potential, i.e. higher dome height at failure with an increased drawing force is given. The maximum thickness reduction values in **Figure 4.33-b)** are evaluated based on the thickness reduction paths starting from the dome center as presented in **Figure 4.33-b)**. The maximum thickness reduction values are located in the middle third of the dome due to the unavoidable friction effect between the punch and the blank, see the metallographic sections in **Figure 4.33-d)**. Ideally, cracking should take place in the middle third of the dome or preferably exactly in the center. The thickness reduction depends on the SPS stacking, too (**Figure 4.33-c)**). The thicker the outer skin sheet is, the higher the thickness reduction at which cracking occurs, i.e. the forming potential is improved.

Moreover, the forming limits of these SPS just before and after cracking is shown in **Figure 4.34)**. In this diagram, it is further emphasized that the forming limits are improved when the thicker skin sheet is the outer one for the asymmetric SPS DD1 0.49/0.6/0.24* and is closer to the DD1 0.49/0.6/0.49. In summary, the asymmetric SPS can provide weight saving together with a good comparable forming potential for symmetric SPS ones.

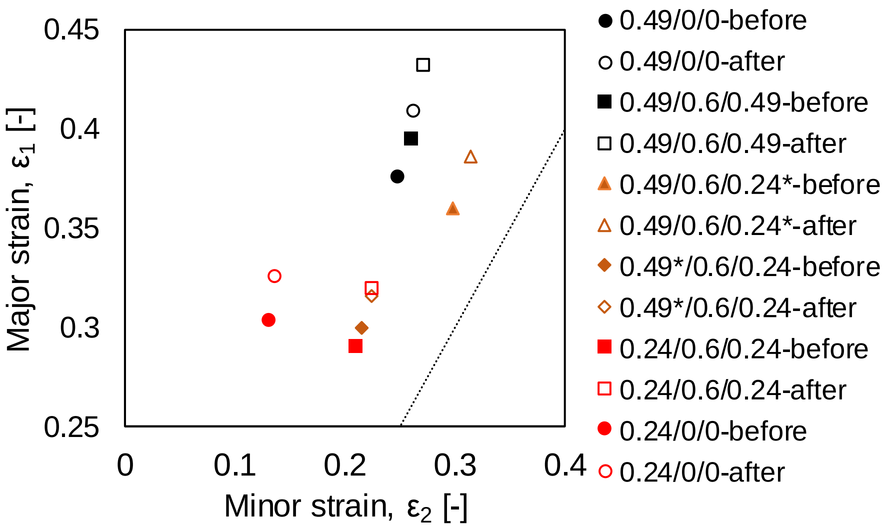

Figure 4.34: The major–minor strain points for different symmetric and asymmetric SPS before and after cracking.

4.3. Summary and conclusions

In this chapter, the formability of non-reinforced MPM was investigated by means of deep drawing and stretch forming for a wide range of steel/polymer/steel laminates (SPS) following the proposed scaling approach in **Figure 3.3**. Primarily, the SPS laminates are prone to cracking due to their low strengthening exponent and forming-related properties (n, r and e_u values) compared to monolithic steels. Additionally, the drawability of the SPS-laminates is limited due to their non-homogeneous thickness structure. The outer skin sheet is subjected to higher tensile stresses, compared to the inner skin. A parametric study on the deep drawability of different symmetric SPS combinations was performed. Therein, the effect of lubrication, skin/core thickness, skin sheet properties and SPS symmetry on the deep drawability by determining the working area for a faultless cupping processes was investigated.

The following conclusions and guidelines regarding the forming behaviour of SPS can be drawn:

1. The effect of the core thickness on the deep drawing working area and the resulting defects was studied on the DD1-laminates containing a 0.49 mm skin sheet thickness with different core thicknesses (0.3, 0.6 and 2.0 mm), i.e. at core volume fractions of 0.23, 0.38 and 0.67, respectively. Increasing the core volume fraction, the working area becomes smaller compared to that of the monolithic steel sheets. Furthermore, for the 2.0 mm core SPS, the relative shearing of the SPS layers is unavoidable even at a very low deep drawing ratio like $ß_0 = 1.5$ (50/33).
2. The mechanical properties of the skin sheets, especially the ductility at failure, r and n values, affect the optimum drawing conditions. The lower values of these properties lead to a reduced $ß_{0,max}$. Furthermore, applying higher blank holding forces F_{BH} is a need to produce good cups. A linear correlation between resulting $ß_{0,max}$ and the r values with the core thickness could be defined. Up to 50% core volume fraction, good cups at a max deep drawing ratio $ß_{0,max} \approx 2$ can be achieved. Moreover, $ß_{0,max}$ can be estimated following some empirical models used normally for the metallic sheets.
3. The drawing force of SPS depends mainly on the thickness and strength of the skin sheets. The core thickness has a minor influence up to a core volume fraction of 50%. At higher fractions, the required drawing force decreases due to the significant influence of the soft elastic core leading to a decrease of the strengthening potential of the SPS. The drawing force can be predicted by some analytical approaches as well.
4. In the studied SPS combinations, the optimum F_{BH} required to deliver good cups should be increased with about 30–50% in respect to the one required for

their monolithic steel sheets. For instance, the DD1 sheet requires approx. 20 kN and its SPS approx. 30 kN.

5. The proposed stepwise investigation approach enabled following the change of the strains on the SPS surfaces during the deep drawing and defining the forming limit, in terms of the cup height, precisely.
6. The mechanical anisotropy of the used steel sheets influences the strain distribution on the drawn cups. This helped interpreting and predicting the failure conditions.
7. The strain distribution over the skin sheets involved in SPS after deep drawing is very different from that over the same sheet if formed separately or in the form of three-layer unjoined laminates. The joined SPS shows the highest straining behaviour and consequently a higher tendency to cracking.
8. In the symmetric SPS, the degree of the straining on the skin sheets depends on the core thickness. At thicker cores, the limiting strain points come closer to the FLC.
9. In the asymmetric SPS, the straining behaviour can be adapted and controlled by tailoring the SPS stacking. So, the thicker skin sheet is oriented to be the outer one, i.e. not in contact with the forming tool. In the case of combining dissimilar steel sheet grades in the same SPS, the good formable one should be placed as the outer one to enable improving the forming potential.

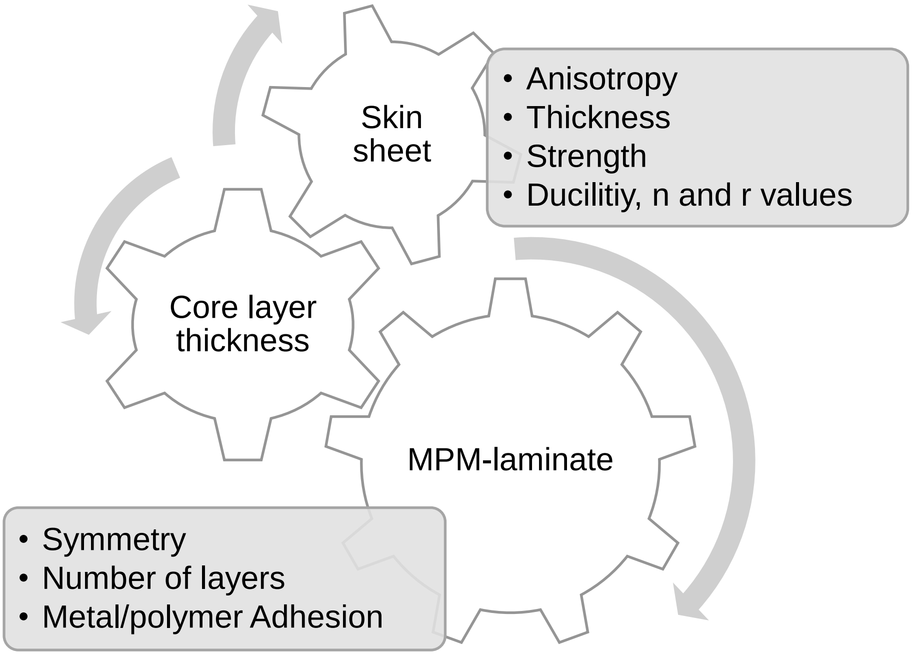

Figure 4.35: An overview of the parameters affecting the forming potential of the non-reinforced laminates

Under stretch forming conditions, further conclusions can be given for symmetric and asymmetric laminates. Similar to deep drawing, the forming limit in terms of the height at failure of the SPS under stretching conditions is the same like that of their outer skin sheet up to 50% core volume fraction. The same behaviour for the drawing force, as stated before, it depends on the volume fraction of the metallic sheet: the higher is the metallic content, the higher is the required forming force. These results were confirmed by the strain distribution over the skin sheet surfaces at failure.

This page intentionally left blank

5. Forming behaviour of the locally reinforced MPM-laminates

Joining of MPM-laminates is one of the major challenges facing their processing due to unavoidable properties of the polymeric core layer, which are:

1. Electrically insulating which hinders the welding process.
2. Mechanically elastic and soft which leads to local dimension distortion and indentation under mechanical pressure.
3. Thermally instable at elevated processing and service temperature like welding and some coating processes.

An overview of the possible joining approaches of the MPM-laminates are described in detail in part 2.5. From these approaches, the local substitution of the core layer, in the assigned joining areas, with metallic reinforcements (RE) is the one considered in the current study. As a result, the previous mentioned obstacles can be avoided by locally reinforcing the MPM-laminates. In this study, the focus will be on three-layered locally reinforced steel/polymer/steel laminates, denoted as R-SPS. This research point is complementary to [Sok12].

Figure 5.1 illustrates the motivation and research demands for the R-SPS. The aim of this study is to define forming limits of the R-SPS considering different properties of the RE compared to the reference non-reinforced ones (SPS) under different loading conditions. For this aim, the systematic methodology to realize these demands are shown in **Figure 5.1**. The input of this study is the characteristic properties of the non-reinforced SPSs given in chapter 4. Moreover, the SPS production scheme should be adapted to enable inserting the RE in the desired location. Later, the semi-finished reinforced flat SPS sheets are shaped with different forming processes, i.e. deep drawing and stretch-forming. The results were evaluated aiming at deriving relevant correlations to describe the forming behaviour in dependence on various REs properties, such as their size, geometry, location in respect to the forming tool and their material (solid or meshed).

Motivation & research demands

- A solution for arbitrary joining processes of the MPM-laminates ➔ by locally reinforcing the core layer. This approach stimulates a number of research needs about their processing:

1. How are the forming limits of the reinforced MPM affected compared to the non-reinforced ones?
2. How can the location of the inserted RE be monitored during forming?
3. What is the effect of inserted RE on the local and global strain distribution under different loading conditions?
4. Which macroscopic forming defects occur?

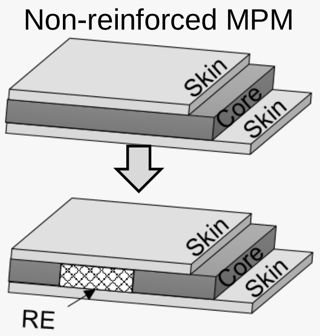

Systematic methodology

- Input: the obtained material properties and the forming guidelines of the non-reinforced laminates.
- Adapting the production scheme to enable inserting the RE in the desired location.

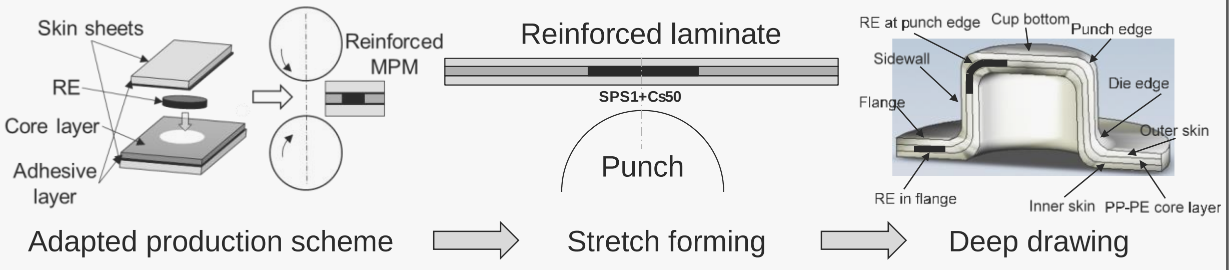

- Stepwise forming of the flat reinforced semi-products by deep drawing and stretch forming.
- Using photogrammetry to:
  - Analyze the local and global strain distribution in the shaped parts and compare it with the reference non-reinforced ones.
  - Compare the surface strains to the previously obtained FLC curves.
  - Monitor the displacement of the RE during the stepwise forming.
- Lock-in thermography analysis to inspect the internal imperfections close to the RE.

Goals

- Providing guidelines for processing and forming of the locally reinforced laminates.
- Determine the influence of inserting the RE on the forming potential considering the effect of the:
  - RE type (solid or mesh-like).
  - Location in respect to the forming tool.
  - Size and geometry.

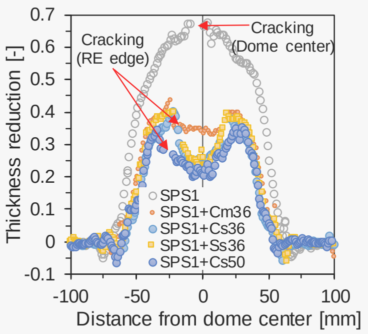

Figure 5.1: Overview of the study on the locally reinforced MPM-laminates.

5.1. Materials and production scheme

From the previously studied non-reinforced SPSs, four combinations were chosen to study the effect of the local reinforcement. Their notations and structures and additionally their mechanical properties are given in **Table 5.1**. To simplify, the non-reinforced laminates are termed as “SPS” and the reinforced ones as “R-SPS.” The main SPS combination used in this study is SS 0.5/0.6/0.5 (here abbreviated as SPS1). The effect of the various RE parameters – like the RE geometry, size, type and location – on the stretching and deep drawability behaviour of SPS1 was intensively studied. Additionally, the influence of reinforcing different SPSs that possess different mechanical properties and skin/core thicknesses was considered. Therefore, the deep-drawable steel grade (DD1) with two thicknesses (0.49 and 0.24 mm) was involved in the form of SPS2–SPS4. For the core, polyolefin (PP-PE) foils with thicknesses of 0.3 and 0.6 mm were used.

Table 5.1: Notation and description of the studied SPS laminates with their mechanical properties.

Notation			f_c [-]	Mechanical properties					
				YS [MPa]	UTS [MPa]	ε_u [%]	ε_f [%]	r [-]	n [-]
SPS1	→	SS 0.5/0.6/0.5	0.38	191±1	392±1	40	49	0.44	0.31
SPS2	→	DD1 0.49/0.6/0.49	0.38	142±7	215±1	16	29	1.72	0.16
SPS3	→	DD1 0.24/0.6/0.24	0.76	102±1	158±1	16	29	1.5	0.15
SPS4	→	DD1 0.24/0.3/0.24	0.38	137±2	209±1	16	28	1.5	0.15

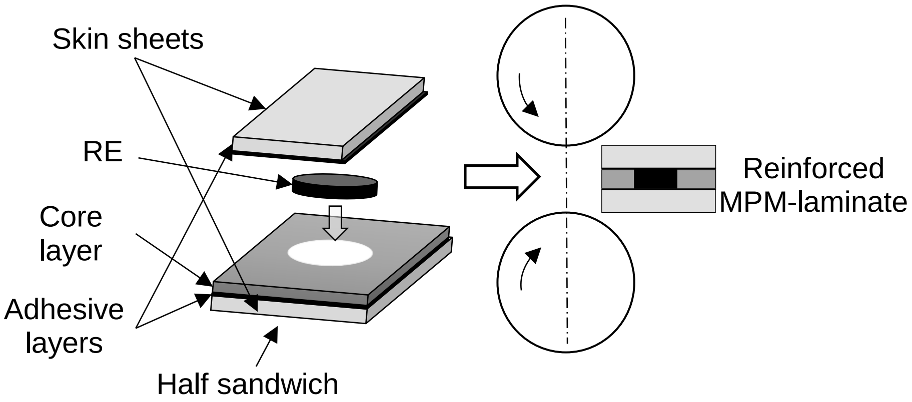

Figure 5.2: The adapted production scheme for locally reinforced MPM-laminates.

Figure 5.2 exhibits the adapted production scheme for the reinforced laminates. The production scheme of the R-SPS is the same as for the SPS described in part 0, except that the polymer core is prepared by cutting the assigned location with the desired RE geometry and size. Afterwards, the RE is placed in its position after producing the half-SPS (**Figure 3.2**) then being rolled under the standard conditions to give the complete R-SPS. More details can be found in [Pal15, Sok12]. After producing the flat R-SPS, they are then prepared for the photogrammetric analysis by introducing the dot-pattern to evaluate the strain distribution during the stepwise forming processes.

5.2. Stretch forming

The stretching experiments were carried out using a 75 mm$^{\varnothing}$ semi-spherical punch with a 180 mm$^{\varnothing}$ SPS blank. The applied blank holding force was 100 kN, sufficient to avoid blank sliding. The punch displacement rate was kept constant at 0.5 mm/s. These experiments were carried out primarily on SPS1 to determine the principal correlations regarding the different RE specifications like size, geometry and type on the formability of the R-SPS. An overview of the studied R-SPSs and their notations are summarized in **Table 5.2**, where the following RE parameters were considered:

1. Size effect (36 mm$^{\varnothing}$ vs. 50 mm$^{\varnothing}$).
2. Geometry effect (circular vs. square).
3. Material effect (solid vs. meshed).

Table 5.2: Summary of the stretching experiments of SPS1.

SPS		RE			Notation
		Geometry	Type	Size [mm]	
SPS1	+	**C**ircular	**s**olid	Ø 36	SPS1+Cs36[a]
				Ø 50	SPS1+Cs50
			mesh	Ø 36	SPS1+Cm36
		Square	**s**olid	36×36	SPS1+Ss36

[a]: SPS1+Cs36 means that the sandwich SPS1 is reinforced with a 36 mm$^{\varnothing}$ circular solid RE placed in the center of the SPS blank.

The stretching tests were performed stepwise in two steps: at a dome height h = 20 mm and until failure. At each drawing step, the drawing force and strain distribution were evaluated. The REs were placed in the center of the SPS blank, i.e. directly in the forming region where the tensile stresses are acting, as shown schematically in **Figure 5.3**. Positioning the REs in the flange is not meaningful for the stretching conditions, where the blank is clamped and no material flow is allowed.

5.2.1. Results

Based on **Table 5.2**, the drawing force–displacement progresses for the stretching experiments of the non-reinforced and the reinforced SPS1 are shown in **Figure 5.4-a)**. The progress of all the force–displacement curves in the two drawing steps, in terms of the slope, are identical, which means that there no different strengthening or stiffening behaviour, as a result of inserting the RE, took place.

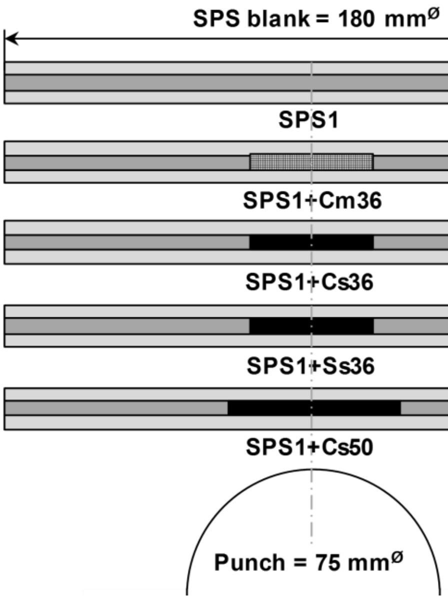

Figure 5.3: Different R-SPS1 under stretching condition (the RE's are centered in the blank) [Har17].

The characteristic results at each step like the maximum drawing forces $F_{d,max}$ and the drawing force difference, $\Delta F_{d,max}$ (in %), following Eq. **(5.1)**, is depicted in **Figure 5.4-b)**. Similarly, the dome height h and its change Δh (in %), following Eq. **(5.2)**, is shown in **Figure 5.4-c)**. The influence of the RE on the stretching behaviour in terms of $F_{d,max}$ and h can be described for the two steps, as follow:

1. In the first step up to h = 20 mm, there is no remarkable $\Delta F_{d,max}$ (~ 1%) for the various REs with the 36 mm size, i.e. Cm36, Cs36 and Ss36. However, the larger RE (Cs50) required ~ 5% higher force to stretch the three-steel layers in the center of the blank.
2. For the drawing step up to failure, the characteristic differences arose in terms of varied or preciously reduced forming limits namely h and $F_{d,max}$ at failure. Analysing this behaviour is the concern of the next paragraphs.

$$\Delta F_{d,max}\ [\%] = 100 \cdot \left(F_{d,max}^{R-SPS} - F_{d,max}^{SPS}\right)/F_{d,max}^{SPS} \tag{5.1}$$

$$\Delta \mathrm{h}\ [\%] = 100 \cdot (h_{R-SPS} - h_{SPS})/h_{SPS} \tag{5.2}$$

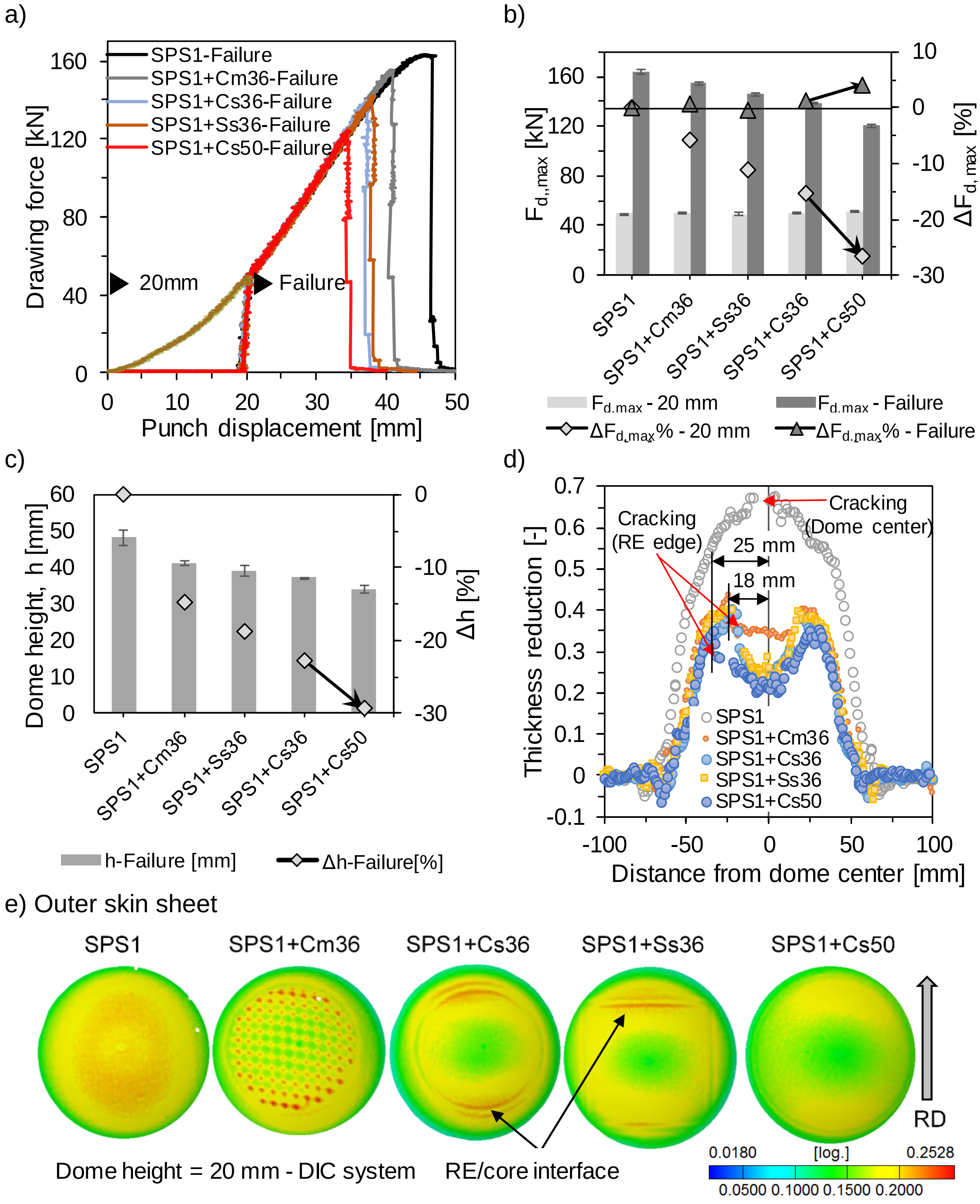

Figure 5.4: a) Drawing force–displacement progress illustrating the effect of the REs on b) the $F_{d,max}$ and its $\Delta F_{d,max}$ %, c) the dome height h and the its Δh% at failure, d) the thickness reduction along a radial section in RD of the different R-SPS1 at failure and e) the log. thickness reduction images over the outer skin sheet at h = 20 mm [Har17].

In principle, due to the heterogeneity at the RE/core interface, particularly at the RE edge, stress concentration and higher thinning rate arise, which accelerate the necking at these regions. Similar effects were reported by [Bol14] during bending of sheet metal laminates (Al / resin / Al) stiffened by pressing different bead structures. He stated that with increasing the bead height, the failure limits were significantly reduced under bending due to the introduced pre-straining during printing those beads. In the current case, there was no pre-straining, however the heterogeneity at the RE edge increased the thinning rate at this region. With larger RE size, the deterioration effect of the RE on the forming becomes clearer, see **Figure 5.4-b)** and **-c)**. The effect of the RE size can be described by comparing the two solid circular REs, i.e. Cs36 vs. Cs50. By increasing the RE size in terms of the $(\varnothing_{RE}/\varnothing_{Punch})$ size ratio from (36/75 = 0.48) to (50/75 = 0.67), the $\Delta F_{d,max}$ decreased in both cases from -15% down to -27% and the Δh at failure was reduced from -23% to -29%, respectively. However, the meshed RE (Cm36) shows the least deterioration effect compared to the solid ones at the same size. In the case of Cm36, Δh was reduced with -15% compared to -23% for the Cs36.

Figure 5.5: Failure images for the different R-SPS1 under stretching conditions (RD: ↑).

In order to interpret these results, the change of the strain distribution locally in the reinforced region and especially at the RE edges on the inner and outer skin sheets was accordingly evaluated and defined. In this regard, **Figure 5.4-d)** shows the thickness reduction, obtained by photogrammetry, along radial sections in RD on the outer skin sheet at failure for SPS1 and R-SPS1 conditions. Based on the thickness reduction images in **Figure 5.4-e)**, the boundary regions of the RE showed local higher thickness reduction compared to the non-reinforced one. On the one hand, failure by cracking occurred at these edges, as expected. On the other hand, cracking of the non-reinforced SPS1 takes place in the dome center, see the thickness reduction section **Figure 5.4-d)** and additionally from **Figure 5.5** and **Figure 5.6-b)**. Cracking of the R-SPS was shifted away from the dome center for a certain displacement according to the size or particularly the circumference of the RE, as shown additionally from the images in **Figure 5.4-d)** and **-e)**. For instance, a shift of the maximum thickness reduction region of ~18 mm and 25 mm occurred exactly the RE edges for the 36 mm and 50 mm RE size, respectively. Moreover, the meshed RE (Cm36) exhibited a higher (better) thickness reduction at failure location compared to the solid one (Cs36). The geometry had a minor influence on the failure conditions as found for the squared Ss36 and the circular Cs36.

In the case of the solid RE’s (Cs36, Cs50 and Ss36) a sharp change/gradient of the thickness reduction at the Re edge took place because of the RE edge. On the contrary, the meshed RE shows a lower gradient, but with localized thinning regions at the mesh nodes. Such nodes can guarantee the electrical connection required for later joining (welding) with a better weight saving approach compared to solid REs.

A further interesting evaluation of the failure position, either at the RE edge of R-SPS1 or in the dome center of SPS1, is shown in **Figure 5.6-a)**, where the average ε_1–ε_2 strain points in the failure position was evaluated up to $h = 20$ mm following the same methodology described in **Figure 3.17** and **Figure 3.27**. Ideally, the ε_1–ε_2 strain progress for the current biaxial stretching should follow the guideline: $\varepsilon_1 = \varepsilon_2$. This case was fulfilled only by the non-reinforced SPS1, as shown from the linear trendline equation. This linear progress was changed for the R-SPS1 to follow 2nd order polynomial approaches. The size effect is very clear, where at the same dome height (20 mm), the major strain values was changed from 0.1 for SPS1 up to 0.17 in the case of SPS1+Cs36 and further to 0.23 for the SPS1+Cs50. The higher gradient of the ε_1–ε_2 strain progress over the R-SPS1 led to cracking at lower dome height, as described before.

Table 5.3. Results of the stretched SPS1 with different REs.

SPS	Dome height at failure [mm]	Drawing force [kN]		Max. thickness reduction [-] [a]				%Δh [%] Eq. **(5.2)**
				Outer skin		Inner skin		
		20 mm	Failure	20 mm	Failure	20 mm	Failure	
SPS1	48±2	50±1	164±4	0.21	0.60	0.14	0.55	Ref.
SPS1+Cm36	41±1	50±1	154±1	0.22	0.43	0.13	0.37	- 15
SPS1+Cs36	37±1	50±1	139±1	0.20	0.43	0.14	0.37	- 23
SPS1+Ss36	39±4	49±1	146±5	0.21	0.42	0.14	0.39	- 19
SPS1+Cs50	34±1	52±1	120±5	0.19	0.37	0.15	0.33	- 29

[a]: the standard deviation of the three specimens is ignorable ≤ ± 0.01.

Furthermore, **Figure 5.6-c)** shows a comparison of the ε_1–ε_2 forming limits over a radial section in RD of the SPS1 and the R-SPS1 in respect to the FLC curve of SPS1. It can be clearly seen that the ε_1–ε_2 strain points for SPS1 met the FLC in the stretching (biaxial) region, as expected. However, in the case of the R-SPS1, the strain points at the dome center decreased dramatically due to the local stress concentration arose at the RE edge. That led to shifting the localization strain zone from the center to the sides based on the RE dimension. **Table 5.3** gives a comparison of the inner and outer skin sheet, it is noteworthy that the thickness reduction differences over the outer and inner skin surface are minor at a dome height of 20 mm, but a significant difference appears at failure.

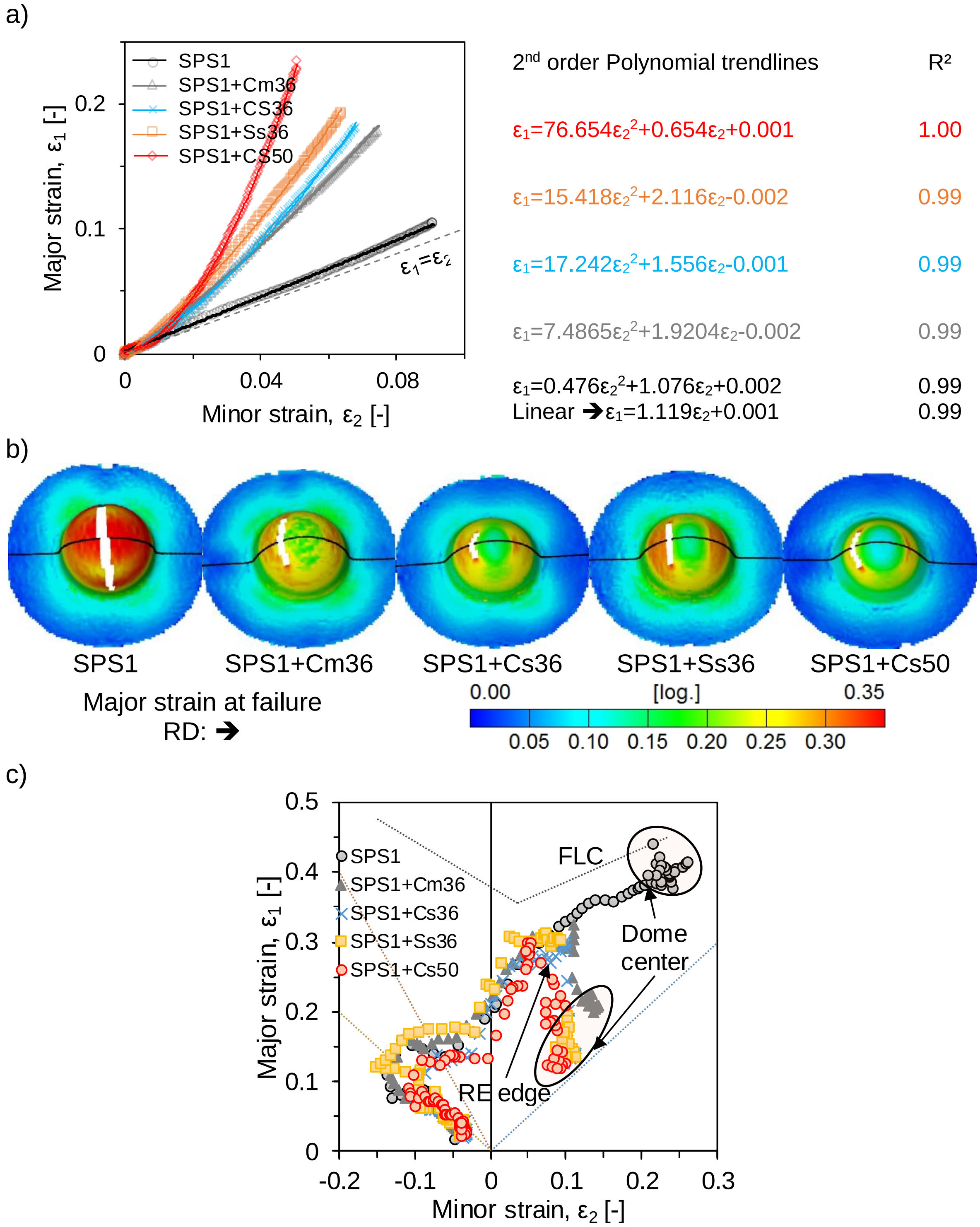

2nd order Polynomial trendlines	R²
$\varepsilon_1=76.654\varepsilon_2^2+0.654\varepsilon_2+0.001$	1.00
$\varepsilon_1=15.418\varepsilon_2^2+2.116\varepsilon_2-0.002$	0.99
$\varepsilon_1=17.242\varepsilon_2^2+1.556\varepsilon_2-0.001$	0.99
$\varepsilon_1=7.4865\varepsilon_2^2+1.9204\varepsilon_2-0.002$	0.99
$\varepsilon_1=0.476\varepsilon_2^2+1.076\varepsilon_2+0.002$	0.99
Linear ➔ $\varepsilon_1=1.119\varepsilon_2+0.001$	0.99

Figure 5.6: a) ε_1–ε_2 strain progress at the RE edge for R-SPS1 and dome center for SPS1 on the outer surface and the corresponding polynomial and linear trendlines (R^2 refers to the quality of the trendline fit with the data: a value of 1 means a perfect fit), b) the major strain images at failure and additionally c) the ε_1–ε_2 strains at failure over a radial section in RD to show their relation with the FLC curve of SPS1.

5.3. Deep drawing

Deep drawing tests were carried out using a 75 mm$^{\varnothing}$ flat punch and a 180 mm$^{\varnothing}$ blank. The punch displacement rate was kept constant at 0.5 mm/s. The deep drawing was performed stepwise in three steps – at 10, 20 mm and until failure – as shown for SPS1 in **Figure 5.7-a) and** photogrammetrically analysed after every step (**Figure 5.7-b)**). The dimensions of the drawing tools are listed in **Table 5.4**. This table is given to consider the geometrical aspects of the forming tools for interpreting the results, as the (gap size/t_{SPS}) ratio has a significant influence on the cup height (h) at failure; for a larger gap, higher h values can be reached because of the larger clearance between the drawing punch and the die which reduces the ironing and friction conditions. Based on [Lan95, Tsc77], the gap size can be 10–30% of the sheet thickness.

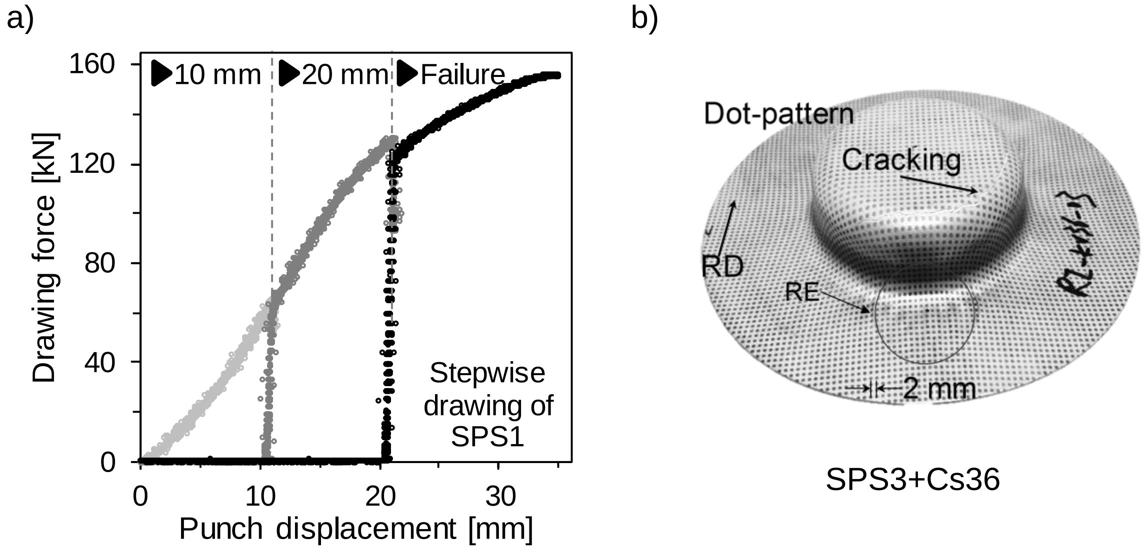

Figure 5.7: a) Punch force–displacement progress for the stepwise drawing of SPS1 (h = 10, 20 mm and at failure) and b) illustration of dot-pattern used for photogrammetric analysis [Har17].

Table 5.4: Drawing tools dimensions.

SPS	t_{SPS}	Drawing die		Gap size**	Gap size/t_{SPS}	(r_D/t) ratio
	[mm]	D_D* [mm]	r_D [mm]	[mm]		
SPS1	1.6	78.8	7	3.8	1.2	4.4
SPS2	1.58				1.2	4.4
SPS3	1.08				1.8	6.5
SPS4	0.78	77	5	2	1.3	6.4

*:D_D: the inner diameter of the drawing die, **: Gap size = (D_D-d_0)/2, d_0: punch diameter = 75 mm.

The RE was placed in different locations in the blank to be positioned later in the cup flange and at the punch edge i.e. at 60 mm and 37.5 mm distance from the blank center, respectively, as presented in **Figure 5.8**. The aim of varying the location is to determine its influence on the failure conditions locally and globally. The performed deep drawing experiments with varied RE sizes, geometries and types for the four used SPSs are listed in **Table 5.5**.

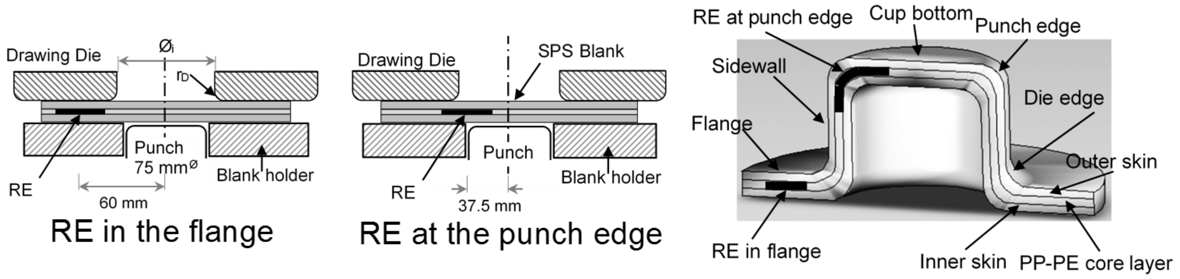

Figure 5.8: Positions of the RE in the SPS blanks.

Table 5.5: Deep drawing experiments of SPS and R-SPS.

SPS	RE				Notation
	Geometry	Size [mm]	Type	Location	
SPS1**+**	**C**ircular	Ø 20	**s**olid	flange	SPS1+Cs20-60mm
			mesh	flange	SPS1+Cm20-60mm
		Ø 36	**s**olid	flange	SPS1+Cs36-60mm
			mesh	flange	SPS1+Cm36-60mm
	Rectangular	36(RD)×10	**s**olid	flange	SPS1+Rs36(RD)10-60mm
		36×10(RD)	**s**olid	flange	SPS1+Rs3610(RD)-60mm
		36×10(RD)	**m**esh	flange	SPS1+Rm3610(RD)-60mm[a]
	Square	10×10[b]	**s**olid	flange	SPS1+Ss10-60mm
		20×20	**s**olid	flange	SPS1+Ss20-60mm
		36×36	**s**olid	punch edge	SPS1+Ss36-37.5mm[c]
SPS2**+**	**C**ircular	Ø 36	**s**olid	flange	SPS2+Cs36-60mm
SPS3**+**			**s**olid	flange	SPS3+Cs36-60mm
SPS4**+**			**s**olid	flange	SPS4+Cs36-60mm

[a] :SPS1+Rs3610RD-60mm is the sandwich SPS1 reinforced with a 36×10 mm^2 **r**ectangular-**s**olid RE; the 10 mm side is directed in rolling direction RD.

[b] : normally one 10×10 mm^2 RE is placed in RD. The number of the REs was considered by inserting two REs (in 0° and 180°) and three ones (in 0°, 90° and 270°)

[c] : SPS1+Ss36-37.5mm is the sandwich SPS1 reinforced with a 36×36 mm^2 **s**quare-**so**lid RE placed at 37.5 mm distance from the blank center.

5.3.1. Drawing force and cup height

The cup height (h) and drawing force (F_d) at failure of the 316L sheet, SPS1 and the reinforced SPS1 with different RE geometries, sizes and locations in the cup are shown in **Figure 5.9-a)**. It can be observed that SPS1 requires F_d as double as the 316L sheet according to the summation approach [Nut08]; however, the cup height for the 316L sheet and the SPS1 at failure is approximately the same, where the SPS exhibits the close forming limits like its skin sheets, as shown in part 3.5 and [Sok12]. These principal results help predicting the drawing force and cup heights at failure.

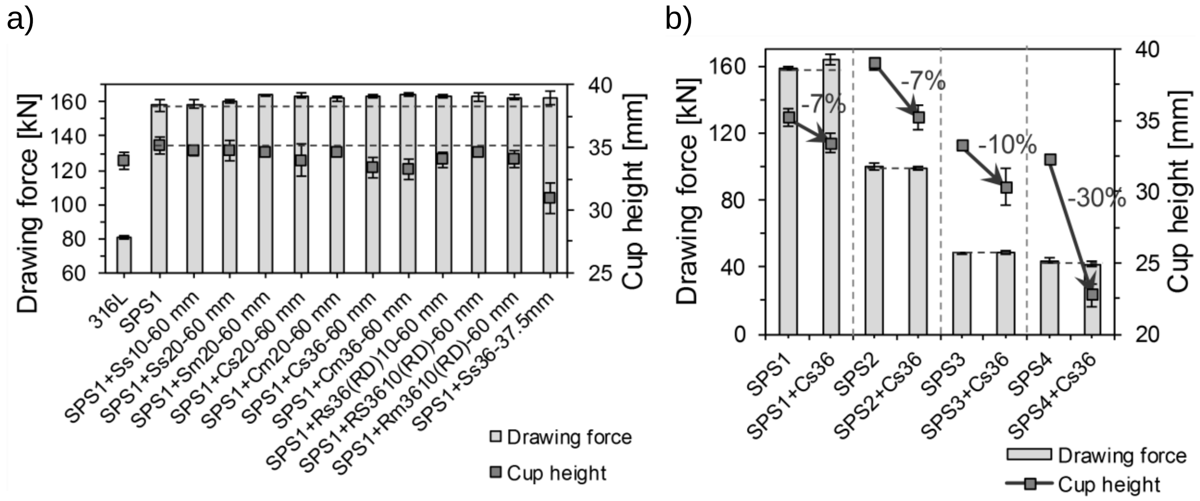

Figure 5.9: a) Drawing force and cup height at failure for different reinforced SPS1 and b) comparing SPS with R-SPSs with a circular solid $36\ \mathrm{mm}^{\varnothing}$ RE placed in the flange. Percentage labels stand for the Δh% following Eq. **(5.2)**.

The effect of inserting the RE on the deep drawing behaviour can be clarified based on the location and the properties of the SPS in terms of F_d and Δh (in %) following Eq. **(5.2)**, as follow:

1. At the punch edge: this can be described with the help of the Ss36 placed at 37.5 mm distance from the blank center, see **Figure 5.9-a)**. Because the RE is placed directly in contact with the punch, significant Δh at failure took place, see the failed cups in **Figure 5.10**. In this case h reduced from 35 mm down to 32 mm, i.e. Δh reached -9%. This is due to the heterogeneity of RE/core interface, like the case of stretch forming in part 5.2, which accelerates failure.
2. In the flange: by comparing F_d for SPS1 and R-SPS1, it was found that inserting the REs has only a minor influence on F_d at failure. However, the change of the cup height Δh (in %) following Eq. **(5.2)** is considerable, as Δh depends on the RE size, thickness and mechanical properties of the SPS as shown principally for SPS1 combinations in **Figure 5.9-a)** and in **Figure 5.9-b)** for the different SPSs (SPS1–SPS4). For the SPS1 conditions, Δh showed different values based on the RE size. It ranges from -1% for the 10×10 mm^2 down to -8% for the solid and mesh large RE, i.e. Cs36 and Cm36. The difference between the solid or meshed RE can be neglected, see **Figure 5.9-a)**.

The effect of varying the skin sheet property and thickness, as well as the core layer thickness on the drawability in terms of F_d and h is described in **Figure 5.9-b)** and the corresponding failed cups in **Figure 5.11** by using the same RE (Cs36) in the flange:

1. With the same skin/core layers thickness ratio (SPS1 and SPS2), SPS2 (based on DD1 steel grade) requires a lower F_d respect to SPS1 due to its lower strength, as can be interpreted from Eq. **(2.29)** [Lan95]. Additionally, due to the

better forming potential of SPS2, a higher height at failure was reached: SPS1 and SPS2 failed at 35 mm and 38 mm, respectively. However, $\Delta h = -7\%$ for both the R-SPS1 and R-SPS2 was found.

2. With the same core thickness (SPS3 and SPS2), SPS3 reaches failure at a lower F_d and h due to the thin skin sheet (0.24 mm) with a higher drop of h, i.e. $\Delta h = -10\%$.
3. With the same thin skin sheet (0.24 mm) but different core thicknesses (SPS3 and SPS4), SPS4 shows approximately the same F_d as SPS3 but with a further reduced cup height. For the SPS4, a significant drop in the cup height of $\Delta h = -30\%$ was found where cracking took place in the cup sidewall at the RE edge and not at the cup-bottom/sidewall, as usual, see **Figure 5.11**.

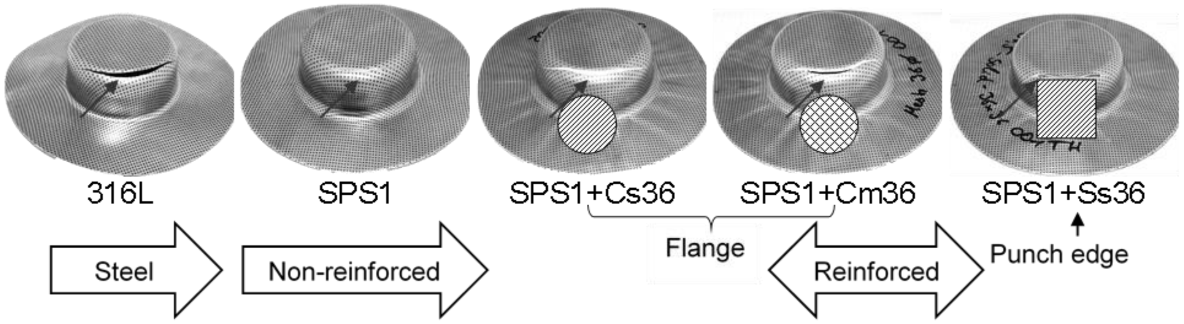

Figure 5.10: Drawn cups at failure for the 316L grades and its SPS1 in addition to three R-SPS1.

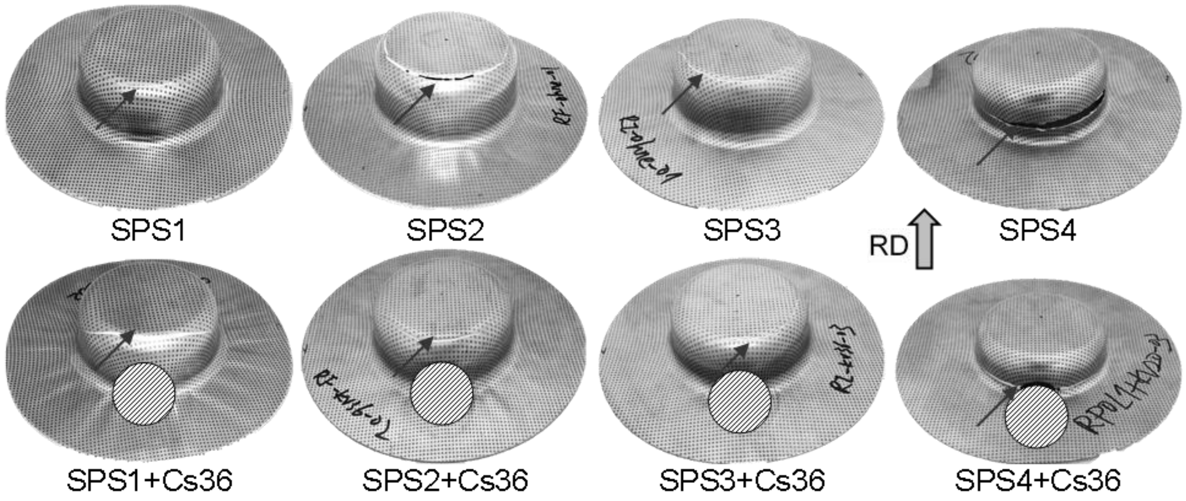

Figure 5.11: Drawn cups at failure for the SPS1–SPS4 and their reinforced ones with Cs36.

Concluding, the R-SPS require the same F_d like SPS but with a reduced cup height at failure. The reduction in the cup height can be attributed to the hindering effect of the RE on the sheet flow. This blocking effect is more remarkable for larger REs and the thinner SPSs. These findings are in-depth explained in the next sections regarding the strain distribution and the flow blocking effect on the RE side.

In addition to the different failure limits of the R-SPSs compared to their SPSs, macroscopic defects were arisen locally in the reinforced region, as presented in **Figure 5.12**. Firstly, cracking of R-SPS took place in the direction where the RE is placed. Further defects and their causes can be described as follow:

1. Local wrinkling in the reinforced region mainly on the outer skin sheet. This is due to the absence of adhesion between the RE and the skin sheets and additionally the thickness tolerance between the core and the RE, see **Figure 5.12-a)**.
2. Local indentation at the RE edges takes place mainly on the inner SPS skin sheet. This defect becomes more significant if the RE is placed in the forming region, as described in **Figure 5.12-b)**.
3. Shifting of RE aside leaving an area in the core layer, in which neither polymer core nor metallic RE exists, as presented in **Figure 5.12-c)**.

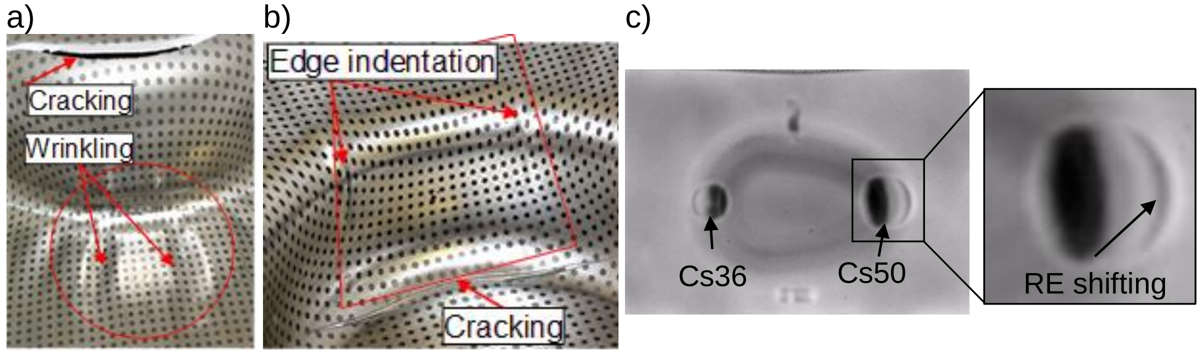

Figure 5.12: Probable local defects of R-SPS under deep drawing: a) wrinkling, b) indentation at the RE edge and c) thermographic images showing the RE shifting [Pal14].

These previously-mentioned defects can be probably avoided by:

1. Joining the RE with the skin sheets by, for instance, spot welding.
2. Tailoring the RE/core interface to avoid the shifting as well as the local indentation.
3. Avoiding inserting the RE in the forming region, if possible, or controlling the RE size to position the RE edges out of this critical area.

5.3.2. Flow behaviour

Studying the flow behaviour of the RE or particularly its displacement during deep drawing is essential to determine its influence on the failure conditions. This flow behaviour was determined by monitoring the elongation (ΔL) of the developed length (L) between the cup and the RE centers at each cup height relative to the original length (L_0), i.e. 60 mm and 37.5 mm for the flange and the punch edge locations, respectively. The developed length includes the cup height, die and punch radii as described in [Doe10]. The higher ΔL values means that the flow is hindered due to the overstretching of the developed length. In the current case, the RE can hinder the flow and cause such overstretching. This length was measured by the DIC strain analyser as depicted in **Figure 5.13**. Such length can be precisely measured before cracking; otherwise, the crack opening is involved which deviates the length value as illustrated in **Figure 5.13** for the failure step.

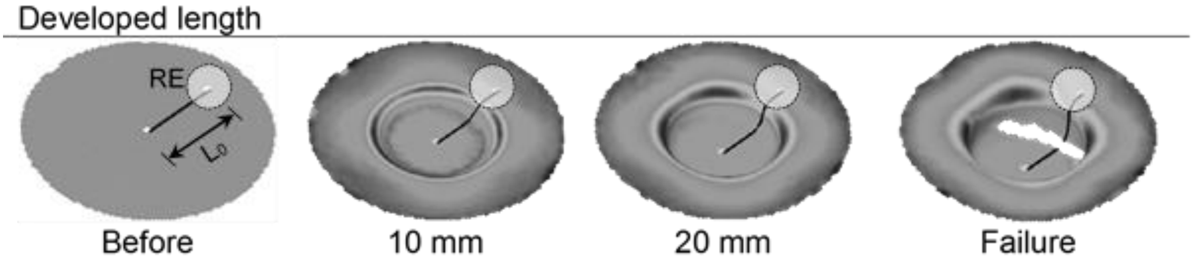

Figure 5.13: The developed length between the RE and cup centers through the three drawing steps (cup heights).

The REs are placed primarily, either in the flange or at the punch edge, in RD, i.e. the 0° direction. The flow can be hindered basically in RE direction, but it can influence the neighbour regions of the cup like the 45° and 315° directions and the opposite side (180°) as well. Therefore, ΔL was measured for all the illustrated directions in **Figure 5.14-a)**, not only the 0° direction in which the RE is placed. The corresponding ΔL results for different R-SPSs in respect to SPSs are presented in **Figure 5.14** and **Figure 5.16**.

The ΔL values of the four SPSs reinforced with Cs36 placed in the flange are shown in **Figure 5.14-b)– -f)** for the outer surfaces. **Figure 5.14-b)** shows the correlation of the ΔL values with the steel sheet (316L), its non-reinforced SPS (SPS1) and the reinforced SPS (R-SPS1) with a Cs36 placed in the flange. It is observed that the 316L showed the highest ΔL for all the drawing steps. Then, R-SPS1 showed locally higher ΔL in the 0° direction, where failure occurs.

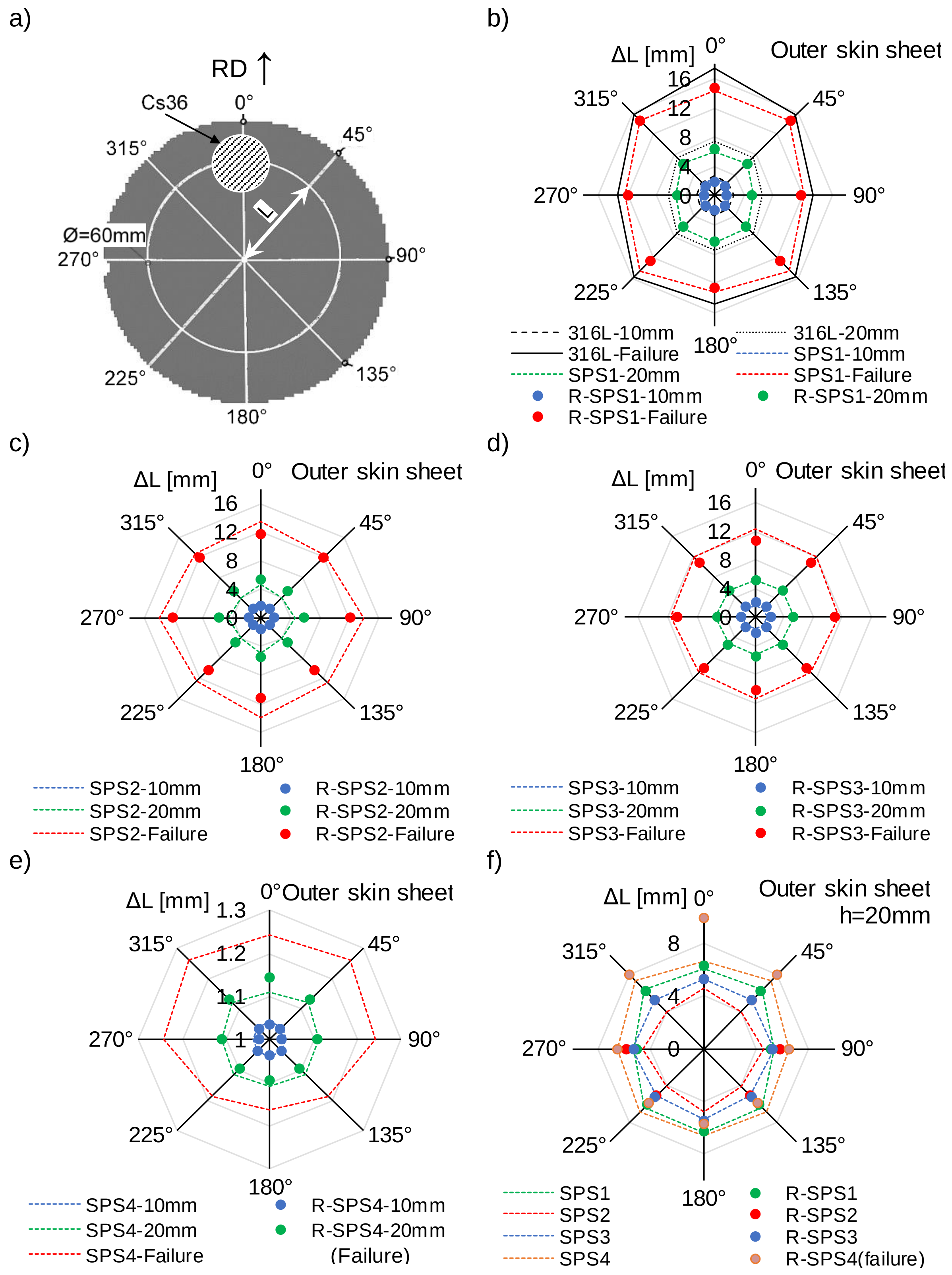

Figure 5.14: a) The different directions considered for evaluating the sheet flow in terms of ΔL for the R-SPSs with Cs36 in the flange and the corresponding results for b) SPS1, c) SPS2, d) SPS3, e) SPS4 and f) ΔL comparison of SPS1–SPS4 at h = 20 mm.

For SPS2–SPS4, at h = 20 mm, the R-SPSs shows higher ΔL due to the overstretching in the reinforced side. However, at failure, because the R-SPS fail at a considerable lower cup height respect to the SPS, so the R-SPS fail at lower ΔL, as well, as the developed length involves the cup height in addition to the rest length in the flange and the cup bottom. So, for a reduced cup height, lower ΔL takes place. It can be also observed that the flow is symmetric for the opposite directions e.g. the 0 and 180° in the stages before failure. However, at failure, the SPS, as well as the R-SPS have higher ΔL. This can be attributed to the involved crack opening in the total length. A comparison between all SPS at h = 20 mm is presented in **Figure 5.14-f)**. SPS4 with the thinner layers shows the highest ΔL which refers to the obviously hindered flow of the reinforced flange. Hence, earlier cracking of R-SPS4 occurs at only h = 22 mm.

The ΔL values for the outer and inner surfaces of SPS1 and its various reinforced conditions at 20 mm cup height are shown in **Figure 5.15-a)** and **-b)**, respectively. It can be stated that ΔL over the inner and outer surfaces of the R-SPS show a minor difference compared to SPS. This can be attributed to the little ratio between the surface area of the RE in respect to the SPS blank, which led to such ignorable effect. For instance, for the Cs36, this ratio is $(D_{RE}^2/D_{Blank}^2 = 36^2/180^2 = 0.04)$.

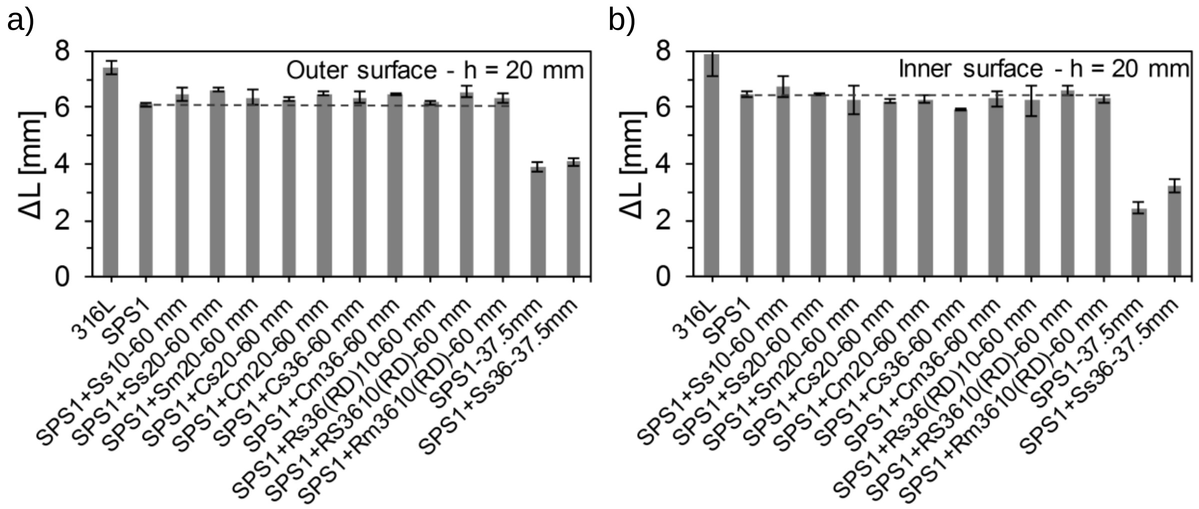

Figure 5.15: Length change over the a) outer and b) inner skin sheets of SPS1 and R-SPS1 drawn at h = 20 mm for different RE properties [Har17].

The effect of inserting more than one RE on the flow behaviour was studied. For this purpose, four combinations of SPS1 reinforced with square solid 10×10 mm^2 RE, i.e. Ss10 in the flange of SPS1 in different numbers and locations were studied, as presented in **Figure 5.16**:

1. SPS1 + 1xSs10 in 0°: **Figure 5.16-a)**.
2. SPS1 + 2xSs10: in 0° and 90°: **Figure 5.16-b)**.
3. SPS1 + 2xSs10: in 0° and 180°: **Figure 5.16-c)**.
4. SPS1 + 3xSs10: in 0°, 180° and 270°: **Figure 5.16-d)**.

For all the conditions, a slight difference in ΔL between SPSs and R-SPSs is observed for the 0° direction, where failure occurs. However, the other directions show different ΔL, which is based on the inherent anisotropic behaviour of the steel sheets.

It can be concluded that the RE located in the flange flows with the SPS sheet with minor differences, however local defects like wrinkling and indentation can take place, as mentioned earlier. Moreover, for thinner SPS, the flow blocking effect becomes very clear leading to about 30% reduction in the cup height at failure.

a) 1xSs10 in 0°

b) 2xSs10: in 0° and 90°

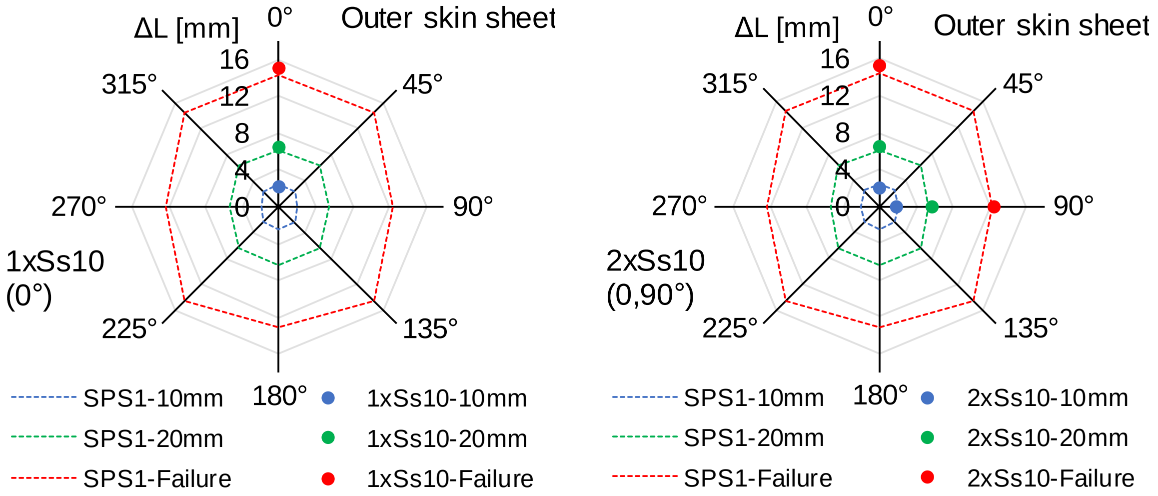

c) 2xSs10: in 0° and 180°

d) 3xSs10: in 0°, 180° and 270°

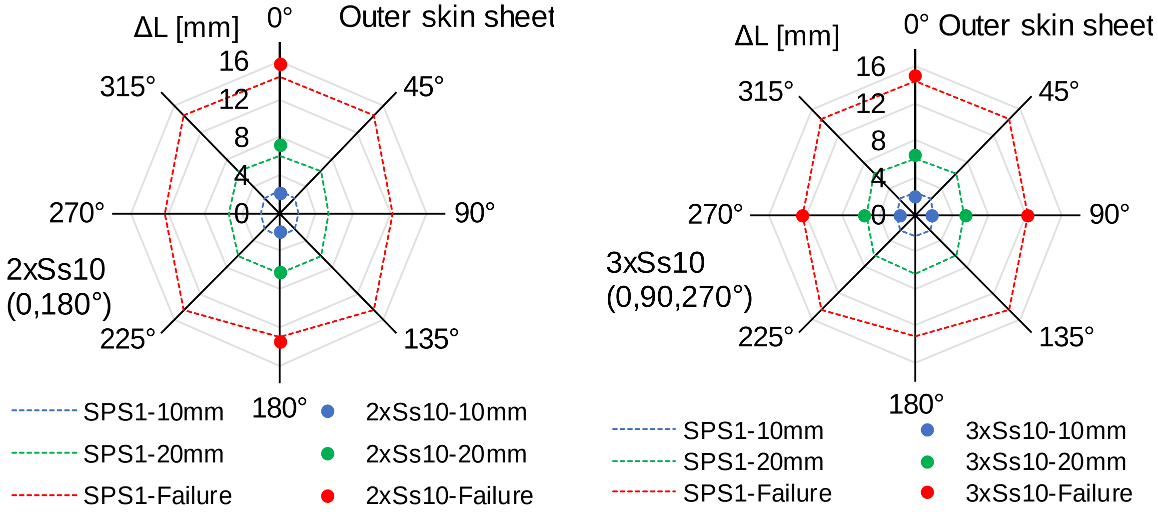

Figure 5.16: The correlation between ΔL and the number of REs of SPS1 reinforced with Ss10 located in the flange.

5.3.3. Strain analysis

In order to interpret the change of the forming limits after inserting the REs in the SPS, it is essential to evaluate the strain distribution of the skin sheets in different regions of the drawn cups to describe the strain deviation behaviour. Three regions, as described in **Figure 5.8**, were monitored:

1. The reinforced region particularly at the RE center.
2. The die rounding close to the RE.
3. The punch rounding where, most likely, cracking takes place.

The major strain distribution over the outer and inner surfaces of R-SPS1 with Cs36 in the flange at the three forming steps is shown in **Figure 5.17**. The left side of the diagrams depicts the non-reinforced side of the R-SPS1 in comparison to the reinforced SPS1 (right side).

The strain evaluation is concerned with the two sides of the R-SPS in respect to SPS, as shown from the radial section in **Figure 5.17-a)** and **–b)**:

1. The left side of the curves, which is the opposite non-reinforced side of the cup. For the inner and outer surfaces, both the major strain progress in R-SPS and SPS are identical at h =10 and 20 mm. However, at failure, SPS failed at higher major strain values, as it failed at higher cup height, see **Figure 5.9-b)**.
2. For the right side, in which the RE is placed. At the RE center, the major strain of the R-SPS is reduced for the inner and outer surfaces of the R-SPS1 because of the reinforcement effect. However, at the edge of the RE towards the die rounding and further away to the punch edge, the SPS outer and inner skins sheets show different straining behaviour.

The outer surface can be differentiated from the inner one as follow:

1. For the outer surface, **Figure 5.17-a)**, the major strain is further decreased at the die rounding, as the reinforcing effect of the Cs36, due to its size, is extended to reach the die rounding. The strain of R-SPS starts to increase in the cup sidewall. Furthermore, at the punch rounding and the cup-bottom, a minor increase of the strain was found at the stages before cracking, i.e. at h = 10 and 20 mm, but decreases at failure stating that failure for R-SPS takes place earlier than for SPS due to the hindered material flow from the reinforced flange.
2. For the inner surface, **Figure 5.17-b)**, a remarkable reduction of the strain at the die rounding was found where RE suppresses the dominant tensile strains. It can be further stated from the strain images that the strain distribution of SPS and R-SPS are quite similar except in the reinforced region.
3. Furthermore, the strain distribution was evaluated through monitoring its change in circular sections in the flange with Ø = 60 mm that passes by the RE center as presented in **Figure 5.18-a)**. To point out the reproducibility of the strain progress along that section **Figure 5.18-b)** shows three sections at the failure stage for the tested three SPS1 specimens as well as their average progress. A negligible deviation was found; therefore, the average strain progress was utilized for the coming illustrations. Due to the inherent anisotropic behaviour of the 316L, the strain values are dependent on the angle

in respect to the rolling direction (0°). The strain in 45° to RD is higher than under 0° and 90°, which is proportional to the mechanical properties, described in part 3.4.2.

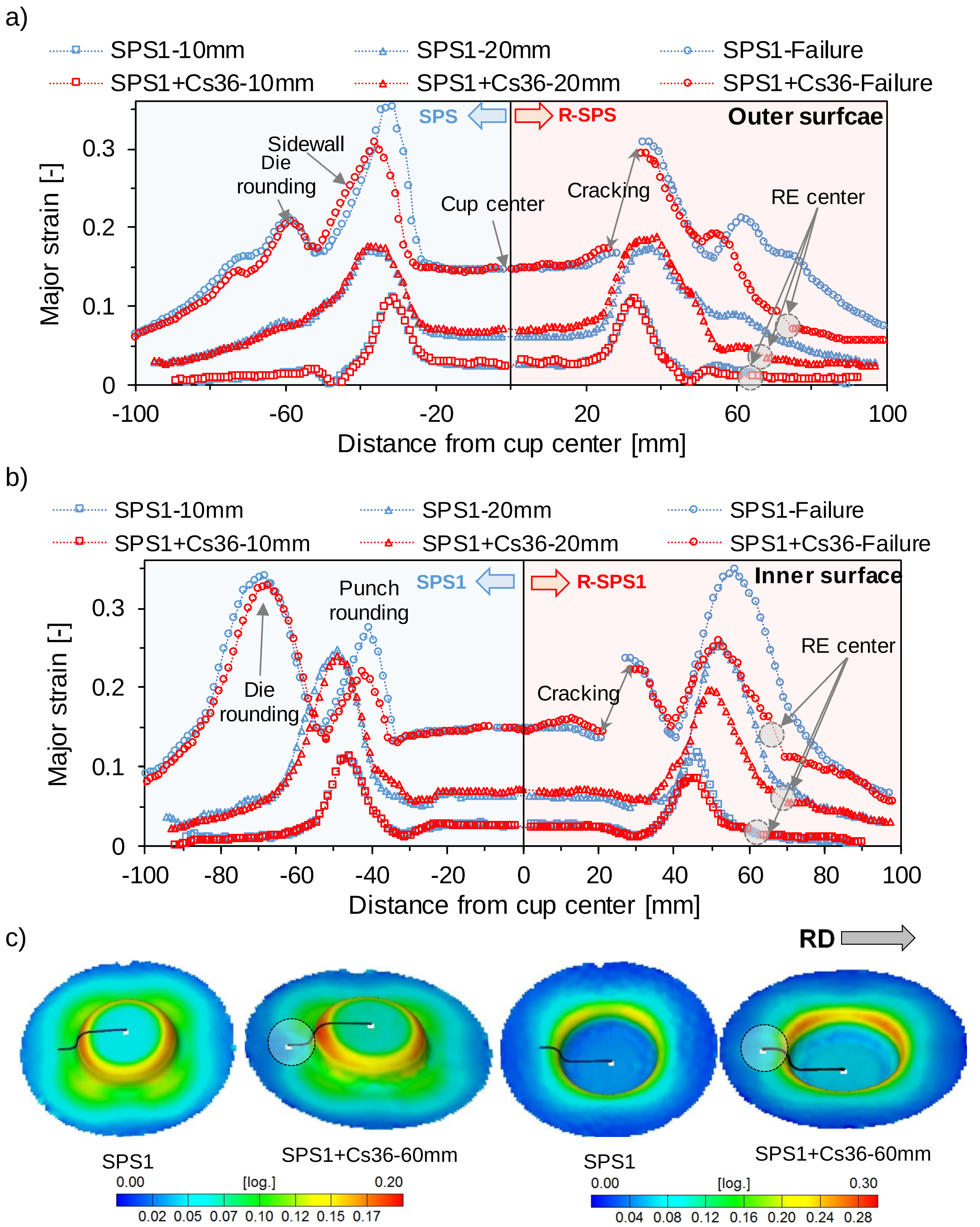

Figure 5.17: Major strain distribution in radial sections for the flange reinforced SPS1+Cs36 in respect to SPS1 at h = 10, 20 mm and at failure for the a) outer and b) inner surfaces and c) the corresponding major strain images at h = 20 mm for the outer and inner surfaces.

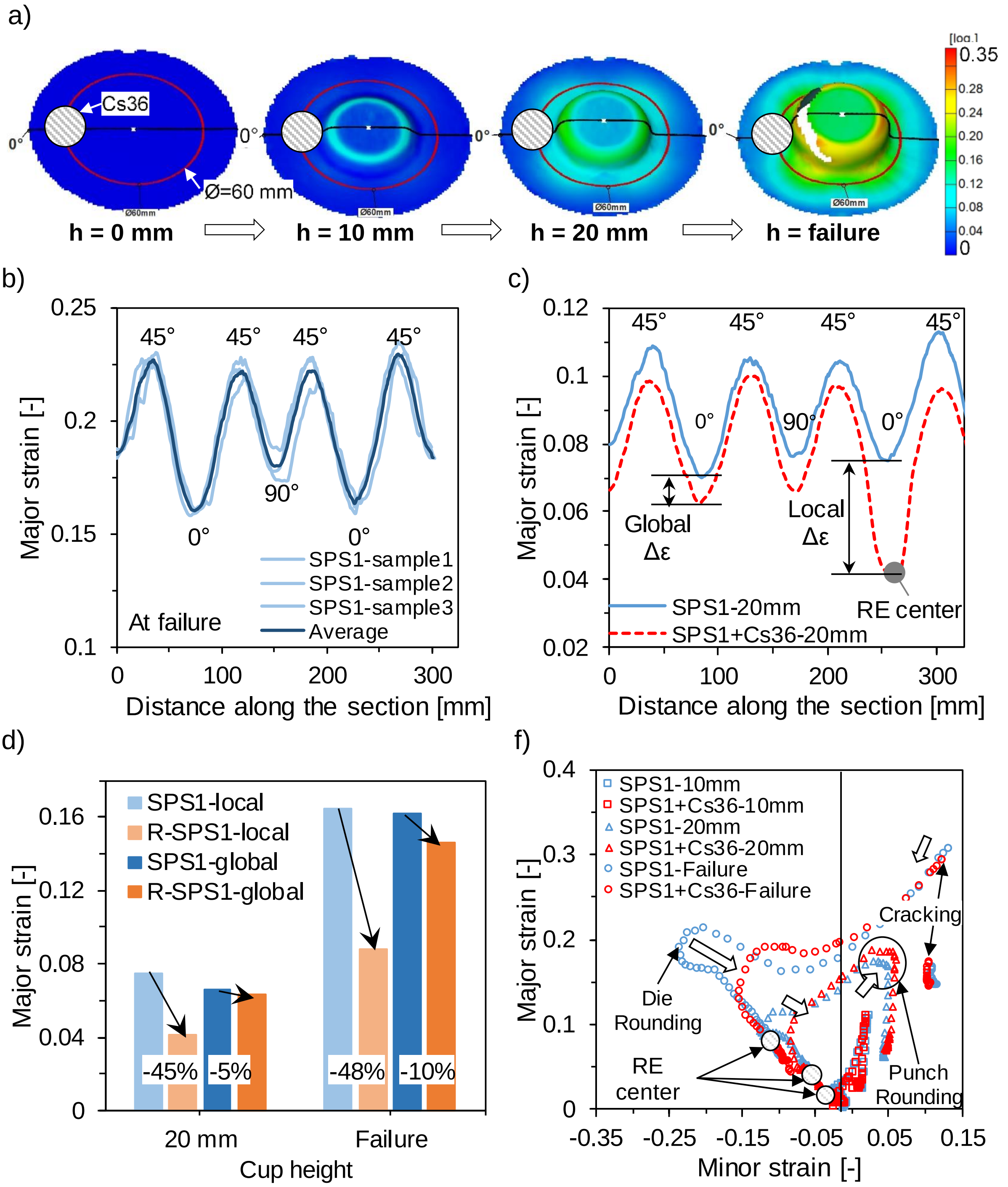

Figure 5.18: Major strain evaluation in 60 mm$^{\varnothing}$ circular section in the flange for SPS1 and SPS1+Cs36 showing: a) the DIC images for the successive forming steps, b) a reproducibility example, c) an evaluation example for the local and global strain change (Δε) and d) the corresponding results at h = 20 mm and at failure, in addition to e) the influence of Δε on the ε_1–ε_2 strain progresses.

The circular sections are evaluated by comparing the major strain progress of the reinforced and the non-reinforced progresses as depicted exemplary in **Figure 5.18-c)** for SPS1+Cs36 in respect to the SPS1 at h = 20 mm, to determine the strain difference Δε:

1. Locally: at the RE center.
2. Globally: the general difference between the major strain progresses of both sections. In this case, the opposite direction to the RE was chosen.

Figure 5.18-d) presents the global and local strain vales for SPS1 and R-SPS1 in addition to Δε% ($\Delta\varepsilon\% = 100 \cdot (\varepsilon_{R-SPS} - \varepsilon_{SPS})/\varepsilon_{SPS}$) at h = 20 mm and at failure. It was found that the global difference ranges between 5% and 10% for h = 20 mm and at failure, however the local Δε% reached 45%. This strain changes led to change the ε_1-ε_2 strain progresses as illustrated in **Figure 5.18-e)**. Because of the blocked material flow at the die rounding, the ε_1-ε_2 progress was suppressed, however they were increased towards the failure conditions and therefore they fail earlier as can be seen from the failed condition.

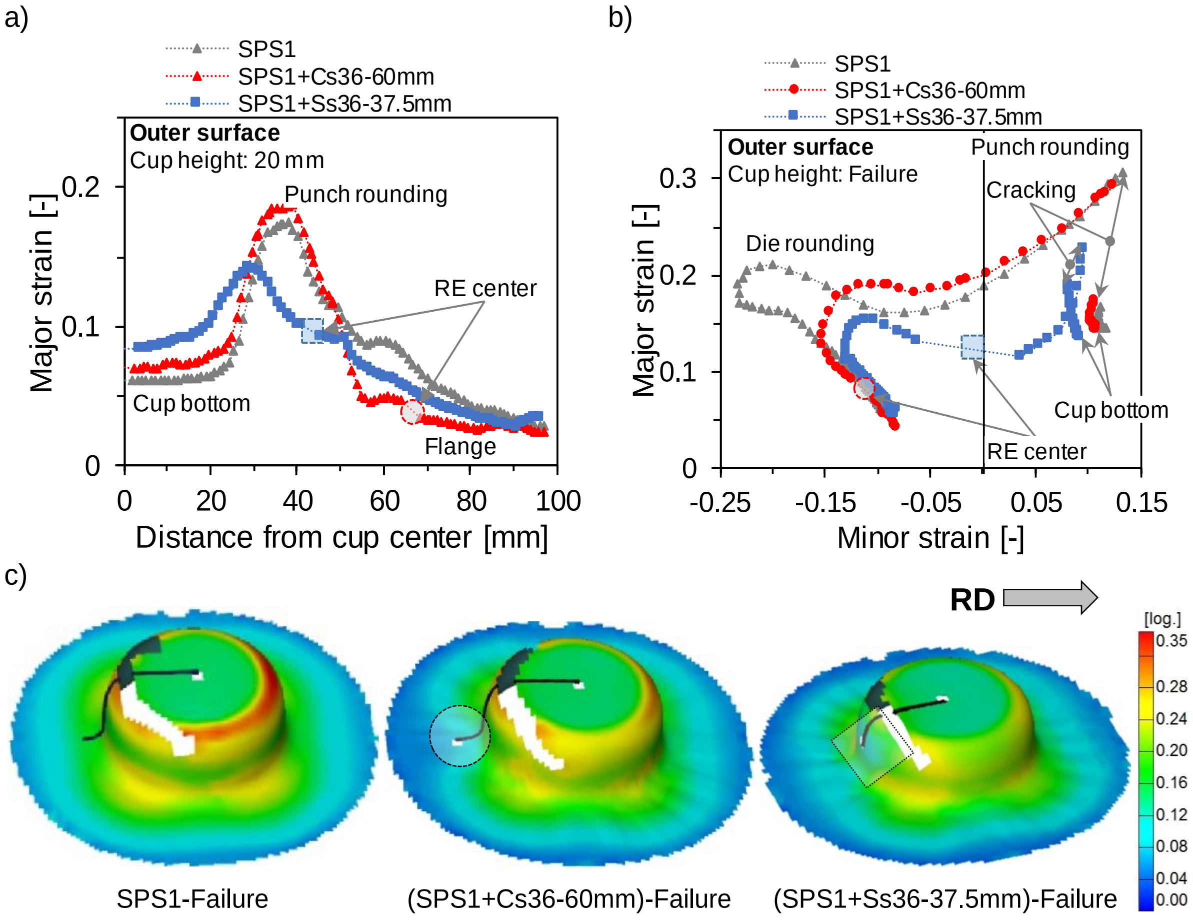

SPS1-Failure (SPS1+Cs36-60mm)-Failure (SPS1+Ss36-37.5mm)-Failure

Figure 5.19: Effect of the RE location (flange and punch edge) on the a) major strain distribution at h = 20 mm and b) ε_1–ε_2 distribution at failure along a radial section in addition to c) DIC images at failure [Har17].

To determine the effect of the RE location on the strain distribution and failure, **Figure 5.19** shows two conditions of R-SPS1: one flange-reinforced SPS1 (Cs36) and the other is reinforced at the punch edge (Ss36), as shown in **Figure 5.19-a)**. The different RE geometry in this comparison can be neglected as described earlier in the stretching part, as the geometry effect, for the same RE size, is not remarkable. The punch edge reinforced SPS1 shows a significant decrement of the major strain at the punch edge, sidewall and the flange. However, the cup-bottom region is overstrained higher than SPS1 and the flange-reinforced SPS1. Furthermore, a major reduction of the failure ε_1–ε_2 strain points in the case of the punch edge reinforced SPS1, as presented in **Figure 5.19-b)**, can be observed due to the sharp RE/core interface arising at the punch rounding with earlier failure.

The effect of the RE size is illustrated in **Figure 5.20-a)** by comparing SPS1 reinforced in the flange with Cs20 in respect to Cs36. It can be observed that the larger RE (Cs36) has a higher $\Delta\varepsilon$ in the reinforced region as well as at the die rounding.

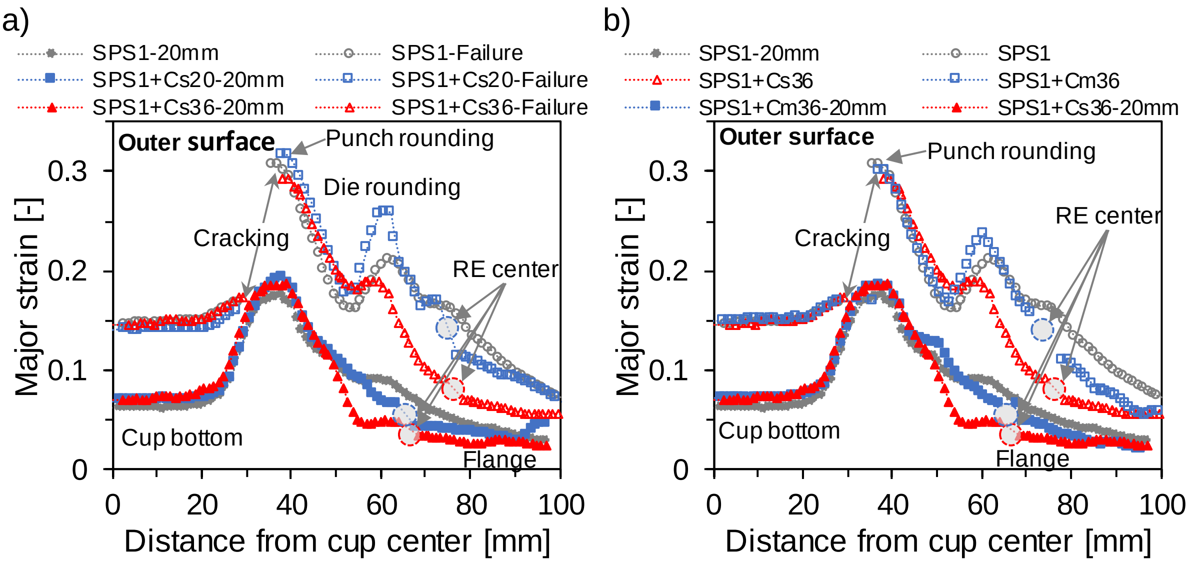

Figure 5.20: Major strain distribution in a radial section from cup center for SPS1 reinforced in the flange region showing the effect of a) the RE size (Cs36 vs. Cs20) and b) the RE material (mesh vs. solid) at h = 20 mm and at failure for the outer surface [Har17].

Figure 5.20-b) shows a comparison of the solid and meshed RE on the major strain distribution over the outer surface. In both cases, the strain was reduced at the RE center but the meshed shows a less difference for the outer surface in respect to SPS1, because the reinforced region of the meshed-reinforced SPS1 is not fully filled either with polymeric core or metallic RE, but with the 3.8 mm mesh size RE. The failure strains (at the punch rounding) of the meshed-reinforced SPS1 exhibited no remarkable reduction in respect to SPS1.

In order to highlight the effect of the size and material on the strain difference $\Delta\varepsilon$ over the circular sections locally at the RE location and globally in the flange, a comparison of SPS1 and R-SPS1 with Cs36, Cm36 and Cs20 is presented in **Figure 5.21-a)**. Moreover, the corresponding local $\Delta\varepsilon$ results, which are evaluated following the concept in **Figure 5.18-c)**, are summarized in **Figure 5.21-b)**. It can be observed that the global difference as well as the local Δε results follow the same order. Based on the local Δε% given in **Figure 5.21-b)**, the solid larger RE (Cs36) shows the highest Δε% values of - 45% at h = 20 mm, however the small solid (Cs20) or the large meshed (Cm36) ones show close results of -24% and -28%, respectively.

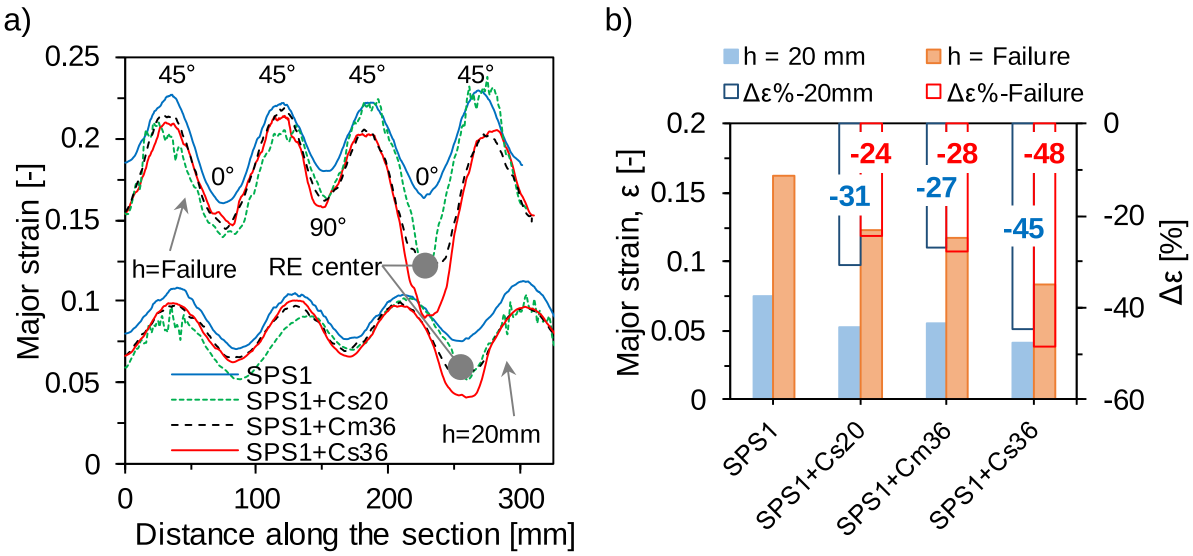

Figure 5.21: a) Major strain distribution in 60 mm^{Ø} circular section in the flange for SPS1 reinforced with three REs (Cs20, Cm36 and Cs36) in respect to SPS1 and b) the corresponding local Δε results at h = 20 mm and at failure.

Figure 5.22 illustrates the effect of inserting the RE, i.e. Cs36, in the flange of the different SPSs (SPS1–SPS4) considering the different skin sheet thicknesses and mechanical properties. Two correlations can be described:

1. At constant core thickness: **Figure 5.22-a)** shows the comparison between the three SPSs (SPS1–SPS3) that contain 0.6 mm core layer with varied skin sheet thickness and properties.

   SPS1 (based on 316L) shows higher strain values in the cup-bottom compared to SPS2 and SPS3 (based on TS245) due to its lower r value and leads therefore to higher affinity to thinning. At the punch rounding, SPS3 exhibits lower strains due to the thin skin sheet (0.24 mm). Minor differences of the failure strains between R-SPSs and SPSs were found at the punch rounding and major ones at the die rounding.
2. At constant skin sheet thickness and properties: **Figure 5.22-b)** is concerned with the effect of the core thickness (0.3 and 0.6 mm) by comparing SPS3 and SPS4. Significant flow blocking was found for the thinner SPS, i.e. SPS4, which led to overstretching of the sidewall, where cracking consequently took place. Another reason facilitating the sheet flow of SPS3 compared to SPS4 is the bigger gap size between the punch and drawing die as shown in **Table 5.4**.

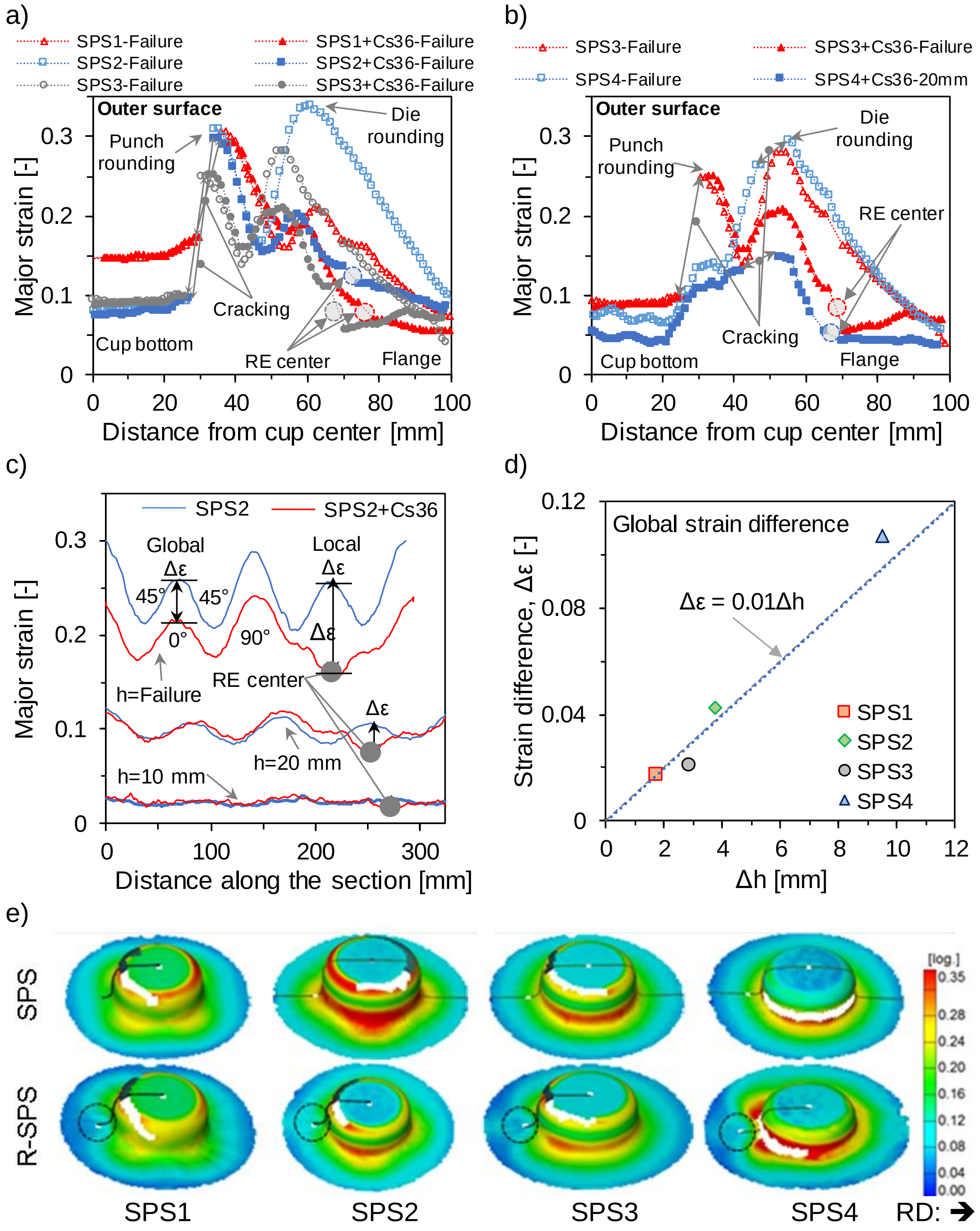

Figure 5.22: Major strain distribution of the SPS containing a) the same core thickness (0.6 mm) namely SPS1–SPS3 and b) the same steel grade and thickness but different core thickness (SPS3 vs. SPS4), c) an evaluation example of the circular sections of SPS2 and d) the global strain difference results with e) their DIC images at failure for the outer surface.

The tendency of the local Δε% can be determined with the help of the circular sections. **Figure 5.22-c)** exhibits a further example showing the effect of the RE on another SPS namely SPS2 and SPS2+Cs36 over the 60 mm$^{\varnothing}$ circular sections at h = 10, 20 mm and failure. The strain progress in respect to RD (0°) is different compared to SPS1 because of the different textures of the steel grades. For SPS2, the 45° shows a lower strain compared to the 0° and 90° directions.

The strain difference between SPS and R-SPS was evaluated globally (over the whole circular section) and locally (only in the reinforced region):

Globally: there is a need to correlate the drop in the cup height Δh with the global major strain difference Δε in the flange. So, **Figure 5.22-d)** shows the relation between Δε ($\Delta\varepsilon = \varepsilon_{SPS} - \varepsilon_{R-SPS}$) and Δh ($\Delta h = h_{SPS} - h_{R-SPS}$) at failure. The failure step was chosen where the global Δε can be neglected at h = 10 and 20 mm, as shown exemplary for SPS2 in **Figure 5.22-c)**. However, the major strain at failure was reduced in R-SPS compared to SPS due to the reduced cup height Δh. Furthermore, a direct or particularity a linear proportionality between Δε and Δh, was stated, as illustrated in **Figure 5.22-d)**. For instance, SPS2 exhibited Δh of 4 mm because of inserting the RE in the flange, that led to a global Δε of 0.04. Additionally, the thinner SPS4 shows the highest Δε and Δh values keeping the linearity.

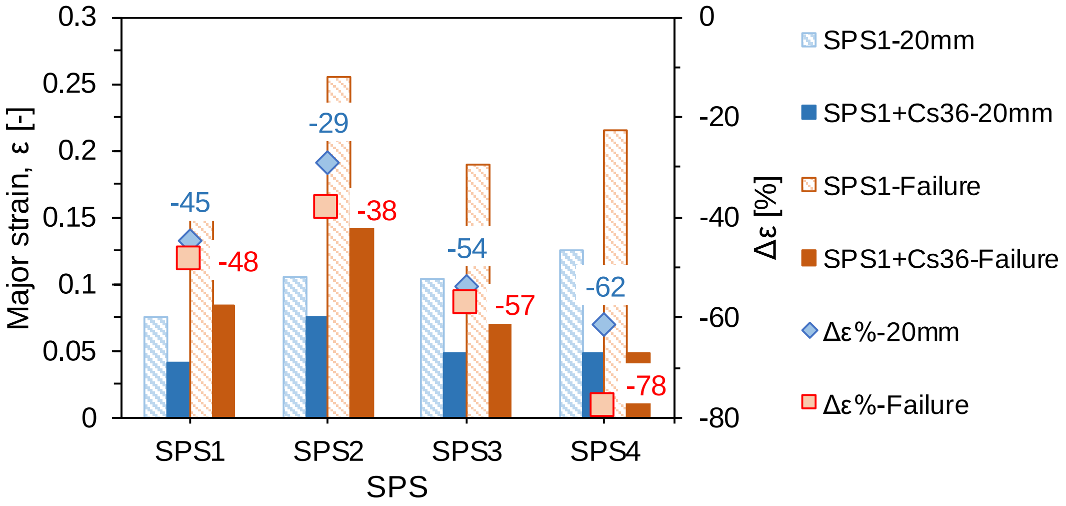

Figure 5.23: Local major strain differences between the different SPSs and the reinforced ones with Cs36 placed in the flange over the 60 mm$^{\varnothing}$ circular section at h = 20 mm and at failure. The labels represent the local Δε%.

Locally at the RE center, a substantial reduction of the strain was found, summarized and depicted in **Figure 5.23**. Δε is correlated to the SPS thickness for the same RE condition (Cs36 placed in the flange). The SPS thickness exhibits the significant influence, regardless the mechanical properties. The thinner the SPS are, the higher is Δε. Furthermore, Δε was correlated to ε_{SPS} in percentage through the Δε%, following $\Delta\varepsilon\% = 100 \cdot \Delta\varepsilon/\varepsilon_{SPS}$. These values are represented in the labels over the column chart for each SPS. As can be observed, the thinnest SPS laminate is the most affected one in the locally (**Figure 5.23**) as well as globally reinforced region (**Figure 5.22-c)**).

5.4. Summary and conclusions

In this chapter, an approach was proposed to adapt the MPM for mechanical and thermal joining methods, which is the local reinforcement of the core layer in the joining region. This reinforcement (RE) initiates heterogeneity in the core layer and particularly at the RE/core interface, in which reduced failure conditions occur. To define the influence of this heterogeneity on the forming potential of the MPM, an experimental methodology was proposed by subjecting the reinforced MPM sheets to different loading conditions, i.e. stretch forming and deep drawing. For this purpose, the effect of the RE size, type, geometry and location in respect to the forming punch was studied on different SPS thicknesses and mechanical properties. Based on the performed experiments, the following conclusions can be drawn:

1. The location of the RE plays the significant role determining in the failure conditions concerning the cup/dome height, maximum forming force and limiting strains. The factors affecting the formability of the R-MPM is presented in **Figure 5.24**.

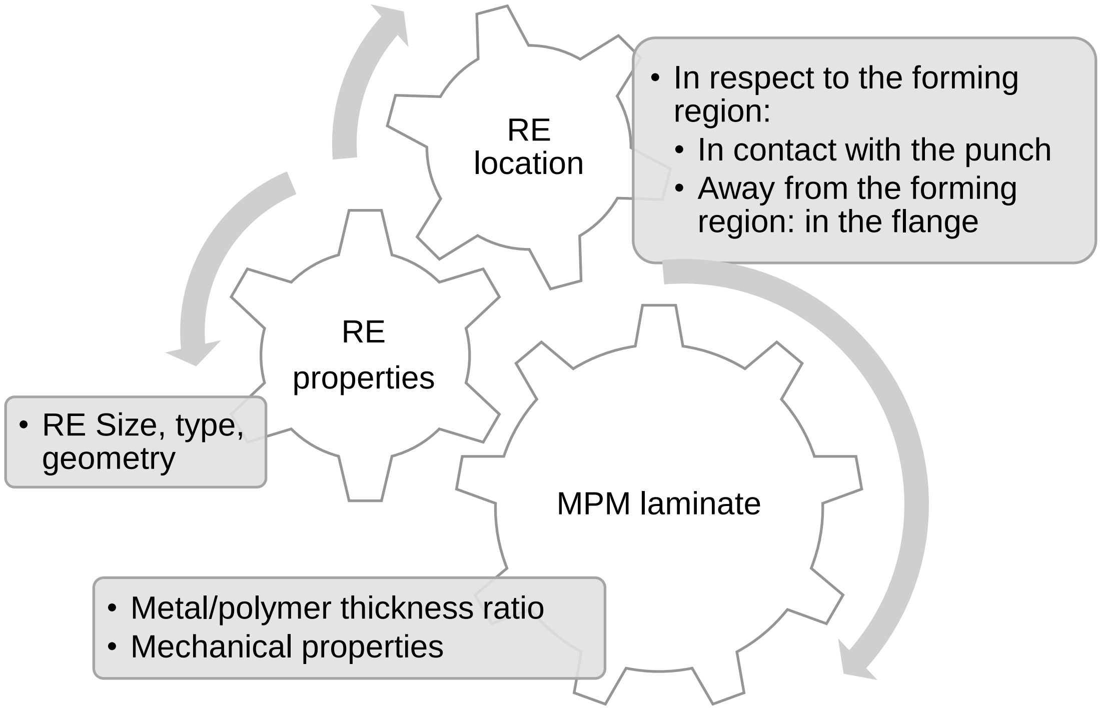

Figure 5.24: Parameters affecting the forming potential of the locally reinforced laminates.

2. If the RE is placed in the flange, i.e. away from the forming region, under deep drawing, minor differences occurred, which is desired to achieve the aimed reinforcing effect. However, the effect of laminate thickness is crucial even for the flange-reinforced MPM. The failure conditions in terms of the cup height can be reduced with 7% for thick SPS (SPS1 and SPS2: 1.6 mm) up to 30% for thinner ones (SPS4: 0.78 mm). Accordingly, the major strain differences occurred locally in the reinforced region that can reach more than 70% for thin MPM and up to 40% for the thicker ones at failure.
3. Due to the reduced cup height at failure, the global strain values in the flange is slightly reduced with about 10% for thick laminates (> 1.1 mm). This percentage increases for thinner laminates (< 0.8 mm): it can reach 50% for SPS4.
4. If the RE is located in the forming region, in a direct contact with the punch, a considerable reduction of the failure conditions in terms of the cup height and limiting strains take place.
5. The mechanical properties and thicknesses of the SPS components are, as expected, the basic parameters determining the deep drawability of the investigated SPS sheets. Accordingly, the flow blocking effect becomes more remarkable for SPS containing thinner SPS layers.
6. In the stretching experiments, the REs with different sizes, types, geometries were placed in the center of the SPS blank. Significant effect on the forming potential arose: the forming limits are increasingly declined with larger REs. Likely was the effect of the solid REs compared to the mesh-like ones. The meshed RE offers more weight saving compared to solid RE and additionally achieves the function of the RE by creating joinable sandwich sheets.

6. Summary and outlook

Due to the growing demands to reduce the fuel consumption and improve the environmental impact of the vehicles, developing alternative lightweight materials plays an essential role. Here, Metal/polymer/metal (MPM) multilayered composite materials are an innovative substitute to the used commercial sheets. MPM provide the desired lightweight potential with comparable structural stiffness in addition to an improved thermal and acoustic isolation properties. The current study is concerned with providing design guidelines and fundamental correlations regarding the production and shaping of low-density, flat, multi-layered and formable MPM systems. With the aid of the proposed investigation approaches, it was possible to produce tailored MPM following an ascending scaling approach starting from the monolithic materials up to multilayered structures.

A thermoplastic polyolefin foil with different thicknesses was common in the produced MPM, as it offers an outstanding forming potential at room temperature. In order to describe the correlation between the characteristic properties of the skin/core layers and their influence on the forming behaviour, diverse skin sheet materials, thicknesses and mechanical properties were considered. They include stainless, dual-phase and deep-drawable steel grades in addition to aluminium and titanium ones for different application fields. Furthermore, the applied production technology by roll bonding allowed the flexibility tailoring arbitrary MPM combinations via utilizing a compatible metal/polymer adhesive agent. Symmetric MPM systems (same skin sheet grade and thickness) and asymmetric ones were produced and characterized aiming at better understanding the forming behaviour for diverse MPM structures.

In addition to determining the characteristic properties of the monomaterials – like the mechanical properties, bending and deep drawability, and forming limit curves – additional specific properties of the MPM, like the adhesion quality and service life durability, were evaluated as well. Accordingly, the principal correlations could be derived for predicting and interpreting the forming behaviour. The metal/polymer interface and failure surface showed an outstanding durable adhesion quality that assured delamination-free forming operations that was confirmed by the performed experiments. Furthermore, the mechanical tensile properties were correlated primarily to the skin/core thickness ratio and the MPM symmetry and additionally could be verified with simple approaches like the rule of mixtures. The formability in terms of the deep drawability and the stretch forming showed a significant correlation with the MPM structure. The limiting drawing ratio (LDR) was reduced for higher core/skin thickness ratios and became more limited for thinner skin sheets. The formability is significantly reduced if the polymer core volume fraction exceeds 50%. In this case, the interlaminar shearing of the MPM layers and the thickness irregularities are unavoidable. The formability was further restricted, if the thinner skin sheets are positioned as the outer skins in asymmetric MPM sheets either in three or five layered systems. Furthermore, the drawing forces and the LDR could be predicted with a deviation up to ±15% utilizing empirical approaches.

Additionally, the core of the MPM sheets was locally reinforced with metallic reinforcements (RE) to enable applying mechanical and thermal joining methods and to reduce the local thinning especially of the thin skin sheets used in the MPM. It was found that inhomogeneity regions were arisen at the RE boundary under deep drawing and stretching conditions leading to reduced forming limits of the skin sheets and accordingly earlier failure. Different parameters were considered like the RE size, geometry, location and type. It was found that the RE location and the MPM thickness or rather the skin sheet thickness are the critical parameters: when the RE is positioned close or in the forming or rather the bending region, the forming limits are significantly reduced.

There is still a need to improve the forming behaviour of the reinforced MPM by means of further solution approaches to avoid the inhomogeneity regions at the interface between the RE and neighbour non-reinforced core and the shifting of the RE during forming. Further motivation is to develop approaches to predict the material flow especially in the surrounding of the reinforced regions considering the RE size and type.

The outlook is based in particular on the research needs and questions regarding the applicability of the of sandwich materials in a form (size and geometry) closer to the application scale utilizing the gained correlation from the current study. In this concern, investigating the crash behaviour of standard profiles like a double hat or Z-profiles is essential. At this point, some preliminary results were performed and published [Har16c, Har16a].

7. Zusammenfassung und Ausblick

Aufgrund der steigenden Anforderungen zur Reduzierung der Kraftstoffverbrauch und dementsprechend verbesserter Umweltauswirkungen der Fahrzeuge spielt die Entwicklung neuer leichter Materialien eine wesentliche Rolle. Metall / Polymer / Metall-Schichtverbunde (MPM) sind hier ein innovativer Ersatz für kommerzielle metallische Werkstoffe. Zusätzlich bieten derartige MPM verbesserte thermische und akustische Effekte bei vergleichbarer oder verbesserter spezifischer Struktursteifigkeit. Die vorliegende Studie beschäftigt sich mit der Herstellung sowie der Formgebung und Charakterisierung leichter, blechförmiger, mehrschichtiger MPM und der Formulierung von Designrichtlinien für ihren Einsatz. Mit Hilfe der vorgeschlagenen Untersuchungsansätze ist es möglich, maßgeschneiderte MPM nach einem aufsteigenden Skalierungsansatz – beginnend mit den monolithischen Materialien bis zum mehrschichtigen Laminataufbau - herzustellen.

Als Kernschicht der MPM wurde ein Thermoplast (PP/PE) in unterschiedlichen Dicken eingesetzt, das bei Raumtemperatur sehr gut formbar ist. Um ein Verständnis für das Zusammenspiel zwischen den Kennwerten der Deck- und Kernschichten und deren Auswirkung auf das Umformverhalten zu gewinnen, wurde der Deckschichtwerkstoff variiert. Dieses sowohl hinsichtlich der Materialsorte, seiner Oberflächenbeschaffenheit wie auch der Blechdicke. Es wurden Deckschichten aus rostfreien, Dualphasenstahl und Tiefzieh-Stahlsorten eingesetzt sowie vereinzelt auch Aluminium- und Titanwerkstoffe für unterschiedliche Applikationsansätze. Als Haftvermittler wurde ein 2-Komponenten-Epoxidharz eingesetzt, das für alle Materialverbindungen durch Walzen eine hervorragende Haftfestigkeit bot. Symmetrische (gleiche Deckschichtdicken bzw. gleiche Metallsorte) und asymmetrische MPM wurden entwickelt und charakterisiert.

Charakteristische Kennwerte – wie mechanische Kennwerte, Biege- und Tiefziehfähigkeit, Grenzformänderungskurven – wurden sowohl für die Monomaterialien wie auch für die MPM ermittelt und durch spezifische Kenngrößen wie Haft- und Dauerfestigkeit der Verbunde ergänzt. Damit ließen sich die wesentlichen Abhängigkeiten zur Vorhersage und Interpretation des Umformverhaltens ableiten. Die Grenzfläche zwischen Metall und Polymer zeigte eine hervorragende, beständige Haftfestigkeit, die einen delaminationsfreien Umformvorgang sicherstellt. Grundsätzlich lassen sich die mechanischen Kennwerte der MPM aus dem Zugversuch durch Anwendung der Mischungsregel ermitteln. Das Umformpotenzial hinsichtlich der Tief- und Streckziehbarkeit unterschiedlicher MPM ist signifikant abhängig vom jeweiligen Schichtaufbau. Das Grenzziehverhältnis beim Tiefziehen reduziert sich mit zunehmendem Kern- /Deckschichtdickenverhältnis und abnehmenden Deckschichtdicken. Das Umformpotenzial wird deutlich reduziert, wenn der Kernvolumenanteil 50% übersteigt. In diesem Fall sind die interlaminare Scherung der MPM-Schichten und Dickenunregelmäßigkeiten unter Tiefziehbedingungen unvermeidbar. Bei asymmetrischen MPM wird das Umformvermögen im Tiefziehprozess stärker eingeschränkt, wenn die dünneren Hautschichten als Außenschicht in sowohl drei- als auch fünflagigen Systemen positioniert sind. Mit den verfügbaren Ansätzen können die Ziehkräfte und das Grenzziehverhältnis mit einer Abweichung bis zu ±15% vorhergesagt werden.

Um mechanische oder auch thermische Verbindungen zu ermöglichen und eine lokale Dickenreduktion der dünnen MPM-Deckschichten zu vermeiden bzw. zu vermindern, wurde der Schichtverbund mit metallischen Einlagen (RE) lokal verstärkt. Beim Tief- und Streckziehen entstehen im Bereich der RE-Ränder im MPM Inhomogenitäten, die das Umformvermögen einschränken und zu einer frühzeitigen Rissbildung führen. Variiert wurden für die Analyse neben der RE-Größe deren Geometrie, der RE-Typ und die Lage in der Umformzone. Hierbei erwiesen sich die RE-Position und die Dicke des MPM-Schichtverbundes als kritische Parameter. Eine signifikante Reduzierung des Umformvermögens tritt auf, wenn die metallische Verstärkung nahe oder im Biegebereich der Umformung platziert wird.

Dieses Thema ist noch nicht abschließend bearbeitet und steht im Fokus weiterer Untersuchungen. Diese haben zum Ziel, Algorithmen zur Vorhersage des Materialflusses - besonders in der Umgebung der lokalen Verstärkungen – in Abhängigkeit von der Lage der Verstärkung, ihrer Größe und ihres Typs zu definieren.

Neben der Verwendung als blechförmige Strukturen weisen die MPM ein erhebliches, vielversprechendes Einsatzpotenzial als Crashelemente auf, wie in ersten Untersuchungen an Doppelhut- und Z-Profilen bereits gezeigt werden konnte [Har16b, Har16c]. Eine gezielte Steuerung und Kontrolle der Energieaufnahme über die Einstellung der Schichtdickenverhältnisse der MPM ist hier möglich.

8. Annexes

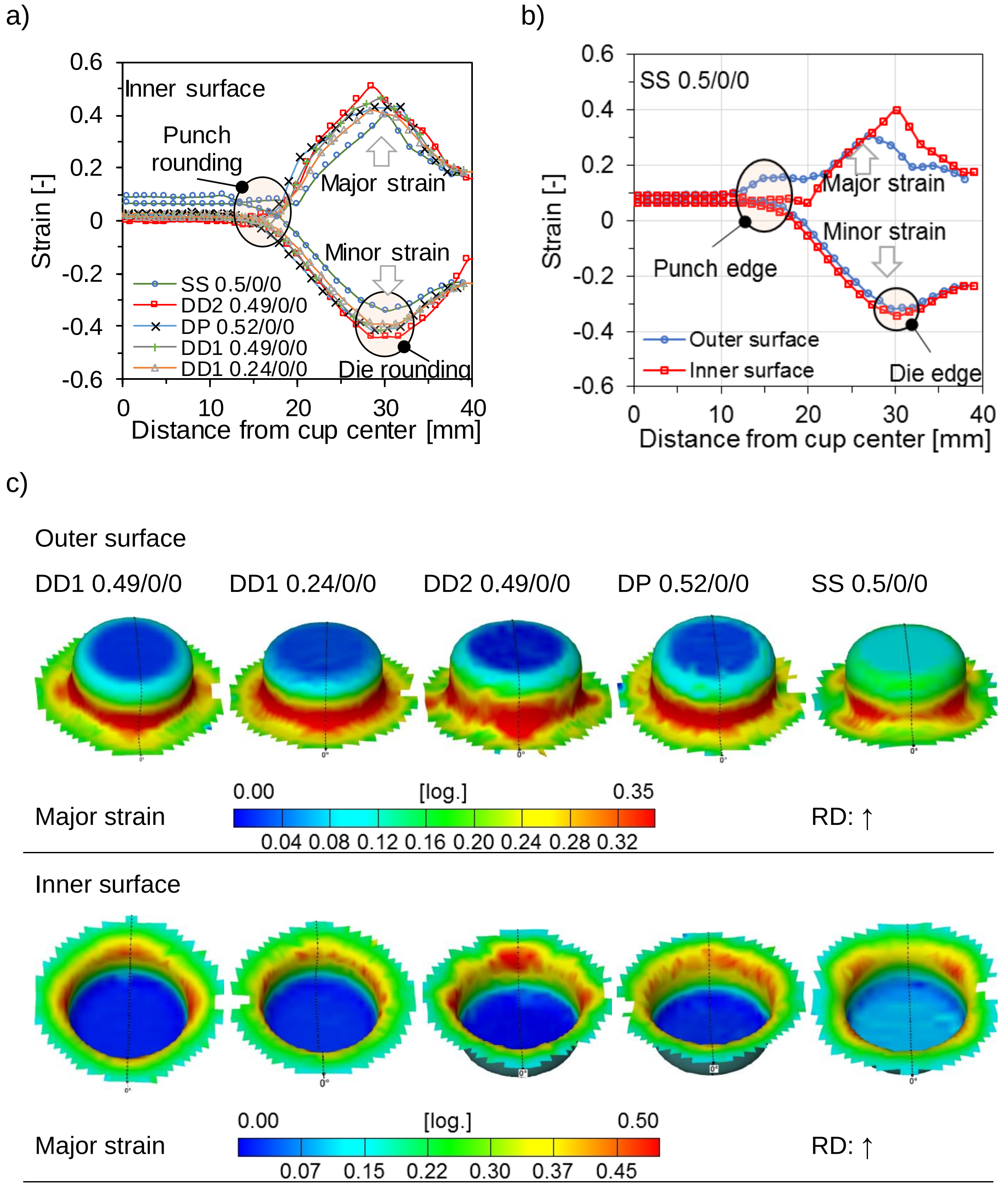

Figure 8.1: Major and minor strain distribution over a) the inner surfaces of the used five steel sheets and b) a comparison of this distribution between the inner and outer surface for the SS sheet, in addition to c) 3D major strain images of the outer and inner surfaces at h = 15 mm.

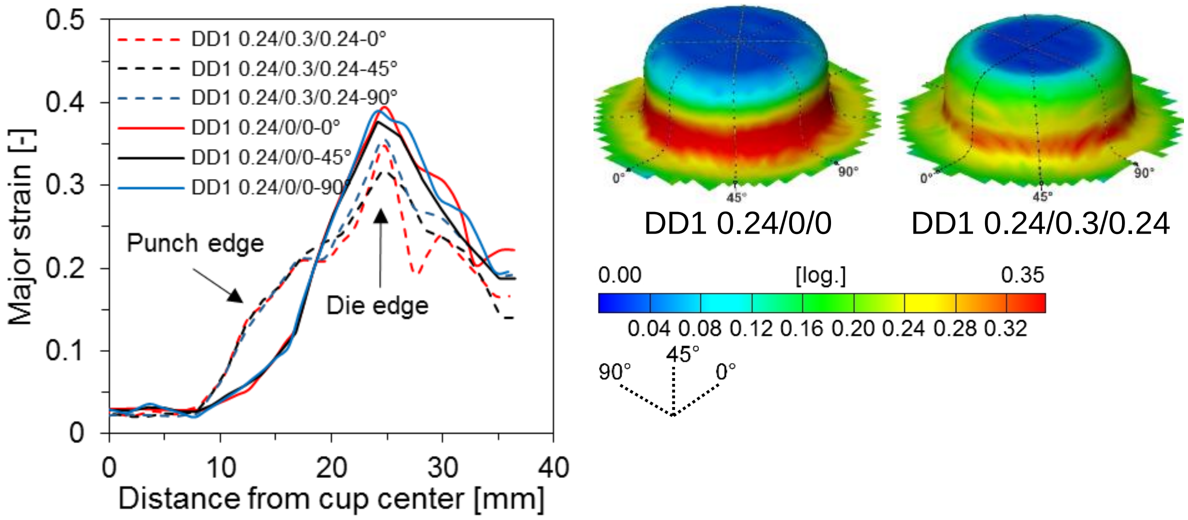

Figure 8.2: Anisotropic major strain distribution of the steel grade DD1 (0.24 mm) and its SPS in 0°, 45° and 90° to RD with their strain images at h = 15 mm.

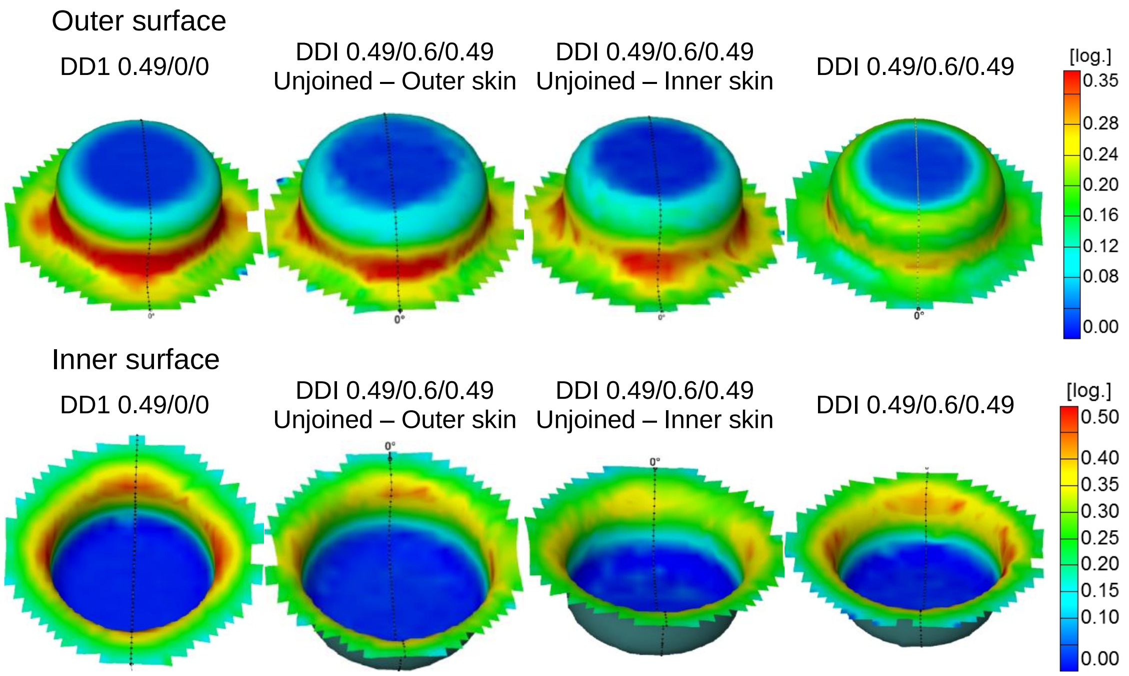

Figure 8.3: The major strain images at h = 15 mm Effect of the adhesion between the SPS layers.

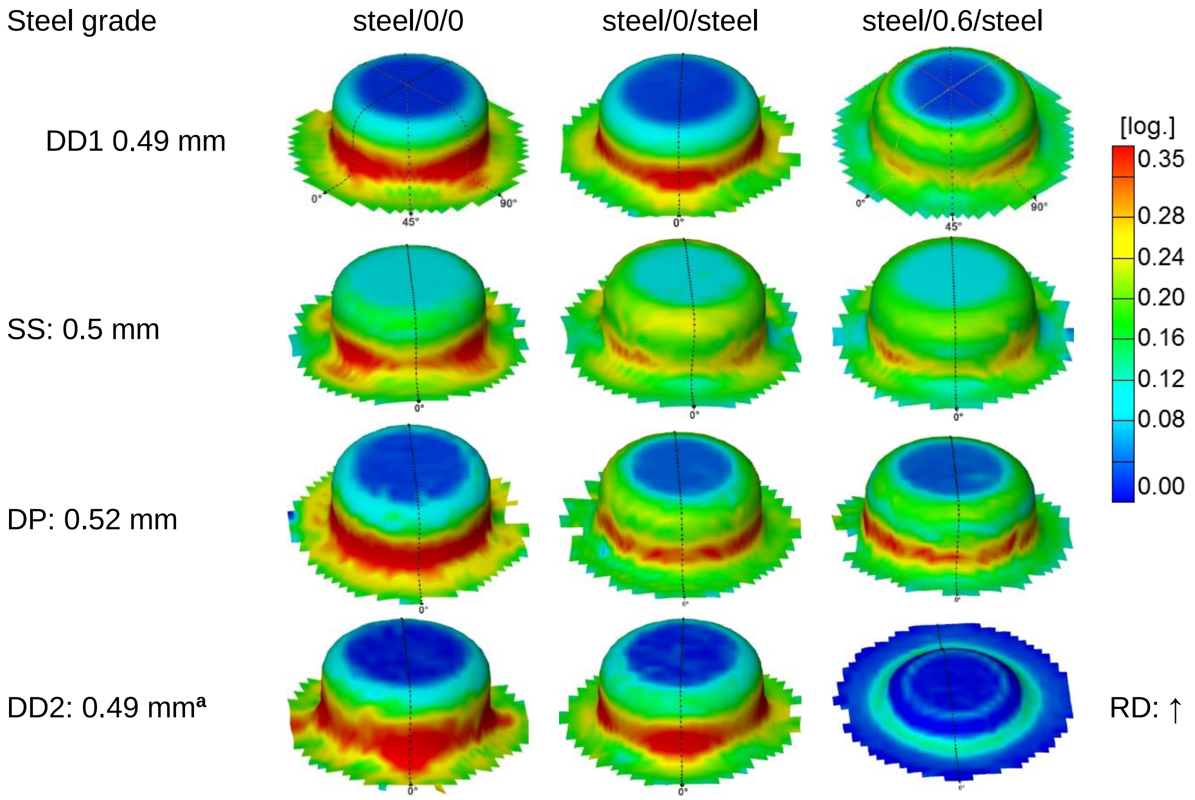

Figure 8.4: Major strain comparison of three configurations: steels (steel/0/0), sheet metal laminates (steel/0/steel) and SPS (steel/0.6/steel) at h = 15 mm determined by photogrammetry. ª: the symmetric SPS based on DD2 fails earlier, so the presented cup only at h = 5 mm.

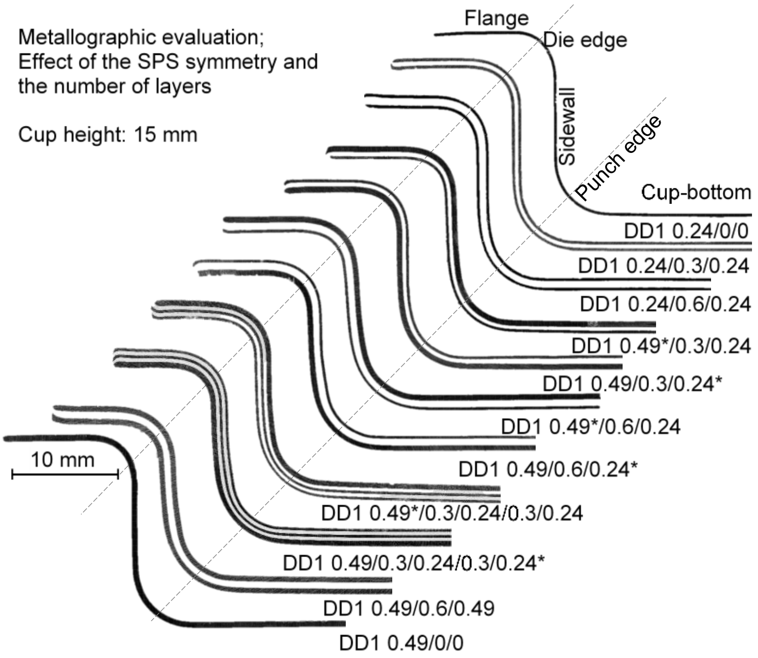

Figure 8.5: Effect of the SPS symmetry and the number of layers on the thickness distribution of the drawn cups at h = 15 mm. *: refers to the skin sheet in contact with the punch.

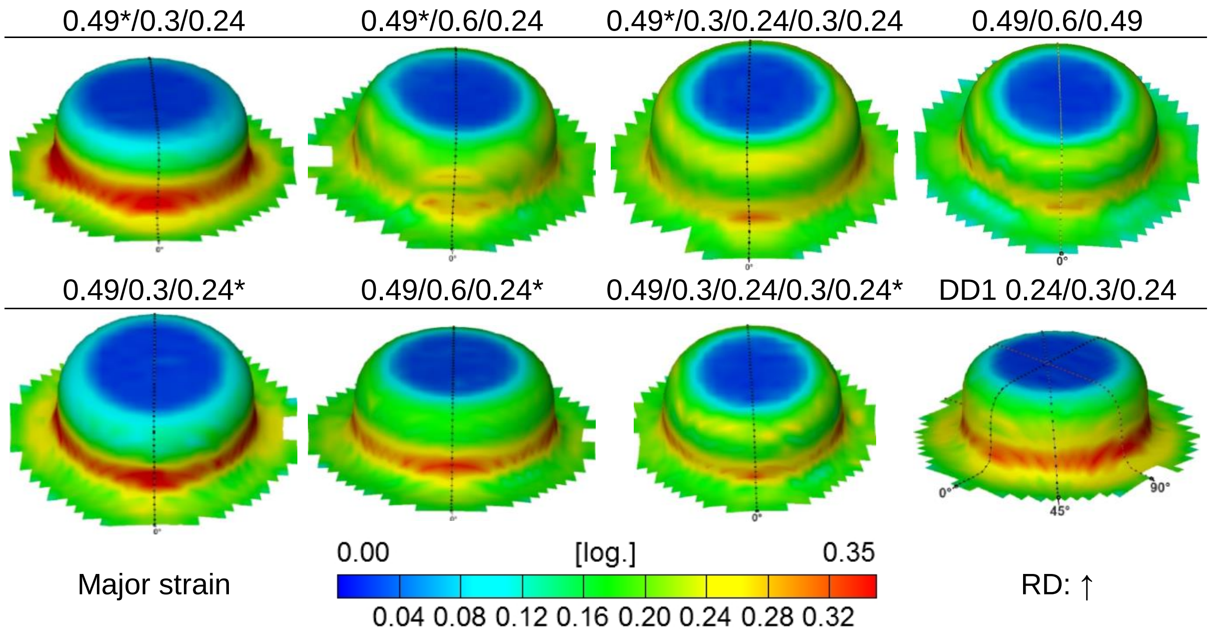

Figure 8.6: Effect of the SPS symmetry and the number of layers for some SPS based on DD1 at h = 15 mm in terms of the major strain images. *: refers to the skin sheet in contact with the punch.

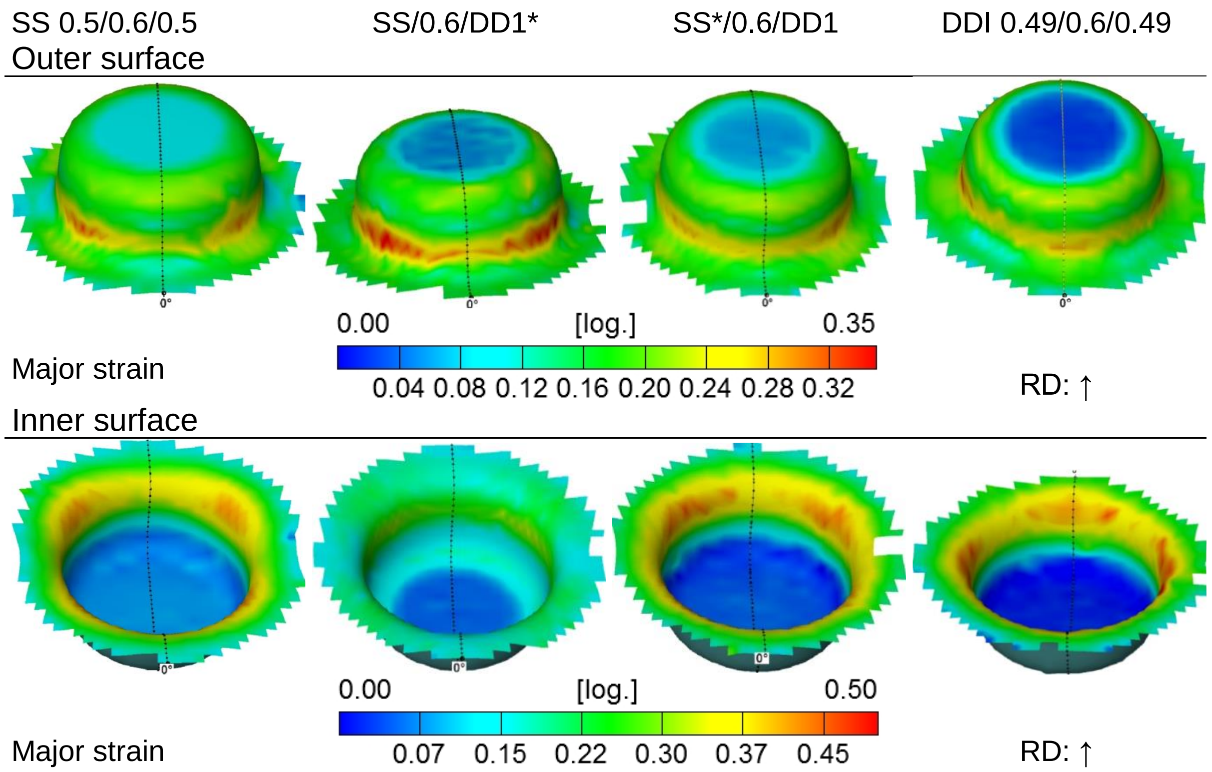

Figure 8.7: Effect of the SPS symmetry based on SS and DD1 grades on the major strain distribution images. *: refers to the skin sheet in contact with the punch.

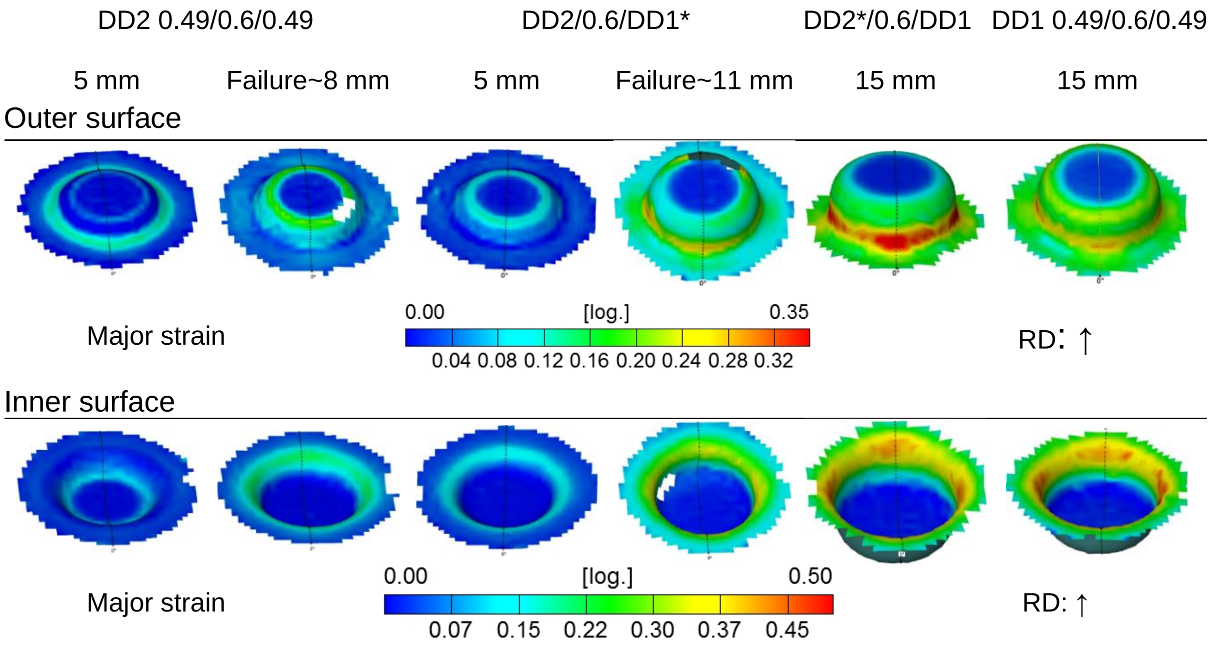

Figure 8.8: Effect of the SPS symmetry based on DD2 and DD1 steel grades on the major strain progresses in terms of the images on the outer and inner surfaces. *: refers to the skin sheet in contact with the punch.

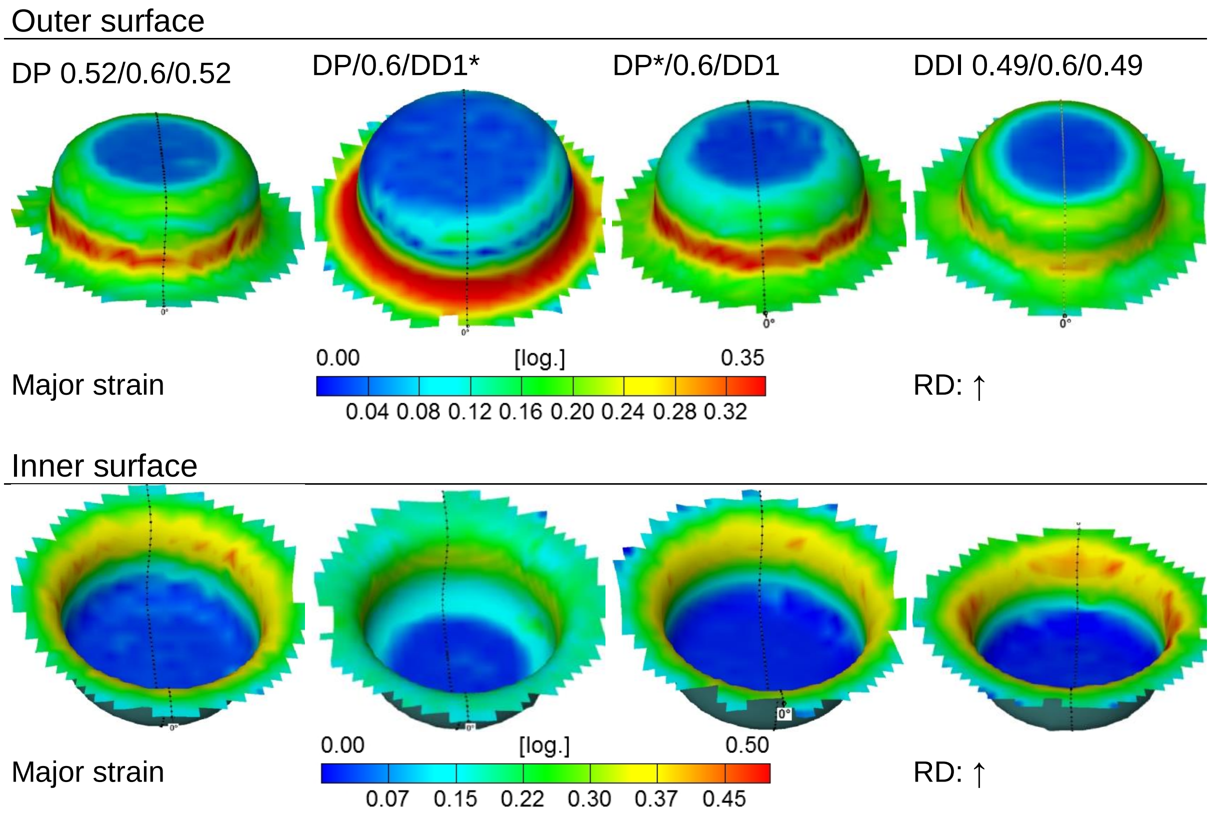

Figure 8.9: Effect of the SPS symmetry based on DP and DD1 grades on the major strain distribution images. *: refers to the skin sheet in contact with the punch.

This page intentionally left blank

Bibliography

[3A15a] 3A Composites GmbH: DIBOND® - the original. http://www.display.3acomposites.com/en/downloads/dibond.html.

[3A15b] 3A Composites GmbH: ALUCOBOND® for transport and industry. http://media.alucobond.com/pdf/alucobond/alucobond_ti/Alucobond_TI_ProInfo_EN.pdf.

[3A15c] 3A Composites GmbH: HYLITE® - The world's thinnest composite panel. http://media.alucobond.com/pdf/hylite/HYLITE_Flyer_EN.pdf.

[Ali13] Ali A.: Strain life failure of HDPE, PP and PMMA polymers. AL- Taqani, 2013 (26), P. 144–153.

[Alt12] Altan, T.; Tekkaya, A.E. Eds.: Sheet metal forming. Fundamentals. ASM International, Materials Park, Oh, 2012.

[Ama09] Amancio-Filho S. and dos Santos J.: Joining of polymers and polymer-metal hybrid structures: Recent developments and trends. Polymer Engineering & Science, 2009 (49), P. 1461–1476.

[Ari94] Arimes T.: HVAC and chemical resistance handbook for the engineer and architect. A compilation. BCT, Lexington Ky., 1994.

[Ash03] Ashby M. and Bréchet Y.: Designing hybrid materials. Acta Materialia, 2003 (51), P. 5801–5821.

[Ash05] Ashby M.: Chapter 13 - Designing Hybrid Materials. In: Materials Selection in Mechanical Design (Third Edition) (Ashby, M. F. Ed.). Butterworth-Heinemann, Oxford, 2005, P. 339–377.

[Ash08] Ashori A. and Nourbakhsh A.: A comparative study on mechanical properties and water absorption behaviour of fiber-reinforced polypropylene composites prepared by OCC fiber and aspen fiber. Polymer Composites, 2008 (29), P. 574–578.

[Asn00] Asnafi N., Langstedt G., Andersson C.-H., Östergren N. and Håkansson T.: A new lightweight metal-composite-metal panel for applications in the automotive and other industries. Thin-Walled Structures, 2000 (36), P. 289–310.

[AST00a] ASTM D1876-00: Test Method for Peel Resistance of Adhesives (T-Peel Test). ASTM International, West Conshohocken, PA, 2000.

[AST00b] ASTM D3165-00: Test Method for Strength Properties of Adhesives in Shear by Tension Loading of Single-Lap-Joint Laminated Assemblies. ASTM International, West Conshohocken, PA, 2000.

[AST08] ASTM E2218-2: Test Method for Determining Forming Limit Curves. ASTM International, West Conshohocken, PA, 2008.

[Atr13] Atrian A. and Fereshteh-Saniee F.: Deep drawing process of steel/brass laminated sheets. Composites Part B: Engineering, 2013 (47), P. 75–81.

[Ber09] Berger L., Lesemann M. and Sahr C.: SuperLight-Car - the Multi-Material Car Body. In: 7. European LS-DYNA Conference. DYNAmore GmbH. Salzburg, Austria, 2009, P. 1–8.

[Ber12] Bergmann J. and Stambke M.: Potential of Laser-manufactured Polymer-metal hybrid Joints. Physics Procedia, 2012 (39), P. 84–91.

[Ber99] Berthelot J.-M.: Classical Laminate Theory. In: Composite Materials (Berthelot, J.-M. Ed.). Springer New York, New York, NY, 1999, P. 287–311.

[Boe97] Boesenkool R., Hurkmans A., Jansen R. and Roukema M.: The development of steelite: the lightweight deep-drawable steel-plastic sandwich for automotive applications. In: Conference on Materials for Lean Weight Vehicles. Inst. of Materials, 1997, P. 61–66.

[Bol05] Bolt, P. J.; Gunnink, J.; van Leeuwen, J.; Nooij, d. M.und Werkhoven, R.: Method and apparatus for reducing wrinkle formation in deep drawing. Patent: US 20050268685 A1, 2005.

[Bol13] Bolay C., Liewald M., Vorhrer A., Stegmaier T., Hager T. and Planck H.: Innovative Schichtverbundwerkstoffe mit textiler Einlage für den Karosseriebau. In: EFB T36-Umformen, Schneiden, Verbinden im Leichtbau (EFB Ed.). EFB, Hannover, 2013, P. 117–133.

[Bol14] Bolay C.: Beitrag zur Umformung von ebenen und versteiften Schichtverbundwerkstoffen. Dissertation. Universität Stuttgart, Stuttgart, Deutschland, 2014.

[Bot06] Botelho E., Silva R., Pardini L. and Rezende M.: A review on the development and properties of continuous fiber/epoxy/aluminum hybrid composites for aircraft structures. Materials Research, 2006 (9), P. 247–256.

[Boz05] Bozhevolnaya E. and Lyckegaard A.: Structurally graded core inserts in sandwich panels. Composite Structures, 2005 (68), P. 23–29.

[Bro05] Brockmann W., Geiß P. and Czarnecki J. von: Prüfverfahren und Eigenschaften von Klebverbindungen. In: Klebtechnik. Wiley-VCH Verlag GmbH & Co. KGaA, 2005, P. 125–203.

[Bro09] Brockmann W., Geiß P., Klingen J. and Schröder B.: Adhesive bonding. Materials, applications and technology; translated by Bettina Mikhail. Wiley-VCH, Weinheim, 2009.

[Bro89] Brockmann W., Dorn L. and Käufer H.: Kleben von Kunststoff mit Metall. Springe-Verlag, Berlin, 1989.

[Buh14] Buhl J.: Umformverhalten und Grenzen von Schichtverbundwerkstoffen. Dissertation. Universität Siegen, Siegen, Deutschland, 2014.

[Bur05] Burchitz I., Boesenkool R., Zwaag, Sybrand van der and Tassoul M.: Highlights of designing with Hylite – a new material concept. Materials & Design, 2005 (26), P. 271–279.

[Cam09] Camanho P., Fink A., Obst A. and Pimenta S.: Hybrid titanium–CFRP laminates for high-performance bolted joints. Composites Part A: Applied Science and Manufacturing, 2009 (40), P. 1826–1837.

[Car09] Carrillo J. and Cantwell W.: Mechanical properties of a novel fiber–metal laminate based on a polypropylene composite. Mechanics of Materials, 2009 (41), P. 828–838.

[Cha10] Chamochin R., de Santayana, M. Cano, Abenojar J., Pantoja M., Ballesteros Y. and del Real, J. C.: The Effect of Surface Treatment on the Behavior of Toughened Acrylic Adhesive/GRP(epoxy) Composite Joints. Journal of Adhesion Science and Technology, 2010 (24), P. 1903–1916.

[Che06] Chen C.-Y., Jui-Chao Kuo, Hao-Long Chen and Weng-Sing Hwang: Experimental Investigation on Earing Behavior of Aluminum/Copper Bimetal Sheet. Materials Transactions, 2006 (47), P. 2434–2443.

[Che09] Chen, Y. L.; Faulkner, D. L.; Parlow, P. M.; Verbrugge, M. W.; Gayden, X. Q.; Fickes, J. D.und Foss, P. H.: Friction stir weld bonding of metal-polymer-metal laminates. Patent: Patent: US 7,628,876 B2, 2009.

[Che93] Chen C. and Lakes R.: Analysis of high-loss viscoelastic composites. Journal of Materials Science, 1993 (28), P. 4299–4304.

[Cor04] Cortes P.: The Tensile and Fatigue Properties of Carbon Fiber-reinforced PEEK-Titanium Fiber-metal Laminates. Journal of Reinforced Plastics and Composites, 2004 (23), P. 1615–1623.

[Cor06] Cortés P. and Cantwell W.: The prediction of tensile failure in titanium-based thermoplastic fibre–metal laminates. Composites Science and Technology, 2006 (66), P. 2306–2316.

[Cos05] Costa M., Almeida S. and Rezende M.: Hygrothermal effects on dynamic mechanical snalysis and fracture behaviour of polymeric composites. Materials Research, 2005 (8), P. 335–340.

[Dav01] Davies, J.M. Ed.: Lightweight sandwich construction. Blackwell Science, Oxford, Malden, MA, 2001.

[Den10] Deng H., Reynolds C., Cabrera N., Barkoula N.-M., Alcock B. and Peijs T.: The water absorption behaviour of all-polypropylene composites and its effect on mechanical properties. Composites Part B: Engineering, 2010 (41), P. 268–275.

[DIN06] DIN 53281: Testing of adhesively bonded joints - Preparation of test specimens. Beuth Verlag GmbH, Berlin, Germany, 2006.

[DIN09a] DIN EN ISO 12004-2: Bestimmung von Grenzformänderungskurven im Labor. Beuth Verlag GmbH, Berlin, 2009.

[DIN09b] DIN 8584-3: Manufacturing processes forming under combination of tensile and compressive conditions-Part 3. Beuth Verlag GmbH, Berlin, 2009.

[DIN14a] DIN EN ISO 10113: Sheet and strip – Determination of plastic strain ratio. Beuth Verlag GmbH, Berlin, 2014.

[DIN14b] DIN EN ISO 10275: Metallic materials - Sheet and strip - Determination of tensile strain hardening exponent. Beuth Verlag GmbH, Berlin, 2014.

[DIN80] DIN 50114: Testing of metals; tensile test on sheet or strip without using an extensometer. Beuth Verlag GmbH, Berlin, 1980.

[Doe10] Doege E. and Behrens B.-A.: Handbuch Umformtechnik. Springer Berlin Heidelberg, Berlin, Heidelberg, 2010.

[Dun06] Dunand M. and Gacel J.-N.: USILIGHT: A Cost-Effective Solution to Lighten Cars. In: SAE 2006 World Congress & Exhibition. SAE International400 Commonwealth Drive, Warrendale, PA, United States, 2006.

[End02] Endemann U., Glaser S. and Völker M.: Verbindungstechnik für Kunststoff-Metall-Hybridstrukturen: Kunststoff und Metall im festen Verbund. Kunststoffe, 2002 (11), P. 110–113.

[Eur16] European Steel and Alloy Grades: EN 10202: 2001 Cold reduced tinmill products. TS245 (1.0372): Electrolytic tinplate and electrolytic chromium/chromium oxide coated steel. http://www.steelnumber.com/en/steel_composition_eu.php?name_id=873#1, accessed December 2016.

[Fin03] Fink A., Kolesnikov B. and Wilmes H.: Hybrid Titanium Composite Material Improving Composite Structure Coupling. In: Proceedings CD: 20th AAAF Colloquium. Paris, France, 2003, P. 1–12.

[Fin13] Fink A.: Local Metal Hybridization of Composite Bolted Joints. In: Adaptive, tolerant and efficient composite structures (Wiedemann, M.; Sinapius, M. Eds.). Springer, Berlin, New York, 2013, P. 251–262.

[Fle12] Fleischer J., Elser J., Gebhardt J. and Weingärtner T.: Entwicklung von hochbelastbaren Krafteinleitungselementen für den hybriden Leichtbau. Lightweight Design. Lightweight Des, 2012 (5), P. 32–37.

[Fon13] Fondriest, D.: Welded metal laminate structure and method for welding a metal laminate structure. Patent: Patent: US 8,410,400 B2, 2013.

[Fra11] Frantz M., Lauter C. and Troester T.: Advanced Manufacturing Technologies for Automotive Structures in Multi-Material Design Consisting of High-Strength Steels and CFRP. In: 56th International Scientific Colloquium. Ilmenau, Deutschland, 2011.

[Gau06] Gauriat, A.; Calvez, C.; Schmit, F.; Nazikkol, C.; Filthaut, C.; Smith, R. H.und Pac, J.: Metal-polyamide/polyethylene-metal laminate. Patent: EP 1651432 B1, 2006.

[Goe05] Goede M., Ferkel H., Stieg J. and Dröder K.: Mischbauweisen Karosseriekonzepte - Innovationen durch bezahlbaren Leichtbau. In: 14. Aachener Kolloquium Fahrzeug- und Motorentechnik 2005, Aachen, 2005.

[Goe09] Goede M.: SuperLIGHT-Car project - An integrated research approach for lightweight car body innovations. In: Innovative Developments for lightweight vehicle structures. Wolfsburg, Germany, 2009, P. 25–38.

[GOM14] GOM mbH: ARAMIS Application Tensile Test. https://support.gom.com/display/DOCS/ARAMIS+Application+Tensile+Test, accessed 2015.

[Gow06] Gower H., Richardson I. and Pieters, R. R. G. M.: Pulsed laser welding of Steelite, a steel polypropylene laminate. Science and Technology of Welding and Joining, 2006 (11), P. 593–599.

[Gow07] Gower H.: Welding of a metal-polymer laminate. PhD Thesis. Delft University of Technology, Netherlands, 2007.

[Gra13] Graf A. and Lachmann L.: Umformeigenschaften von hybriden Schichtverbunden. In: 19. Symposium Verbundwerkstoffe und Werkstoffverbunde (Wanner, A.; Weidenmann, K. A. Eds.). Conventus Congressmanagement & Marketing, Jena, Germany, 2013, P. 511–519.

[Gre06] Gresham J., Cantwell W., Cardew-Hall M., Compston P. and Kalyanasundaram S.: Drawing behaviour of metal–composite sandwich structures. Composite Structures, 2006 (75), P. 305–312.

[Gro12] Großmann K., Bräunling S., Hardtmann A., Staiger E. and Kerber T.: 3D-Textil-Blech-Verbunde. UTFscience, 2012 (2), P. 1–5.

[Gro13] Großmann K., Cherif C., Staiger E., Ulbricht V. and Linse T.: 3D-Bauteile aus Blech und Textil durch umformende Verbundherstellung. EFB Forschungsbericht Nr. 383. EFB, Hannover, 2013.

[Hab09a] Habenicht G.: Kleben. Grundlagen, Technologien, Anwendungen. Springer, Berlin, 2009.

[Hab09b] Habenicht G.: Applied adhesive bonding. A practical guide for flawless results. Wiley-VCH, Weinheim, Chichester, 2009.

[Häl13] Hälsig A., Podlesak F., Mayr P., Trautmann M., Döhler C., Nestler D. and Wielage B.: Dissimilar joints between metal and fibre-reinforced plastics. In: 19. Symposium Verbundwerkstoffe und Werkstoffverbunde (Wanner, A.; Weidenmann, K. A. Eds.). Conventus Congressmanagement & Marketing, Jena, Germany, 2013, P. 343–349.

[Han12] Hankeln F., Gorny B., Lauter C., Schmidt H. and Damerow U.: Simulation and Manufacturing of Deep Drawn Parts Reinforced by Carbon Fibre Prepregs. In: Mechanics of Nano, Micro and Macro Composite Structures. Politecnico di Torino, Italien, 2012.

[Har14a] Harhash M., Carradò A. and Palkowski H.: Forming Limit Diagram of Steel/Polymer/Steel Sandwich Systems for the Automotive Industry. In: Advanced Composites for Aerospace, Marine, and Land Applications. John Wiley & Sons, Inc., 2014, P. 243–254.

[Har14b] Harhash M., Sokolova O., Carradò A. and Palkowski H.: Mechanical properties and forming behaviour of laminated steel/polymer sandwich systems with local inlays – Part 1. Compos. Struct., 2014 (118), P. 112–120.

[Har14c] Harhash M., Carradò A. and Palkowski H.: Lightweight titanium/polymer/titanium sandwich sheet for technical and biomedical application. Materialwissenschaft und Werkstofftechnik, 2014 (45), P. 1084–1091.

[Har16a] Harms V.: Crashrelevante Bauteile aus metallischen Sandwichen mit unverstärktem Polymerkern. M.Sc. Thesis. TU Clausthal, Clausthal-Zellerfeld, Deutschland, 2016.

[Har16b] Harhash M., Carradò A. and Palkowski H.: Deep- and Stretch-Forming of Steel/Polymer/Steel Laminates. In: 2. Int. Conf. "Euro Hybrid Materials & Structures". DGM. Kaiserslautern, Deutschland, 2016, P. 69–74.

[Har16c] Harhash M., Harms V., Carradò A. and Palkowski H.: Metall-Polymer Sandwichverbunde: nicht nur ein Leichtbaupotential. In: 23. Sächsische Fachtagung Umformtechnik. Dresden, Deutschland, 2016, P. 32-41.

[Har17] Harhash M., Carradò A. and Palkowski H.: Mechanical properties and forming behaviour of laminated steel/polymer sandwich systems with local inlays – Part 2. Stretching and Deep Drawing. Composite Structures, 2017 (160), P. 1081–1094.

[Hay94] Hayashi H. and Nakagawa T.: Recent trends in sheet metals and their formability in manufacturing automotive panels. Journal of Materials Processing Technology, 1994 (46), P. 455–487.

[Hin03] Hino R., Goto Y. and Yoshida F.: Springback of sheet metal laminates in draw-bending. Journal of Materials Processing Technology, 2003 (139), P. 341–347.

[Hir12] Hirt G., Bleck W., Bobzin K., Brecher C., Bührig-Polaczek A., Haberstroh E., Klocke F., Loosen P., Michaeli W., Poprawe R., Reisgen U., Taleb Araghi B., Arntz K., Bagcivan N., Bambach M., Bäumler S., Beckemper S., Bergweiler G., Breitbach T., Buchholz S., Bültmann J., Diettrich J., Do-Khac D., Eilbracht S., Emonts M., Flock D., Gerhardt K., Gillner A., Göttmann A., Grönlund O., Hartmann C., Heinen D., Herfs W., Hermani J.-P., Holtkamp J., Ivanov T., Jakob M., Janssen A., Karlberger A., Klaiber F., Kutschmann P., Neuß A., Prahl U., Roderburg A., Rosen C.-J., Rösner A., Saeed-Akbari A., Scharf M., Scheik S., Schleser M., Schöngart M., Stein L., Steiners M., Stollenwerk J., Theiß S. and Wunderle J.: Hybrid Production Systems. In: Integrative Production Technology for High-Wage Countries (Brecher, C. Ed.). Springer Berlin Heidelberg, Berlin, Heidelberg, 2012, P. 435–696.

[Hor14] Hora, P.; Volk, W. Eds.: Time-dependent Methods for the Evaluation of FLC. Zurich, Switzerland, 2014.

[Huf08] Hufenbach W., Jaschniski J., Weber T. and Weck D.: Numerical and experimental investigations on HYLITE sandwich sheets as an alternative sheet metal. Archives of Civil and Mechanical Engineering, 2008 (8), P. 67–80.

[Huf96] Hufenbach W. and Adam F.: Strukturierung und Klassifizierung von Stahlblech-Mehrschichtverbunden. Verl. und Vertriebsges. mbH, Düsseldorf, 1996.

[IEA15] IEA: IEA Statictics: CO_2 Emissions from Fuel Combustion- Highlights (2015 Edition), Paris, France, 2015.

[Jan13] Jandel A.-S. and Meuthen B.: Coil Coating. Bandbeschichtung: Verfahren, Produkte und Märkte. Springer Vieweg, Wiesbaden, 2013.

[Jas12] Jaschinski J.: Zum Strukturverhalten dünnwandiger Leichtbau-Sandwichbleche. Dissertation. TU Dresden, Dresden, Deutschland, 2012.

[Joh96] Johnson W., Li E. and Miller J.: High temperature hybrid titanium composite laminates. An early analytical assessment. Applied Composite Materials, 1996 (3), P. 379–390.

[Joh98] Johnson W., Cobb T., Lowther S. and St Clair T.: Hybrid titanium composite laminates: a new aerospace material. NASA Technical Reports Server (NTRS), 1998 (Report No.: 20040105645), P. 1–3.

[Joo13] Joo M., Suh D. and Bhadeshia H.: Mechanical Anisotropy in Steels for Pipelines. ISIJ International, 2013 (53), P. 1305–1314.

[Jür09] Jürgen Leohold; Oliver Scroeter Eds.: Innovative Developments for lightweight vehicle structures. Wolfsburg, Germany, 2009.

[Kah14] Kah P., Suoranta R. and Martikainen M.: Techniques for Joining Dissimilar Materials: Metals and Polymers. Rev. Adv. Mater. Sci., 2014 (36), P. 152–164.

[Kal12] Kalyanasundaram S., DharMalingam S., Venkatesan S. and Sexton A.: Effect of process parameters during forming of self reinforced – PP based fiber metal laminate. In: Mechanics of Nano, Micro and Macro Composite Structures. Politecnico di Torino, Italien, 2012.

[Kar12] Kardes N.: Deep Drawing of Round and Rectangular Cups. In: Sheet metal forming (Altan, T.; Tekkaya, A. E. Eds.). ASM International, Materials Park, Oh, 2012, P. 105–127.

[Kar97] Karlsson K. and TomasÅström B.: Manufacturing and applications of structural sandwich components. Composites Part A: Applied Science and Manufacturing, 1997 (28), P. 97–111.

[Kee65] Keeler S.: Determination of Forming Limits in Automotive Stampings. Sheet Metal Industries, 1965 (42), P. 683–691.

[Kim03] Kim K., Kim D., Choi S., Chung K., Shin K., Barlat F., Oh K. and Youn J.: Formability of AA5182/polypropylene/AA5182 sandwich sheets. Journal of Materials Processing Technology, 2003 (139), P. 1–7.

[Kim08] Kim B. and Lee D.: Characteristics of joining inserts for composite sandwich panels. Composite Structures, 2008 (86), P. 55–60.

[Kim13] Kim H., Leea M. and Kang C.: The Fabrication of a Hybrid Material Using the Technique of Hot-Press Molding. Materials and Manufacturing Processes, 2013 (28).

[Kim97] Kim J.-K. and Yu T.-X.: Forming and failure behaviour of coated, laminated and sandwiched sheet metals. a review. Journal of Materials Processing Technology, 1997 (63), P. 33–42.

[Lam15a] Lamera AB: Hybrix™ - products & technology. http://www.lamera.se/eng/index.php?option=com_content&task=view&id=13&Itemid=30, accessed 29 Dec 2015.

[Lam15b] Lambiase F.: Mechanical behaviour of polymer–metal hybrid joints produced by clinching using different tools. Materials & Design, 2015 (87), P. 606–618.

[Lan06] Lange G.: Beitrag zum Umformverhalten von dreischichtigen austenitischen Sandwichverbunden mit polymerer Kernschicht. Dissertation. TU Clausthal, Clausthal-Zellerfeld, Deutschland, 2006.

[Lan95] Lange, K. Ed.: Handbook of metal forming. Society of Manufacturing Engineers, Dearborn, Mich., 1995.

[Lau11] Lauter C., Frantz M. and Tröster T.: Großserientaugliche Herstellung von Hybridwerkstoffen durch Prepregpressen. Lightweight Design, 2011 (4), P. 48–54.

[Lau14] Laurenz R.: Stahlentwicklung aus Sicht der Fügetechnik. In: Der Ausschuss für Technik (AfT) -Tagung. Halle (Saale), Deutschland, 2014.

[Lim11] Lim J. and Lee D.: Development of the hybrid insert for composite sandwich satellite structures. Composites Part A: Applied Science and Manufacturing, 2011 (42), P. 1040–1048.

[Lis93] Liston E., Martinu L. and Wertheimer M.: Plasma surface modification of polymers for improved adhesion: a critical review. Journal of Adhesion Science and Technology, 1993 (7), P. 1091–1127.

[Liu12] Liu J.-g., Liu W. and WANG J.-x.: Influence of interfacial adhesion strength on formability of AA5052/polyethylene/AA5052 sandwich sheet. Transactions of Nonferrous Metals Society of China, 2012 (22), P. s395–s401.

[Liu13a] Liu J.-g. and Xue W.: Formability of AA5052/polyethylene/AA5052 sandwich sheets. Transactions of Nonferrous Metals Society of China, 2013 (23), P. 964–969.

[Liu13b] Liu J., Liu W. and Xue W.: Forming limit diagram prediction of AA5052/polyethylene/AA5052 sandwich sheets. Materials & Design, 2013 (46), P. 112–120.

[Man14] Mandolfino C., Lertora E. and Gambaro C.: Cold Plasma Pretreatment of Carbon Fibre Composite Substrates to Improve Adhesive Bonding Performance. Advances in Aerospace Engineering, 2014 (2014), P. 1–7.

[Mar02] Marciniak Z., Duncan J. and Hu S.: Mechanics of sheet metal forming. Butterworth-Heinemann, Oxford, Boston, 2002.

[Mar10] Marks P. and Tirler W.: Internationaler Stahlvergleich. Beuth, Berlin, Wien, Zürich, 2010.

[Mar13] Marklund E., Hellström P. and Wingborg J.: Report Nr. 1315: Evaluation of CFRP-Hybrix^{TM} integrated joints, Swerea SICOMP AB, Sweden, 2013.

[Mar79] Marciniak Z. and Kuczyński K.: The forming limit curve for bending processes. International Journal of Mechanical Sciences, 1979 (21), P. 609–621.

[McG05] McGinnis M., Pessiki S. and Turker H.: Application of three-dimensional digital image correlation to the core-drilling method. Experimental Mechanics, 2005 (45), P. 359–367.

[Mck07] Mckown S. and Cantwell W.: Investigation of Strain-rate Effects in Self-reinforced Polypropylene Composites. Journal of Composite Materials, 2007 (41), P. 2457–2470.

[Mer10] Merklein M., Kuppert A. and Geiger M.: Time dependent determination of forming limit diagrams. CIRP Annals - Manufacturing Technology, 2010 (59), P. 295–298.

[Mer14] Merklein M., Kuppert A. and Affronti E.: An Improvement of the Time Dependent Method Based on the Coefficient of Correlation for the Determination of the Forming Limit Curve. Advanced Materials Research, 2014 (1018), P. 215–222.

[Moh05] Mohr D.: On the role of shear strength in sandwich sheet forming. International Journal of Solids and Structures, 2005 (42), P. 1491–1512.

[Nes13] Nestler D., Böger T. and Wielage B.: Fügeverbindung zwischen CFK und Metall auf Basis des Lötens. In: 19. Symposium Verbundwerkstoffe und Werkstoffverbunde (Wanner, A.; Weidenmann, K. A. Eds.). Conventus Congressmanagement & Marketing, Jena, Germany, 2013, P. 336–342.

[Nes14a] Nestler D., Jung H., Arnold S., Wielage B., Nendel S. and Kroll L.: Thermoplastische Hybridlaminate mit variabler Metallkomponente. Materialwissenschaft und Werkstofftechnik, 2014 (45), P. 531–536.

[Nes14b] Nestler D.: Beitrag zum Thema Verbundwerkstoffe - Werkstoffverbunde. Status quo und Forschungsansätze. Univ.-Verl., Chemnitz, 2014.

[Nes16] Nestler D., Trautmann M., Nendel S., Wagner G. and Kroll L.: Innovative hybrid laminates of aluminium alloy foils and fibre-reinforced thermoplastic layers. Materialwissenschaft und Werkstofftechnik, 2016 (47), P. 1121–1131.

[Neu06] Neugebauer R. and Scheffler S.: Schaffung umformtechnischer Grundlagen bei der Verarbeitung von Metall-Kunststoff-Verbunden. EFB Forschungsbericht Nr. 248. EFB, Hannover, 2006.

[Nut08] Nutzmann M.: Umformung von Mehrschichtverbundblechen für Leichtbauteile im Fahrzeugbau. Dissertation. RWTH Aachen, Aachen, Deutschland, 2008.

[Pal06] Palkowski H., Giese P., Wesling V., Lange G., Spieler S. and Göllner J.: Neuartige Sandwichverbunde – Herstellung, Umformverhalten, Fügen und Korrosionsverhalten. Materialwissenschaft und Werkstofftechnik, 2006 (37), P. 605–612.

[Pal11] Palkowski H.: Herstellung maßgeschneiderter hochfester, hybrider Sandwichstrukturen: SFB675 - Teil A3, Clausthal-Zellerfeld, Germany, 2011.

[Pal12] Palaniswamy H. and Billur E.: Ch. 4: Plastic Deformation-Flow Stress, Anisotropy, and Formability. In: Sheet metal forming (Altan, T.; Tekkaya, A. E. Eds.). ASM International, Materials Park, Oh, 2012, P. 33–52.

[Pal14] Palkowski H.: Das Umformverhalten von Stahl/Polymer/Stahl-Sandwichverbunden mit lokalen, flächigen Verstärkungen, Abschlussbericht: DFG PA 837/21-1. DFG, Clausthal-Zellerfeld, Deutschland, 2014.

[Pal15] Palkowski H., Sokolova O. and Carradò A.: Sandwich Materials. In: Encyclopedia of automotive engineering (Crolla, D.; Foster, D. E. et al. Eds.). Wiley, Chichester, West Sussex, United Kingdom, 2015, P. 1–17.

[Pal16] Palkowski H. and Carradò A.: Metal-Polymer-Metal Laminates for Lightweight Application. Key Engineering Materials, 2016 (684), P. 323–334.

[Par10] Parsa M., Ettehad M., Matin P. and Al Ahkami, S. Nasher: Experimental and Numerical Determination of Limiting Drawing Ratio of Al3105-Polypropylene-Al3105 Sandwich Sheets. Journal of Engineering Materials and Technology, 2010 (132), P. 31004.

[Par13] Parsa M., Ettehad M. and Matin P.: Forming Limit Diagram Determination of Al 3105 Sheets and Al 3105/Polypropylene/Al 3105 Sandwich Sheets Using Numerical Calculations and Experimental Investigations. Journal of Engineering Materials and Technology, 2013 (135), P. 31003.

[Pat13] Patberg, L.; Hempowitz, H.und Mayer, S.: Application-specific weldable composite metal sheet. Patent: Patent: WO 2013164173 A1, 2013.

[Per11] Perterer M., Wedekind M. and Baier H.: Imperfektionsbewertung von Faserverbund-Metallstrukturen mit zerstörungsfreien Prüfverfahren. In: Deutscher Luft- und Raumfahrtkongress (DGLR Ed.). DGLR, Germany, 2011, P. 1–7.

[Pic07] Pickin C., Young K. and Tuersley I.: Joining of lightweight sandwich sheets to aluminium using self-pierce riveting. Materials & Design, 2007 (28), P. 2361–2365.

[Raj15] Rajabi A., Kadkhodayan M., Manoochehri M. and Farjadfar R.: Deep-drawing of thermoplastic metal-composite structures: Experimental investigations, statistical analyses and finite element modeling. Journal of Materials Processing Technology, 2015 (215), P. 159–170.

[Rey07] Reyes G. and Kang H.: Mechanical behaviour of lightweight thermoplastic fiber–metal laminates. Journal of Materials Processing Technology, 2007 (186), P. 284–290.

[Rod12] Rodríguez R., Paiva W. de, Sollero P., Bertoni Rodrigues M. and Albuquerque É. de: Failure criteria for adhesively bonded joints. International Journal of Adhesion and Adhesives, 2012 (37), P. 26–36.

[Rod14] Rodríguez-Vidal E., Lambarri J., Soriano C., Sanz C. and Verhaeghe G.: A Combined Experimental and Numerical Approach to the Laser Joining of Hybrid Polymer – Metal Parts. Physics Procedia, 2014 (56), P. 835–844.

[Rom71] Romanowski V.: Handbuch der Stanzereitechnik (5. Aufl.). Verlag Technik VEB, Berlin, 1971, ©1965.

[Sat14] Satheeshkumar V. and Narayanan R.: Formability of adhesive-bonded steel sheets with artificial finite adhesive defects. The Journal of Strain Analysis for Engineering Design, 2014 (49), P. 286–300.

[Sat15] Satheeshkumar V. and Narayanan R.: Experimental evaluation and prediction of deep drawability of adhesive bonded steel sheets. Materialwissenschaft und Werkstofftechnik, 2015 (46), P. 713-735.

[Sax15] Saxena K., Das I. and Mukhopadhyay J.: Evaluation of bending limit curves of aluminium alloy AA6014-T4 and dual phase steel DP600 at ambient temperature. International Journal of Material Forming, 2015

[Sch13] Schulze K., Hausmann J. and Wielage B.: The Stability of Different Titanium-PEEK Interfaces against Water. Procedia Materials Science, 2013 (2), P. 92–102.

[Sch14] Schricker K., Stambke M., Bergmann J., Bräutigam K. and Henckell P.: Macroscopic Surface Structures for Polymer-Metal Hybrid Joints Manufactured by Laser Based Thermal Joining. Physics Procedia, 2014 (56), P. 782–790.

[Sch15] Scholz P., Schieck F., Müller R., Seidlitz H., Gerstenberger C., Osiecki T., Grbic N., Behrens B.-A., Vucetic M. and Neumann A.: Umformprozessketten für Bauteile aus Faser-Kunststoff/Metall-Verbunden. In: EFB T40-Intermezzo der hybriden Werkstofflösungen: Hat Blech eine Zukunft? (EFB Ed.). EFB, Hannover, 2015, P. 151–171.

[Sch93] Schijve, J.: Report LR-715: Development of fibre-metal laminates, ARALL and GLARE, new fatigue resistant materials. Delft University of Technology, 1993.

[Sem90] Semiatin, S.L. Ed.: ASM handbook - Vol. 14B. ASM International, Materials Park, Ohio, 1990-.

[Sgu15] Sguazzo C. and Hartmann S.: Experimental investigations on PP-PE foil specimens. In: PAMM Proceedings in Applied Mathematics and Mechanics, 2015, P. 229–230.

[Sha14] Sharma S.: Sandwich Steels for Crash Energy Absorption Applications. PhD Thesis. University of Warwick, Warwick, UK, 2014.

[Sic14] Sickert M. and Haberstroh E.: Thermal Direct Joining for Hybrid Plastic Metal Structures. In: 1. Int. Conf. "Euro Hybrid Materials & Structures". DGM. Stade, Deutschland, 2014, P. 42–45.

[Sie55] Siebel E. and Weiss H.: Untersuchungen an einigen Problemen des Tiefziehens. I. Teil. VS Verlag für Sozialwissenschaften, Wiesbaden, s.l., 1955.

[Sok11a] Sokolova O., Carradò A. and Palkowski H.: Adhesion and Formability of Thin Steel/Polymer/Steel Hybrid Sandwich Composites. steel research international, 2011 (Special edition), P. 435–440.

[Sok11b] Sokolova O., Carradò A. and Palkowski H.: Metal–polymer–metal sandwiches with local metal reinforcements: A study on formability by deep drawing and bending. Composite Structures, 2011 (94), P. 1–7.

[Sok12] Sokolova O.: Study of metal/polymer/metal hybrid sandwich composites for the automotive industry. Dissertation. TU Clausthal, Clausthal-Zellerfeld, Deutschland, 2012.

[Son08] Song K.-I., Choi J.-Y., Kweon J.-H., Choi J.-H. and Kim K.-S.: An experimental study of the insert joint strength of composite sandwich structures. Composite Structures, 2008 (86), P. 107–113.

[Sta14] Staiger E., Hild M., Hund R.-D., Cherif C., Bräunling S. and Hardtmann A.: Hybridverbunde aus Blech Und Textil Oberflächen Haftungsgerecht Gestalten. adhäsion Kleben & Dichten, 2014 (58), P. 32–35.

[Sta15] Staiger E., Diestel O., Cherif C., Bräunling S. and Hardtmann A.: Hybridverbundbauteile durch In-situ-Umform-Fügen. In: 7. Landshuter Leichtbau-Colloquium (2015) (Huber, O.; Bicker, M. et al. Eds.). Fachhochschule Landshut, Landshut, Germany, 2015.

[Tek15] Tekkaya A., Hahn M., Hiegemann L., Weddeling C. and Ben Khalifa N.: Umformen faserverstärkter thermoplastischer Kunststoff-Halbzeuge mit metallischen Deckblechen für den Leichtbau. In: EFB T40-Intermezzo der hybriden Werkstofflösungen: Hat Blech eine Zukunft? (EFB Ed.). EFB, Hannover, 2015, P. 185–199.

[Thy09a] ThyssenKrupp Stahl AG: BONDAL® Composite material with structure-borne sound damping properties, 2009.

[Thy09b] ThyssenKrupp Steel Europe AG: Bondal®: Steel sandwich material for effective reduction of structure-borne sound, 2009.

[Thy12] ThyssenKrupp Stahl AG: Litecor liegt im Leichtbautrend. Die moderne Art wirtschaftlich zu bauen, 2012.

[Thy14a] ThyssenKrupp Stahl AG: Application Potential of Litecor in the Body. ATZextra worldwide, 2014 (19), P. 108–111.

[Thy14b] ThyssenKrupp Steel Europe AG: Bondal E Improves the Acoustics of Electric Motors. In: The Project ThyssenKrupp InCar plus: Solutions for Automotive Efficiency (HEINTZEL, A. Ed.). Springer Automotive Media, 2014.

[Thy14c] ThyssenKrupp Steel Europe AG: Leichtbau bei Tür-Aussenhaut. ATZextra, 2014 (19), P. 115–118.

[Thy14d] ThyssenKrupp Stahl AG: Einsatzpotenzial von Litecor in der Karosserie. ATZextra, 2014 (19), P. 108–111.

[Thy14e] ThyssenKrupp Steel Europe AG: Weight reduction with steel: LITECOR from ThyssenKrupp Steel Europe joins the race. https://www.thyssenkrupp-steel.com/en/press/press-releases/press-release-6552.html.

[Tom01] Tomblin J., Yang C. and Harter P.: Investigation of Adhesive Test Methods for Thick Bondline Joints. Report No. DOT/FAA/AR-01/33, 2001.

[Tsc77] Tschätsch H.: Taschenbuch Umformtechnik. Verfahren, Maschinen, Werkzeuge. Hanser, München, Wien, 1977.

[Tse10] Tseng H.-C., Hung C. and Huang C.-C.: An analysis of the formability of aluminum/copper clad metals with different thicknesses by the finite element method and experiment. The International Journal of Advanced Manufacturing Technology, 2010 (49), P. 1029–1036.

[Ucs10] Ucsnik S., Scheerer M., Zaremba S. and Pahr D.: Experimental investigation of a novel hybrid metal–composite joining technology. Composites Part A: Applied Science and Manufacturing, 2010 (41), P. 369–374.

[VDA09] VDA: Acting for Climate Protection - CO_2-Reduction in the Automotive Industry. On the right track, Frankfurt am Main, Germany, 2009.

[VDA10] VDA238-100: VDA 238-100 Plate bending test for metallic materials. Verband der Automobilindustrie e. V. (VDA), Berlin, Germany, 2010.

[Vel05] Velthuis R., Mitschang P. and Schlarb A.: Prozessführung zur Herstellung und Eigenschaften von Metall / Faser-Kunststoff-Verbunden. Institut für Verbundwerkstoffe GmbH, Kaiserslautern, 2005

[Vol11] Volk W. and Hora P.: New algorithm for a robust user-independent evaluation of beginning instability for the experimental FLC determination. International Journal of Material Forming, 2011 (4), P. 339–346.

[von05] von Hippel P.: Mean, Median, and Skew: Correcting a Textbook Rule. Journal of Statistics Education, 2005 (13), P. https://ww2.amstat.org/publications/jse/v13n2/vonhippel.html.

[Wei07] Weiss M., Dingle, M. E., Rolfe, B. F. and Hodgson, P. D.: The Influence of Temperature on the Forming Behavior of Metal/Polymer Laminates in Sheet Metal Forming. Journal of Engineering Materials and Technology, 2007 (129), P. 530–537.

[Wie11] Wielage B., Nestler D., Steger H., Kroll L., Tröltzsch J. and Nendel S.: CAPAAL and CAPET – New Materials of High-Strength, High-Stiff Hybrid Laminates. In: Integrated Systems, Design and Technology 2010. Springer Berlin Heidelberg, 2011, P. 23–35.

[Wu14] Wu W., Abliz D., Jiang B., Ziegmann G. and Meiners D.: A novel process for cost effective manufacturing of fiber metal laminate with textile reinforced pCBT composites and aluminum alloy. Composite Structures, 2014 (108), P. 172–180.

[Yan10] Yang T.: Investigation of the strain distribution with lubrication during the deep drawing process. Tribology International, 2010 (43), P. 1104–1112.

[Zin15] Zinn C.: Intrinsische Herstellung hybrider Strukturkomponenten in einem modifizierten RTM-Prozess (SPP1712 Antrag). In: DGM-FA Hybride Werkstoffe und Strukturen. DGM. Paderborn, Deutschland, 2015.

[Zwi15] Zwick/Roell: videoXtens - High precision without contact! Product Information. http://www.zwick.com/en/products/extensometers/non-contact-extensometers/videoxtensr.html, accessed 17 Jan 2016.

List of figures and tables

List of figures

List of tables

Curriculum vitae

Name: Mohamed Harhash

Date of birth: 13.09.1982

Place of birth: Gharbeya, Egypt

Education

04.2012–04.2017: Clausthal University of Technology (TU Clausthal), Institute of Metallurgy (IMET), Metal Forming and Processing
Degree: Doctor of Engineering (Dr.-Ing.)

09.2006–08.2010: Suez University (formerly “Suez Canal University”), Faculty of Petroleum and Mining Engineering, Metallurgy and Materials Engineering
Degree: Master’s degree (M.Sc.)

09.1999–07.2004: Suez University, Faculty of Petroleum and Mining Engineering, Metallurgy and Materials Engineering
Degree: Bachelor’s degree (B.Sc.)

Professional Experience

Since 04.2012: Doctoral candidate and research assistant at IMET, TU Clausthal

Since 03.2006: Teaching and research assistant at Suez University, Faculty of Petroleum and Mining Engineering, Metallurgical & Materials Engineering Department

10.2006–09.2011: Teaching and research assistant.at the German University in Cairo (GUC), Faculty of Engineering and Materials Science (EMS)

Scholarships/Awards

- GERLS scholarship (Call 2011) for a full PhD study at IMET, TU Clausthal
- DAAD Internship (08–09.2008) at IMET, TU Clausthal
- IAESTE scholarship (07–10.2003) at TU Berlin
- Awarded from the Egyptian engineering syndicate due to academic excellence, 2005

Further Qualifications

- Languages: Arabic (native language), German and English
- Computer skills: MS office, MS project, Citavi, Endnote, Abaqus and Origin

This page intentionally left blank

Publications and presentations

Journal papers

Harhash M., O. Sokolova, A. Carradò and H. Palkowski: Mechanical properties and forming behaviour of laminated steel/polymer sandwich systems with local inlays–Part 1. Compos. Struct., 2014, 118; p. 112–120.

Harhash M., A. Carradò and H. Palkowski: Lightweight titanium/polymer/titanium sandwich sheet for technical and biomedical application. Materialwissenschaft und Werkstofftechnik, 2014, 45; p. 1084–1091.

Harhash M., A. Carradò and H. Palkowski: Mechanical Properties and Forming Behaviour of Laminated Steel/Polymer Sandwich Systems with local inlays–Part 2. Stretching and Deep Drawing. Composite Structures, 2017, 160; p. 1081–1094.

Nosova E., N. Lukonina, M. Khramova, M. Harhash and H. Palkowski: Stamping ability of three- and five-layer aluminum-polymer composites (in russ.). Construction of composite materials, 2016, 3; p. 30–37.

Sguazzo C., M. Harhash, M. Grafenhorst, H. Palkowski and S. Hartmann: Deep drawing of a layered composite: material characterization and finite-element simulation. PAMM, 2014, 14; p. 245–246.

Harms V., M. Harhash, A. Carradó and H. Palkowski: Energy Absorption Behavior of Metal/Polymer/Metal Sandwich Crash Structures. Key Engineering Materials, 2017, 746; p. 275–281.

Proceedings

Harhash M., A. Carradò and H. Palkowski: Forming Limit Diagram of Steel/Polymer/Steel Sandwich Systems for the Automotive Industry. In (Sano, T.; Srivatsan, T. S. et al. Eds.): Advanced Composites for Aerospace, Marine, and Land Applications. John Wiley & Sons, Inc., 2014; p. 243–254.

Harhash M., A. Carradò and H. Palkowski: Forming Potential of Low-Density Laminates. In (Wiche, H.; Wesling, V. et al. Eds.): 1. Niedersächsisches Symposium Materialtechnik, 12.-13.02.2016, Clausthal-Zellerfeld. Shaker, Herzogenrath, 2015; p. 53–60.

Harhash M., H. Palkowski, C. Sguazzo and S. Hartmann: Experimental and numerical investigations of metal/polymer/metal laminates: thermo-mechanical and forming characteristics. In (Clausthaler Zentrum für Materialtechnik Ed.): Berichtsband Clausthaler Zentrum für Materialtechnik. Zeitraum 2013-2015. Shaker, Herzogenrath Verlag, 2016; p. 31–45.

Harhash M., V. Harms, A. Carradò and H. Palkowski: Metall-Polymer Sandwichverbunde: nicht nur ein Leichtbaupotential. In (Brosius, A. Ed.): 23. Sächsische Fachtagung Umformtechnik. Den Eigenschaften Form geben, Dresden, Deutschland, 2016; p. 32-41.

Harhash M., A. Carradò and H. Palkowski: Deep- and Stretch-Forming of Steel/Polymer/Steel Laminates. In (Hausmann, J.; Siebert, M. Eds.): 2. Int. Conf. "Euro Hybrid Materials & Structures". DGM, 2016; p. 69–74.

Presentations

Characterization of Laminated Steel/Polymer Sandwich Systems: Mechanical Properties and Forming Behavior. The 17th International Conference on Composite Structures (ICCS17). Porto, Portugal, 17.–21.06.2013.

Effect of core thickness on the mechanical properties and the formability of three layered steel/polymer/steel sandwich structures. 19. Symposium Verbundwerkstoffe und Werkstoffverbunde. Karlsruhe, Germany, 03.–05.07.2013.

Lightweight Ti/Polymer/Ti Sandwich Sheet for Technical and Biomedical Applications. International Congress on Light Materials (Euro LightMat 2013). Bremen, Germany, 03.–05.09.2013.

Forming of Low-Density Laminates. 7. Landshuter Leichtbau-Colloquium (LLC). Hochschule Landshut, Landshut, 25.–26.02.2015.

Forming Potential of Low-Density Laminates. DGM Fachausschusssitzung “Hybride Werkstoffe und Strukturen”. Paderborn University, Paderborn, Germany, 04.–05.03.2015.

Stretch- and Deep-Drawing of Reinforced Low Density Steel/Polymer/Steel Sandwich Laminates. The 19th International Conference on Composite Structures (ICCS19). Porto, Portugal, 05.–09.09.2016.

Sandwichverbunde mit angepassten Eigenschaften für den Automotivbereich. Metallurgie-Kolloquium und Alumnitreffen 2016. Institute of Metallurgy. Clausthal-Zellerfeld, Germany, 03.–04.11.2016.